

Dissertation

博士論文

Quantum Theory and Experimental Demonstration of a
Coherent Computing System with Optical Parametric
Oscillators

(光パラメトリック発振器を用いたコヒーレント計算機
の量子論及び実装実験)

Graduate School of Information Science and Technology
the University of Tokyo

In Partial Fulfillment of the Requirements for the Degree of
Doctor of Philosophy

Kenta Takata

高田 健太

©2014 by Kenta Takata. All Rights Reserved.

Abstract

It is quite non-trivial to give the best answers of many tasks in our daily life and business, such as planning an efficient travel route, arranging a good rotating roster and designing a compact electric circuit. Such problems can be modeled as combinatorial optimization problems, and many of them belong to non-deterministic polynomial (NP)-complete and NP-hard classes. It is believed that they cannot be solved in a polynomial time, and are intractable for digital computing algorithms.

One of the fundamental combinatorial optimization problems relevant with physics is to find a ground state of Ising Hamiltonian. This is called Ising problem and includes NP-Hard instances. Many schemes originating from physics such as simulated annealing, quantum annealing and adiabatic quantum computation are being vastly studied for this problem. However, their full potentials are still being explored. We have recently proposed a new emulator for the Ising spin system named coherent Ising machine, which is an oscillator network coupled with mutual injections. In the machine, each spin is mapped to a degree of freedom in the intracavity field of each oscillator, and the spin-spin interaction is mimicked by the mutual injections. The problem Hamiltonian is incorporated in the total photonic gain i.e. the effective loss of the system. The gradually pumped system is expected to oscillate in the state with the artificial spin configuration giving the minimum loss, which corresponds to one of the ground states.

There are two types of the Ising machine proposed, the injection-locked laser network machine and the degenerate optical parametric oscillator (DOPO) network machine, and the latter has a binary nature. A DOPO has one of the two relative phases 0 or π , and these binary and out-of-phase states can be utilized as an artificial spin. The initial benchmarking with a semi-classical model has shown a promising result on NP-hard instances up to 20 variables. However, regarding its working principle, it is important if the machine has any quantum properties available for computation, because quantum computing is the only paradigm having some theoretical evidences to possibly surpass digital computing. Also, proof-of-principle experiments and prospects for the realization of a system for large-size problems are desired.

In this thesis, I study the machine based on DOPOs both theoretically and experimentally. On the theoretical side, I focus on the physics of the DOPO network coupled with mutual injections and investigate its quantum states. Here, I develop a fully quantum mechanical model for the network using the positive P representation, and numerically simulate the system of two DOPOs with out-of-phase mutual injections.

Here, I explicitly consider the signal field in the mutual injection path between the two DOPO facets as a cavity mode. The stochastic simulation with a small noise parameter has been conducted under the gradually increasing pumping rate from the below to above of the threshold. The result has shown that small incoherent intracavity loss rates are indispensable in quantum effects in the system. When the incoherent loss in the injection path has the same order as the coherent transmission rates at the DOPO facets, the signal fields in the two DOPOs have the quantum correlation in terms of the squeezed quadrature amplitude $\hat{p} = (\hat{a} - \hat{a}^\dagger)/2i$. This also indicates the entanglement between the two DOPO fields. When the loss of the injection path is fairly smaller than the transmission, the two intracavity fields can show weak coherent superposition components via the small fringes in the distribution functions for \hat{p} . The superposition components with a small noise parameter and under a relatively non-transient operation have not been expected by previous relevant studies on a single DOPO. It suggests that the mutual injection path storing the squeezed vacuum is simple realization of the squeezed reservoir, which suppresses the decoherence on the superposition components.

On the experimental side, I perform the first-time and second-time experimental demonstrations of the coherent Ising machines based on degenerate optical parametric oscillators in collaboration with Alireza Marandi at Stanford University. The system is based on the time-multiplexed DOPO network composed of femtosecond DOPO pulses running in a single ring cavity. Each DOPO pulse randomly takes one of the binary phase states with their phase difference being π and is utilized as an artificial spin. The signal pulses keep the phase coherence allowing the interference between them. Mutual injections are achieved by the optical delay lines implemented with pairs of input and output couplers placed in the resonator. The first system built by us contains four DOPO pulses at 2 μm and three delay lines. Also, I have designed and constructed another system with 16 signal pulses at telecom wavelengths. They have been applied to instances on one-dimensional ring and cubic graphs. Very high success probabilities to find ground states of them indicate a big potential of this machine for intractable optimization problems.

Acknowledgement

I would extend my deepest gratitude for many individuals who greatly helped me in my PhD course.

First and foremost, I definitely appreciate Professor Yoshihisa Yamamoto, who has guided me as a principal investigator for the entire program. He has always treated me as a someone engaged in science, given me chances for discussion and advice when needed, and pointed a higher achievement for my goal. He gave me quite a big opportunity to work on the experimental research in Stanford University for a half year, and the experiment also in RIKEN after coming back. I have seen that he has been always working on something novel powerfully with his sharp insight and profound knowledge, involving many prominent scientists, to animate the current and future technology of Japan, and the world. I think I have learned many from him, but five years still might not suffice. Without him, I could not have completed this thesis.

I am really grateful to Professor Jun Adachi, who kindly accepted me after Professor Yamamoto resigned his job at NII for the government project, wholly for me to continue my study in the PhD course. I can imagine that he would not be comfortable to care an unfamiliar student in his group. However, he saw to it that I did not need to mind this difficult situation. It was a big help and relief to me.

I am much in debt to Shoko Utsunomiya, who kicked off the coherent computing project with Professor Yamamoto and me, took over and organized the research group in NII and supported me mainly in my experimental work.

I keep my appreciation to Professors Masaaki Tanaka and Shinobu Ohya, who were the principal investigators in my undergraduate research. I learned basics of science and research in their group, and it is still a fundamental part of me.

I am deeply thankful to many faculties of the University of Tokyo including my dissertation and oral examination committees: Professors Kenjiro Taura, Kazuro Kikuchi, Kazuyuki Aihara and Motoichi Ohtsu. Professor Seigo Tarucha kindly took care of the lab in RIKEN and supported me there after Professor Yamamoto's leaving. Professor Hitoshi Iba gave me chances to talk and discuss my research as an advisory faculty. Professor Yasunobu Nakamura always provided constructive advice to me when we met at workshops and conferences.

I also would like to appreciate prominent scientists who largely helped me in my Ph.D years. I am really grateful to Professor Robert L. Byer who kindly accepted my joining the experiment in his lab at Stanford University. I was benefited from Professor

ACKNOWLEDGEMENT

Ken-ichi Kawarabayashi at National Institute of Informatics for fruitful discussion and inspiring me to study computational science and graph theory. The experimental class by Professor Koji Igarashi, now in Osaka University, educated me a lot and possibly heralded the change of my research field to laser science and quantum optics. Professor Yoshiro Takahashi at Kyoto University took thought for me at workshops and conferences and gave me chances for valuable discussions.

Yamamoto group is a totally special organization which straddles various branches. I would like to thank all the members in the group. Alireza Marandi is my great mentor since my six-month stay at Stanford University in 2013 for the experimental work on the four-oscillator system. He is really an expert on experiment, and kindly taught me his techniques. The experience there with him was the most exciting time to me in my Ph.D course. Talking with him also gave me the cue to work on the quantum theory of degenerate parametric oscillators. This thesis is largely inspired and guided by him. Zhe Wang founded the theoretical basis of the coherent computer based on degenerate parametric oscillators and hence introduced me into this subject. Discussion with him served as a trigger to significantly brush up my theoretical work. Kai Wen was my collaborator for the study in my master thesis. He has a really quick mind and also is fast at work, then sped up our research. I wish him every success in his new territory. Peter L. McMahon and Kristiaan De Greve kindly treated me when I visited Stanford for the conference. Na Young Kim was the host when I stayed at Stanford in my first year of the course. She kindly taught me the basics of the experiment on polaritons and arranged the group meeting. Leo Yu kindly helped me about the roster of the group talk, but unfortunately I have not paid my debt to him yet. Kirk Ingold in Byer group helped me in the lab with Alireza and had friendly talks with me during my stay at Stanford.

In the NII group, Shuhei Tamate gave me the most help for the startup of the lab in RIKEN. He also kindly dealt with many office jobs about the lab and the moving of the office in NII. Discussion with him led to improvement in the result of my simulation work. Kenichiro Kusudo gave advice to and helped me in my stay at Stanford last year. I could enjoy my life there thanks to him. Tomoyuki Horikiri kindly guided me on how to handle the servo controlling system. He stayed at the apartment in Palo Alto which I was in after my leaving and kindly helped me with some important postal matters of mine. I thank them also for their friendships. And, I spent a fun time with Naoyuki Masumoto, Natsuko Ishida, Kai Yan, Nobuyuki Takahashi, Tomoya Matsukawa, Yasuhiro Matsuo, Md Javed Rouf Talukder, Yorihiro Nobuta, Koki Matsushita, Yoshitaka Haribara, Taro Kambara, Daiki Maruo and Hiromasa Sakaguchi and had interaction with Taisei Suzuki in Koashi group, the University of Tokyo.

In the RIKEN group, Eisuke Abe helped me a lot when I set up the lab in RIKEN. I have enjoyed technical and private talks with Michael Fraser since he was in NII. I also had a great time there with Takeshi Fukuhara, Makoto Yamaguchi, Toshihiko Sasaki, Yuichi Katori and Timothee Leleu.

I would like to appreciate the administration staffs in Yamamoto group: Yukiko Sato, Yoko Shioda, Tomoko Notoya and Risa Aihara in NII, Yurika Peterman and Rieko

ACKNOWLEDGEMENT

Sakaki in Stanford. They have been really professional so I can always have trusted in their work. I also deeply thank Lola R. Enriquez in Stanford who kindly and patiently resolved the clerical oversight on my on-line account.

I would like to thank Hiroyasu Tajima, Mitsuki Kimura, Yuta Masuyama, Shota Nagayama, Daisuke Sakuma, Takanobu Suzuki and Ryuta Yamamoto for their friendships and technical talks. It is my anchorage that they also have hung in there for their student lives. I also thank Hiroki Nishibayashi, Daisuke Kubota and Shunichi Tsunoda who took thought for me also when I was in very hard times.

Finally, I would like to thank my family, my parents, brothers and relatives for their continuous supports till I have come this far.

December 2014

Contents

Abstract	ii
Acknowledgement	iv
1 Introduction	1
1.1 Computational Complexity	1
1.1.1 Time complexity	1
1.1.2 NP problems	2
1.1.3 NP-hard problems	2
1.1.4 NP-complete problems	2
1.2 Ising Model and Ising Problem	3
1.2.1 Combinatorial optimization problems	3
1.2.2 Ising model	3
1.2.3 Hardness of Ising model	4
1.2.4 MAX-CUT problem	5
1.3 Complexity Classes in Layers	6
1.4 Recent Trends of Quantum Computing	6
1.4.1 Gate model quantum computer	6
1.4.2 Quantum simulator	8
1.4.3 Quantum annealer	8
1.5 Coherent Computing	10
1.5.1 Injection-locked laser network system	10
1.5.2 Degenerate optical parametric oscillator system	12
1.5.3 Agendas	12
1.6 Thesis Structure	13
2 Quantum Theory of DOPO	15
2.1 Degenerate Optical Parametric Oscillator	15
2.2 Total System Hamiltonian	15
2.3 Theoretical Model for DOPO as Open Quantum System	16
2.3.1 Master equation for single-mode damped harmonic oscillator	17
2.3.2 Master equation for a DOPO	24
2.3.3 Positive P -representation	24

2.3.4	Quantum mechanical Fokker-Planck equation	26
2.3.5	Stochastic differential equations	28
2.4	Properties of DOPO	30
2.4.1	Classical solution for steady state	30
2.4.2	Potential solution in quantum theory for steady state	31
2.4.3	Output squeezing spectra	36
2.4.4	Macroscopic superposition state	41
2.4.5	Entanglement Between Two DOPOs Under Evanescent Coupling	45
2.5	Coherent Ising machine	49
2.6	Summary	50
3	Quantum States in Two DOPOs Coupled with Mutual Injection	52
3.1	Introduction	52
3.2	Derivation of Theoretical Model	53
3.2.1	System overview	53
3.2.2	System Hamiltonian	54
3.2.3	Stochastic equations	55
3.2.4	Adiabatic elimination of mid cavity mode	58
3.3	Simulation Substances	59
3.3.1	Simulation setting	59
3.3.2	Observable moments and distribution functions	60
3.3.3	Criterion for entanglement	61
3.3.4	Quantum discord	61
3.4	Simulation Result	63
3.4.1	Mean photon number	64
3.4.2	Correlation function of quadrature amplitudes	65
3.4.3	Total fluctuation of EPR-type operators	68
3.4.4	Quantum discord	68
3.4.5	Distribution functions for quadrature amplitudes	70
3.5	Discussion	73
3.5.1	Other theoretical schemes	73
3.5.2	Accuracy and limit of simulation	74
3.5.3	Application for coherent Ising machine	75
3.6	Conclusion	75
4	Design and Operation of Pulsed Sub-Harmonic OPO	77
4.1	Introduction and Basic Theory	77
4.1.1	Pulsed OPO	77
4.1.2	Condition for large gain	78
4.1.3	Quasi phase matching	79
4.1.4	Gain bandwidth	80
4.1.5	Phase sensitive gain and phase states at degeneracy	81
4.1.6	Frequency states	81
4.2	Design of a Pulsed OPO	82

CONTENTS

4.2.1	Pump laser	82
4.2.2	Cavity stability	82
4.2.3	Mode matching	84
4.2.4	Astigmatism compensation with angled mirrors	85
4.2.5	Poling period of nonlinear crystal	87
4.2.6	Gain bandwidth	89
4.2.7	Pulse walk off	89
4.2.8	Electrical cavity locking system	90
4.2.9	Other information of the system	90
4.3	Operation of a 16-Pulse OPO with Telecom Wavelengths	91
4.3.1	Cavity modes in scanning operation	92
4.3.2	Power stability in continuous operation	92
4.3.3	Pulse pattern	92
4.3.4	Output power	94
4.3.5	Spectrum	94
4.3.6	Pulse duration	94
4.3.7	Coherence property	96
4.4	Summary	97
5	Demonstration of Coherent Ising Machine with Time-Multiplexed DOPO Networks	98
5.1	Background	98
5.1.1	Short introduction	98
5.1.2	Phase transition in DOPOs	99
5.1.3	Gradual pumping scheme of the Ising machine	100
5.2	Experiment on the 4-pulse system	100
5.2.1	Setup and implementation	100
5.2.2	Result	103
5.3	Experiment on the 16-pulse system	104
5.3.1	Implementation	104
5.3.2	Result	108
5.4	Discussion	118
5.5	Conclusion	119
6	Conclusion	120
6.1	Summary	120
6.2	Future prospects	121
A	Simulation Result of the Two-DOPO System with Statistical Convergence	123
B	Additional Data of the Experiment	126
B.1	RF spectrum	126
B.2	Beam spot	126

CONTENTS

Bibliography	128
List of Related Publication	143

List of Figures

1.1	Dimensionality of the Ising model [1–3].	4
1.2	Inclusion relation between the major time complexity classes and examples of the problems in each.	7
1.3	A schematic illustration of a coherent computing system for the $N = 4$ Ising model. OSC: oscillator, EXT: external signal, DT: detector, IS: isolator, OC: optical components. Some unnecessary paths are omitted. . .	11
2.1	Schematic representation of a optical parametric oscillator.	16
2.2	Average photon numbers of the signal and pump modes dependent on the pumping rate in the classical model. $\gamma_s = 1$, $\gamma_p = 10$, $\kappa = 0.14142$	32
2.3	Quasi-distribution function $P(\alpha_s, \beta_s)$ in the classical subspace for a DOPO under the adiabatic elimination. (a) $\lambda = \varepsilon_p/\varepsilon_{th} = 0.5$. (b) $\lambda = 2$. $\gamma_s = 1$, $\gamma_p = 2$ and $\kappa = 1$	34
2.4	The average photon numbers dependent on the normalized pumping rate. $\gamma_s = 0.2$, $\gamma_p = 1$ and $\kappa = 0.2$	35
2.5	The variances in the fluctuation of the quadrature amplitudes which show squeezing. $\gamma_s = 0.2$, $\gamma_p = 1$ and $\kappa = 0.2$	36
2.6	The resonant output fluctuation variance $S_{OUT}(\omega = 0)$ dependent on the pump rate (a) below the threshold and (b) above the threshold. $\gamma_s = 0.2$, $\gamma_p = 1$ and $\kappa = 0.2$	40
2.7	The output fluctuation spectra for quadrature amplitudes with (a) $\lambda = 1$ and (b) $\lambda = 10$. $\gamma_s = 0.2$, $\gamma_p = 1$ and $\kappa = 0.2$	40
2.8	The intracavity fluctuation variance for quadrature amplitudes (a) below and (b) above the threshold in the first-order approximation. $\gamma_s = 0.2$, $\gamma_p = 1$ and $\kappa = 0.2$	42
2.9	Distribution functions for the quadrature amplitudes of the cat states with $\alpha = 5$. (a) $P_{+, \alpha}(x)$, (b) $P_{-, \alpha}(x)$, (c) $P_{+, \alpha}(p)$ and (d) $P_{-, \alpha}(p)$	43
2.10	Quasi-distribution functions for the normalized variables $P_{ss}(X_\eta, Y_\mu)$ in the classical subspace of the positive P-representation. (a) $\lambda = 0.5$, (b) $\lambda = 1$ and (c) $\lambda = 2$. $g = 3$	44

2.11	Transient of the distribution functions (a) $P(x)$ and (b) $P(p)$ of the DOPO signal field. $g = 3$, $\lambda = 15$ and $\Delta\tau = 2 \times 10^{-5}$. The system is abruptly pumped at $\tau = 0$. 20000 samples were used. I made sure that the distribution functions were well convergent by 10000 samples.	45
2.12	Fluctuation spectrum of the sum of the EPR-type operators $\langle\Delta u_-^2\rangle + \langle\Delta v_+^2\rangle$. (a) Frequency dependence with $\varepsilon_p = 0.5\varepsilon_{th}$. (b) Pump rate dependence at resonance $\omega = 0$. $\gamma_s = \gamma_p = \kappa = J_p = \Delta_p = 1$. $J_s = \Delta_s$. $S_{u-,OUT} + S_{v+,OUT} < 1$ represents the entanglement between the fields in the two DOPOs.	49
2.13	Transit of the in-phase quadrature amplitude x_i in a coherent Ising machine composed of two DOPOs with an out-of-phase mutual injection. $\lambda = 2$ and $\xi_{ij} = -1$	51
3.1	Schematic drawings of the system. (a) The whole system comprising two DOPOs and the mutual injection path between them as a cavity. The two dichroic mirrors in this mid cavity are assumed to pass the pump field completely and highly reflect the signal field. (b) Beamsplitter interaction between the DOPO fields and the central cavity mode. The spacial phase of the mid cavity field needs to be considered.	54
3.2	Transient of the intracavity photon number in a DOPO dependent on (a) the signal loss of the system under $\gamma_c = 2\gamma_s$, (b) the mid-cavity decay rate γ_c and (c) the mutual injection coefficient ξ . In (c), the center cavity is adiabatically eliminated. The normalized oscillation threshold depends on the effective mutual injection strength, varying with the parameters. 20000 stochastic runs for each curve.	66
3.3	Time dependency of the correlation functions for the signal quadrature amplitudes. (a) The loss in the system with $\gamma_c = 2\gamma_s$, (b) the center cavity loss γ_c and (c) the mutual injection strength ξ are varied. x_j are negatively and macroscopically correlated along with the oscillation. p_j are positively and microscopically correlated before the oscillation. 20000 stochastic runs for each curve.	67
3.4	Time evolution of the total fluctuation in the EPR-type operators $\langle\Delta u_+^2\rangle + \langle\Delta v_-^2\rangle$ dependent on (a) the loss in the system with $\gamma_c = 2\gamma_s$, (b) the mid-cavity loss γ_c and (c) the coupling coefficient ξ . $\langle\Delta u_+^2\rangle + \langle\Delta v_-^2\rangle < 1$ means the entanglement between the DOPO signal fields. 20000 stochastic runs for each curve.	69
3.5	Quantum discord when the state is approximated as a bipartite Gaussian state. Squeezing in the DOPOs below the threshold and the mutual injection give a large discord. Coherent fields above the threshold in them and a coherent classical communication lead to a finite discord. 20000 stochastic runs for each curve.	71

LIST OF FIGURES

3.6	Distribution functions at different time points for (a) x_j and (b) p_j . The dashed lines in (a) are Gaussian fitting curves with $\sigma = (6.6, 9.1, 13.5, 20.0)$ for $\tau = (29, 31, 33, 35)$. The insets in (b) show the zoomed curves around the side peaks. 200000 trajectories are used. $\gamma_s = 0.1$, $\gamma_c = 0.2$ and $g = 0.01$	72
3.7	Variances of p_1 (blue curve) and p_2 (red curve). The two curves are almost identical due to the same form of the SDEs for each DOPO. 200000 trajectories are used. $\gamma_s = 0.1$, $\gamma_c = 0.2$ and $g = 0.01$	74
4.1	Schematic illustration of the pulsed OPO system. HWP: half wave plate. PBS: polarizing beam splitter. M: mirror. PD: photo detector. OC: output coupler. PZT: piezoelectric transducer.	83
4.2	Cavity stability dependent on the short cavity length. The width of stability range is found to be $520 \mu\text{m}$. The minimum spot size in the crystal is $8.2 \mu\text{m}$ for the stablest short cavity length.	83
4.3	The pump spot size dependent on the propagation distance. Solid line: the simulated spot size with the measured data of the pump laser and a lens pair. Dashed line: the desired spot size calculated from the waist $w_p = 5.80 \mu\text{m}$ at the middle of the crystal. Dots: mean of the measured spot sizes in vertical (x) and horizontal (y) directions.	86
4.4	Simplified drawing of the system with angled concave mirrors. FM: flat mirror. CM: concave mirror. θ_M : mirror angle. t_C : thickness of the crystal. The reference in the propagation direction (z axis) is taken so that the free-space propagation lengths before and after short arm cavity are the same.	86
4.5	Simulated stability range depending on the short cavity length for a 4.8 m cavity with curved mirrors with a ROC of 50 mm and a 1-mm long PPLN crystal at Brewster angle. (a) Stability ranges for the two orthogonal components of the beam and different mirror angles θ_M drawn by colored points. (b) Width of the range of the whole signal beam for varying θ_M	88
4.6	Quasi phase matching condition (a) for the poling period and crystal temperature under a fixed degenerate signal wavelength $\lambda_s = 1.588 \mu\text{m}$. (b) That for the degenerate signal wavelength and temperature in a crystal with a period of $20.4 \mu\text{m}$	88
4.7	Normalized gain spectrum for the signal mode. Different curves are for different crystal lengths. A 1 mm-long crystal has a good bandwidth for the given pump laser properties.	90
4.8	A schematic of the servo controller used to keep the signal output power maximum.	91
4.9	Average power of the OPO output dependent on the cavity length, showing longitudinal oscillation peaks. The average pump power is 300 mW.	93
4.10	Temporal stability of the average output power of the OPO locked to the strongest oscillation peak. The average pump power is 300 mW.	93

LIST OF FIGURES

4.11	Temporal pulse envelopes for (a) peak 1, (b) peak 2 and (c) peak 3. The average pump power is 300 mW.	93
4.12	Average output powers of the tops of the three oscillation peaks dependent on the pump power. One of the two output couplers with 10% reflection is used to take the signal.	95
4.13	Optical power spectra for the three oscillation peaks.	95
4.14	Autocorrelation trace of the two-photon absorption for the degenerate OPO pulses.	96
4.15	The interference output of pairs of adjacent DOPO pulses. (a) A high-visibility example. (b) A low-visibility example. High-intensity pulses come from pairs of in-phase pulses. Low-intensity pulses are because of pairs of out-of-phase pulses. Each pulse randomly takes a relative phase of 0 or π , leading to a random pulse-intensity configuration at every operation.	97
5.1	Schematic illustration of the optical field for an OPO pumped (a) below the threshold and (b) above the threshold	100
5.2	Mapped energy and probability landscapes in the DOPO network (a) below the threshold and (b) above the threshold, illustrating the gradual pumping scheme.	101
5.3	A schematic of a coherent Ising machine based on a 4-pulse DOPO. The pump laser is a femtosecond fiber laser with a center wavelength of 1045 nm. The three delay lines implement the optical coupling between the pulses. An unequal-arm Michelson interferometer measures the relative phases of adjacent DOPO pulses.	102
5.4	Illustration of the couplings between DOPO pulses with the optical delay lines. Delay 1, 2 and 3 give $(J_{12}, J_{23}, J_{34}, J_{41})$, $(J_{13}, J_{24}, J_{31}, J_{42})$ and $(J_{14}, J_{21}, J_{32}, J_{43})$, respectively.	103
5.5	All the possible pulse patterns of the output of the unequal-arm Michelson interferometer in the 4-DOPO system. We do not have a time reference in the measurement hence we do not distinguish a pulse pattern and its cyclic permutations.	105
5.6	(a) Slow detector readout and (b) histogram of the measured interferometer output pulse patterns for the system with no mutual injection. The expected frequencies of the low, middle and high intensities of the detector signal in (a) is 1:6:1. That for the output pulse trains [0000], [1100], [1010] and [1111] in (b) is 1:4:2:1.	105

5.7	(a) Slow detector readout and (b) histogram of the measured interferometer output pulse patterns for the system with out-of-phase couplings between all the DOPO pulses via the three delay lines. Here, the MAX-CUT problem for the four-node complete graph is programmed in the system. The expected frequencies of the low, middle and high intensities of the detector signal in (a) is 1:2:0. That for the output pulse trains [0000], [1100], [1010] and [1111] in (b) is 1:0:2:0. No erroneous pattern is obtained in 1000 independent trials as seen in (b).	106
5.8	A coherent Ising machine based on a 16-pulse DOPO. The pump laser is a Ti:sapphire femtosecond pulse laser with a center wavelength of 794 nm. The two servo controllers are used to operate the system stably under the operation of the chopper.	107
5.9	Detector readouts for the system without the mutual injection. (a) An example of the interferometer pulse patterns measured with the fast detector. (b) The average output power under the chopping with a frequency of 60 Hz. (c) Distribution of the average output power out of 1500 trials.	109
5.10	The temporal interferometer output power for the system with a single delay line. (a) Fast detector readout in the case of in-phase unidirectional couplings. (b) That for out-of-phase unidirectional couplings. (c) Slow detector readout under the scanning of the delay path length.	111
5.11	Fast detector readouts of the interferometer output for the 16-DOPO pulse system with the bidirectional in-phase couplings in the form of the one-dimensional ring. The performance depends on the temporal interference between the cavity pulses and injected pulses. (a) The stablest state corresponding to the ground state of the ferromagnetic Hamiltonian. (b) An excited state with two domains of in-phase pulses. (c) An excited state seen when the locking points of the delay lines are not good. Finite residual coupling phases rotate the phases of the boundary pulses and make the output peak powers non-discrete around them. The mapped spin configuration for each output is added.	113
5.12	Fast detector signal of the output for the 16-DOPO system with the bidirectional out-of-phase couplings in one dimension. (a) The state with the minimum gain, corresponding to the ground state of the anti-ferromagnetic Hamiltonian. (b) An excited state with two clusters of out-of-phase pulses. (c) An excited state for the case of bad locking points of delay lines. The output peak powers are not binary around the boundary pulses. The mapped spin configuration for each output is added.	113

5.13	An example of the normalized slow detector readout for the (a) signal and (b) pump interference in the case of the emulation of the 1-D ring ferromagnetic Ising model of 16 spins. The peaks around the maximum level in (a) correspond to the phase state configuration with the global in-phase order hence one of the ground states of the ferromagnetic Ising model. The power fluctuation of them is about 5% to the mean thus the ground states can be detected with the average power. The arrowed peak in (a) is a possible error, however, it can be seen in (b) that it is just due to a sudden degradation of the visibility of the interferometer by environmental noise. Such inessential and few errors are omitted in the evaluation of the success probability.	114
5.14	An example of the slow detector readout for the (a) signal and (b) pump interference in the case of the emulation of the 1-D ring anti-ferromagnetic Ising model of 16 spins. The PD signal is normalized by the maximum power in the ferromagnetic case. The arrowed peak with a relatively high level in (a) is counted as an intrinsic error because the corresponding power level of the pump interferometer output is as high as the other ones.	114
5.15	(a) The cubic graph implemented in the system with the three delay lines of 0.3, 2.4 and 4.5 m. (b) Fast detector signal of the interferometer output corresponding to the ground states of the anti-ferromagnetic Ising problem on (a). A mapped spin configuration along with the spatial pulse sequence in the ring cavity is added. Red dashed lines denote the frustration between adjacent artificial spins.	116
5.16	The interferometer output pulse patterns for the two failed cases both of which correspond to local minima. (a) reflects the couplings along with the diameter chords of the graph. (b) is affected by the anti-ferromagnetic order of the 1-D ring structure. Red dashed lines for the mapped spin configuration in (a) mean the frustration between adjacent spins. Note that all the couplings along with the diameter chords ($J_{n \ n+8(mod\ 16)}$) are frustrated in (b), although it is not directly reflected in the output signal.	117
5.17	A possible implementation for a closed delay line. It replaces a cavity mirror (M3, 4 or 5 in Fig. 5.8) with a partially transmitting mirror. The transmitted pulses are fed back with a short ring cavity. The cavity length is locked with the resonance of the pump beam detected by the Si PD. . .	119
A.1	Simulation result of the 2-DOPO system with 200000 samples. $\gamma_s = 0.1$, $\gamma_c = 0.2$ and $g \sim 0.01$. (a) Signal photon number in DOPO1. (b) Variances of the quadrature amplitudes $V(x_1)$ and $V(p_1)$ indicating the intracavity squeezing. (c) Correlation function $\langle x_1 x_2 \rangle$. (d) Correlation function $\langle p_1 p_2 \rangle$. (e) Total fluctuation of the EPR-type operators $\langle \Delta u^2 \rangle + \langle \Delta v^2 \rangle$. (f) Gaussian quantum discord in the system.	124

- A.2 Simulation result of the 2-DOPO system with 200000 samples up to $\tau = 50$. $\gamma_s = 0.03$, $\gamma_c = 0.25$ and $g \sim 0.03$. (a) Signal photon number in DOPO1. (b) Variances of the quadrature amplitudes $V(x_1)$ and $V(p_1)$ indicating the intracavity squeezing. (c) Correlation function $\langle x_1 x_2 \rangle$. (d) Correlation function $\langle p_1 p_2 \rangle$. (e) Total fluctuation of the EPR-type operators $\langle \Delta u^2 \rangle + \langle \Delta v^2 \rangle$. (f) Gaussian quantum discord in the system. . . . 125
- B.1 RF spectra for the signal modes of the DOPO without delay lines. The peak frequency is 1.00956 GHz and corresponds to the pulse repetition frequency. The pump power is 300 mW. (a) The strongest degenerate mode (peak 1 in Chapter 4). (b) The second strongest non-degenerate mode (peak 2). (b) has side peaks indicating the unstable operation. . . . 127
- B.2 Beam spots measured with a slit beam profiler for the DOPO with three delay lines. The system is strongly pumped and has degenerate modes in an odd and even frequency state. (a) Spot of an even frequency state (suitable for coherent computing). (b) One in an odd frequency state. . . 127

Chapter 1

Introduction

I give an extensive introduction for the coherent computing and the work in this thesis from interdisciplinary points of view.

1.1 Computational Complexity

1.1.1 Time complexity

Information technology is indispensable in our modern life. General-purpose devices such as personal computers and smart phones are so prevalent that they enable us to daily search for the meaning of an unfamiliar word, see the weather forecast and the schedule of trains, find a good route to the conference hall, book a room of the hotel, and buy some gadgets online, etc. Industry also utilizes information processing for various kinds of business like developing products, merchandise control, and dealing with stocks and currencies. Nowadays we take these technologies surrounding us for granted.

In terms of computation, such a function is regarded as a problem to return the desired output according to the input from users. Here, the problem is decomposed into elementary arithmetic processes and memory/file processes on certain types of variables [4]. The difficulty of the problem [5] can be classified with the number of these operations necessary to finish it depending on the input size (problem size), because this directly reflects the corresponding time consumption for a constant computing resource. The degrees of the difficulty defined in this sense are called *complexity classes*. For example, the problems in the class P can be solved with polynomial numbers of operations to the problem size (polynomial time). On the other hand, those in the class $EXPTIME$ require exponentially growing computational times to the best-known algorithms for the deterministic Turing machine (DTM), which is the abstract of the digital computing paradigm. Such problems are called intractable. Unarmed with good algorithms reflecting the problem structures, we will need more than a century to solve the problems believed to be in $EXPTIME$ such as Traveling Salesman Problem (TSP) and Knapsack Problem with several tens of variables.

1.1.2 NP problems

There is another concept of a hypothetical computing model called nondeterministic Turing machine (NDTM). Informally, it is allowed to run an arbitrary number of computing processes parallelly. The problems which can be solved in a polynomial time with a NDTM are called NP problems, and their complexity is defined as the class NP. NP is defined for decision problems which can be answered with the statement “Yes” or “No”. We can also think that NP means the polynomial-time verifiability for the best candidate of the condition for the decision “Yes”, and that the best candidate is picked by the hypothetical device called “guessing module” of NDTM in a polynomial time. For example, integer factorization is in NP because whether a given prime number can factor the number in question can be determined in a polynomial time with the Euclidean algorithm. NP is an important concept to identify the set of the intractable problems which are as hard as each other, rather than characterize the practical computational time to solve these with a modern digital computer. However, in general it is believed that $P \neq NP$ and there are problems which are in the finite region $NP - P$ and presumed to be in EXPTIME.

1.1.3 NP-hard problems

The problems to which all the NP problems can be reduced in a polynomial time are called NP-hard problems. If we could solve a NP-hard problem, we can give the solutions of all the NP problems. Thus, it is said NP-hard problems are *at least as difficult as* NP problems.

1.1.4 NP-complete problems

The problems both in NP and NP-hard are defined as NP-complete problems. Because of the NP-hardness, NP-complete problems can be thought to be most difficult NP problems and be as complex as each other. The polynomial-time reducibility from all the NP problems sounds even imaginary, however, Stephen Cook [6] showed in 1971 that any general NTDM algorithm can be expressed as an instance of the satisfiability problem (SAT) for a Boolean expression of a set of binary variables. With this celebrated proof, SAT was recognized as the first NP-complete problem. One year later, Karp [7] found 21 NP-complete problems via polynomial reductions originating from SAT, then expanded the significance of studies on computational complexity. Now, there are at least hundreds of NP-complete problems found [5], and if we would like to prove a decision problem to be intractable, all we have to do is find a polynomial reduction from any NP-complete problem in the list to the problem considered. Finding a polynomial time algorithm to solve one NP-complete problem means solving all the NP problems, winning a millennium prize [8], and will enormously advance our civilization, involving medicine, physics, entertainment and technology [9]. The question about if such a “golden ticket” exists is still unsettled [10].

1.2 Ising Model and Ising Problem

1.2.1 Combinatorial optimization problems

The main task in computation is often to maximize or minimize a function $f(\vec{X})$ depending on discrete variables \vec{X} , and such problems are called *combinatorial optimization problems* [11]. Combinatorial optimization is one of the function problems and outside decision problems. The number of candidates for the optimized solution for one of them is finite but extraordinary. Even for binary variables $\{0, 1\}$, it grows exponentially (2^N) to the number of variables N . Polynomial time algorithms to solve some of them which exploit their implicit structures have been found, and none for the other problems. Many of these intractable ones are NP-hard (or called #P [5]). The decision problem version of such a problem (“Is there any condition giving a value of $f(\vec{X})$ equal to or more/less than a prescribed constant?”) is often in NP-complete problems. For them, both exact algorithms to get the best solution, currently at the expense of exponential time resources, and approximation algorithms which guarantee values of $f(\vec{X})$ with certain ratios for the best are being vastly studied. Can physicists contribute to this massive challenge? In terms of physics, the Ising model [1, 12] is one of the most famous arenas providing with intractable combinatorial optimization.

1.2.2 Ising model

Ising model describes approximate behavior of interacting spin-1/2 particles, say, electrons in a lattice. An electron has a degree of freedom called *spin*, whose classical counterpart is the axial rotation. Spins give magnetic moments and hence interacting spins lead to magnetic orders in some materials. Exchange interaction due to Coulomb force and electronic kinetics and magnetic dipole-dipole interaction between spins give a quadratic term for the spin variables to the system Hamiltonian [13]. A 1/2 spin $\vec{\sigma}$ is described with three 2×2 matrices, however, if we only consider the component along with the main axis (set down as the z -axis), it can be reduced to a binary numeric variable $\sigma_z = \pm 1$. $\sigma_z = +1$ and -1 are called *up spin* and *down spin*, respectively. Without any magnetic anisotropy from other factors, the effective Hamiltonian is just given by the function depending on the two-body interaction terms [12]

$$\mathcal{H} = - \sum_{i < j} J_{ij} \sigma_{zi} \sigma_{zj} \quad (\sigma_{zi} = \pm 1), \quad (1.1)$$

where i and j are indices of the spins. Eq. (1.1) is called *Ising Hamiltonian*. Here, J_{ij} is real and denotes the magnitude of interaction. In this notation, $J_{ij} > 0$ means ferromagnetic interaction between spin i and j , $J_{ij} < 0$ anti-ferromagnetic, and $J_{ij} = 0$ no interaction. We are interested in the *ground states*, the states with the minimum energy eigenvalue, expected to be realized in the nature. Here, the problem to find a ground state of the Ising Hamiltonian is called *Ising problem*.

1.2.3 Hardness of Ising model

The hardness of analyzing the Ising model sharply depends on the dimension of the spin lattice as summarized in Fig. 1.1. Historically, Ernst Ising [1] derived the partition function of the one dimensional spin lattice analytically with statistical mechanics in 1925. He showed that the one-dimensional system does not show a ferromagnetic phase transition or spontaneous magnetization under a finite temperature. He thus misunderstood that the model would not show those also in two- and three-dimensional lattices. In 1944, however, Lars Onsager [2] deduced the exact expression for the logarithm of the partition function (Helmholtz free energy) using the transfer matrix method. The result showed that it actually does show a ferromagnetic phase transition in two-dimensional lattices without an external magnetic field. Nevertheless, the proof was quite non-trivial so that he needed inspiration from the quantitative work by H. A. Kramers and G. H. Wannier [14, 15]. Also, other proofs based on spinor analysis [16], combinatorics [17] and quantum field theory [18] were studied afterwards. Important properties such as magnetization [19] and spin correlation function [20] were calculated separately. Note also that the Ising problem in square lattices can be solved in a polynomial time with a method called perfect matching in graph theory [21].

How is that for a three-dimensional lattice? Unfortunately, the exact solution for the partition function has not been found yet. Correspondingly, the Ising problem and evaluating the partition function for the grid of two-layer square lattices, the smallest three-dimensional graphs, were proven to be NP-hard by Francisco Barahona [3] in 1982. Later, the NP-hardness of these was extended for arbitrary non-planar graphs [22]. As for approximation algorithms, a polynomial-time probabilistic algorithm achieving a desired accuracy and success probability, called fully polynomial randomized approximation scheme (FPRAS), has been proposed for calculating the partition function of an arbitrary *ferromagnetic* Ising model (where $J_{ij} \geq 0$ for all i and j) [23]. The method is based on a well-known Monte Carlo simulation, but the Markov chain here is defined for the subgraphs of the edge set reflecting the interaction profile, which itself does not have any physical significance. On the other hand, it has been proven that such an algorithm for the anti-ferromagnetic model does not exist for the outside of the restricted parameter region [24, 25]. An important point supporting this fact is that the anti-ferromagnetic Ising problem is closely related to the maximum-cut (MAX-CUT) problem, which is one of the Karp's NP-complete problems [7].

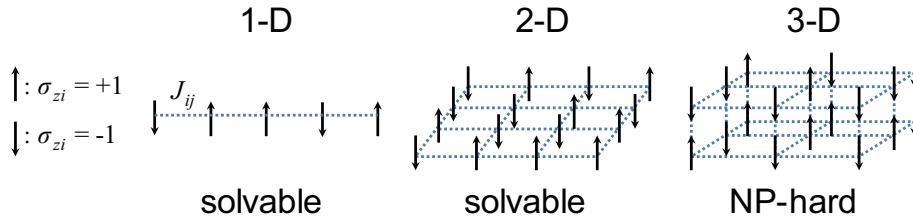


Figure 1.1: Dimensionality of the Ising model [1–3].

1.2.4 MAX-CUT problem

MAX-CUT problem is a decision problem for graphs. A graph $G = \{V, E\}$ is composed of a set of vertices V and that of edges E connecting two vertices. A partition of V into two disjoint subsets V_1 and V_2 is called a *cut*. A *cut size* is the number of edges between vertices of different subsets of a cut. MAX-CUT (the version actually called Simple MAX-CUT [26]) is defined as follows.

MAX-CUT

INSTANCE: A graph G with undirected edges and a positive integer c .

QUESTION: Is there any cut whose size is c or larger?

And for clarity, the function problem to find the maximum cut size of a graph is called #MAX-CUT here.

MAX-CUT can be reduced to the anti-ferromagnetic Ising problem in the following way [23, 27]. We assign a spin to each vertex of a given graph, and set $\sigma_{zi} = +1$ for a vertex in V_1 and $\sigma_{zi} = -1$ for one in V_2 . Here, a cut (V_1, V_2) corresponds to a spin configuration $\sigma = \{+1, -1\}^N$. We consider a quantity $(-\sigma_{zi}\sigma_{zj} + 1)/2$ for an edge between vertex i and j . This gives 1 when the edge crosses the cut and 0 otherwise. Thus, the cut size is obtained as the summation of those for all the edges

$$|\text{cut}(\sigma)| = \frac{|E|}{2} - \frac{1}{2} \sum_E \sigma_{zi} \sigma_{zj} = \frac{|E|}{2} - \frac{1}{2} \sum_{i < j} [\mathbf{I}^M]_{ij} \sigma_{zi} \sigma_{zj}. \quad (1.2)$$

Here, $|E|$ is the number of edges and is a constant for the given graph at most $N(N-1)/2$, and \mathbf{I}^M is the incidence matrix of the considered graph. Thus, the maximum $|\text{cut}(\sigma)|$ means the minimum $\sum_E \sigma_{zi} \sigma_{zj}$, corresponding to the Ising Hamiltonian with $J_{ij} = -1$ for all the edges of the graph and $J_{ij} = 0$ for each pair of vertices without an edge in between. Therefore, the solutions of the Ising problem and #MAX-CUT have one-to-one correspondence. If we can solve the anti-ferromagnetic Ising problem, we can solve #MAX-CUT and vice versa. Also, the complexity of this reduction is $\mathcal{O}(N^2)$. Thus, the Ising problem for anti-ferromagnetic systems is NP-hard. The NP-hardness of MAX-CUT holds even for 3-regular graphs [28], thus the corresponding instances of the Ising problem are also that hard.

What is interesting is that the limitation of approximation algorithms for #MAX-CUT problem has been theoretically obtained. M. X. Goemans and D. P. Williamson [29] proposed an approximation algorithm based on semidefinite programming for mapped continuous-vector variables and random rounding back to discrete variables. This guarantees of an approximation ratio of 87.8% to the best cut size and gives a theoretical upper bound for the solution. On the other hand, it has been shown that approximating MAX-CUT within a factor of 94.1% is NP-hard [30]. In other words, it is believed that the barrier between easiness and intractability is just 6.3% difference in the approximation factor in MAX-CUT problem.

1.3 Complexity Classes in Layers

Here I summarize the inclusion relation between the time complexity classes under the assumption that $P \neq NP$ in Fig. 1.2. It is almost trivial that $P \subseteq NP$ [5], and **NP-hard** can have problems harder than **NP-complete**. The relation among some NP problems such as the graph isomorphism [5] and the unknotting problem [31], P and **NP-hard** is still unclear. Here I add the class **BQP** (Bounded-error Quantum Polynomial) [32], containing the problems which can be solved with a quantum Turing machine in a polynomial time. E. Bernstein and U. Vazirani [32] showed that a quantum computer can emulate a classical computer ($P \subseteq BQP$), and that **BQP** includes its classical counterpart **BPP** (Bounded-error Probabilistic Polynomial, $BPP \subseteq BQP$). Also, **BQP** has some problems for which no classical polynomial-time algorithms have been found, such as integer factorization and discrete logarithm [33]. The relation between **BQP** and **NP** is still unclear. Nevertheless, this observation indicates the expectation that a quantum computer can be more powerful than a digital computer.

1.4 Recent Trends of Quantum Computing

Computing with physical systems to attack intractable problems, especially with quantum ones, is a paradigm attracting attention. Here, I refer to the current status of the three major blueprints for realizing large-scale quantum computation beyond the reach of digital computing.

1.4.1 Gate model quantum computer

The gate model [34, 35] is the most vastly studied form of quantum computing. It utilizes quantum mechanical two-level systems called *qubits*. The basic idea is the parallel computing on the exponentially scaling number (2^N) of states in a single device and process, which is based on massive quantum-mechanical superposition, correlation and filtering on it. Historically, Paul Benioff [36] described computational processes using the dynamics of a quantum system in 1980. Richard Feynman [37] pointed out that simulating a quantum system with a digital computer requires exponential resources of both time and its memory. He further proposed exploiting a controllable quantum system to simulate another which we would like to know about, and implied the possible advantage of quantum computing systems digital computers. Later, David Deutsch formulated the concepts of a quantum Turing machine (QTM) [38] and a quantum circuit [39] composed of quantum gates. He and Richard Jozsa [40] also found the first quantum algorithm giving an exponential speedup compared to classical algorithms. In 1994, Peter Shor [33] proposed the polynomial-time quantum algorithms to solve integer factorization and to calculate discrete logarithm which are both NP problems, and this led to extensive studies on quantum computing and quantum information. Also, Lov Grover [41, 42] gave a search algorithm on an unstructured state space using queries to quantum oracles, and showed that it can achieve a quadratic speedup compared to classical algorithms.

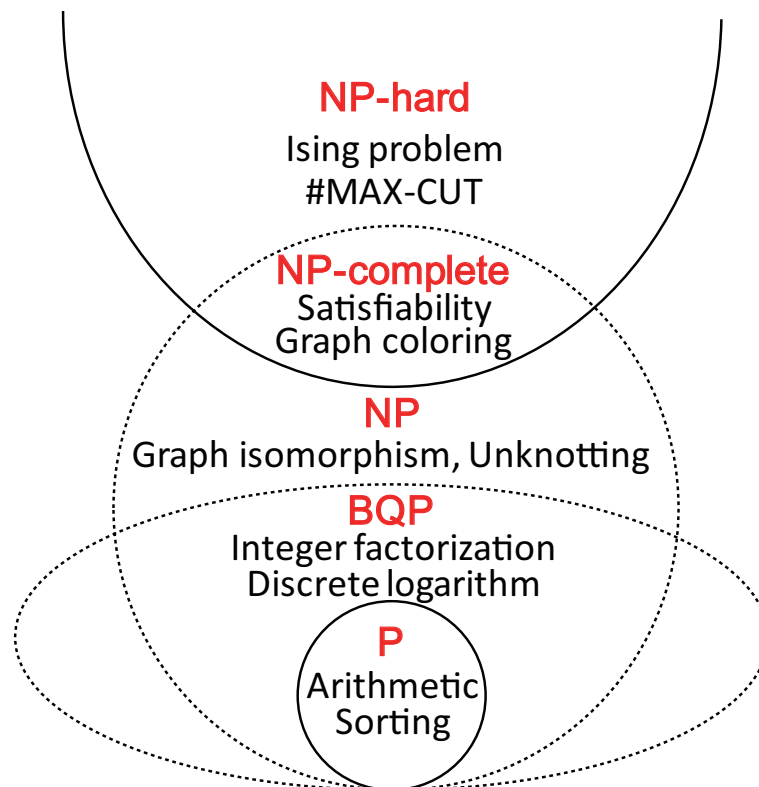


Figure 1.2: Inclusion relation between the major time complexity classes and examples of the problems in each.

Despite the promising prospects from the theoretical side, there are major obstacles in realizing large-scale quantum computing devices. Quantum coherence of a system can be destructed by the coupling to the environment, and this process is called *decoherence* [43]. To implement a quantum computer, error correction [44] is needed for accurate computation and protection of the system from decoherence. Measurement-based quantum computation (MBQC) [45–48], where a quantum network of global quantum coherence and entanglement is initially prepared and the computation is executed by a series of measurements on the system, showed a simplified way to construct a universal quantum computer. Also, an error correcting code highly compatible with MBQC called *surface code* [49–51] was proposed, and it gave a relatively realistic error threshold of the elementary operations to guarantee computation. On the experimental side, the technology of superconducting (SC) qubits [52–54] has been especially improved. Recent work [55] reported a system composed of five SC qubits under extremely precise controls, meeting the error threshold of the surface code. However, an estimation [56] says that hundreds of millions ($\sim 10^8$) of qubits have to be in operation to execute 2048-bit integer factorization under the surface code error correction. Both theoretical and experimental attempts will be made to realize a large circuit model device.

An efficient quantum algorithm for NP-complete problems has not been found yet. However, there is a trend [57–61] to evaluate the quantum complexity of computing the partition function of the Ising model and develop quantum approximation algorithms for it.

1.4.2 Quantum simulator

Quantum simulator [62] is a straightforward concept along with the Feynman’s idea [37]. In the device, indistinguishable particles are scattered into a trapping potential forming a lattice. In such a system, intrinsic or artificial [63] interaction between the particles will give the non-trivial properties which are theoretically difficult to evaluate. Clarifying the physics of exotic phenomena like magnetism, superconductivity and superfluidity is the main purpose of quantum simulation. Systems of atomic gases [64–69], trapped ions [70–74], and exciton-polaritons [75–79] etc. have been extensively studied. However, each system faces some challenges such as scalability, controllability and stability, and is in the way to unveil the profound essences of these quantum-mechanical orders.

1.4.3 Quantum annealer

Quantum annealing [80] is a method more specialized in combinatorial optimization and based on quantum mechanical adiabatic theorem. It was proposed by T. Kadowaki and H. Nishimori [81] in 1998 for the quantum mechanical Ising model with an external transverse magnetic field, as an extension of simulated annealing [82]. In 2000, a generalized scheme named adiabatic quantum computation (AQC) [83] was developed by E. Farhi *et al.* The main processes of these are essentially the same. We initially prepare a trivial ground state of an easily realizable Hamiltonian. Then, we gradually introduce the component of the Hamiltonian to be solved and decrease the initial component.

If the modulation of the entire Hamiltonian is sufficiently slow, the system holds the ground state during the process. Finally, the problem Hamiltonian gets dominant and a ground state is expected to be measured there. When we consider the Ising model with a transverse field, the time-dependent Hamiltonian can be written as [83]

$$\mathcal{H}(t) = -s_a(t) \sum_i \hat{\sigma}_{xi} - s_b(t) \left[\sum_{i < j} J_{ij} \hat{\sigma}_{zi} \hat{\sigma}_{zj} + \sum_i h_i \hat{\sigma}_{zi} \right]. \quad (1.3)$$

Here, $s_a(t)$ and $s_b(t)$ are the coefficients for the initial and problem Hamiltonian. Basically, a linear schedule is adopted, i.e. $s_a(t) = 1 - t/t_r$, $s_b(t) = t/t_r$ and $0 \leq t \leq t_r$. t_r is the running time given as a parameter. The first term of Eq. (1.3) denotes the single spin energies in a transverse field, and the third term gives those in a vertical field. It has been shown that AQC has the same computational power as a circuit model quantum computer [84].

E. Farhi *et al.* [85] applied AQC to the NP-complete exact cover problem and showed that it gives a quadratic scaling of the computational time to get a finite success probability on the problem size up to 20. However, a study with a quantum Monte Carlo (QMC) method on the same problem up to the size $N = 256$ [86] revealed that the system shows a first-order phase transition in the middle of the process. There, the energy gap between the ground and excited states gets exponentially small on N . It means that an exponentially scaling computational time is required to prevent the prepared state from jumping to an excited state. The phase transition has been seen in other literature [87, 88], and there are trials to avoid them by changing the initial Hamiltonian and parameters [87, 89]. Also, a study [90] indicates that thermally assisted tunneling around the minimum gap can improve the success probability.

In 2010, a Canadian company named D-Wave Systems reported the release of the first commercial quantum annealer with 128 superconducting qubits [91]. However, D-Wave had been questioned then [92] because they had not published any experimental evidence supporting the assertion that their systems actually conducted *quantum* annealing. Some positive results on the test problems with relatively small systems were reported in stages: one with 8 qubits by D-Wave in 2011 [93] and 16 qubits by the team of University of Southern California (USC) in 2013 [94]. D-Wave also observed the thermally assisted tunneling available for a speedup in certain problems [95]. The extended team of USC further tested the device of 108 qubits [96], and showed the experimental result was well correlated with that of a QMC simulation of the system, not with that of simulated annealing or a classical spin-dynamics simulation. The D-Wave machine began to be recognized as a somewhat quantum entity, however, an evidence of a significant quantum speedup of the machine compared to simulated annealing has not been obtained [96] even with a 512 qubit system [97]. The annealing machine in sale seems to need to be brushed up further in terms of the system size and the variation in the properties of its qubits.

1.5 Coherent Computing

As shown in the previous section, studies on each model are under challenging situations. We have recently proposed a concept named *coherent computing* or *coherent Ising machine* [98, 99] to compute the Ising problem with a photonic network of coupled optical oscillators. The general composition of the system with continuous-wave (CW) oscillators is presented in Fig. 1.3. In the system, each spin of the Ising model is mapped to the state of the light of each oscillator, and the interaction between the spins is mimicked by the mutual injections. The oscillators can hold their states with the stimulated emission, and the energies of their photons are much higher than those of lattice vibrations. Thus, the system is robust to the environmental noise and can operate in the room temperature. In addition, the number of components required to build the system is at most $\mathcal{O}(N^2)$, and the system can have moderate controllability that enables us to program a wide range of instances. There are two systems with different oscillators proposed, and here I summarize these and their current problems.

1.5.1 Injection-locked laser network system

We proposed the concept of coherent computing with a model of a prototype system based on injection-locked lasers in 2011 [98]. This system is composed of a master laser and slave lasers. The master signal is injected into all the slave lasers in oscillation via the external signal lines (EXTs in Fig. 1.3) to lock their optical frequencies and initialize the polarizations to the vertical polarization $|V\rangle$. The i th spin is mapped to the normalized difference of the continuous field amplitudes A_{Ri} and A_{Li} for the two circular polarization components $|R\rangle$ and $|L\rangle$ in the i th slave laser, i.e. $\tilde{\sigma}_i \equiv (A_{Ri} - A_{Li}) / (A_{Ri} + A_{Li})$. This is monitored with each detector (DT) as in Fig. 1.3. The mutual injection is introduced at a certain point of time $t = 0$. Here, each path of the mutual injection (OC in Fig. 1.3) has a horizontal polarizer which leads to an injection signal proportional to $A_{Ri} - A_{Li}$ for the both circular polarization amplitudes. The time evolution of the system is described as a series of nonlinear rate equations for A_{Ri} , A_{Li} and the inverted carrier number N_{Ci} with spontaneous emission noise terms. When the gain coefficient E_{CVi} for the photons of each slave laser is modeled to be proportional to N_{Ci} (linear gain model), the gain of the whole system $\sum_i E_{CVi}$ in the steady state can be written as

$$\sum_i E_{CVi} = N\gamma_c - \zeta_a \sum_i \sqrt{2 - \tilde{\sigma}_i^2} - \alpha_a \sum_{i < j} J_{ij} \tilde{\sigma}_i \tilde{\sigma}_j, \quad (1.4)$$

where γ_c , ζ_a and α_a are the cavity decay rate, the common attenuation coefficients for the master signal and mutual injection, respectively. The last term corresponds to the programmed Ising Hamiltonian (1.1) where J_{ij} is reflected in the magnitude and phase shift of the mutual injection, controlled with OC. When the mutual injection is dominant, i.e. $\zeta_a \leq \alpha_a$, the problem Hamiltonian is well mapped to the total gain of the oscillator network. A single laser oscillates with the minimum gain coefficient possible, where the gain balances the cavity loss. Correspondingly, we expect that the laser network with

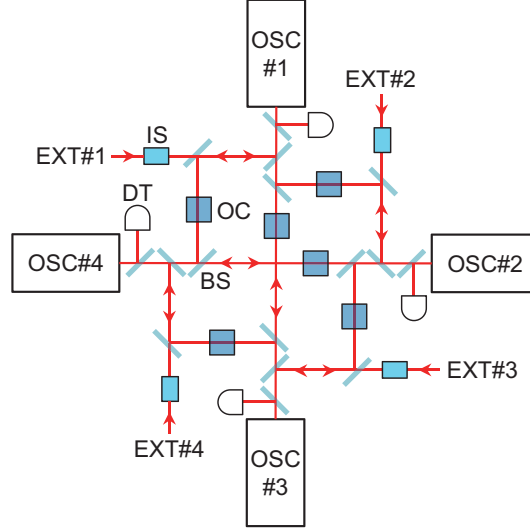


Figure 1.3: A schematic illustration of a coherent computing system for the $N = 4$ Ising model. OSC: oscillator, EXT: external signal, DT: detector, IS: isolator, OC: optical components. Some unnecessary paths are omitted.

mutual injections oscillates with the minimum total gain, or effective loss for photons. This indicates the maximum number of photons in the system via dynamical interference due to phase locking, and can be regarded as a self-organization.

We showed that in the case of some simple instances without frustration, the computational time of the machine is determined by the cavity loss and mutual injection intensity for each slave laser and not exponential with the number of lasers N [99]. However, we found that in the simulations on MAX-CUT problem in 3-regular (cubic) graphs, the system frequently gives a wrong answer where some lasers show $\tilde{\sigma}_i \sim 0$. This means that the system is trapped into an intermediate state which does not correspond to any candidate of the solution of the Ising problem. This error comes from the fact that the spins are mapped to the continuous variables, and that the laser does not have any mechanism to take a certain phase (phase-insensitive oscillator).

We proposed two operational schemes [100] which gradually increase the pumping power to the slave lasers or the mutual injection intensity among them, and numerically tested them with certain instances of the Ising model without frustration. There, we showed the system can achieve a better success probability and effective computational time to find a ground state with the proposed schemes than those with the abrupt introduction of the mutual injection at $t = 0$. However, it did not seem to be the essential solution for that error in itself. Eventually, we have to rely on a heuristic self-learning algorithm [101, 102] which repeatedly injects an external signal into a part including a couple of lasers with $\tilde{\sigma}_i \sim 0$ to make it locally optimum. It got a better result than the 87.8% approximation algorithm [29] for some sampled NP-hard instances up to

$N = 800$ spins. However, the difficulty of a relaxation problem with continuous variables in the laser network system is presumed to be essentially the same as what limits the performance of that approximation algorithm.

1.5.2 Degenerate optical parametric oscillator system

Recently, a coherent computing system with degenerate optical parametric oscillators (DOPOs) has been proposed [103] to resolve the difficulty of the laser system. In this system, the pump field is needed as an external input instead of the master signal. A DOPO uses only a single polarization, and a spin is mapped to the relative phase of the intracavity DOPO field to that of the pump field. OCs in Fig. 1.3 contain just attenuators and phase shifters. At the oscillation, a DOPO takes one of the binary phase states $|0\rangle$ and $|\pi\rangle$ whose complex amplitudes are out-of-phase to each other. Thus, it is expected that the system can avoid the intermediate states which the laser system is seriously affected by. In the benchmarking on MAX-CUT problem in 3-regular graphs, the system could solve all the possible instances up to $N = 20$ with fixed parameters. The running time needed to find a solution was nearly linear with N . The success probability in the worst case decreased down to about 10% for $N = 20$ there, however, it was shown that adjusting parameters could enable improving the performance. This system is better than the laser system, at least in the sense that it does not need a self-learning algorithm to get a discrete spin configuration for the Ising model.

1.5.3 Agendas

Then, is coherent computing better than any digital computing algorithms and more efficient for NP-hard problems? Unfortunately, this question is still open. A crucial question is if the coherent computing systems have any quantum features available for the computation or not, because quantum computing is the only paradigm which has been extensively studied in theory and has some positive evidences for the superiority over digital computing, as shown in the previous section. However, it has not been sufficiently considered so far.

Unfortunately, the laser system will not show significant macroscopic quantum effects as it is. The light of a laser driven by a classical current well above oscillation threshold can be written with the Glauber-Sudarshan $P(\alpha)$ representation [104–106]. This is the diagonal description for the density operator $\hat{\rho}$ with coherent states, namely (quasi)probabilistic distribution $P(\alpha)$ for a mixture, and a coherent state $|\alpha\rangle$ can be understood as a strong classical field with small quantum noise. Thus, a single laser itself does not show any macroscopic superposition components. Furthermore, it will be difficult for two laser fields with mutual injection to have quantum correlation, because each beam has fluctuation larger than the vacuum level due to the spontaneous emission. The properties of the system with small numbers of photons should be explored.

How about the DOPO system? Unfortunately, the quantum effects essential for quantum computing have yet to be taken into the theory, and a fully quantum mechanical simulation on a large system is computationally hard as Feynman pointed out. The

model in the proposal [103] is given with a set of semi-classical c-number Langevin equations, and it reproduces squeezing as the quantum mechanical Fokker-Planck equation for the generalized $P(\alpha)$ representation [107, 108] does. However, it is known the quadratic squeezing process itself can be treated classically if we accept Heisenberg uncertainty (or phenomenological spontaneous emission noise) [109]. Also, Gottesman-Knill theorem [110, 111] indicates that it is not enough for the system to exert the performance limit of quantum computing.

Another question is on the scalability of the system. However the nominal size and driving power of a coherent computing system are quadratic and linear with the number of oscillators N , extending a photonic network like one in Fig. 1.3 to the level of hundreds and thousands of oscillators sounds technically difficult.

This thesis partially answers these questions in terms of the DOPO system. The former part contains the theoretical work investigating the quantum properties of the two DOPOs with mutual injection, which is the minimum coherent computing system. Here, the system is described fully quantum-mechanically with a model called positive P representation [107, 108]. Then, some important quantum mechanical properties such as macroscopic superposition, entanglement and quantum correlation are numerically presented. The latter part gives experimental demonstrations of the coherent computing. Here I exploit ultrashort pulse DOPOs which share a single ring cavity for oscillation and optical delay lines for mutual injection. Such a time-bin implementation greatly simplifies the implementation of the system, and enables us to reach experimental evidences for coherent computing even on NP-complete instances. I show the results of two experimental projects. The first one is collaborative work with Alireza Marandi in Stanford University. Here, we successfully compute the MAX-CUT problem (anti-ferromagnetic Ising problem) on the complete graph of four vertices using an OPO with four pulses and three optical delay lines to couple them. The second one utilizes a 16-pulse OPO with a telecom central wavelength. Here, the system with 16 artificial spins is applied to the ferromagnetic and anti-ferromagnetic one-dimensional ring and an NP-hard instance of MAX-CUT problem on a cubic graph. The success probabilities for them more than 99.7 % indicate the large computational possibility of coherent computing for more complex problems.

1.6 Thesis Structure

This thesis is structured as follows. I start in the next chapter with an introductory explanation and the quantum theory of a single DOPO. Here, I also review relevant previous studies. In the third chapter, I extend the quantum-mechanical model for a DOPO for a system of two DOPOs with mutual injection. After some remarks on the significance of the model, I show the result of probabilistic simulations on the system with out-of-phase mutual injection. In the fourth chapter, I present a way to design a femtosecond pulsed optical parametric oscillator (OPO) and the experimental properties of the constructed system. Chapter five shows the results of two experimental demonstrations for coherent computing with pulsed DOPOs. Chapter six concludes the dissertation and refers to

some possible directions of the research on coherent computing.

Chapter 2

Quantum Theory of DOPO

The optical parametric oscillator [112, 113] is based on the quadratic nonlinear optical process. It involves correlated photon pairs hence has enabled us to study various quantum effects such as anti-bunching [108, 114, 115], squeezing [116–122], macroscopic superposition [123–130], entanglement and further the Einstein-Podolsky-Rosen (EPR) paradox [131–142] and quantum teleportation [143–145] both theoretically and experimentally. In this chapter, I review the quantum theory of a single degenerate optical parametric oscillator (DOPO) based on the positive P representation [107] and its application to studies on some quantum effects important in this thesis.

2.1 Degenerate Optical Parametric Oscillator

Fig. 2.1 shows a schematic drawing of a optical parametric oscillator. The system [146–148] is composed of an optical cavity and a quadratic nonlinear crystal in it. Here, an external pump field is injected into the cavity. I assume that the pump intensity is so large that the pump field can be approximated by a classical field. The χ_2 process divides a pump photon with a frequency ω_p into two photons of lower frequencies. A split photon with the higher frequency ω_s is called a *signal* photon, and the other with ω_i an *idler* photon. It is supposed that the energy and momentum of the photons are conserved in the χ_2 process, i.e. $\omega_p = \omega_s + \omega_i$ and $\vec{k}_p = \vec{k}_s + \vec{k}_i$, where \vec{k}_p , \vec{k}_s and \vec{k}_i are the wave vector of the pump, signal and idler, respectively. The condition is referred to as *phase matching*. This enables a large gain and then oscillation of the low-frequency modes. A careful design of the cavity and crystal can make the signal and idler frequency identical, that is, the *degenerate* operation with $\omega_i = \omega_s$ and $\omega_p = 2\omega_s$.

2.2 Total System Hamiltonian

In this section and the next, I review the derivation of the theoretical model for a DOPO according to the work by P. D. Drummond, K. J. McNeil and D. F. Walls [108]. First of all, the system has electromagnetic fields of the pump mode and the degenerate signal

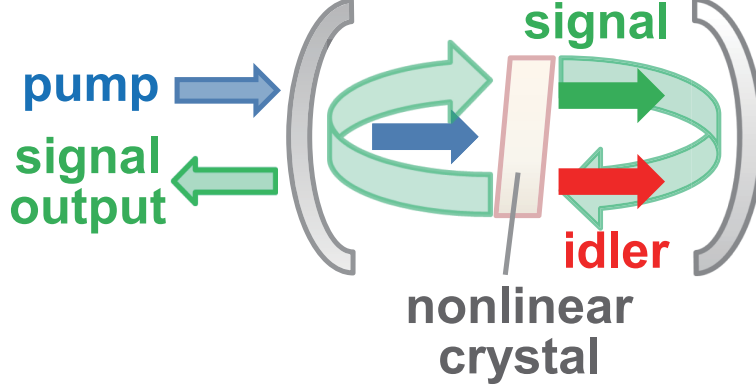


Figure 2.1: Schematic representation of an optical parametric oscillator.

mode, with their bosonic annihilation operators \hat{a}_p and \hat{a}_s , respectively. We suppose it also couples weakly to the reservoir of thermal photons. The Hamiltonian of the total system is written in parts with the time-reversible and irreversible components $\hat{\mathcal{H}}_{\text{rev}}$ and $\hat{\mathcal{H}}_{\text{irrev}}$ in terms of the system

$$\begin{aligned}
 \hat{\mathcal{H}} &= \hat{\mathcal{H}}_{\text{rev}} + \hat{\mathcal{H}}_{\text{irrev}}, \\
 \hat{\mathcal{H}}_{\text{rev}} &= \hbar\omega_p \hat{a}_p^\dagger \hat{a}_p + \hbar\omega_s \hat{a}_s^\dagger \hat{a}_s \\
 &\quad + i\hbar \frac{\kappa}{2} \left(\hat{a}_s^{\dagger 2} \hat{a}_p - \hat{a}_p^\dagger \hat{a}_s^2 \right) \\
 &\quad + i\hbar \left[\varepsilon_p \hat{a}_p^\dagger \exp(-i\omega_d t) - \varepsilon_p^* \hat{a}_p \exp(i\omega_d t) \right], \\
 \hat{\mathcal{H}}_{\text{irrev}} &= \hbar \left(\hat{a}_s \hat{\Gamma}_{Rs}^\dagger + \hat{\Gamma}_{Rs} \hat{a}_s^\dagger \right) + \hbar \left(\hat{a}_p \hat{\Gamma}_{Rp}^\dagger + \hat{\Gamma}_{Rp} \hat{a}_p^\dagger \right). \tag{2.1}
 \end{aligned}$$

Here, κ is the nonlinear interaction coefficient for the signal photons. The third term of $\hat{\mathcal{H}}_{\text{rev}}$ denotes the nonlinear process involving a pump photon and two signal photons, and the last term means coherent excitation of the intracavity pump photons by classical field injection $\varepsilon_p \exp(-i\omega_d t)$. ε_p is the injected field amplitude including the transmission rate at the cavity facet. $\omega_d \sim \omega_p$ is the frequency of the driving field, allowing a small detuning. The irreversible process $\hat{\mathcal{H}}_{\text{irrev}}$ is the coupling to the environment modeled with the continuum of thermal modes. $\hat{\Gamma}_{Rp}$ and $\hat{\Gamma}_{Rs}$ are the reservoir operators for the pump and signal modes.

2.3 Theoretical Model for DOPO as Open Quantum System

Based on the Hamiltonian (2.1), we derive the stochastic equations of motion for the c -number field variables, which are appropriate for analysis and probabilistic simulations. We obtain the master equation for the system density operator first, then convert it to

the Fokker-Planck equation for the quasi-distribution function describing the field state under a phase-space representation. Finally, we reach the corresponding Ito stochastic differential equations via Ito's rule.

2.3.1 Master equation for single-mode damped harmonic oscillator

First, We focus on the irreversible part $\hat{\mathcal{H}}_{\text{irrev}}$ which leads to decay of the field. For simplicity, I treat the system of a single mode oscillator with the thermal reservoir here. The extension to the multi-mode case is trivial because of linearity of the equation of motion. Here I follow the derivation in Carmichael's texts [149].

Liouville von-Neumann equation

We start with the time-dependent Schrödinger equation for a pure state vector $|\psi_i\rangle$

$$i\hbar \frac{\partial}{\partial t} |\psi_i\rangle = \hat{\mathcal{H}} |\psi_i\rangle. \quad (2.2)$$

With Eq. (2.2) and its conjugate, We have the equation of motion for a density operator of a pure state

$$i\hbar \frac{\partial}{\partial t} |\psi_i\rangle\langle\psi_i| = \hat{\mathcal{H}} |\psi_i\rangle\langle\psi_i| - |\psi_i\rangle\langle\psi_i| \hat{\mathcal{H}}. \quad (2.3)$$

Here, the Hermiticity of $\hat{\mathcal{H}}$ is used. Eq. (2.3) is linear with respect to the matrix states, thus the generalized density operator including a probabilistic mixture

$$\hat{\rho} = \sum_i p_i |\psi_i\rangle\langle\psi_i| \quad (0 \leq p_i \leq 1), \quad (2.4)$$

obeys the equation

$$\frac{\partial \hat{\rho}}{\partial t} = \frac{1}{i\hbar} [\hat{\mathcal{H}}, \hat{\rho}]. \quad (2.5)$$

Eq. (2.5) is referred to as *Liouville-von Neumann equation* in the Schrödinger picture.

The theoretical framework of the density operator is valid also for the systems for which we only have partial knowledge, such as open systems, ensembles of particles in an imperfect sample and artificially prepared states under a probabilistic condition.

Exact von Neumann equation in interaction picture

The Hamiltonian of a damped harmonic oscillator $\hat{\mathcal{H}}_{DO}$ reads

$$\hat{\mathcal{H}}_{DO} = \hat{\mathcal{H}}_S + \hat{\mathcal{H}}_R + \hat{\mathcal{H}}_{SR}, \quad (2.6)$$

where $\hat{\mathcal{H}}_S$ and $\hat{\mathcal{H}}_R$ are the Hamiltonians only for the system and reservoir operators, respectively. $\hat{\mathcal{H}}_{SR}$ is the interaction Hamiltonian including both operators. We aim at getting the equation of motion for the system density operator $\rho(t)$ which is the partial trace of that for the total system $\varrho(t)$

$$\hat{\rho}(t) = \text{tr}_R [\hat{\varrho}(t)], \quad (2.7)$$

because the expectation value of an arbitrary system operator \hat{O}_S can be obtained with the system density operator

$$\langle \hat{O}_S \rangle = \text{tr}_S \{ \hat{O}_S \text{tr}_R [\hat{\rho}(t)] \} = \text{tr}_S \left[\hat{O}_S \hat{\rho}(t) \right]. \quad (2.8)$$

It means that the dynamics of the system density operator suffices to know the phenomena we are interested in.

To simplify the calculation, we switch to the interaction picture. Here, all the operators in the interaction picture $\{\tilde{O}(t)\}$ are in charge of the free processes of the system \hat{H}_S and reservoir \hat{H}_R themselves as

$$\tilde{O}(t) = e^{(i/\hbar)(\hat{H}_S + \hat{H}_R)t} \hat{O} e^{-(i/\hbar)(\hat{H}_S + \hat{H}_R)t}, \quad (2.9)$$

where \hat{O} is the original operator in the Schrödinger picture. Instead, the density operator in the interaction picture is virtually affected only by the interaction Hamiltonian

$$\frac{\partial \tilde{\rho}}{\partial t} = \frac{1}{i\hbar} \left[\tilde{\mathcal{H}}_{SR}(t), \tilde{\rho} \right], \quad (2.10)$$

though we have to consider the time dependency of $\tilde{\mathcal{H}}_{SR}(t)$ due to Eq. (2.9). Formal integration of Eq. (2.10) gives

$$\tilde{\rho}(t) = \rho(0) + \frac{1}{i\hbar} \int_0^t dt' \left[\tilde{\mathcal{H}}_{SR}(t'), \tilde{\rho}(t') \right]. \quad (2.11)$$

And, straightforward substitution of Eq. (2.11) into Eq. (2.10) leads to the integro-differential equation up to the second order to $\tilde{\mathcal{H}}_{SR}(t)$

$$\frac{\partial \tilde{\rho}}{\partial t} = \frac{1}{i\hbar} \left[\tilde{\mathcal{H}}_{SR}(t), \tilde{\rho}(0) \right] - \frac{1}{\hbar^2} \int_0^t dt' \left[\tilde{\mathcal{H}}_{SR}(t), \left[\tilde{\mathcal{H}}_{SR}(t'), \tilde{\rho}(t') \right] \right]. \quad (2.12)$$

Born and Markov approximation

We apply some approximations to Eq. (2.12). First, we assume that the system and reservoir do not have any correlation at the initial state $t = 0$. Then, $\tilde{\rho}(0) = \hat{\rho}(0)$ can be written as a product state of the initial density operators for the system $\hat{\rho}(0)$ and reservoir \hat{R}_0

$$\hat{\rho}(0) = \hat{\rho}(0) \hat{R}_0. \quad (2.13)$$

Next, we consider taking the partial trace of Eq. (2.12) in terms of reservoir states. We can easily see that $e^{(i/\hbar)\hat{H}_R t}$ and $e^{-(i/\hbar)\hat{H}_R t}$ in $\tilde{\rho}$ vanish in the trace operation by using the energy eigenvectors for the reservoir, namely,

$$\text{tr}_R(\tilde{\rho}) = e^{(i/\hbar)\hat{H}_S t} \hat{\rho} e^{-(i/\hbar)\hat{H}_S t} = \tilde{\rho}. \quad (2.14)$$

As a result, we have the equation for the system density operator

$$\frac{\partial \tilde{\rho}}{\partial t} = -\frac{1}{\hbar^2} \int_0^t dt' \text{tr}_R \left\{ \left[\tilde{\mathcal{H}}_{SR}(t), \left[\tilde{\mathcal{H}}_{SR}(t'), \tilde{\rho}(t') \right] \right] \right\}. \quad (2.15)$$

Here, we have eliminated the first term of Eq. (2.12) with the assumption $\text{tr}_R [\tilde{\mathcal{H}}_{SR}(t)R_0] = 0$. It means that the average coupling between R_0 and the system is zero, and this can be always achieved by changing the energy reference of the system by $\text{tr}_R [\tilde{\mathcal{H}}_{SR}(t)R_0]$.

The assumption for the process is that the system and reservoir are uncorrelated at the initial state, and that the interaction between them is very weak. Thus, it is reasonable to suppose that the system $\tilde{\rho}(t)$ deviates from a separable state only by the first order in \hat{H}_{SR} . In addition, the reservoir is so huge that its state R_0 is virtually unaffected by the interaction. They lead to the expression

$$\hat{\rho}(t) = \tilde{\rho}(t)\hat{R}_0 + \mathcal{O}(\hat{H}_{SR}). \quad (2.16)$$

Correspondingly, the terms higher than second order of \hat{H}_{SR} in the differential equation (2.15) are not significant, thus we neglect them. Then we have

$$\frac{\partial \tilde{\rho}}{\partial t} = -\frac{1}{\hbar^2} \int_0^t dt' \text{tr}_R \left\{ \left[\tilde{\mathcal{H}}_{SR}(t), \left[\tilde{\mathcal{H}}_{SR}(t'), \tilde{\rho}(t')\hat{R}_0 \right] \right] \right\}. \quad (2.17)$$

This is our first major approximation and called *Born approximation*.

The second major approximation limits the dynamics to a Markov process. It means that the time evolution of the system is determined only with its present state, thus we replace $\tilde{\rho}(t')$ in Eq. (2.17) by $\tilde{\rho}(t)$. The resulting master equation under *Born-Markov approximation* is

$$\frac{\partial \tilde{\rho}}{\partial t} = -\frac{1}{\hbar^2} \int_0^t dt' \text{tr}_R \left\{ \left[\tilde{\mathcal{H}}_{SR}(t), \left[\tilde{\mathcal{H}}_{SR}(t'), \tilde{\rho}(t)\hat{R}_0 \right] \right] \right\}. \quad (2.18)$$

Markov approximation is based on the assumption that the reservoir is large and hardly influenced from the interaction hence the correlation time for the reservoir variables is very short. We return to the equation only with Born approximation, and reconsider this later.

We write the interaction Hamiltonian in a bilinear form for system and reservoir operators s_i and Γ_i

$$\hat{H}_{SR} = \hbar \sum_i \hat{s}_i \hat{\Gamma}_i. \quad (2.19)$$

It keeps the same form also in the interaction picture, namely

$$\tilde{H}_{SR}(t) = \hbar \sum_i \tilde{s}_i(t) \tilde{\Gamma}_i(t). \quad (2.20)$$

We substitute this somewhat explicit expression for the interaction into the equation

under the Born approximation (2.17) and obtain

$$\begin{aligned}
 \frac{\partial \tilde{\rho}}{\partial t} &= - \sum_{i,j} \int_0^t dt' \text{tr}_R \left\{ \left[\tilde{s}_i(t) \tilde{\Gamma}_i(t), \left[\tilde{s}_j(t') \tilde{\Gamma}_j(t'), \tilde{\rho}(t') \hat{R}_0 \right] \right] \right\} \\
 &= - \sum_{i,j} \int_0^t dt' \left\{ \left[\tilde{s}_i(t) \tilde{s}_j(t') \tilde{\rho}(t') - \tilde{s}_j(t') \tilde{\rho}(t') \tilde{s}_i(t) \right] \langle \tilde{\Gamma}_i(t) \tilde{\Gamma}_j(t') \rangle_R \right. \\
 &\quad \left. + \left[\tilde{\rho}(t') \tilde{s}_j(t') \tilde{s}_i(t) - \tilde{s}_i(t) \tilde{\rho}(t') \tilde{s}_j(t') \right] \langle \tilde{\Gamma}_j(t') \tilde{\Gamma}_i(t) \rangle_R \right\}, \tag{2.21}
 \end{aligned}$$

Here, the cyclic relation of the trace $\text{tr}(\hat{A}\hat{B}\hat{C}) = \text{tr}(\hat{C}\hat{A}\hat{B}) = \text{tr}(\hat{B}\hat{C}\hat{A})$ has been used. Also, the two-time correlation functions for the reservoir operators read

$$\langle \tilde{\Gamma}_i(t) \tilde{\Gamma}_j(t') \rangle_R = \text{tr}_R \left[R_0 \tilde{\Gamma}_i(t) \tilde{\Gamma}_j(t') \right], \tag{2.22}$$

$$\langle \tilde{\Gamma}_j(t') \tilde{\Gamma}_i(t) \rangle_R = \text{tr}_R \left[R_0 \tilde{\Gamma}_j(t') \tilde{\Gamma}_i(t) \right]. \tag{2.23}$$

After all, the effect of the reservoir has been written as a series of two-time correlation functions for reservoir operators. The time dependence of the system operator $\tilde{s}_j(t')$ is not essential and can be canceled in the Schrödinger picture. Thus, Markov approximation, namely replacement $\tilde{\rho}(t')$ by $\tilde{\rho}(t)$ means a very short correlation time of the reservoir operators compared to the time scale where $\tilde{\rho}(t)$ varies. Ideally,

$$\langle \tilde{\Gamma}_i(t) \tilde{\Gamma}_j(t') \rangle_R \propto \delta(t - t'). \tag{2.24}$$

Master equation for a damped oscillator

We move to an explicit model composed of a single mode cavity field with a frequency ω_C as the system, and a continuum of traveling thermal modes as the reservoir. They couples via a partially transmitting mirror. We do not assume certain mode properties of the reservoir because it is parametrized later with their spectral density $G(\omega)$. The Hamiltonian of the total system Eq. (2.6) is written in parts as

$$\hat{H}_S = \hbar \omega_C \hat{a}^\dagger \hat{a}, \tag{2.25}$$

$$\hat{H}_R = \sum_j \hbar \omega_j \hat{r}_j^\dagger \hat{r}_j, \tag{2.26}$$

$$\hat{H}_{SR} = \sum_j \hbar \left(\kappa_j^* \hat{a} \hat{r}_j^\dagger + \kappa_j \hat{a}^\dagger \hat{r}_j \right) = \hbar \left(\hat{a} \hat{\Gamma}^\dagger + \hat{\Gamma}^\dagger \hat{a} \right) \tag{2.27}$$

Here, \hat{a} and \hat{a}^\dagger are the annihilation and creation operators for the system mode. ω_j is the frequency of the j th mode of the reservoir, and \hat{r}_j and \hat{r}_j^\dagger are the corresponding annihilation and creation operators. The system-reservoir interaction under the rotating wave approximation comprises the couples of an annihilation and a creation operator, i.e.

$\hat{a}\hat{r}_j^\dagger$ and $\hat{a}^\dagger\hat{r}_j$. And, its magnitude is parametrized by the coupling coefficients κ_j . The reservoir is in the thermal equilibrium at temperature T and has the density operator

$$\hat{R}_0 = \prod_j e^{-\hbar\omega_j\hat{r}_j^\dagger\hat{r}_j/k_B T} \left(1 - e^{-\hbar\omega_j/k_B T}\right), \quad (2.28)$$

which is diagonal in terms of the Fock state basis. k_B is the Boltzmann's constant.

The correspondence of the operators for Eq. (2.21) is

$$\hat{s}_1 = \hat{a}, \quad \hat{s}_2 = \hat{a}^\dagger, \quad (2.29)$$

$$\hat{\Gamma}_1 = \Gamma^\dagger = \sum_j \kappa_j^* \hat{r}_j^\dagger, \quad \hat{\Gamma}_2 = \Gamma = \sum_j \kappa_j \hat{r}_j, \quad (2.30)$$

in the Schrödinger picture. With the commutation relation $[\hat{a}_i, \hat{a}_i^\dagger] = 1$ and $[\hat{r}_i, \hat{r}_j^\dagger] = \delta_{ij}$, we have the operators in the interaction picture as follows

$$\tilde{s}_1 = e^{i\omega_C \hat{a}^\dagger \hat{a} t} \hat{a} e^{-i\omega_C \hat{a}^\dagger \hat{a} t} = \hat{a} e^{-i\omega_C t}, \quad (2.31)$$

$$\tilde{s}_2 = e^{-i\omega_C \hat{a}^\dagger \hat{a} t} \hat{a}^\dagger e^{i\omega_C \hat{a}^\dagger \hat{a} t} = \hat{a}^\dagger e^{i\omega_C t},$$

$$\tilde{\Gamma}_1(t) = \tilde{\Gamma}^\dagger(t) = e^{i\sum_n \omega_n \hat{r}_n^\dagger \hat{r}_n t} \left(\sum_j \kappa_j^* \hat{r}_j^\dagger \right) e^{-i\sum_n \omega_n \hat{r}_n^\dagger \hat{r}_n t} \quad (2.32)$$

$$= \sum_j \kappa_j^* \hat{r}_j^\dagger e^{i\omega_j t}, \quad (2.33)$$

$$\tilde{\Gamma}_2(t) = \tilde{\Gamma}(t) = \sum_j \kappa_j \hat{r}_j e^{-i\omega_j t}. \quad (2.34)$$

Eqs. (2.19) and (2.27) show that the indices take $i = 1, 2$ and $j = 1, 2$. Substitution of Eqs. (2.31) - (2.34) into Eq. (2.21) yields the equation with sixteen terms

$$\begin{aligned} \frac{\partial \tilde{\rho}}{\partial t} = & - \int_0^t dt' \left\{ \left[\hat{a} \hat{a} \tilde{\rho}(t') - \hat{a} \tilde{\rho}(t') \hat{a} \right] e^{-i\omega_C(t+t')} \langle \tilde{\Gamma}^\dagger(t) \tilde{\Gamma}^\dagger(t') \rangle_R + \text{h.c.} \right. \\ & + \left[\hat{a}^\dagger \hat{a}^\dagger \tilde{\rho}(t') - \hat{a}^\dagger \tilde{\rho}(t') \hat{a}^\dagger \right] e^{i\omega_C(t+t')} \langle \tilde{\Gamma}(t) \tilde{\Gamma}(t') \rangle_R + \text{h.c.} \\ & + \left[\hat{a} \hat{a}^\dagger \tilde{\rho}(t') - \hat{a}^\dagger \tilde{\rho}(t') \hat{a} \right] e^{-i\omega_C(t-t')} \langle \tilde{\Gamma}^\dagger(t) \tilde{\Gamma}(t') \rangle_R + \text{h.c.} \\ & \left. + \left[\hat{a}^\dagger \hat{a} \tilde{\rho}(t') - \hat{a} \tilde{\rho}(t') \hat{a}^\dagger \right] e^{i\omega_C(t-t')} \langle \tilde{\Gamma}(t) \tilde{\Gamma}^\dagger(t') \rangle_R + \text{h.c.} \right\}. \end{aligned} \quad (2.35)$$

Here, the reservoir correlation functions can be obtained explicitly with the multi-mode

Fock state basis as

$$\langle \tilde{\Gamma}^\dagger(t) \tilde{\Gamma}^\dagger(t') \rangle_R = 0, \quad (2.36)$$

$$\langle \tilde{\Gamma}(t) \tilde{\Gamma}(t') \rangle_R = 0, \quad (2.37)$$

$$\langle \tilde{\Gamma}^\dagger(t) \tilde{\Gamma}(t') \rangle_R = \sum_j |\kappa_j|^2 e^{i\omega_j(t-t')} \bar{n}(\omega_j, T), \quad (2.38)$$

$$\langle \tilde{\Gamma}(t) \tilde{\Gamma}^\dagger(t') \rangle_R = \sum_j |\kappa_j|^2 e^{-i\omega_j(t-t')} [\bar{n}(\omega_j, T) + 1], \quad (2.39)$$

where

$$\bar{n}(\omega_j, T) = \text{tr}_R \left(R_0 \hat{r}_j^\dagger \hat{r}_j \right) = \frac{e^{-\hbar\omega_j/k_B T}}{1 - e^{-\hbar\omega_j/k_B T}}, \quad (2.40)$$

is the mean number of photons with a frequency ω_j in thermal equilibrium at temperature T . Eqs. (2.38) and (2.39) have a summation over the reservoir oscillator modes. We transform the summation into an integration for the density of states $G(\omega)$, such that $G(\omega)d\omega$ means the number of modes in the interval from ω to $\omega + d\omega$.

After changing the variable t' by $\tau = t - t'$ and substituting Eqs. (2.36) - (2.39) into (2.35), we have

$$\begin{aligned} \frac{\partial \tilde{\rho}}{\partial t} = & - \int_0^t d\tau \left\{ \left[\hat{a} \hat{a}^\dagger \tilde{\rho}(t - \tau) - \hat{a}^\dagger \tilde{\rho}(t - \tau) \hat{a} \right] e^{-i\omega_C \tau} \langle \tilde{\Gamma}^\dagger(t) \tilde{\Gamma}(t - \tau) \rangle_R + \text{h.c.} \right. \\ & \left. + \left[\hat{a}^\dagger \hat{a} \tilde{\rho}(t - \tau) - \hat{a} \tilde{\rho}(t - \tau) \hat{a}^\dagger \right] e^{i\omega_C \tau} \langle \tilde{\Gamma}(t) \tilde{\Gamma}^\dagger(t - \tau) \rangle_R + \text{h.c.} \right\}, \end{aligned} \quad (2.41)$$

with the expressions for the finite reservoir correlation functions

$$\langle \tilde{\Gamma}^\dagger(t) \tilde{\Gamma}(t - \tau) \rangle_R = \int_0^\infty d\omega e^{i\omega\tau} G(\omega) |\kappa(\omega)|^2 \bar{n}(\omega, T), \quad (2.42)$$

$$\langle \tilde{\Gamma}(t) \tilde{\Gamma}^\dagger(t - \tau) \rangle_R = \int_0^\infty d\omega e^{-i\omega\tau} G(\omega) |\kappa(\omega)|^2 [\bar{n}(\omega, T) + 1]. \quad (2.43)$$

Here, $\bar{n}(\omega, T)$ has the same form as Eq. (2.40).

A sufficiently short correlation time for the reservoir means that $G(\omega)$, $|\kappa(\omega)|^2$ and $\bar{n}(\omega, T)$ are spectrally broad enough around the cavity frequency ω_C . There are some positive discussions for the condition in the text [149], thus we proceed with the assumption that it is well satisfied. We just replace $\tilde{\rho}(t - \tau)$ with $\tilde{\rho}(t)$ and leave the integration in (2.42) and (2.43) for the later estimation. We then have the master equation under the Born-Markov approximation as

$$\frac{\partial \tilde{\rho}}{\partial t} = \alpha_d \left(\hat{a} \tilde{\rho} \hat{a}^\dagger - \hat{a}^\dagger \hat{a} \tilde{\rho} \right) + \beta_d \left(\hat{a} \tilde{\rho} \hat{a}^\dagger + \hat{a}^\dagger \tilde{\rho} \hat{a} - \hat{a}^\dagger \hat{a} \tilde{\rho} - \tilde{\rho} \hat{a} \hat{a}^\dagger \right) + \text{h.c.}, \quad (2.44)$$

with the coefficients

$$\alpha_d = \int_0^t d\tau \int_0^\infty d\omega e^{-i(\omega-\omega_C)\tau} G(\omega) |\kappa(\omega)|^2, \quad (2.45)$$

$$\beta_d = \int_0^t d\tau \int_0^\infty d\omega e^{-i(\omega-\omega_C)\tau} G(\omega) |\kappa(\omega)|^2 \bar{n}(\omega, T). \quad (2.46)$$

Here, the upper limit t in the integrations in Eqs. (2.45) and (2.46) denotes a typical time scale where $\tilde{\rho}$ evolves. It is assumed to be much longer than the reservoir correlation time within which the integrand significantly varies, thus we can formally take $t \rightarrow \infty$ and get

$$\lim_{t \rightarrow \infty} \int_0^t d\tau e^{-i(\omega-\omega_C)\tau} = \pi \delta(\omega - \omega_C) + i \frac{P_C}{\omega - \omega_C}, \quad (2.47)$$

where P_C is the Cauchy principal value. With Eq. (2.47), α_d and β_d are more explicitly evaluated as

$$\alpha_d = \pi G(\omega_C) |\kappa(\omega_C)|^2 + i\Delta, \quad (2.48)$$

$$\beta_d = \pi G(\omega_C) |\kappa(\omega_C)|^2 \bar{n}(\omega_C, T) + i\Delta', \quad (2.49)$$

with

$$\Delta = P_C \int_0^\infty d\omega \frac{G(\omega) |\kappa(\omega)|^2}{\omega_C - \omega}, \quad (2.50)$$

$$\Delta' = P'_C \int_0^\infty d\omega \frac{G(\omega) |\kappa(\omega)|^2}{\omega_C - \omega} \bar{n}(\omega, T). \quad (2.51)$$

After we set

$$\gamma = \pi G(\omega_C) |\kappa(\omega_C)|^2, \quad \bar{n} = \bar{n}(\omega_C, T), \quad (2.52)$$

as parameters, we get the master equation for a damping oscillator in the interaction picture

$$\begin{aligned} \frac{\partial \tilde{\rho}}{\partial t} = & -i\Delta [\hat{a}^\dagger \hat{a}, \tilde{\rho}] + \gamma \left(2\hat{a} \tilde{\rho} \hat{a}^\dagger - \hat{a}^\dagger \hat{a} \tilde{\rho} - \tilde{\rho} \hat{a}^\dagger \hat{a} \right) \\ & + 2\gamma \bar{n} \left(2\hat{a} \tilde{\rho} \hat{a}^\dagger + \hat{a}^\dagger \tilde{\rho} \hat{a} - \hat{a}^\dagger \hat{a} \tilde{\rho} - \tilde{\rho} \hat{a} \hat{a}^\dagger \right). \end{aligned} \quad (2.53)$$

To transform the equation back into the Schrödinger picture, we write $\hat{\rho}$ with $\tilde{\rho}(t)$

$$\hat{\rho} = e^{-(i/\hbar)(\hat{H}_S + \hat{H}_R)t} \tilde{\rho}(t) e^{(i/\hbar)(\hat{H}_S + \hat{H}_R)t}, \quad (2.54)$$

and differentiate it in time, resulting in

$$\frac{\partial \hat{\rho}}{\partial t} = \frac{1}{i\hbar} [\hat{\mathcal{H}}_S, \hat{\rho}] + e^{-(i/\hbar)\hat{\mathcal{H}}_S t} \frac{\partial \tilde{\rho}}{\partial t} e^{(i/\hbar)\hat{\mathcal{H}}_S t}. \quad (2.55)$$

The first term in Eq. (2.55) adds a phase rotation term $-i\omega_C [\hat{a}^\dagger \hat{a}, \hat{\rho}]$, and the second term gives the same form as Eq. (2.53) just with $\tilde{\rho}$ replaced by $\hat{\rho}$. Finally, we reach the master equation for a cavity mode in a thermal bath as

$$\begin{aligned} \frac{\partial \hat{\rho}}{\partial t} = & -i\omega'_C [\hat{a}^\dagger \hat{a}, \hat{\rho}] + \gamma \left(2\hat{a}\hat{\rho}\hat{a}^\dagger - \hat{a}^\dagger \hat{a}\hat{\rho} - \hat{\rho}\hat{a}^\dagger \hat{a} \right) \\ & + 2\gamma\bar{n} \left(\hat{a}\hat{\rho}\hat{a}^\dagger + \hat{a}^\dagger \hat{\rho}\hat{a} - \hat{a}^\dagger \hat{a}\hat{\rho} - \hat{\rho}\hat{a}\hat{a}^\dagger \right). \end{aligned} \quad (2.56)$$

with

$$\omega'_C = \omega_C + \Delta. \quad (2.57)$$

2.3.2 Master equation for a DOPO

Let us get back to the Hamiltonian of the DOPO, Eq. (2.1). Now, we can reduce the irreversible part H_{irrev} using Eq. (2.56). Here, we ignore the frequency detuning due to the thermal bath, namely $\Delta = 0$ in Eq. (2.57), and apply Eq. (2.56) for both the pump and signal modes. The resulting master equation for the DOPO is given by

$$\begin{aligned} \frac{\partial \hat{\rho}}{\partial t} = & \frac{1}{i\hbar} [\hat{\mathcal{H}}_{\text{rev}}, \hat{\rho}] \\ & + \gamma_s \left(2\hat{a}_s\hat{\rho}\hat{a}_s^\dagger - \hat{a}_s^\dagger \hat{a}_s\hat{\rho} - \hat{\rho}\hat{a}_s^\dagger \hat{a}_s \right) \\ & + \gamma_p \left(2\hat{a}_p\hat{\rho}\hat{a}_p^\dagger - \hat{a}_p^\dagger \hat{a}_p\hat{\rho} - \hat{\rho}\hat{a}_p^\dagger \hat{a}_p \right) \\ & + 2\gamma_s\bar{n}_s \left(\hat{a}_s\hat{\rho}\hat{a}_s^\dagger + \hat{a}_s^\dagger \hat{\rho}\hat{a}_s - \hat{a}_s^\dagger \hat{a}_s\hat{\rho} - \hat{\rho}\hat{a}_s\hat{a}_s^\dagger \right) \\ & + 2\gamma_p\bar{n}_p \left(\hat{a}_p\hat{\rho}\hat{a}_p^\dagger + \hat{a}_p^\dagger \hat{\rho}\hat{a}_p - \hat{a}_p^\dagger \hat{a}_p\hat{\rho} - \hat{\rho}\hat{a}_p\hat{a}_p^\dagger \right). \end{aligned} \quad (2.58)$$

Here, γ_s and γ_p are the cavity decay rate for the signal and pump fields. \bar{n}_s and \bar{n}_p are the mean photon numbers at temperature T for the signal and pump frequencies ω_s and ω_p . Note that the free phase rotation terms $-i\omega_s [\hat{a}_s^\dagger \hat{a}_s, \hat{\rho}]$ and $-i\omega_p [\hat{a}_p^\dagger \hat{a}_p, \hat{\rho}]$ are included in $\frac{1}{i\hbar} [\hat{\mathcal{H}}_{\text{rev}}, \hat{\rho}]$.

2.3.3 Positive P -representation

To treat the master equation using numerical variables, we need to expand the density operator $\hat{\rho}$ explicitly with a certain basis set [150]. The discrete Fock state basis $\{|n\rangle\}$ is the most elementary and complete in the Hilbert space. However, the resulting equation has infinite density matrix elements and hence we have to truncate ones for states with large numbers of particles. Thus, the accuracy of the analysis is limited by the truncation, and it is not suitable for systems of many particles, such as optical oscillators and electronic ensembles.

The coherent state basis $\{|\alpha\rangle\}$ enables us to deal with such systems via complex variables $\{\alpha\}$ and quasi-distribution functions for them. There are some forms to expand the density operator with coherent states, and such schemes are called *phase space*

representations. The Glauber-Sudarshan P -representation $\hat{\rho} = \int P(\alpha) |\alpha\rangle\langle\alpha| d^2\alpha$ [104–106], a diagonal expansion with coherent states, was firstly proposed and led to the theoretical analysis on the quantum statistics and spectra of the laser light. “Quasi-distribution” here reflects the fact that coherent states are not orthogonal to each other, and the function is not always positive and analytical. Such a case, where the quasi-distribution cannot be regarded as a genuine probabilistic distribution, is a major problem when the system is numerically analyzed by stochastic simulations [151]. Unfortunately, it is known that the Glauber-Sudarshan P -representation does not always have a well-behaved positive $P(\alpha)$ function. In the Wigner representation [152], the quasi-distribution W always exists but can be negative. Husimi’s Q -representation [153] has a positive quasi-distribution $Q(\alpha) = \langle\alpha|\hat{\rho}|\alpha\rangle$, however, the corresponding density operator is not necessarily positive-semidefinite and Hermitian. The R -representation [106] provides a function $R(\alpha^*, \beta)$ without any singularity, however, that is generally complex.

P. D. Drummond and C. W. Gardiner [107] proposed the generalized P -representations which involve two variables α and β as the R -representation and have a variation in the integration element. Especially, the *positive P -representation*

$$\hat{\rho} = \int P(\alpha, \beta) \frac{|\alpha\rangle\langle\beta^*|}{\langle\beta^*|\alpha\rangle} d^2\alpha d^2\beta, \quad (2.59)$$

has all the properties favorable for a statistical analysis. First, there exists a positive P -representation for any quantum density operator $\hat{\rho}$. Also, $P(\alpha, \beta)$ is always positive ($0 \leq P(\alpha, \beta) \leq 1$) and normalizable ($\int P(\alpha, \beta) d^2\alpha d^2\beta = 1$). Here, α and β can vary in the whole complex plane independently. Furthermore, the Fokker-Planck equation corresponding to the master equation for the time evolution of $P(\alpha, \beta)$, if exists, only has drift terms and a positive semidefinite diffusion matrix, which are physically appropriate.

In the positive P -representation, normally ordered moments can be obtained via a Monte-Carlo integration as other probabilistic simulation schemes do, namely

$$\langle(\hat{a}^\dagger)^n (\hat{a})^m\rangle = \int \beta^n \alpha^m P(\alpha, \beta) d^2\alpha d^2\beta. \quad (2.60)$$

It enables us to investigate various physical quantities in numerical studies with this scheme.

Operator algebra

Here, I show how an operator equation is converted into one for the quasi-distribution $P(\alpha, \beta)$. We define and deform explicitly the projection operator in Eq. (2.59) as [107]

$$\begin{aligned} \hat{\Lambda}(\alpha, \beta) &= \frac{|\alpha\rangle\langle\beta^*|}{\langle\beta^*|\alpha\rangle} \\ &= \exp\left(\alpha\hat{a}^\dagger - \alpha\beta\right) |0\rangle\langle 0| \exp(\beta\hat{a}). \end{aligned} \quad (2.61)$$

The eigen-equation for the coherent state and partial differentiation on $\hat{\Lambda}(\alpha, \beta)$ give

$$\hat{a}\hat{\Lambda}(\alpha, \beta) = \alpha\hat{\Lambda}(\alpha, \beta), \quad (2.62)$$

$$\hat{a}^\dagger\hat{\Lambda}(\alpha, \beta) = \left(\frac{\partial}{\partial\alpha} + \beta\right)\hat{\Lambda}(\alpha, \beta), \quad (2.63)$$

$$\hat{\Lambda}(\alpha, \beta)\hat{a} = \left(\frac{\partial}{\partial\beta} + \alpha\right)\hat{\Lambda}(\alpha, \beta), \quad (2.64)$$

$$\hat{\Lambda}(\alpha, \beta)\hat{a}^\dagger = \beta\hat{\Lambda}(\alpha, \beta). \quad (2.65)$$

For Eqs. (2.63) and (2.64), we have transferred the differential operators from $\hat{\Lambda}(\alpha, \beta)$ to $P(\alpha, \beta)$ via integration by parts, provided that the boundary terms vanish. It means that $P(\alpha, \beta)$ decays sufficiently fast for both α and β and is zero at infinite distances. As a result, we have the operator algebra rules for the generalized P -representation

$$\hat{a}\hat{\rho} = \int [\alpha P(\alpha, \beta)] \hat{\Lambda}(\alpha, \beta) d^2\alpha d^2\beta, \quad (2.66)$$

$$\hat{a}^\dagger\hat{\rho} = \int \left[\left(-\frac{\partial}{\partial\alpha} + \beta \right) P(\alpha, \beta) \right] \hat{\Lambda}(\alpha, \beta) d^2\alpha d^2\beta, \quad (2.67)$$

$$\hat{\rho}\hat{a} = \int \left[\left(-\frac{\partial}{\partial\beta} + \alpha \right) P(\alpha, \beta) \right] \hat{\Lambda}(\alpha, \beta) d^2\alpha d^2\beta, \quad (2.68)$$

$$\hat{\rho}\hat{a}^\dagger = \int [\beta P(\alpha, \beta)] \hat{\Lambda}(\alpha, \beta) d^2\alpha d^2\beta. \quad (2.69)$$

Note that $\hat{\Lambda}(\alpha, \beta)$ remains unchanged under the annihilation and creation operations, thus successive applications of Eqs. (2.66) - (2.69) are allowed.

2.3.4 Quantum mechanical Fokker-Planck equation

The master equation together with the operator algebra Eqs. (2.66) - (2.69) lead us to *the quantum-mechanical Fokker-Planck equation* (FPE) for time evolution of the distribution for the signal and pump variables [108]

$$\begin{aligned} \frac{\partial}{\partial t} P(\vec{\alpha}) = & \left\{ \frac{\partial}{\partial\alpha_s} [(\gamma_s + i\omega_s)\alpha_s - \kappa\beta_s\alpha_p] \right. \\ & + \frac{\partial}{\partial\beta_s} [(\gamma_s - i\omega_s)\beta_s - \kappa\alpha_s\beta_p] \\ & + \frac{\partial}{\partial\alpha_p} \left[(\gamma_p + i\omega_p)\alpha_p - \varepsilon_p \exp(-i\omega_d t) + \frac{\kappa^2}{2}\alpha_s^2 \right] \\ & + \frac{\partial}{\partial\beta_p} \left[(\gamma_p - i\omega_p)\beta_p - \varepsilon_p^* \exp(i\omega_d t) + \frac{\kappa^2}{2}\beta_s^2 \right] \\ & \left. + \frac{1}{2} \left[\frac{\partial^2}{\partial\alpha_s^2} (\kappa\alpha_p) + \frac{\partial^2}{\partial\beta_s^2} (\kappa\beta_p) + \Gamma_s \frac{\partial^2}{\partial\alpha_s \partial\beta_s} + \Gamma_p \frac{\partial^2}{\partial\alpha_p \partial\beta_p} \right] \right\} P(\vec{\alpha}), \end{aligned} \quad (2.70)$$

where $\vec{\alpha} = (\alpha_s, \alpha_p, \beta_s, \beta_p)$. $\Gamma_m = 4\gamma_m n_m^{th}$ ($m = p, s$) is the thermal diffusion amplitude.

Here, we move to the rotating frame of the driving field. α_p and α_s implicitly have their frequencies near to $-\omega_p$ and $-\omega_s$ due to their free Hamiltonians. Then, we define the slowly varying fields on the rotating frame

$$\alpha'_p(t) = \alpha_p \exp(i\omega_d t), \quad \alpha'_s(t) = \alpha_s \exp\left(i\frac{\omega_d}{2}t\right), \quad (2.71)$$

where $\omega_d \sim \omega_p$ and $\omega_d/2 \sim \omega_s$. We substitute Eq. (2.71) into Eq. (2.70) with the chain rules for partial differentiation written explicitly as

$$\frac{\partial}{\partial \alpha_p} f(\alpha'_p(\alpha_p)) = \frac{\partial \alpha'_p}{\partial \alpha_p} \frac{\partial f}{\partial \alpha'_p} = \exp(i\omega_d t) \frac{\partial f}{\partial \alpha'_p}, \quad (2.72)$$

$$\frac{\partial}{\partial \alpha_s} f(\alpha'_s(\alpha_s)) = \frac{\partial \alpha'_s}{\partial \alpha_s} \frac{\partial f}{\partial \alpha'_s} = \exp\left(i\frac{\omega_d}{2}t\right) \frac{\partial f}{\partial \alpha'_s}, \quad (2.73)$$

then have

$$\begin{aligned} \frac{\partial}{\partial t} P(\vec{\alpha}(t), t) = \frac{\partial}{\partial t} P(\vec{\alpha}) + \left[-\frac{\partial}{\partial \alpha'_s} \left(i\frac{\omega_d}{2} \alpha'_s \right) + \frac{\partial}{\partial \beta'_s} \left(i\frac{\omega_d}{2} \beta'_s \right) \right. \\ \left. - \frac{\partial}{\partial \alpha'_p} (\omega_d \alpha'_p) + \frac{\partial}{\partial \beta'_p} (i\omega_d \beta'_p) \right] P(\vec{\alpha}(t), t), \end{aligned} \quad (2.74)$$

where $\vec{\alpha}(t) = (\alpha_s(t), \alpha_p(t), \beta_s(t), \beta_p(t))$. Eqs. (2.70) - (2.74) give the FPE in the rotating frame

$$\begin{aligned} \frac{\partial}{\partial t} P(\vec{\alpha}) = & \left\{ \frac{\partial}{\partial \alpha'_s} [(\gamma_s + i\Delta_s) \alpha'_s - \kappa \beta'_s \alpha'_p] \right. \\ & + \frac{\partial}{\partial \beta'_s} [(\gamma_s - i\Delta_s) \beta'_s - \kappa \alpha'_s \beta'_p] \\ & + \frac{\partial}{\partial \alpha'_p} \left[(\gamma_p + i\Delta_p) \alpha'_p - \varepsilon_p + \frac{\kappa^2}{2} \alpha'^2_s \right] \\ & + \frac{\partial}{\partial \beta'_p} \left[(\gamma_p - i\Delta_p) \beta'_p - \varepsilon_p^* + \frac{\kappa^2}{2} \beta'^2_s \right] \\ & \left. + \frac{1}{2} \left[\frac{\partial^2}{\partial \alpha'^2_s} (\kappa \alpha'_p) + \frac{\partial^2}{\partial \beta'^2_s} (\kappa \beta'_p) + \Gamma_s \frac{\partial^2}{\partial \alpha'_s \partial \beta'_s} + \Gamma_p \frac{\partial^2}{\partial \alpha'_p \partial \beta'_p} \right] \right\} P(\vec{\alpha}), \end{aligned} \quad (2.75)$$

$\Delta_s = \omega_s - \omega_d/2$ and $\Delta_p = \omega_p - \omega_d$ are the frequency detuning between the cavity fields and the driving field. Later, we take back the notation and use it for the variables in the rotating frame, namely $(\alpha'_s, \alpha'_p, \beta'_s, \beta'_p) \rightarrow (\alpha_s, \alpha_p, \beta_s, \beta_p)$.

2.3.5 Stochastic differential equations

Here we derive a series of stochastic differential equations [154] for the variables whose distribution function obeys a given Fokker-Planck equation. A stochastic differential equation describes a probabilistic time evolution with mathematical rigor, avoiding singularities as in Langevin equations. We adopt the Ito stochastic integral and start with an Ito stochastic differential equation (SDE) for a single variable $X(t)$

$$dX(t) = A_I[X(t), t] dt + B_I[X(t), t] dW(t), \quad (2.76)$$

where $A_I[X(t), t]$ and $B_I[X(t), t]$ are the drift and diffusion coefficients, respectively. $dW(t) = W(t + dt) - W(t)$ is the Wiener increment in an infinitesimal time interval dt dependent on the Wiener process $W(t)$, the mathematical description of the Brownian motion. $dW(t)$ is independent of those at other time points $dW(t')$ ($t \neq t'$) and obeys the normal distribution $N(0, dt)$, indicating $\langle dW(t) \rangle = 0$ and $\langle dW(t)^2 \rangle = dt$. For the stochastic increment in the time interval between t and $t + dt$, the Ito integral evaluates the diffusion coefficient $B_I[X(t), t]$ at the initial point t . This ensures the martingale property of the process.

Ito's rule

We show the correspondence between an SDE for a single variable X and the Fokker-Planck equation for the distribution $P(X)$, and extend to multi-variable cases, according to Gardiner's text [154]. First, when $X(t)$ satisfies the SDE (2.76), *Ito's formula* for time evolution of an arbitrary function $f[X(t)]$ is

$$\begin{aligned} df[X(t)] = & \left\{ A_I[X(t), t] \left(\frac{\partial f[X(t)]}{\partial X} \right) + \frac{1}{2} B_I[X(t), t]^2 \left(\frac{\partial^2 f[X(t)]}{\partial X^2} \right) \right\} dt \\ & + B_I[X(t), t] \left(\frac{\partial f[X(t)]}{\partial X} \right) dW(t). \end{aligned} \quad (2.77)$$

Using the stochastic average of Eq. (2.77) with $\langle dW(t) \rangle = 0$, we have

$$\begin{aligned} \langle df[X(t)] \rangle / dt &= \frac{d}{dt} \langle df[X(t)] \rangle \\ &= \langle A_I[X(t), t] \partial_X f + \frac{1}{2} B_I[X(t), t]^2 \partial_X^2 f \rangle, \end{aligned} \quad (2.78)$$

where the partial derivative in X is written in short as ∂_X . On the other hand, $(d/dt)\langle f[X(t)] \rangle$ can also be described with a conditional probability density $P(X, t|X_0, t_0)$ for a transition from a initial condition (X_0, t_0) , thus

$$\begin{aligned} \frac{d}{dt} \langle f[X(t)] \rangle &= \int dX f(X) \partial_t P(X, t|X_0, t_0) \\ &= \int \left[A_I(X, t) \partial_X f + \frac{1}{2} B_I(X, t)^2 \partial_X^2 f \right] P(X, t|X_0, t_0). \end{aligned} \quad (2.79)$$

Here, we have used Eq. (2.78). Note that $\partial_t f(X) = 0$. As we did for Eqs. (2.67) and (2.68), we integrate the second line of Eq. (2.79) by parts provided that all the boundary terms vanish. As a result, we get

$$\int dX f(X) \partial_t P = \int dX f(X) \left\{ -\partial_X [A_I(X, t)P] + \frac{1}{2} \partial_X^2 [B_I(X, t)^2 P] \right\}. \quad (2.80)$$

Since $f(X)$ is arbitrary, this means

$$\partial_t P(X, t|X_0, t_0) = -\partial_X [A_I(X, t)P(X, t|X_0, t_0)] + \frac{1}{2} \partial_X^2 [B_I(X, t)^2 P(X, t|X_0, t_0)]. \quad (2.81)$$

This is the FPE equivalent to the SDE (2.76) up to second order in $dW(t)$. Eq. (2.81) is also valid for an initial state with a fixed distribution.

The connection between SDEs and FPEs can be extended for the SDE of N -variable vector \vec{X}

$$d\vec{X} = \vec{A}(\vec{X}, t) dt + \mathbf{B}(\vec{X}, t) d\vec{W}(t), \quad (2.82)$$

where $\mathbf{B}(\vec{X}, t)$ is a diffusion amplitude matrix and $d\vec{W}(t)$ is an N -variable Wiener increment. The corresponding FPE for the conditional probability density $P(\vec{X}, t|\vec{X}_0, t_0) \equiv P$ is

$$\partial_t P = -\sum_i \partial_{X_i} [A_i(\vec{X}, t)P] + \frac{1}{2} \sum_{i,j} \partial_{X_i} \partial_{X_j} \left\{ [\mathbf{B}(\vec{X}, t) \mathbf{B}^T(\vec{X}, t)]_{ij} P \right\}. \quad (2.83)$$

Here, note that $\mathbf{B}\mathbf{B}^T$ is not changed under an orthogonal transformation $\mathbf{B} \rightarrow \mathbf{S}\mathbf{B}$ with $\mathbf{S}\mathbf{S}^T = \mathbf{1}$. Thus, the SDE corresponding to an FPE is not unique.

Stochastic differential equations for a DOPO

Eqs. (2.75), (2.82) and (2.83) give the SDEs for $\vec{\alpha}$ describing a DOPO in the rotating frame [108]

$$d \begin{bmatrix} \alpha_s \\ \beta_s \end{bmatrix} = \begin{bmatrix} -(\gamma_s + i\Delta_s) \alpha_s + \kappa \beta_s \alpha_p \\ -(\gamma_s - i\Delta_s) \beta_s + \kappa \alpha_s \beta_p \end{bmatrix} dt + \begin{bmatrix} \kappa \alpha_p & \Gamma_s \\ \Gamma_s & \kappa \beta_p \end{bmatrix}^{1/2} \begin{bmatrix} dW_{\alpha s}(t) \\ dW_{\beta s}(t) \end{bmatrix}, \quad (2.84)$$

$$d \begin{bmatrix} \alpha_p \\ \beta_p \end{bmatrix} = \begin{bmatrix} \varepsilon_p - (\gamma_p + i\Delta_p) \alpha_p - \frac{\kappa}{2} \alpha_s^2 \\ \varepsilon_p^* - (\gamma_p - i\Delta_p) \beta_p - \frac{\kappa}{2} \beta_s^2 \end{bmatrix} dt + \begin{bmatrix} 0 & \Gamma_p \\ \Gamma_p & 0 \end{bmatrix}^{1/2} \begin{bmatrix} dW_{\alpha p}(t) \\ dW_{\beta p}(t) \end{bmatrix}. \quad (2.85)$$

Here, α_s , β_s , α_p and β_p undergo independent noise processes when Γ_s and Γ_p are negligible. However, α_m and β_m ($m = s, p$) are complex conjugate in terms of statistical averages, i.e. $\langle \beta_m \rangle = \langle \alpha_m \rangle^*$ because $\langle \hat{a}_m \rangle = \langle \alpha_m \rangle$ and $\langle \hat{a}_m^\dagger \rangle = \langle \beta_m \rangle$ from Eq. (2.60).

Adiabatic elimination of the pump field

Here, we neglect the thermal noise ($\Gamma_s = \Gamma_p = 0$) considering the fact that the energies of pump and signal photons are much higher than those of thermal photons in the environment. In addition, the driving field is set to be completely resonant for the pump ($\Delta_s = \Delta_p = 0$). Furthermore, I choose the phase reference as that of the driving field, representing $\varepsilon_p^* = \varepsilon_p$. When the damping rate for the pump mode is much larger than that of the signal ($\gamma_p \gg \gamma_s$), the pump variables can be approximated as those for the steady state. It means $d\alpha_p/dt = d\beta_p/dt = 0$ in Eq. (2.85) and hence gives

$$\alpha_p^{ss} = \frac{1}{\gamma_p} \left(\varepsilon_p - \frac{\kappa}{2} \alpha_s^2 \right), \quad \beta_p^{ss} = \frac{1}{\gamma_p} \left(\varepsilon_p - \frac{\kappa}{2} \beta_s^2 \right). \quad (2.86)$$

We substitute Eq. (2.86) into (2.84) and take the diagonal diffusion amplitude matrix to get the SDEs for the DOPO under the *adiabatic elimination of the pump field*

$$d\alpha_s = \left[-\gamma_s \alpha_s + \frac{\kappa}{\gamma_p} \left(\varepsilon_p - \frac{\kappa}{2} \alpha_s^2 \right) \beta_s \right] dt + \sqrt{\frac{\kappa}{\gamma_p} \left(\varepsilon_p - \frac{\kappa}{2} \alpha_s^2 \right)} dW_{\alpha s}(t), \quad (2.87)$$

$$d\beta_s = \left[-\gamma_s \beta_s + \frac{\kappa}{\gamma_p} \left(\varepsilon_p^* - \frac{\kappa}{2} \beta_s^2 \right) \alpha_s \right] dt + \sqrt{\frac{\kappa}{\gamma_p} \left(\varepsilon_p^* - \frac{\kappa}{2} \beta_s^2 \right)} dW_{\beta s}(t). \quad (2.88)$$

Normalized equations

I also show the normalized SDEs for the signal variables useful for an analysis and simulation [124]

$$d\eta = [-\eta + \mu (\lambda - \eta^2)] d\tau + g \sqrt{\lambda - \eta^2} dW_\eta(\tau), \quad (2.89)$$

$$d\mu = [-\mu + \eta (\lambda - \mu^2)] d\tau + g \sqrt{\lambda - \mu^2} dW_\mu(\tau). \quad (2.90)$$

Here, $\eta = g\alpha_s$, $\mu = g\beta_s$ and $g = \kappa/\sqrt{2\gamma_s\gamma_p}$ is the normalized parametric gain coefficient serving as a noise parameter. $\lambda = \varepsilon_p/\varepsilon_{th}$ is the positive and real pumping rate and $\varepsilon_{th} = \gamma_s\gamma_p/\kappa$ is the classical oscillation threshold for the DOPO. The time is scaled with the lifetime of the signal field, i.e. $\tau = \gamma_s t$. $dW_\eta(\tau)$ and $dW_\mu(\tau)$ are independent real Wiener increments satisfying $\langle dW_\eta(\tau) \rangle = \langle dW_\mu(\tau) \rangle = 0$ and $\langle dW_\eta^2(\tau) \rangle = \langle dW_\mu^2(\tau) \rangle = d\tau$.

Starting with the vacuum state $\eta = \mu = 0$, the system does not go beyond the region $|\eta| \leq \sqrt{\lambda}$, $|\mu| \leq \sqrt{\lambda}$ because of the continuity of the drift term and Wiener process. Also, η and μ do not fail to be real because all the terms are real. It is therefore enough to discuss the inside of the limited range for Eqs. (2.89) and (2.90), and this is called *classical subspace*.

2.4 Properties of DOPO

2.4.1 Classical solution for steady state

Here, I review the important properties of the DOPO. First, the semi-classical rate equations for the mean field variables $\langle \alpha_s \rangle = \alpha_{sa}$ and $\langle \alpha_p \rangle = \alpha_{pa}$ can be derived by

taking the statistical average of Eqs. (2.84) and (2.85) as [155]

$$\frac{\partial \alpha_{sa}}{\partial t} = \kappa \alpha_{sa}^* \alpha_{pa} - \gamma_s \alpha_{sa}, \quad (2.91)$$

$$\frac{\partial \alpha_{pa}}{\partial t} = \varepsilon_p + \frac{\kappa}{2} \alpha_{sa}^2 - \gamma_p \alpha_{pa}, \quad (2.92)$$

where $\langle \beta_s \rangle = \alpha_{sa}^*$ and $\langle \beta_p \rangle = \alpha_{pa}^*$. Considering the stability of the solutions via the eigenvalue equation for the fluctuation, the mean field variables in the steady state are given by

$$\alpha_{sa}^{ss} = 0, \quad \alpha_{pa}^{ss} = \frac{\varepsilon_p}{\gamma_p} \quad (\varepsilon_p \leq \varepsilon_{th}), \quad (2.93)$$

$$\alpha_{sa}^{ss} = \pm \sqrt{\frac{2}{\kappa} (\varepsilon_p - \varepsilon_{th})}, \quad \alpha_{pa}^{ss} = \frac{\gamma_s}{\kappa} \quad (\varepsilon_p > \varepsilon_{th}), \quad (2.94)$$

where $\varepsilon_{th} = \gamma_s \gamma_p / \kappa$ is the classical oscillation threshold. The system shows a critical point phase transition at $\varepsilon_p = \varepsilon_{th}$ where the state jumps to another stable branch. When in oscillation, the signal amplitude can take one of the two amplitudes, which are phase-locked to the driving field and completely out-of-phase to each other. Here, the pump amplitude saturates. Fig. 2.2 shows the mean photon numbers of the signal $|\alpha_{sa}^{ss}|^2$ and pump $|\alpha_{pa}^{ss}|^2$ modes for the classical model. The photon number of the signal above the threshold grows linearly with the pumping rate.

2.4.2 Potential solution in quantum theory for steady state

For the model with the pump variables adiabatically eliminated (2.87) and (2.88), we can obtain the quasi-distribution $P(\alpha_s, \beta_s)$ in the steady state. The corresponding Fokker-Planck equation is

$$\begin{aligned} \frac{\partial}{\partial t} P(\alpha_s, \beta_s) = & \left\{ \frac{\partial}{\partial \alpha_s} \left[\gamma_s \alpha_s - \frac{\kappa}{\gamma_p} \left(\varepsilon_p - \frac{\kappa}{2} \alpha_s^2 \right) \beta_s \right] \right. \\ & + \frac{\partial}{\partial \beta_s} \left[\gamma_s \beta_s - \kappa \alpha_s \frac{\kappa}{\gamma_p} \left(\varepsilon_p - \frac{\kappa}{2} \beta_s^2 \right) \right] \\ & \left. + \frac{1}{2} \left[\frac{\partial^2}{\partial \alpha_s^2} \frac{\kappa}{\gamma_p} \left(\varepsilon_p - \frac{\kappa}{2} \alpha_s^2 \right) + \frac{\partial^2}{\partial \beta_s^2} \frac{\kappa}{\gamma_p} \left(\varepsilon_p - \frac{\kappa}{2} \beta_s^2 \right) \right] \right\} P(\alpha_s, \beta_s), \end{aligned} \quad (2.95)$$

and we find a potential solution [150] in the condition $\partial P / \partial t = 0$. When a Fokker-Planck equation is written as

$$\partial_t P(\vec{X}) = \left[- \sum_i \partial_{X_i} A_i(\vec{X}) + \frac{1}{2} \sum_{i,j} \partial_{X_i} \partial_{X_j} D_{ij}(\vec{X}) \right] P(\vec{X}) = 0, \quad (2.96)$$

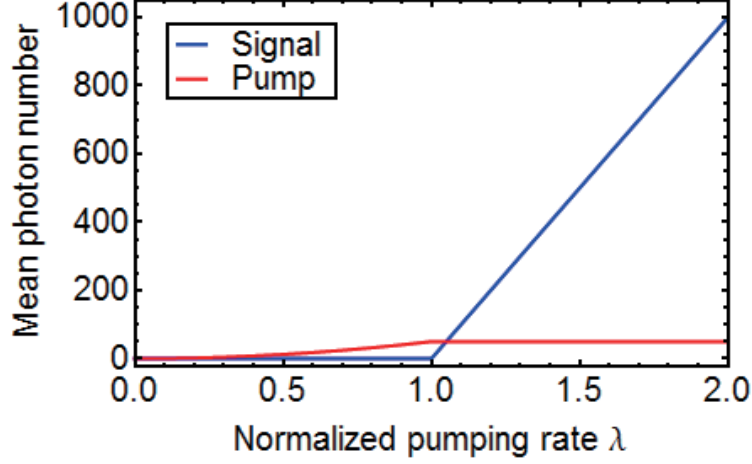


Figure 2.2: Average photon numbers of the signal and pump modes dependent on the pumping rate in the classical model. $\gamma_s = 1$, $\gamma_p = 10$, $\kappa = 0.14142$.

we suppose that each differential component is zero, i.e.

$$\partial_{X_i} \left[-A_i(\vec{X})P(\vec{X}) + \frac{1}{2} \sum_j \partial_{X_j} D_{ij}(\vec{X})P(\vec{X}) \right] = 0. \quad (2.97)$$

This indicates that each variable is static in time. First, we expect that the inside of the bracket of Eq. (2.97) is zero and obtain

$$\sum_j D_{ij}(\vec{X}) [\partial_{X_j} \ln P] = 2A_i(\vec{X}) - \sum_j \partial_{X_j} D_{ij}(\vec{X}). \quad (2.98)$$

Here I used $(\partial_{X_j} P)/P = \partial_{X_j} \ln P$. If we write $-\ln P \equiv \phi(\vec{X})$,

$$-\vec{\nabla} \phi(\vec{X}) = 2\mathbf{D}^{-1} \left\{ \vec{A}(\vec{X}) - [\vec{\nabla}^T \mathbf{D}^T]^T \right\} \equiv \vec{F}(\vec{X}). \quad (2.99)$$

We can say that ϕ and \vec{F} have a relation for a generalized potential and force. If the elements of \vec{F} satisfy the *potential condition*

$$\frac{\partial F_j}{\partial X_i} = \frac{\partial F_i}{\partial X_j} \quad \left(= -\frac{\partial^2 \phi}{\partial X_i \partial X_j} \right), \quad (2.100)$$

we can integrate $\{F_i\}$ and obtain the potential ϕ such that

$$P(\vec{X}) = N_m \exp \left[-\phi(\vec{X}) \right]. \quad (2.101)$$

Eq. (2.100) means that ϕ does not depend on the integration path.

We can find the generalized force for Eq. (2.95) as

$$F_\alpha = -\frac{\partial\phi}{\partial\alpha_s} = 2\beta_s + \frac{4\gamma_p\left(\frac{\kappa^2}{2\gamma_p} - \gamma_s\right)\alpha_s}{2\kappa\varepsilon_p - \kappa^2\alpha_s^2} \quad (2.102)$$

$$F_\beta = -\frac{\partial\phi}{\partial\beta_s} = 2\alpha_s + \frac{4\gamma_p\left(\frac{\kappa^2}{2\gamma_p} - \gamma_s\right)\beta_s}{2\kappa\varepsilon_p - \kappa^2\beta_s^2} \quad (2.103)$$

which obviously meet the potential condition (2.100). We can easily integrate Eqs. (2.102) and (2.103) and find a potential satisfying both of them. As a result, we have the quasi-distribution for the steady state [108]

$$P(\alpha_s, \beta_s) = N_m \exp \left[2\alpha_s\beta_s + \frac{2\bar{\gamma}_s\gamma_p}{\kappa^2} \ln(c_p^2 - \kappa^2\alpha_s^2) + \frac{2\bar{\gamma}_s\gamma_p}{\kappa^2} \ln(c_p^2 - \kappa^2\beta_s^2) \right], \quad (2.104)$$

where

$$c_p = \sqrt{2\kappa\varepsilon_p}, \quad \bar{\gamma}_s = \gamma_s - \frac{\kappa^2}{2\gamma_p}. \quad (2.105)$$

In the classical subspace, we can set the variables $\alpha_s = X_\alpha$, $\beta_s = Y_\beta$ as real numbers. Fig. 2.3 displays the quasi-distribution for the pumping rate below and above the threshold. In (a), the distribution gets broader in the direction where $X_\alpha = Y_\beta$ due to the pump below the threshold. In (b), the DOPO is in oscillation and the distribution is divided into two parts for the finite amplitudes out-of-phase, with $\langle X_\alpha \rangle = \langle Y_\beta \rangle$. It takes the nonlinear pump noise into account in addition to the classical solution (2.93) and (2.94). Here, the normalization factor N_m is calculated by integration in the classical subspace. Note that Eq. (2.104) has some numerical instability because the distribution quickly diverges with $\alpha_s\beta_s$ and $2\bar{\gamma}_s\gamma_p/\kappa^2$, and it makes difficult to investigate the cases of many photons.

Generalized moments

Although the integration of $P(\alpha_s, \beta_s)$ in Eq. (2.104) on the path where $\beta_s = \alpha_s^*$ diverges, it is known that it can be computable in the *complex P-representation* which has the same Fokker-Planck equation as the positive *P-representation* but the integral element $d\alpha d\beta$ on a certain path in the phase space. When the path where all the singular points are surrounded and the boundary terms vanish is taken, we can acquire the general moments as follows [108]

$$\begin{aligned} I_{nm} = \langle \hat{a}^{\dagger n} \hat{a}^m \rangle &= N'_m \sum_{l=0}^{\infty} \frac{2^l}{l!} \left(\frac{-c_p}{\kappa} \right)^{l+n} \left(\frac{-c_p}{\kappa} \right)^{l+m} \\ &\quad \times {}_2F_1(-(l+n), j_1; j_2; 2) {}_2F_1(-(l+m), j_1; j_2; 2), \end{aligned} \quad (2.106)$$

$$j_1 = \frac{2\gamma_s\gamma_p}{\kappa^2}, \quad j_2 = \frac{4\gamma_s\gamma_p}{\kappa^2}, \quad (2.107)$$

where ${}_2F_1$ is the Gaussian hypergeometric function. Note that the normalization factor N'_m can be obtained with the identity $I_{00} = 1$.

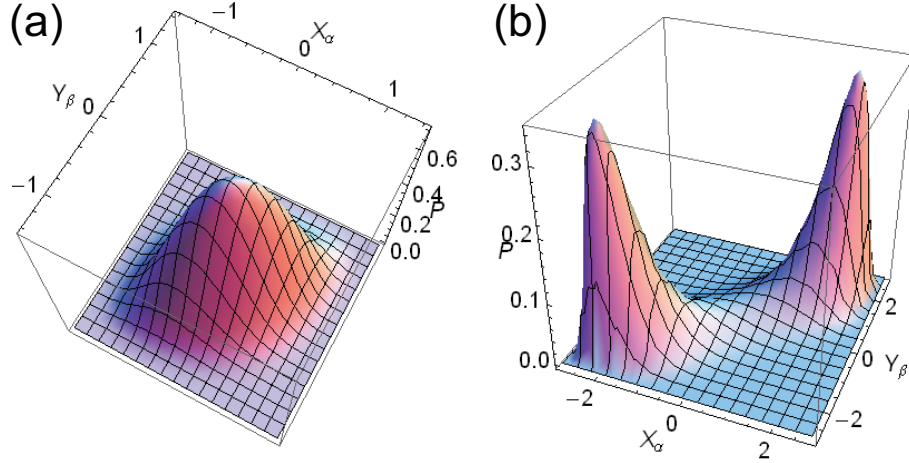


Figure 2.3: Quasi-distribution function $P(\alpha_s, \beta_s)$ in the classical subspace for a DOPO under the adiabatic elimination. (a) $\lambda = \varepsilon_p/\varepsilon_{th} = 0.5$. (b) $\lambda = 2$. $\gamma_s = 1$, $\gamma_p = 2$ and $\kappa = 1$.

Photon number in quantum theory

The photon number of the signal mode $\langle \hat{n}_s \rangle = \langle \hat{a}_s^\dagger \hat{a}_s \rangle$ can be calculated as $I_{11} = \langle \beta_s \alpha_s \rangle$ in Eq. (2.106). It is shown in Fig. 2.4 as dependence on the normalized pumping rate λ . Here I add the line given by the classical model to the figure. Unlike the classical solution, the rigorous curve obtained by quantum theory shows finite intensities also below the threshold. This indicates squeezing of the noise intensity in the quadrature amplitudes, leading to finite photon numbers. When above the threshold, a DOPO has less photons than the classically expected values. However, it converges at the line from the classical theory as the pumping rate increases. Here, the summation in Eq. (2.106) is truncated at $l = 300$ in the calculation. Again, I note that the formula (2.106) can have numerical instability where the value rises discontinuously at a certain pump rate and becomes unphysical. Thus, it is difficult to consider a large loss rate and a small nonlinear coefficient.

Quadrature amplitude operators

We can also see the intracavity squeezing property in the quadrature amplitudes, which can be defined as [156]

$$\hat{x} = \frac{\hat{a}_s + \hat{a}_s^\dagger}{2}, \quad \hat{p} = \frac{\hat{a}_s - \hat{a}_s^\dagger}{2i}. \quad (2.108)$$

Classically, \hat{x} and \hat{p} correspond to the cosine (real) and sine (complex) components of the complex field amplitude, respectively. In a DOPO, the signal field is phase-locked to the driving field in average, thus $\langle \hat{x} \rangle = (\langle \alpha_s \rangle + \langle \beta_s \rangle)/2$ gets finite above the threshold. On the other hand, it means that the mean field does not have any orthogonal component

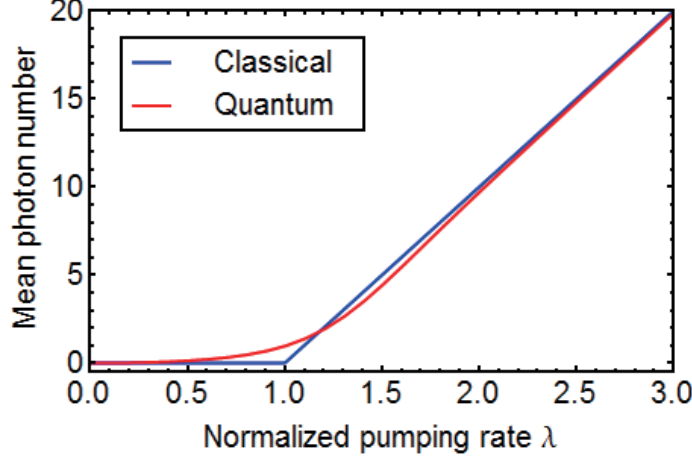


Figure 2.4: The average photon numbers dependent on the normalized pumping rate. $\gamma_s = 0.2$, $\gamma_p = 1$ and $\kappa = 0.2$.

and hence $\langle \hat{p} \rangle = (\langle \alpha_s \rangle - \langle \beta_s \rangle)/2i = 0$ for any pumping rates, as seen in (2.93) and (2.94). \hat{x} and \hat{p} are a pair of canonical operators satisfying the commutation relation

$$[\hat{x}, \hat{p}] = \frac{i}{2}, \quad (2.109)$$

which is straightforward from $[\hat{a}, \hat{a}^\dagger] = 1$. This excludes the possibility of simultaneous determination of the eigenvalues of \hat{x} and \hat{p} .

Intracavity squeezing in quadrature amplitudes

Squeezing [116] is referred to as a process where the quantum noise in a quadrature amplitude is enlarged while that in the other amplitude is reduced below the vacuum fluctuation level. They can be evaluated as the variances of the fluctuation of the operators $\Delta \hat{x} = \hat{x} - \langle \hat{x} \rangle$ and $\Delta \hat{p} = \hat{p} - \langle \hat{p} \rangle$

$$\begin{aligned} \Delta x^2 &= \langle \hat{x}^2 \rangle - \langle \hat{x} \rangle^2 \\ &= \frac{1}{4} \left[1 + \langle \hat{a}_s^2 \rangle + 2\langle \hat{a}_s^\dagger \hat{a}_s \rangle + \langle \hat{a}_s^{\dagger 2} \rangle - \left(\langle \hat{a}_s \rangle + \langle \hat{a}_s^\dagger \rangle \right)^2 \right], \end{aligned} \quad (2.110)$$

$$\begin{aligned} \Delta p^2 &= \langle \hat{p}^2 \rangle - \langle \hat{p} \rangle^2 \\ &= \frac{1}{4} \left[1 - \langle \hat{a}_s^2 \rangle + 2\langle \hat{a}_s^\dagger \hat{a}_s \rangle - \langle \hat{a}_s^{\dagger 2} \rangle + \left(\langle \hat{a}_s \rangle - \langle \hat{a}_s^\dagger \rangle \right)^2 \right], \end{aligned} \quad (2.111)$$

which includes the moments up to second order. The relative magnitudes of them to the vacuum level $1/4$ are shown in Fig. 2.5. The noise level for the orthogonal component Δp^2 falls down near to -3 dB ($1/2$) around the oscillation threshold. This is because

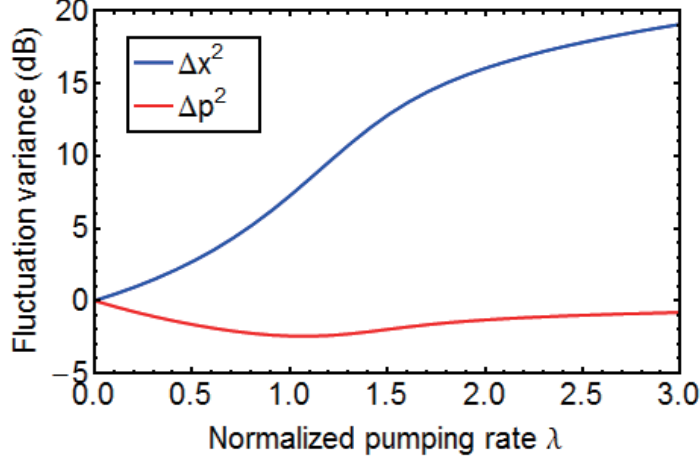


Figure 2.5: The variances in the fluctuation of the quadrature amplitudes which show squeezing. $\gamma_s = 0.2$, $\gamma_p = 1$ and $\kappa = 0.2$.

the pumping works as a loss for $\alpha_s - \beta_s$. Δx^2 increases with the pumping rate due to the nonlinear gain and pump noise and keeps a finite value at the threshold, while the linearized analysis introduced later shows a divergence there. The realistic result in quantum theory comes from the fact it rigorously considers the nonlinearity of the noise term, namely the depletion of the pump field.

2.4.3 Output squeezing spectra

Earlier, I showed that squeezing can be seen in the variances of the fluctuation from the average field. Here, we further see that the spectral noise intensity for the output field at the steady state can be computed by the linearized analysis [150] on the SDEs for such fluctuation variables. In the SDEs (2.84) and (2.85) with a resonant driving field and thermal noise neglected, we decompose the field variables into their classical steady solutions and small fluctuation components around them, i.e.

$$\vec{\alpha}(t) = (\alpha_s^{ss} + \Delta\alpha_s(t), \beta_s^{ss} + \Delta\beta_s(t), \alpha_p^{ss} + \Delta\alpha_p(t), \beta_p^{ss} + \Delta\beta_p(t))^T. \quad (2.112)$$

We substitute (2.112) into (2.84) and (2.85), and neglect the second and higher order terms with regard to fluctuation variables. Furthermore, we approximate the pump variables in the diffusion terms as their steady values. As a result, we have a series of

linearized SDEs for fluctuation variables as follows

$$d\vec{\Delta\alpha} = -\mathbf{A}\vec{\Delta\alpha} + \mathbf{B}d\vec{W}(t), \quad (2.113)$$

$$\mathbf{A} = \begin{pmatrix} \gamma_s & -\kappa\alpha_p^{ss} & -\kappa\beta_s^{ss} & 0 \\ -\kappa\beta_p^{ss} & \gamma_s & 0 & -\kappa\alpha_s^{ss} \\ \kappa\alpha_s^{ss} & 0 & \gamma_p & 0 \\ 0 & \kappa\beta_s^{ss} & 0 & \gamma_p \end{pmatrix}, \quad (2.114)$$

$$\mathbf{B} = \begin{pmatrix} \sqrt{\kappa\alpha_p^{ss}} & 0 & 0 & 0 \\ 0 & \sqrt{\kappa\alpha_p^{ss}} & 0 & 0 \\ 0 & 0 & 0 & 0 \\ 0 & 0 & 0 & 0 \end{pmatrix}, \quad (2.115)$$

where $\vec{\Delta\alpha} = (\Delta\alpha_s(t), \Delta\beta_s(t), \Delta\alpha_p(t), \Delta\beta_p(t))^T$. $(\alpha_s^{ss}, \beta_s^{ss}, \alpha_p^{ss}, \beta_p^{ss})$ are computed by Eqs. (2.93) and (2.94) as real numbers. Eq. (2.113) has a linear drift matrix and constant diffusion amplitude. Such a model is called an *Ornstein-Uhlenbeck process*.

The Noise spectra for quadrature amplitudes in the normalized order are defined as the Fourier transform of the two-time fluctuation variances. For example [150],

$$S_x(\omega) = \int T \langle : \hat{x}_s(t+\tau) \hat{x}_s(t) : \rangle e^{-i\omega\tau} d\tau, \quad (2.116)$$

$$\begin{aligned} T \langle : \hat{x}_s(t+\tau) \hat{x}_s(t) : \rangle &= \frac{1}{4} \left[\langle \hat{a}_s(t+\tau), \hat{a}_s(t) \rangle + \langle \hat{a}_s^\dagger(t), \hat{a}_s^\dagger(t+\tau) \rangle \right. \\ &\quad \left. + \langle \hat{a}_s^\dagger(t+\tau), \hat{a}_s(t) \rangle + \langle \hat{a}_s^\dagger(t), \hat{a}_s(t+\tau) \rangle \right]. \end{aligned} \quad (2.117)$$

Here, “ $::$ ” means the normal ordering for the bosonic operators, and “ T ” is the time ordering where $\hat{a}_s(t+\tau)$ is placed at the left of $\hat{a}_s(t)$ and $\hat{a}_s^\dagger(t+\tau)$ comes to the right of $\hat{a}_s^\dagger(t)$ when $\tau > 0$. $\langle \hat{A}, \hat{B} \rangle = \langle \hat{A}\hat{B} \rangle - \langle \hat{A} \rangle \langle \hat{B} \rangle$ is the covariance of the two operators. Note that the model is in the rotation frame, thus $\omega = 0$ corresponds to the resonant frequency of the signal ω_s .

Let us limit to the signal mode for simplicity. The normal- and time-ordered covariance matrix for the bosonic operators [117, 118]

$$T : \mathbf{C}(\tau) := \begin{pmatrix} \langle \hat{a}_s(t+\tau), \hat{a}_s(t) \rangle & \langle \hat{a}_s^\dagger(t), \hat{a}_s(t+\tau) \rangle \\ \langle \hat{a}_s^\dagger(t+\tau), \hat{a}_s(t) \rangle & \langle \hat{a}_s^\dagger(t), \hat{a}_s^\dagger(t+\tau) \rangle \end{pmatrix}, \quad (2.118)$$

corresponds to that of the c -number variables α_s and β_s in the positive P -representation

$$\mathbf{C}_{PP}(\tau) = \begin{pmatrix} \langle \alpha_s(t+\tau), \alpha_s(t) \rangle & \langle \alpha_s(t+\tau), \beta_s(t) \rangle \\ \langle \beta_s(t+\tau), \alpha_s(t) \rangle & \langle \beta_s(t+\tau), \beta_s(t) \rangle \end{pmatrix}. \quad (2.119)$$

It is based on the trivial extension of the correspondence between the operator description and Glauber-Sudarshan P -representation. Also, the noise spectrum density for an

Ornstein-Uhlenbeck process in the steady state, that is the Fourier transform of (2.119), is given by [154]

$$\mathbf{S}_\alpha(\omega) = (\mathbf{A} + i\omega\mathbf{I})^{-1} \mathbf{B}\mathbf{B}^T (\mathbf{A}^T - i\omega\mathbf{I})^{-1}, \quad (2.120)$$

where \mathbf{I} is the identity matrix. Note that the covariance does not depend on t in the steady state. The spectrum (2.120) for (2.113) - (2.115) include the components for the pump variables, but we can concentrate on the 2×2 partial matrix for the signal components. Also, the input-output analysis in the Heisenberg picture has revealed the relation between the covariance of the internal and output fields in the cases of the vacuum and a coherent input field [117]

$$\begin{aligned} \langle \hat{a}_{s,OUT}(t+\tau), \hat{a}_{s,OUT}(t) \rangle &= 2\gamma_s \langle \hat{a}_s(t+\tau), \hat{a}_s(t) \rangle, \\ \langle \hat{a}_{s,OUT}^\dagger(t), \hat{a}_{s,OUT}^\dagger(t+\tau) \rangle &= 2\gamma_s \langle \hat{a}_s^\dagger(t), \hat{a}_s^\dagger(t+\tau) \rangle, \\ \langle \hat{a}_{s,OUT}^\dagger(t), \hat{a}_{s,OUT}(t+\tau) \rangle &= 2\gamma_s \langle \hat{a}_s^\dagger(t), \hat{a}_s(t+\tau) \rangle. \end{aligned} \quad (2.121)$$

Here, note that γ_s is the decay rate for the field variable and that for the photons is two times larger. Finally, (2.116), (2.120) and (2.121) lead to the normally ordered spectral noise amplitude for the output quadrature amplitudes

$$: S_{x,OUT}(\omega) : = \frac{2\gamma_s}{4} \{ [\mathbf{S}_\alpha(\omega)]_{11} + [\mathbf{S}_\alpha(\omega)]_{22} + [\mathbf{S}_\alpha(\omega)]_{12} + [\mathbf{S}_\alpha(\omega)]_{21} \}, \quad (2.122)$$

$$: S_{p,OUT}(\omega) : = \frac{2\gamma_s}{4} \{ -[\mathbf{S}_\alpha(\omega)]_{11} - [\mathbf{S}_\alpha(\omega)]_{22} + [\mathbf{S}_\alpha(\omega)]_{12} + [\mathbf{S}_\alpha(\omega)]_{21} \}. \quad (2.123)$$

They are dimensionless quantities, and the observable output noise spectra contain the vacuum fluctuation $1/4$ due to the commutation relation for the bosonic operators in the frequency domain. The final result therefore is

$$\begin{aligned} S_{x,OUT}(\omega) &= \frac{1}{4} + : S_{x,OUT}(\omega) : \\ &= \frac{1}{4} + \frac{\gamma_s}{2} \{ [\mathbf{S}_\alpha(\omega)]_{11} + [\mathbf{S}_\alpha(\omega)]_{22} + [\mathbf{S}_\alpha(\omega)]_{12} + [\mathbf{S}_\alpha(\omega)]_{21} \}, \end{aligned} \quad (2.124)$$

$$\begin{aligned} S_{p,OUT}(\omega) &= \frac{1}{4} + : S_{p,OUT}(\omega) : \\ &= \frac{1}{4} + \frac{\gamma_s}{2} \{ -[\mathbf{S}_\alpha(\omega)]_{11} - [\mathbf{S}_\alpha(\omega)]_{22} + [\mathbf{S}_\alpha(\omega)]_{12} + [\mathbf{S}_\alpha(\omega)]_{21} \}, \end{aligned} \quad (2.125)$$

and they are computed with Eqs. (2.93), (2.94), (2.114), (2.115) and (2.120).

Eqs. (2.93) and (2.94) indicate that Eqs. (2.124) and (2.125) result in different expressions for the cases of the above and below of the threshold. When below the

threshold, the spectra are written in relatively simple forms as [150]

$$S_{x,OUT}(\omega) = \frac{1}{4} + \frac{\frac{\varepsilon_p \kappa}{\gamma_p} \gamma_s}{\left(\frac{\varepsilon_p \kappa}{\gamma_p} - \gamma_s\right)^2 + \omega^2} = \frac{1}{4} + \frac{\gamma_s^2 \lambda}{\gamma_s^2 (\lambda - 1)^2 + \omega^2}, \quad (2.126)$$

$$S_{p,OUT}(\omega) = \frac{1}{4} - \frac{\frac{\varepsilon_p \kappa}{\gamma_p} \gamma_s}{\left(\frac{\varepsilon_p \kappa}{\gamma_p} + \gamma_s\right)^2 + \omega^2} = \frac{1}{4} - \frac{\gamma_s^2 \lambda}{\gamma_s^2 (\lambda + 1)^2 + \omega^2}, \quad (2.127)$$

where the introduction of the normalized pumping rate $\lambda = \kappa \varepsilon_p / (\gamma_s \gamma_p)$ eliminates γ_p and κ in the rightmost side. Especially, we see that the resonant components $S_{x,OUT}(\omega = 0)$ and $S_{p,OUT}(\omega = 0)$ depend only on λ within the first order. When in the case of the above the threshold, the result is much more complicated so I compute it numerically.

Fig. 2.6 displays the pumping dependence of the resonant fluctuation variance of the output signal amplitudes (a) below and (b) above the threshold. Here, $S_{x,OUT}(\omega = 0)$ diverges at the threshold as seen in Eq. (2.126). Above the threshold, it converges at $1/4$, which is the value of a coherent state. The noise in p shows perfect squeezing $S_{p,OUT} = 0$ at the threshold regardless of any parameters in the scope of the first order approximation. Also, it also converges at $1/4$ well above the threshold, thus a highly pumped DOPO with many photons will emit light being approximately a coherent state as a laser does. In (b), I had some points very near to the threshold which gave negative values of $S_{p,OUT}$. Considering that the deformation and substitution are done appropriately with Mathematica and the absolute values of the points are beyond the extent of tiny errors, I presume we have to take the nonlinear components out of this model into account to obtain realistic values there.

Fig. 2.7 shows the spectra of the fluctuation in the output quadrature amplitudes for (a) at the threshold and (b) above the threshold. As shown in (a), the fluctuation in x diverges and that in p vanishes at resonance, while they approach the vacuum level $1/4$ as the frequency deviation increases. When well above the threshold [Fig. 2.7(b)] they look like more symmetric and have more than one peak, i.e. a side-peak response, as reported previously [150].

The fluctuation variance of the intracavity single-mode field corresponds to the total noise in the frequency domain. Thus, the normally ordered variances of the internal quadrature amplitudes can be obtained by integral of the noise spectra

$$\langle : \Delta \hat{x}^2 : \rangle = \frac{1}{2\pi} \frac{1}{2\gamma_s} \int_{-\infty}^{\infty} : S_{x,OUT}(\omega) : d\omega, \quad (2.128)$$

$$\langle : \Delta \hat{p}^2 : \rangle = \frac{1}{2\pi} \frac{1}{2\gamma_s} \int_{-\infty}^{\infty} : S_{p,OUT}(\omega) : d\omega, \quad (2.129)$$

where Eq. (2.121) is used again to get back to the internal field variables. Especially, $\langle : \Delta \hat{p}^2 : \rangle$ at the threshold ($\lambda = 1$) can be calculated easily with (2.127) as

$$\langle : \Delta \hat{p}^2 : \rangle|_{\lambda=1} = -\frac{1}{4\pi} \int_{-\infty}^{\infty} \frac{\gamma_s}{4\gamma_s^2 + \omega^2} d\omega = -\frac{1}{8}, \quad (2.130)$$

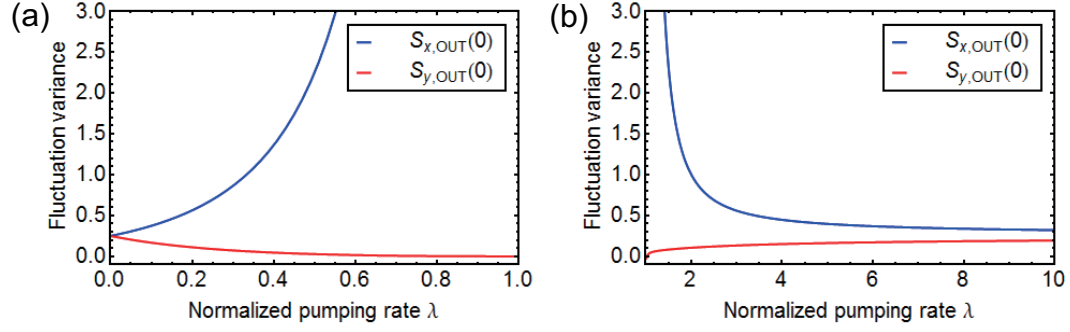


Figure 2.6: The resonant output fluctuation variance $S_{OUT}(\omega = 0)$ dependent on the pump rate (a) below the threshold and (b) above the threshold. $\gamma_s = 0.2$, $\gamma_p = 1$ and $\kappa = 0.2$.

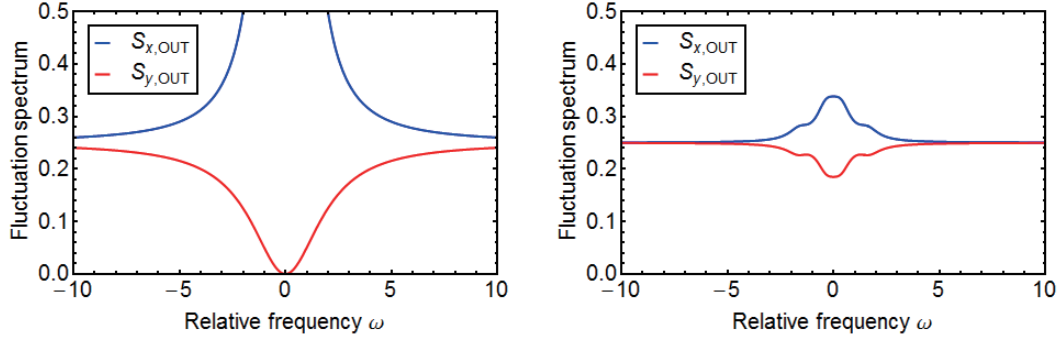


Figure 2.7: The output fluctuation spectra for quadrature amplitudes with (a) $\lambda = 1$ and (b) $\lambda = 10$. $\gamma_s = 0.2$, $\gamma_p = 1$ and $\kappa = 0.2$.

which results in -3 dB squeezing [118].

Fig. 2.8 shows the steady-state intracavity fluctuation variances for the quadrature amplitudes in the first order approximation. Here I adopt relative variances to the vacuum level 1/4 to compare this with the result from quantum theory, i.e. Fig. 2.5. We see there is a sharp contrast of characteristics in $\langle \Delta x^2 \rangle$. In the linearized analysis, $\langle \Delta x^2 \rangle$ diverges at the threshold and falls back nearly to the vacuum level well above the threshold [Fig. 2.8(a) and (b)]. On the other hand, the full quantum theory predicts that Δx^2 keeps finite at the threshold. However, the difference between $\langle \Delta x^2 \rangle$ in the linearized analysis [Fig. 2.8] and Δx^2 in the full quantum theory [Fig. 2.5] above the threshold originates from just the difference in the reference of x . The former considers the reference $(\alpha_s^{ss} + \beta_s^{ss})/2 \neq 0$, while the latter takes $\langle \hat{x} \rangle = 0$. The maximum squeezing of $\langle \Delta p^2 \rangle$ in the quantum theory [Fig. 2.5] is about -3 dB, which is exactly obtained in the linearized analysis. In the latter, however, we find some discontinuity of the curve at the threshold, reflecting the deterministic bifurcation at the critical point.

2.4.4 Macroscopic superposition state

The macroscopic superposition states [157], also called *Schrödinger's cat states*, are quantum-mechanical superpositions of two coherent states with opposite phases, namely

$$|\Psi_{\pm}(\alpha)\rangle = \frac{1}{\sqrt{2 \pm 2e^{-2\alpha^2}}} (|-\alpha\rangle \pm |\alpha\rangle), \quad (2.131)$$

where the normalization factor $1/\sqrt{2 \pm 2e^{-2\alpha^2}}$ comes from the fact that $|-\alpha\rangle$ and $|\alpha\rangle$ are not orthogonal to each other. If we explicitly expand $|\Psi_{\pm}(\alpha)\rangle$ with the Fock states, we have

$$|\Psi_{\pm}(\alpha)\rangle = \frac{e^{\alpha^2/2}}{\sqrt{2 \pm 2e^{-2\alpha^2}}} \sum_{n=0}^{\infty} \frac{\alpha^n}{n!} [(-1)^n \pm 1] |n\rangle. \quad (2.132)$$

Here, we see that $|\Psi_+(\alpha)\rangle$ has only the states of even numbers of photons and $|\Psi_-(\alpha)\rangle$ includes only those of odd numbers. Thus, $|\Psi_+(\alpha)\rangle$ and $|\Psi_-(\alpha)\rangle$ are called *even cat* and *odd cat* states, respectively.

With the density operators for those pure states $|\Psi_+(\alpha)\rangle\langle\Psi_+(\alpha)|$ and $|\Psi_-(\alpha)\rangle\langle\Psi_-(\alpha)|$, we can write their probability distribution functions for the quadrature amplitudes as

$$P_{\pm,\alpha}(z) = \langle z|\hat{\rho}|z\rangle = \frac{1}{2 \pm 2e^{-2\alpha^2}} (\langle z|-\alpha\rangle \pm \langle z|\alpha\rangle) (\langle -\alpha|z\rangle \pm \langle \alpha|z\rangle), \quad (2.133)$$

where $z = x, p$. If we limit α to finite real numbers for simplicity, the inner products for the eigenstates of α and (2.108) [125]

$$\begin{aligned} \langle x|\alpha\rangle &= \left(\frac{\pi}{2}\right)^{-\frac{1}{4}} \exp\left(-2x^2 + 2x\alpha - \frac{\alpha^2}{2} - \frac{|\alpha|^2}{2}\right), \\ \langle p|\alpha\rangle &= \left(\frac{\pi}{2}\right)^{-\frac{1}{4}} \exp\left(-2p^2 - i2p\alpha + \frac{\alpha^2}{2} - \frac{|\alpha|^2}{2}\right), \end{aligned} \quad (2.134)$$

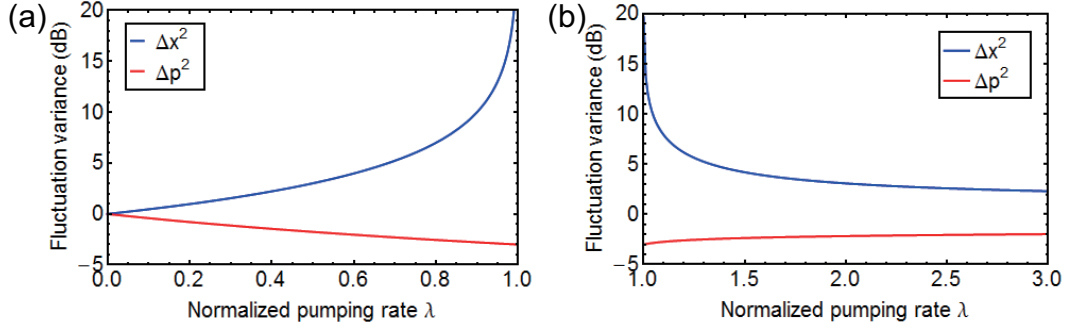


Figure 2.8: The intracavity fluctuation variance for quadrature amplitudes (a) below and (b) above the threshold in the first-order approximation. $\gamma_s = 0.2$, $\gamma_p = 1$ and $\kappa = 0.2$.

lead to the explicit expressions for Eq. (2.133) as [156]

$$P_{\pm, \alpha}(x) = \sqrt{\frac{2}{\pi}} \frac{1}{1 \pm e^{-2\alpha^2}} \left[\pm e^{-2(x^2 + \alpha^2)} + \frac{1}{2} e^{-2(x+\alpha)^2} + \frac{1}{2} e^{-2(x-\alpha)^2} \right], \quad (2.135)$$

$$P_{\pm, \alpha}(p) = \sqrt{\frac{2}{\pi}} \frac{1}{1 \pm e^{-2\alpha^2}} \exp(-2p^2) [1 \pm \cos(4p\alpha)]. \quad (2.136)$$

Fig. 2.9 displays an example of a series of the distribution functions $P_{\pm, \alpha}(x)$ (2.135) and $P_{\pm, \alpha}(p)$ (2.136) with $\alpha = 5$. Both $P_{+, \alpha}(x)$ and $P_{-, \alpha}(x)$ are divided into two parts with their peaks at $x = \pm\alpha$ [Fig. 2.9(a), (b)]. $P_{+, \alpha}(p)$ and $P_{-, \alpha}(p)$ show sinusoidal fringes characteristic of quantum interference between $|- \alpha\rangle$ and $|\alpha\rangle$. $P_{+, \alpha}(p)$ for an even cat has a peak at $p = 0$, while $P_{-, \alpha}(p)$ for an odd cat has a dip there, i.e. $P_{-, \alpha}(p = 0) = 0$.

A DOPO also shows bifurcation in x around the threshold, and when the photon number is small quantum noise will allow switching among the states with positive and negative amplitudes. Also, subharmonic generation is an intrinsic two-photon process for the signal mode, thus it is likely to realize a state of even-number photons in a DOPO with a small loss. We therefore expect that it may have such quantum superposition components.

Quasi-distribution function in the classical subspace

Regarding a possible superposition in a DOPO, M. Wolinsky and H. J. Carmichael [124] investigated the quasi-distribution function for the normalized variables in the classical subspace of the positive P -representation. As shown before for Eq. (2.104), the potential method for the normalized SDEs (2.89) and (2.90) enables us to reach the distribution for real variables $\eta = X_\eta$ and $\mu = Y_\mu$

$$P_{ss}(X_\eta, Y_\mu) = N_m [(\lambda - X_\eta^2)(\lambda - Y_\mu^2)]^{1/g^2 - 1} e^{2X_\eta Y_\mu / g^2}, \quad (2.137)$$

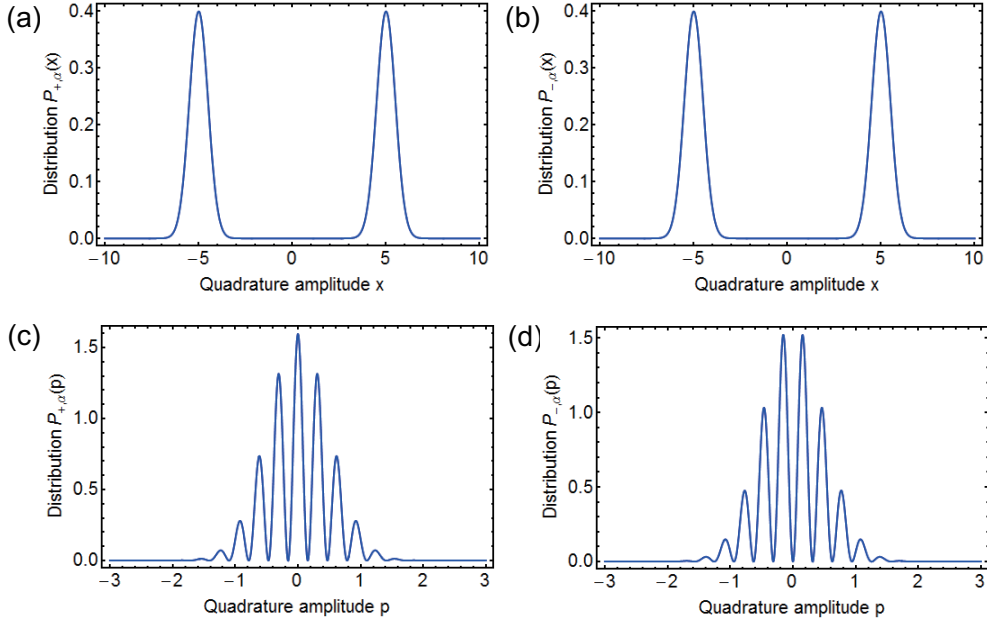


Figure 2.9: Distribution functions for the quadrature amplitudes of the cat states with $\alpha = 5$. (a) $P_{+, \alpha}(x)$, (b) $P_{-, \alpha}(x)$, (c) $P_{+, \alpha}(p)$ and (d) $P_{-, \alpha}(p)$.

where $|X_\eta|, |Y_\mu| \leq \sqrt{\lambda}$. This is essentially the same form as Eq. (2.104), however, the parameter determining the noise magnitude is only g in Eq. (2.137). Thus, this improves the numerical stability.

When $g \geq 1$, the nonlinear process gets dominant over the dissipation and the distribution dramatically changes from that of an ordinary DOPO (Fig. 2.3) as shown in Fig. 2.10. Here, quantum noise sweeps the state to the corners of the boundary where the noise is canceled due to pump depletion. Furthermore, the distribution has the components indicating $X_\eta = -Y_\mu = \pm\sqrt{\lambda}$, which correspond to non-diagonal states $|\sqrt{\lambda}/g\rangle\langle -\sqrt{\lambda}/g|$ and $|- \sqrt{\lambda}/g\rangle\langle \sqrt{\lambda}/g|$ and are impossible in the classical model. This happens also below the classical threshold, and the non-diagonal parts decay as the pumping rate increases. They showed that it approaches a set of δ functions

$$\begin{aligned}
 & P_{ss}(X_\eta, Y_\mu) \\
 &= \frac{1}{2(1 + e^{4\lambda/g^2})} \left[\delta(X_\eta - \sqrt{\lambda})\delta(Y_\mu - \sqrt{\lambda}) + \delta(X_\eta + \sqrt{\lambda})\delta(Y_\mu + \sqrt{\lambda}) \right] \\
 &+ \frac{1}{2(1 + e^{-4\lambda/g^2})} \left[\delta(X_\eta - \sqrt{\lambda})\delta(Y_\mu + \sqrt{\lambda}) + \delta(X_\eta + \sqrt{\lambda})\delta(Y_\mu - \sqrt{\lambda}) \right],
 \end{aligned} \tag{2.138}$$

which qualitatively reproduces the property seen in Fig. 2.10. Eq. (2.138) indicates that in the large noise limit $4\lambda/g^2 \ll 1$, the system is in an even cat state $|\Psi_+(\alpha)\rangle$.

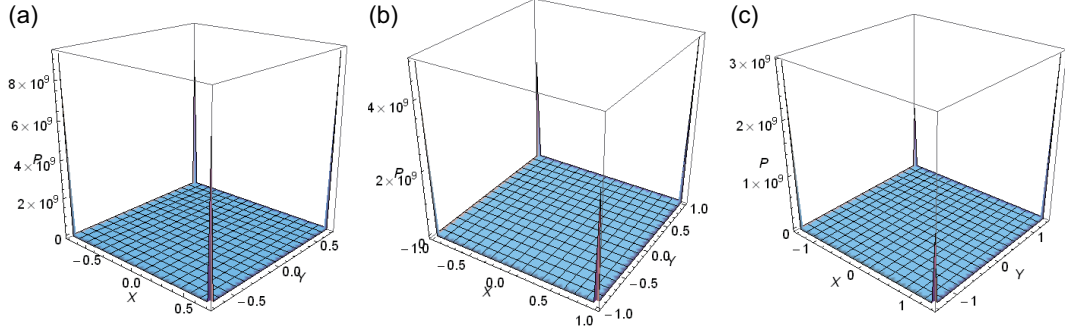


Figure 2.10: Quasi-distribution functions for the normalized variables $P_{ss}(X_\eta, Y_\mu)$ in the classical subspace of the positive P-representation. (a) $\lambda = 0.5$, (b) $\lambda = 1$ and (c) $\lambda = 2$. $g = 3$.

On the other hand, M. D. Reid and B. Yurke [156] investigated the approximated steady-state Wigner function and distribution functions for the quadrature amplitudes corresponding to Eq. (2.137) with some parameters. Also, they argued that features of quantum states such as a negative Wigner function and an oscillation in the distribution $P(p)$ were not seen in the cases of finite photon numbers. It is not surprising that the large pumping and small noise regime would not give these properties as seen in Eq. (2.138), Fig. 2.3 and 2.10. Nevertheless, there still remains a fundamental question in their model and its numerical convergence, namely if it can reproduce a state well approximated as an even cat with a small pumping amplitude and large quantum noise, as Fig. 2.10 (a) does.

L. Krippner, W. J. Munro and M. D. Reid [125] simulated the normalized Stratonovich SDEs for a DOPO extensively and studied the transient distribution functions for the quadrature amplitudes by numerical integration on the formula

$$P(z) = \langle z | \hat{\rho} | z \rangle = \int P(\alpha, \beta) \frac{\langle z | \alpha \rangle \langle \beta^* | z \rangle}{\langle \beta^* | \alpha \rangle} d^2\alpha d^2\beta \quad (z = x, p). \quad (2.139)$$

As a result, they found an oscillation and at least some deviation from a Gaussian function in $P(p)$ with various parameters, and concluded that a sufficiently large noise parameter ($g \gtrsim 2.5$) and a strong pumping would be enough to obtain a transient macroscopic superposition component in a DOPO.

I simulated the Ito SDEs (2.89) and (2.90) with a set of parameters ($g = 3$, $\lambda = 15$) comparable with one in the study [125] to see if these reproduce oscillations in $P(p)$. Ito SDEs keep the martingale property of the processes while the impulsive noise processes eliminate their ordinary analyticity. Fig. 2.11 (a) presents the time evolution of $P(x)$ in a DOPO. A large pumping rate makes $P(x)$ bifurcate into two peaks within a short time $\tau = 0.15$. Fig. 2.11 (b) displays the transient of $P(p)$. Corresponding to the bifurcation of $P(x)$, small side peaks are formed in $P(p)$ around $\tau = 0.15$. They get less visible as time advances, however, $P(p)$ keeps the gentle slopes deviated from Gaussian curves on

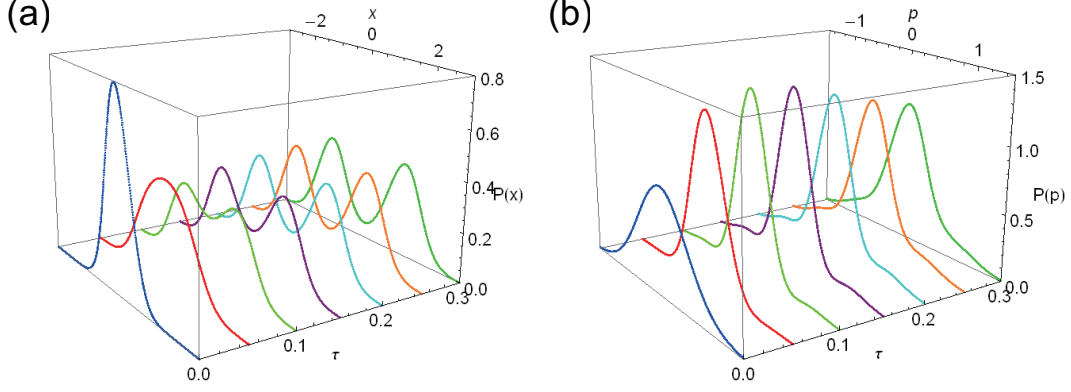


Figure 2.11: Transient of the distribution functions (a) $P(x)$ and (b) $P(p)$ of the DOPO signal field. $g = 3$, $\lambda = 15$ and $\Delta\tau = 2 \times 10^{-5}$. The system is abruptly pumped at $\tau = 0$. 20000 samples were used. I made sure that the distribution functions were well convergent by 10000 samples.

its sides. It indicates weak transient superposition components kept after the oscillation of the DOPO with a finite x .

2.4.5 Entanglement Between Two DOPOs Under Evanescent Coupling

Relatively recently, the entanglement between the fields in two DOPOs has been studied. Here, I introduce the theoretical results [137, 139] on them coupled by evanescent coupling, which have successfully demonstrated the feature. Evanescent coupling is near-field interaction of light waves leaking from one medium to another, and is modeled with the Hamiltonian for a two-DOPO system

$$\mathcal{H}_{evc} = \hbar J_s \left(\hat{a}_{s1} \hat{a}_{s2}^\dagger + \hat{a}_{s1}^\dagger \hat{a}_{s2} \right) + \hbar J_p \left(\hat{a}_{p1} \hat{a}_{p2}^\dagger + \hat{a}_{p1}^\dagger \hat{a}_{p2} \right), \quad (2.140)$$

where J_s and J_p are the coupling strength for the signal and pump fields, and the numbers (1 and 2) are indices of the DOPOs. Hence the master equation is linear in terms of Hamiltonian components, we can derive the FPE and SDEs for the system by just adding the components coming from Eq. (2.140) to the equations for two distinct DOPOs. We can use the standard methods from (2.58) to (2.89) and (2.90) introduced before, and the resulting SDEs for the signal and variables $(\alpha_{s1}, \beta_{s1}, \alpha_{s2}, \beta_{s2}, \alpha_{p1}, \beta_{p1}, \alpha_{p2}, \beta_{p2})$ in the

positive P -representation are

$$d\alpha_{s1} = [-(\gamma_s + i\Delta_s)\alpha_{s1} + \kappa\beta_{s1}\alpha_{p1} + iJ_s\alpha_{s2}]dt + \sqrt{\kappa\alpha_{p1}}dW_{\alpha s1}, \quad (2.141)$$

$$d\beta_{s1} = [-(\gamma_s - i\Delta_s)\beta_{s1} + \kappa\alpha_{s1}\beta_{p1} - iJ_s\beta_{s2}]dt + \sqrt{\kappa\beta_{p1}}dW_{\beta s1}, \quad (2.142)$$

$$d\alpha_{s2} = [-(\gamma_s + i\Delta_s)\alpha_{s2} + \kappa\beta_{s2}\alpha_{p2} + iJ_s\alpha_{s1}]dt + \sqrt{\kappa\alpha_{p2}}dW_{\alpha s2}, \quad (2.143)$$

$$d\beta_{s2} = [-(\gamma_s - i\Delta_s)\beta_{s2} + \kappa\alpha_{s2}\beta_{p2} - iJ_s\beta_{s1}]dt + \sqrt{\kappa\beta_{p2}}dW_{\beta s2}, \quad (2.144)$$

$$d\alpha_{p1} = \left[\varepsilon_{p1} - (\gamma_p + i\Delta_p)\alpha_{p1} - \frac{\kappa}{2}\alpha_{s1}^2 + iJ_b\alpha_{p2} \right] dt, \quad (2.145)$$

$$d\beta_{p1} = \left[\varepsilon_{p1} - (\gamma_p - i\Delta_p)\beta_{p1} - \frac{\kappa}{2}\beta_{s1}^2 - iJ_b\beta_{p2} \right] dt, \quad (2.146)$$

$$d\alpha_{p2} = \left[\varepsilon_{p2} - (\gamma_p + i\Delta_p)\alpha_{p2} - \frac{\kappa}{2}\alpha_{s2}^2 + iJ_b\alpha_{p1} \right] dt, \quad (2.147)$$

$$d\beta_{p2} = \left[\varepsilon_{p2} - (\gamma_p - i\Delta_p)\beta_{p2} - \frac{\kappa}{2}\beta_{s2}^2 - iJ_b\beta_{p1} \right] dt, \quad (2.148)$$

Here, the evanescent coupling lets the field variables shift each other's phases due to the $\pm\pi/2$ phase terms ($\pm i$). I again assume that the drive fields are the phase reference.

Criterion for entanglement

An entangled state [34] is defined as a state of more than one particles which cannot be described as a product state (for example, $\hat{\rho} \neq \sum_i p_i \hat{\rho}_{1i} \otimes \hat{\rho}_{2i}$ for two-particle systems). For continuous variable states with the quadrature amplitude operators \hat{x}_i and \hat{p}_i (2.108) satisfying (2.109), we consider the pairs of EPR-type operators which characterize the correlation between them

$$\hat{u}_{\pm} = \hat{x}_1 \pm \hat{x}_2, \quad \hat{v}_{\mp} = \hat{p}_1 \mp \hat{p}_2, \quad (2.149)$$

and their fluctuation operators

$$\Delta\hat{u}_{\pm} = \hat{u}_{\pm} - \langle\hat{u}_{\pm}\rangle, \quad \Delta\hat{v}_{\mp} = \hat{v}_{\mp} - \langle\hat{v}_{\mp}\rangle. \quad (2.150)$$

The sufficient criterion for the entanglement in two continuous variable states with these operators is [158]

$$\langle\Delta\hat{u}_{+}^2\rangle + \langle\Delta\hat{v}_{-}^2\rangle < 1, \text{ or } \langle\Delta\hat{u}_{-}^2\rangle + \langle\Delta\hat{v}_{+}^2\rangle < 1. \quad (2.151)$$

It means that the correlation between the quadrature amplitudes of the two particles is beyond the vacuum fluctuation level, and that is classically impossible. An entangled state is also referred to as a state which cannot be produced with a vacuum state and local operations and classical communication (LOCC) [159]. Thus, it guarantees the existence of a quantum communication channel which is realized by the interaction between the particles.

Linearized analysis for fluctuation in EPR-type operators

To examine the entanglement, we can apply the linearized analysis introduced before. Here, we assume that the pump variables are adiabatically eliminated and equal to each other, $\alpha_{p1}^{ss} = \alpha_{p2}^{ss} = \beta_{p1}^{ss} = \beta_{p2}^{ss} = \varepsilon_{ss}$. Also, the detuning parameters are set to be equal to the coupling coefficients, i.e. $J_s = \Delta_s$, $J_p = \Delta_p$. This allows the interfered fields defined as

$$\begin{aligned} A_{+s} &= \alpha_{s1} + \alpha_{s2}, & B_{+s} &= \beta_{s1} + \beta_{s2}, \\ A_{-s} &= \alpha_{s1} - \alpha_{s2}, & B_{-s} &= \beta_{s1} - \beta_{s2}, \end{aligned} \quad (2.152)$$

to obtain the steady solutions in average

$$A_{+s}^{ss} = B_{+s}^{ss} = A_{-s}^{ss} = B_{-s}^{ss} = 0 \quad \left(\varepsilon_p < \frac{\gamma_s \gamma_p}{\kappa} \right). \quad (2.153)$$

$$A_{+s}^{ss} = B_{+s}^{ss} = \pm 2\sqrt{\frac{2}{\kappa} \left(\varepsilon_p - \frac{\gamma_s \gamma_p}{\kappa} \right)}, \quad A_{-s}^{ss} = B_{-s}^{ss} = 0 \quad \left(\varepsilon_p > \frac{\gamma_s \gamma_p}{\kappa} \right). \quad (2.154)$$

Note that the oscillation threshold $\varepsilon_{th} = \gamma_s \gamma_p / \kappa$ is the same as that of a single DOPO. Taking the summations and subtractions of the Eqs. (2.141) - (2.144), we have the SDEs for the sum and difference modes

$$dA_{+s} = [-(\gamma_s + i\Delta)A_{+s} + \kappa\varepsilon_{ss}B_{+s} + iJ_sA_{+s}]dt + \sqrt{\kappa\varepsilon_{ss}}(dW_{\alpha s1} + dW_{\alpha s2}), \quad (2.155)$$

$$dB_{+s} = [-(\gamma_s - i\Delta)B_{+s} + \kappa\varepsilon_{ss}A_{+s} - iJ_sB_{+s}]dt + \sqrt{\kappa\varepsilon_{ss}}(dW_{\beta s1} + dW_{\beta s2}), \quad (2.156)$$

$$dA_{-s} = [-(\gamma_s + i\Delta)A_{-s} + \kappa\varepsilon_{ss}B_{-s} - iJ_sA_{-s}]dt + \sqrt{\kappa\varepsilon_{ss}}(dW_{\alpha s1} - dW_{\alpha s2}), \quad (2.157)$$

$$dB_{-s} = [-(\gamma_s - i\Delta)B_{-s} + \kappa\varepsilon_{ss}A_{-s} + iJ_sB_{-s}]dt + \sqrt{\kappa\varepsilon_{ss}}(dW_{\beta s1} - dW_{\beta s2}). \quad (2.158)$$

Let us limit the analysis to the below-threshold case [137]. Here, the average signal fields vanish thus we do not need to consider the nonlinear dependence in the steady pump modes. Then we have $\varepsilon_{ss} = \varepsilon_p / \gamma_p$, and a drift and a diffusion amplitude matrix for the fluctuation variables $(\Delta A_{+s}, \Delta B_{+s}, \Delta A_{-s}, \Delta B_{-s})$ are obtained

$$\mathbf{A}_{\pm} = \begin{pmatrix} \gamma_s & -\kappa\varepsilon_{ss} & 0 & 0 \\ -\kappa\varepsilon_{ss} & \gamma_s & 0 & 0 \\ 0 & 0 & \gamma_s + 2iJ_s & -\kappa\varepsilon_{ss} \\ 0 & 0 & -\kappa\varepsilon_{ss} & \gamma_s - 2iJ_s \end{pmatrix}, \quad (2.159)$$

$$\mathbf{B}_{\pm} = \begin{pmatrix} \sqrt{\kappa\varepsilon_{ss}} & 0 & \sqrt{\kappa\varepsilon_{ss}} & 0 \\ 0 & \sqrt{\kappa\varepsilon_{ss}} & 0 & \sqrt{\kappa\varepsilon_{ss}} \\ \sqrt{\kappa\varepsilon_{ss}} & 0 & -\sqrt{\kappa\varepsilon_{ss}} & 0 \\ 0 & \sqrt{\kappa\varepsilon_{ss}} & 0 & -\sqrt{\kappa\varepsilon_{ss}} \end{pmatrix}. \quad (2.160)$$

The variables corresponding to the EPR-type operators can be defined as

$$u_+ = x_{s1} + x_{s2} = \frac{1}{2}(A_{s+} + B_{s+}), \quad (2.161)$$

$$u_- = x_{s1} - x_{s2} = \frac{1}{2}(A_{s-} + B_{s-}), \quad (2.162)$$

$$v_+ = p_{s1} + p_{s2} = \frac{1}{2i}(A_{s+} - B_{s+}), \quad (2.163)$$

$$v_- = p_{s1} - p_{s2} = \frac{1}{2i}(A_{s-} - B_{s-}). \quad (2.164)$$

Thus, we can compute the normally ordered noise spectra for the EPR-type operators using Eqs. (2.120), (2.122) and (2.123). Adding the vacuum fluctuation of the two DOPOs to each component, the observable output fluctuation spectra of the EPR-type operators are given as

$$S_{u+,OUT}(\omega) = \frac{1}{2} + \frac{2\gamma_s\gamma_p\kappa\varepsilon_p}{(\gamma_s\gamma_p - \kappa\varepsilon_p)^2 + \gamma_p^2 + \omega^2}, \quad (2.165)$$

$$S_{v+,OUT}(\omega) = \frac{1}{2} - \frac{2\gamma_s\gamma_p\kappa\varepsilon_p}{(\gamma_s\gamma_p + \kappa\varepsilon_p)^2 + \gamma_p^2 + \omega^2}, \quad (2.166)$$

$$S_{u-,OUT}(\omega) = \frac{1}{2} + \frac{2\gamma_s\gamma_p\kappa\varepsilon_p((\gamma_s\gamma_p + \kappa\varepsilon_p)^2 - \gamma_p^2(4J_s^2 - \omega^2))}{(\gamma_p^2(\gamma_s^2 + 4J_s^2 - \omega^2) - \kappa\varepsilon_p)^2 + 4\gamma_s^2\gamma_p^4\omega^2}, \quad (2.167)$$

$$S_{v-,OUT}(\omega) = \frac{1}{2} - \frac{2\gamma_s\gamma_p\kappa\varepsilon_p((\gamma_s\gamma_p - \kappa\varepsilon_p)^2 - \gamma_p^2(4J_s^2 - \omega^2))}{(\gamma_p^2(\gamma_s^2 + 4J_s^2 - \omega^2) - \kappa\varepsilon_p)^2 + 4\gamma_s^2\gamma_p^4\omega^2}. \quad (2.168)$$

The spectral properties in the fluctuation in $\langle\Delta u_-^2\rangle + \langle\Delta v_+^2\rangle$ are depicted in Fig. 2.12. In (a), we see that the spectral components around the resonant frequency satisfy Eq. (2.151), meaning that they are lower than the total vacuum fluctuation and the system shows the entanglement. The fluctuation there gets larger for the system with less interaction. Fig. 2.12 (b) shows that the fluctuation at resonance dependent on the pumping rate. Larger interaction leads to a stronger correlation. However, the improvement in noise suppression by the coupling is not so drastic in $J_s > 1$. On the other hand, when J_s is smaller than the cavity loss rate, the system can lose the entanglement before reaching the oscillation threshold.

The result indicates that when the system has interaction of the same extent as dissipation, the system can acquire entanglement between its elements. Note that the condition for obtaining a state with the EPR paradox [133] is tighter, while this system can satisfy it. This condition involves the fluctuation of each quadrature amplitude and their covariances, which can be obtained with the calculation in Sec. 2.4.3. In addition, it has been shown that the linearized analysis for this system above the threshold can also achieve the criterion for the entanglement [139].

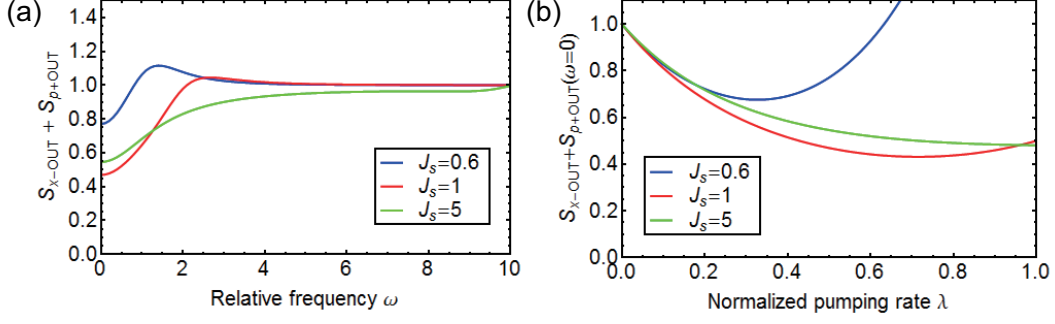


Figure 2.12: Fluctuation spectrum of the sum of the EPR-type operators $\langle \Delta u_-^2 \rangle + \langle \Delta v_+^2 \rangle$. (a) Frequency dependence with $\varepsilon_p = 0.5\varepsilon_{th}$. (b) Pump rate dependence at resonance $\omega = 0$. $\gamma_s = \gamma_p = \kappa = J_p = \Delta_p = 1$. $J_s = \Delta_s$. $S_{u-,OUT} + S_{v+,OUT} < 1$ represents the entanglement between the fields in the two DOPOs.

2.5 Coherent Ising machine

Finally, I refer to the theory of a coherent Ising machine based on DOPOs proposed by Z. Wang *et al* [103]. They deduced a set of c -number Langevin equations with phenomenological mutual injection terms by approximating the operators in the corresponding Heisenberg-Langevin equations as c -numbers. They are equivalent to the SDEs in the Wigner representation which truncates the third order components in the original Fokker-Planck equation. Here, the mapped Ising spin is expressed as the sign of the in-phase quadrature amplitude $x_i = (\alpha_i + \alpha_i^*)/2$ in each DOPO, i.e. $\sigma_i = 1$ if $x_i > 0$ and $\sigma_i = -1$ if $x_i < 0$ where i is the index for DOPOs. The coupled semi-classical rate equations for the quadrature amplitudes x_i and $p_i = (\alpha_i - \alpha_i^*)/(2i)$ are given as

$$\frac{d}{d\tau} x_i = [-1 + \lambda - (x_i^2 + p_i^2)] x_i + \sum_{j \neq i}^N \xi_{ij} x_j, \quad (2.169)$$

$$\frac{d}{d\tau} p_i = [-1 - \lambda - (x_i^2 + p_i^2)] p_i + \sum_{j \neq i}^N \xi_{ij} p_j. \quad (2.170)$$

Here, the orthogonal components p_i are damped due to the nonlinear loss, namely $p_i^{ss} = 0$. Also, a perturbation expansion method leads to the fact that the total effective gain for the in-phase amplitudes $\sum_i \lambda - (x_i^2 + p_i^2)$ at the steady state above the threshold depends on the mapped Hamiltonian

$$\sum_i \lambda - (x_i^2 + p_i^2) = N - \sum_{i \neq j} \xi_{ij} \sigma_i \sigma_j + \mathcal{O}\left(\frac{\epsilon^3 N^4}{(\lambda - 1)^3}\right) \quad (2.171)$$

with some finite error terms. ϵ is the small number appeared in the perturbation expansion. Extensive numerical benchmarking with Eqs. (2.169) and (2.170) starting with

randomized vacuum states has been conducted. An example of transits of the c -number amplitudes x_i for a two-site anti-ferromagnetic Ising model is shown in Fig. 2.13. The DOPOs have a mutual injection which has a coupling phase of π , namely $\xi_{12} < 0$. Pumped above the threshold, the system settles into a state with an out-of-phase order of the coherent signal amplitudes due to the mutual injection, in a time with the order of the cavity lifetime. This corresponds to the ground state of the mapped Hamiltonian, that is an anti-ferromagnet of two spins in opposite directions. They found the ground states in all the instances of the unweighted anti-ferromagnetic Ising model (the MAX-CUT problem) in cubic graphs with the number of spins up to $N = 20$. Also, they showed that though the success probability in the worst instance decreases with the problem size, they can make some improvement by changing the parameters.

2.6 Summary

In this chapter, I reviewed the quantum theory of a degenerate optical parametric oscillator and the properties predicted by it. I introduced the positive P -representation exploiting two c -number variables to describe a continuous variable field state inside a cavity. Then, the series of stochastic differential equations suitable for numerical simulations were derived via the Fokker-Planck equation. We saw that the quantum noise from the pump field could affect the characteristics of a DOPO. The rigorous potential solution for the Fokker-Planck equation predicted that the photon number would be finite also below the oscillation threshold, and that above the threshold would be smaller than that of the classical solution. Furthermore, the squeezing properties for both the intracavity and output fields are calculated and discussed with the rigorous formula for the moment and the linearized analysis. When the nonlinear process was dominant, the system would have a macroscopic superposition component at the steady state in the small photon number limit, and also in a transit with a finite photon number. The system of two DOPOs could also show entanglement between the two field states via evanescent coupling. Finally I referred to a semi-classical model for a coherent Ising machine based on a network of DOPOs. The Ising Hamiltonian was mapped to the total gain for the in-phase amplitudes, and the system would get toward the ground state via the nonlinear dynamics due to the mutual injection. The benchmarking with the rate equations showed that the performance bounded by its classical framework was good enough to obtain the ground states of all the instances of the anti-ferromagnetic Hamiltonians for the cubic graph systems with up to twenty nodes.

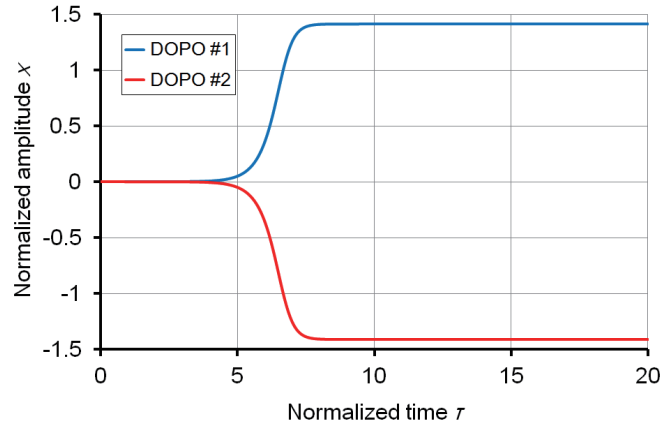


Figure 2.13: Transit of the in-phase quadrature amplitude x_i in a coherent Ising machine composed of two DOPOs with an out-of-phase mutual injection. $\lambda = 2$ and $\xi_{ij} = -1$.

Chapter 3

Quantum States in Two DOPOs Coupled with Mutual Injection

3.1 Introduction

An important open question is if the coherent Ising machines have any quantum features available for the computation. It is because quantum computation [34] is the only physical computing paradigm which has the theoretical evidences that it possibly surpasses digital computing [33, 42]. The previous theoretical models [98, 99, 103] for the Ising machines can deal with quantum effects up to the quadratic squeezing process. However, It is known that squeezing can be reproduced by a classical model which takes the vacuum fluctuation into account phenomenologically [109, 160]. In addition, Gottesman-Knill theorem [110, 111] shows that such a quadratic process is not enough for the system to exert the performance limit of quantum computing. On the other hand, the coherent superposition (Schrödinger's kitten and cat) states [157] are well generated by the third-order process (Kerr effect) [161] and can show negative values of the Wigner function [126], thus they can be an essential resource for quantum computation. Furthermore, to preserve quantum information of a pure state with correlated particles, there need to be entanglement between them. Fortunately, a transient state with superposition components in a single DOPO [125] and entanglement between two DOPOs with evanescent coupling [137, 139] have been theoretically reported, as seen in the previous chapter. However, the previous models including mutual injections are all in the semi-classical framework in the sense that there is the one-to-one correspondence between the simulation variables and the physical quantities under a single-shot measurement. Such a model in principle cannot treat the quantum effects where non-diagonal components of the density operator play a crucial role. At least, there is an argument that even if a coherent Ising machine can be a good quantum computing device, the simulated benchmarking can give only the performance of its classical counterpart.

In this chapter, I study a fully quantum mechanical model for the system of two DOPOs with out-of-phase mutual injections using the positive P -representation [107]. Here, I extend the theoretical model for a single DOPO [108] to the one for the considered

system by adding the sub-harmonic cavity mode in the mutual injection path between the facets of the two DOPOs (called *mid cavity* afterwards). This provides a quantum-theoretical framework for an oscillator network coupled with mutual injections. In this model, the loss rate for this mid cavity comes to be an important factor of the dissipation for the whole system. Also, the adiabatic elimination of this mid cavity mode results in the linear mutual injection terms for the DOPO field variables, which have been introduced phenomenologically in the previous study [103]. In this limit, the mid cavity works as a coherent communication channel for the two DOPOs, and the intracavity fields of them below the oscillation threshold can be entangled due to the quantum correlation between the squeezed quadrature amplitudes $\hat{p} = (\hat{a} - \hat{a}^\dagger)/(2i)$. When the system is sufficiently closed, the mid cavity mode becomes a shared noise store containing a squeezed vacuum. This destroys the entanglement because of an enhanced fluctuation in the extended quadrature amplitude $\hat{x} = (\hat{a} + \hat{a}^\dagger)/2$. However, the noise induces weak fringes of the distribution functions of p in the transit, indicating coherent superposition components in the DOPOs even with a small noise parameter. This suggests that an empty feedback path for DOPOs is realization of a “squeezed heat bath” [123, 162], which was introduced as hypothetical environment to protect macroscopic superposition from dephasing.

This chapter is organized as follows. In Sec. 3.2, I describe the Ito stochastic differential equations (SDEs) for the field variables in the system and relate the mid-cavity mode to the phenomenological injection term which was previously studied. In Sec. 3.3, I give the simulation setting and review some ingredients for the simulated quantities and properties. In Secs. 3.4 and 3.5, I discuss the simulation result and simulation schemes for this system. Sec. 3.6 concludes this chapter.

3.2 Derivation of Theoretical Model

3.2.1 System overview

First of all, I describe the system treated in this chapter. Fig. 3.1 shows schematic illustrations of it. As shown in (a), it is composed of two DOPOs and the mutual injection path between them as the mid cavity. The two angled mirrors in this central cavity are assumed to be dielectric. It means that they can highly reflect and confine the signal field of a frequency ω_s while entirely transmit the driving field with a frequency $\omega_d \sim \omega_p = 2\omega_s$, where ω_p is the frequency of the pump mode. The identical strong driving field ε_p enters each DOPO to excite the pump mode. It is assumed to be classical and the phase reference. The bosonic annihilation and creation operators for the pump and signal modes in the DOPOs are defined as $(\hat{a}_{pj}, \hat{a}_{pj}^\dagger)$ and $(\hat{a}_{sj}, \hat{a}_{sj}^\dagger)$, where $j = 1, 2$ is the index for the DOPOs. Also, those for the mid-cavity signal mode are written as $(\hat{a}_c, \hat{a}_c^\dagger)$. Fig. 3.1 (b) displays the coupling between the DOPO signal fields and the mid cavity field as beamsplitter interaction. Here, the mid cavity field interacts with the two DOPO fields at distant points, thus we have to consider the spatial phase term explicitly. When I take the z axis as shown in Fig. 3.1 (a), with its origin at the facet of DOPO#1, the

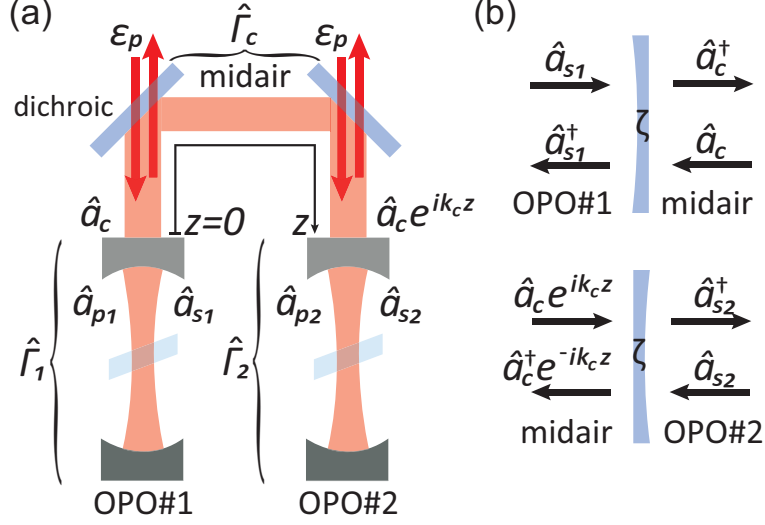


Figure 3.1: Schematic drawings of the system. (a) The whole system comprising two DOPOs and the mutual injection path between them as a cavity. The two dichroic mirrors in this mid cavity are assumed to pass the pump field completely and highly reflect the signal field. (b) Beamsplitter interaction between the DOPO fields and the central cavity mode. The spacial phase of the mid cavity field needs to be considered.

electric field operator for the signal mode in the center cavity can be written as

$$\hat{E}(z, t) = \vec{\epsilon}_{kc} \left(\mathcal{E}_{kc} \hat{a}_c e^{-i\omega_s t + ik_c z} + \mathcal{E}_{kc}^* \hat{a}_c^\dagger e^{i\omega_s t - ik_c z} \right), \quad (3.1)$$

where $\vec{\epsilon}_{kc}$ is the polarization vector, \mathcal{E}_{kc} is the characteristic electric field amplitude and k_c is the wave number. Thus, the bosonic operators at the facet of DOPO#2 have phase factors depending on the center cavity length and are written as $\hat{a}_c \exp(ik_c z)$ and $\hat{a}_c^\dagger \exp(-ik_c z)$. When $\exp(ik_c z) = \exp(-ik_c z) = 1$ the mutual injection is an in-phase coupling, and it is out-of-phase if $\exp(ik_c z) = \exp(-ik_c z) = -1$.

3.2.2 System Hamiltonian

The Hamiltonian for the system is an extension of that for a single DOPO [108], and can be written as

$$\mathcal{H} = \mathcal{H}_{free} + \mathcal{H}_{int} + \mathcal{H}_{pump} + \mathcal{H}_{res} + \mathcal{H}_{BS}, \quad (3.2)$$

where the free Hamiltonian for the relevant modes is

$$\mathcal{H}_{free} = \sum_{j=1}^2 \left(\hbar\omega_p \hat{a}_{pj}^\dagger \hat{a}_{pj} + \hbar\omega_s \hat{a}_{sj}^\dagger \hat{a}_{sj} \right) + \hbar\omega_s \hat{a}_c^\dagger \hat{a}_c. \quad (3.3)$$

The quadratic nonlinear interaction Hamiltonian is

$$\mathcal{H}_{int} = i\hbar \sum_{j=1}^2 \left[\frac{\kappa}{2} \left(\hat{a}_{sj}^{\dagger 2} \hat{a}_{pj} - \hat{a}_{pj}^{\dagger} \hat{a}_{sj}^2 \right) \right], \quad (3.4)$$

where κ denotes the coupling coefficient in terms of the subharmonic mode. The driving Hamiltonian is described by

$$\mathcal{H}_{pump} = i\hbar \sum_{j=1}^2 \left[\varepsilon_p \hat{a}_{pj}^{\dagger} \exp(-i\omega_d t) - \varepsilon_p \hat{a}_{pj} \exp(i\omega_d t) \right], \quad (3.5)$$

where the classical pumping flux ε_p is set to be positive and real. The reservoir Hamiltonian for the signal and pump modes is written as

$$\mathcal{H}_{res} = \hbar \sum_{j=1}^2 \left(\hat{a}_{sj} \hat{\Gamma}_{Rsj}^{\dagger} + \hat{\Gamma}_{Rsj} \hat{a}_{sj}^{\dagger} + \hat{a}_{pj} \hat{\Gamma}_{Rpj}^{\dagger} + \hat{\Gamma}_{Rpj} \hat{a}_{pj}^{\dagger} \right) + \left(\hat{a}_c \hat{\Gamma}_{Rc}^{\dagger} + \hat{\Gamma}_{Rc} \hat{a}_c^{\dagger} \right), \quad (3.6)$$

where $\hat{\Gamma}_{Rsj}$, $\hat{\Gamma}_{Rpj}$ and $\hat{\Gamma}_{Rc}$ are the heat bath operators for the signal, pump and mid-cavity signal mode. Finally, the beamsplitter interaction Hamiltonian between the central cavity mode and DOPO signal modes is denoted by

$$\mathcal{H}_{BS} = i\hbar\zeta \left(\hat{a}_c \hat{a}_{s1}^{\dagger} - \hat{a}_c^{\dagger} \hat{a}_{s1} + \hat{a}_{s2} \hat{a}_c^{\dagger} e^{-ik_c z} - \hat{a}_{s2}^{\dagger} \hat{a}_c e^{ik_c z} \right), \quad (3.7)$$

where ζ is the interaction coefficient. Note that \mathcal{H}_{BS} considers a part of dissipation of the signal fields as coherent transmissions and reflections at the cavity facets.

3.2.3 Stochastic equations

With the standard technique to treat the thermal bath [149] (in Chapter 2), I have the master equation for the density operator of the system. Here, I neglect the thermal detuning term. Furthermore, I introduce the positive P representation [107] for the five modes

$$\hat{\rho} = \int P(\boldsymbol{\alpha}, \boldsymbol{\beta}) \frac{|\boldsymbol{\alpha}\rangle \langle \boldsymbol{\beta}^*|}{\langle \boldsymbol{\beta}^* | \boldsymbol{\alpha} \rangle} d^{10} \boldsymbol{\alpha} d^{10} \boldsymbol{\beta}, \quad (3.8)$$

to expand the density operator with a well-behaved probability distribution function $P(\boldsymbol{\alpha}, \boldsymbol{\beta})$. Here, $\boldsymbol{\alpha} = (\alpha_{s1}, \alpha_{s2}, \alpha_{p1}, \alpha_{p2}, \alpha_c)^T$ and $\boldsymbol{\beta} = (\beta_{s1}, \beta_{s2}, \beta_{p1}, \beta_{p2}, \beta_c)^T$ contain ten c -number variables to describe the state. $|\boldsymbol{\alpha}\rangle = |\alpha_{s1}\rangle |\alpha_{s2}\rangle |\alpha_{p1}\rangle |\alpha_{p2}\rangle |\alpha_c\rangle$ and $\langle \boldsymbol{\beta}^*| = \langle \beta_c^*| \langle \beta_{p2}^*| \langle \beta_{p1}^*| \langle \beta_{s2}^*| \langle \beta_{s1}^*|$ are the coherent product states for the total system. The positive P representation never fails to give a positive and appropriately normalized distribution function for every quantum state. α_X and β_X undergo statistically independent processes in probabilistic simulations while they are complex conjugate in average, i.e. $\langle \alpha_X \rangle = \langle \beta_X \rangle^*$.

I substitute Eq. (3.8) into the master equation and use the operator algebra [107] for the probability distribution description. After switching to the rotating frame with the driving frequency ω_d for the pump and $\omega_d/2$ for the signal mode, we obtain the Fokker-Planck equation (FPE) for the distribution $P(\vec{\alpha}, \vec{\beta})$:

$$\begin{aligned}
 & \frac{\partial}{\partial t} P(\vec{\alpha}, \vec{\beta}) \\
 &= \left\{ \sum_{j=1}^2 \left[\frac{\partial}{\partial \alpha_{sj}} \left((\gamma_s + i\Delta_s) \alpha_{sj} - \kappa \beta_{sj} \alpha_{pj} \right) \right. \right. \\
 & \quad + \frac{\partial}{\partial \beta_{sj}} \left((\gamma_s - i\Delta_s) \beta_{sj} - \kappa \alpha_{sj} \beta_{pj} \right) \\
 & \quad + \frac{\partial}{\partial \alpha_{pj}} \left((\gamma_p + i\Delta_p) \alpha_{pj} - \varepsilon_p + \frac{\kappa^2}{2} \alpha_{sj}^2 \right) \\
 & \quad + \frac{\partial}{\partial \beta_{pj}} \left((\gamma_p - i\Delta_p) \beta_{pj} - \varepsilon_p + \frac{\kappa^2}{2} \beta_{sj}^2 \right) \\
 & \quad \left. + \frac{1}{2} \left(\frac{\partial^2}{\partial \alpha_{pj}^2} \kappa \alpha_{pj} + \frac{\partial^2}{\partial \beta_{pj}^2} \kappa \beta_{pj} + \frac{\partial^2}{\partial \alpha_{sj} \partial \beta_{sj}} \Gamma_{sj} + \frac{\partial^2}{\partial \alpha_{pj} \partial \beta_{pj}} \Gamma_{pj} \right) \right] \\
 & \quad + \left[\frac{\partial}{\partial \alpha_c} (\gamma_c + i\Delta_s) \alpha_c + \frac{\partial}{\partial \beta_c} (\gamma_c + i\Delta_s) \beta_c + \frac{1}{2} \frac{\partial^2}{\partial \alpha_c \partial \beta_c} \Gamma_c \right. \\
 & \quad - \frac{\partial}{\partial \alpha_{s1}} \zeta \alpha_c - \frac{\partial}{\partial \beta_{s1}} \zeta \beta_c + \frac{\partial}{\partial \alpha_{s2}} \zeta \alpha_c e^{i\theta} + \frac{\partial}{\partial \beta_{s2}} \zeta \beta_c e^{-i\theta} \\
 & \quad \left. + \frac{\partial}{\partial \alpha_c} \zeta (\alpha_{s1} - \alpha_{s2} e^{-i\theta}) + \frac{\partial}{\partial \beta_c} \zeta (\beta_{s1} - \beta_{s2} e^{i\theta}) \right] \Big\} P(\vec{\alpha}, \vec{\beta}), \tag{3.9}
 \end{aligned}$$

where $\theta = k_c z$, and $\Delta_s = \omega_s - \omega_d/2$ and $\Delta_p = \omega_p - \omega_d$ are the detuning between the cavity modes and the driving field. The components of the last three columns in Eq. (3.9) come from the beamsplitter coupling.

With the Ito's rule [154] which gives the correspondence between the FPEs and SDEs, we reach a series of Ito SDEs for the c -number variables α and β

$$\begin{aligned}
 d \begin{bmatrix} \alpha_{s1} \\ \beta_{s1} \end{bmatrix} &= \begin{bmatrix} -(\gamma_s + i\Delta_s) \alpha_{s1} + \kappa \beta_{s1} \alpha_{p1} + \zeta \alpha_c \\ -(\gamma_s - i\Delta_s) \beta_{s1} + \kappa \alpha_{s1} \beta_{p1} + \zeta \beta_c \end{bmatrix} dt \\
 & \quad + \begin{bmatrix} \kappa \alpha_{p1} & \Gamma_s \\ \Gamma_s & \kappa \beta_{p1} \end{bmatrix}^{1/2} \begin{bmatrix} dW_{\alpha s1}(t) \\ dW_{\beta s1}(t) \end{bmatrix}, \tag{3.10}
 \end{aligned}$$

$$\begin{aligned}
 d \begin{bmatrix} \alpha_{s2} \\ \beta_{s2} \end{bmatrix} &= \begin{bmatrix} -(\gamma_s + i\Delta_s) \alpha_{s2} + \kappa \beta_{s2} \alpha_{p2} - \zeta \alpha_c e^{i\theta} \\ -(\gamma_s - i\Delta_s) \beta_{s2} + \kappa \alpha_{s2} \beta_{p2} - \zeta \beta_c e^{-i\theta} \end{bmatrix} dt \\
 & \quad + \begin{bmatrix} \kappa \alpha_{p2} & \Gamma_s \\ \Gamma_s & \kappa \beta_{p2} \end{bmatrix}^{1/2} \begin{bmatrix} dW_{\alpha s2}(t) \\ dW_{\beta s2}(t) \end{bmatrix}, \tag{3.11}
 \end{aligned}$$

$$d \begin{bmatrix} \alpha_{p1} \\ \beta_{p1} \end{bmatrix} = \begin{bmatrix} \varepsilon_p - (\gamma_p + i\Delta_p) \alpha_{p1} - \frac{\kappa}{2} \alpha_{s1}^2 \\ \varepsilon_p - (\gamma_p - i\Delta_p) \beta_{p1} - \frac{\kappa}{2} \beta_{s1}^2 \end{bmatrix} dt + \begin{bmatrix} 0 & \Gamma_p \\ \Gamma_p & 0 \end{bmatrix}^{1/2} \begin{bmatrix} dW_{\alpha p1}(t) \\ dW_{\beta p1}(t) \end{bmatrix}, \tag{3.12}$$

$$d \begin{bmatrix} \alpha_{p2} \\ \beta_{p2} \end{bmatrix} = \begin{bmatrix} \varepsilon_p - (\gamma_p + i\Delta_p) \alpha_{p2} - \frac{\kappa}{2} \alpha_{s2}^2 \\ \varepsilon_p - (\gamma_p - i\Delta_p) \beta_{p2} - \frac{\kappa}{2} \beta_{s2}^2 \end{bmatrix} dt + \begin{bmatrix} 0 & \Gamma_p \\ \Gamma_p & 0 \end{bmatrix}^{1/2} \begin{bmatrix} dW_{\alpha p2}(t) \\ dW_{\beta p2}(t) \end{bmatrix}, \quad (3.13)$$

$$d \begin{bmatrix} \alpha_c \\ \beta_c \end{bmatrix} = \begin{bmatrix} -(\gamma_c + i\Delta_s) \alpha_c - \zeta \alpha_{s1} + \zeta \alpha_{s2} e^{i\theta} \\ -(\gamma_c - i\Delta_s) \beta_c - \zeta \beta_{s1} + \zeta \beta_{s2} e^{-i\theta} \end{bmatrix} dt + \begin{bmatrix} 0 & \Gamma_c \\ \Gamma_c & 0 \end{bmatrix}^{1/2} \begin{bmatrix} dW_{\alpha c}(t) \\ dW_{\beta c}(t) \end{bmatrix}, \quad (3.14)$$

where $dW_X(t)$ is the real Wiener increment statistically independent of each other. This corresponds to the noise term in the equivalent Langevin equation whose autocorrelation is a delta function.

Here, I consider the case of a resonant driving $\Delta_s = \Delta_p = 0$ and zero temperature $\Gamma_s = \Gamma_p = \Gamma_c = 0$. In addition, I adiabatically eliminate the pump variables with an assumption that the pump fields decay sufficiently faster than the signal fields. We can take diagonal diffusion amplitude matrices for the DOPO signal fields, then we have a simplified model as follows

$$d\alpha_{s1} = \left[-\gamma_s \alpha_{s1} + \frac{\kappa}{\gamma_p} \left(\varepsilon_p - \frac{\kappa}{2} \alpha_{s1}^2 \right) \beta_{s1} + \zeta \alpha_c \right] dt + \sqrt{\frac{\kappa}{\gamma_p} \left(\varepsilon_p - \frac{\kappa}{2} \alpha_{s1}^2 \right)} dW_{\alpha s1}(t), \quad (3.15)$$

$$d\beta_{s1} = \left[-\gamma_s \beta_{s1} + \frac{\kappa}{\gamma_p} \left(\varepsilon_p - \frac{\kappa}{2} \beta_{s1}^2 \right) \alpha_{s1} + \zeta \beta_c \right] dt + \sqrt{\frac{\kappa}{\gamma_p} \left(\varepsilon_p - \frac{\kappa}{2} \beta_{s1}^2 \right)} dW_{\beta s1}(t), \quad (3.16)$$

$$d\alpha_{s2} = \left[-\gamma_s \alpha_{s2} + \frac{\kappa}{\gamma_p} \left(\varepsilon_p - \frac{\kappa}{2} \alpha_{s2}^2 \right) \beta_{s2} - \zeta \alpha_c e^{i\theta} \right] dt + \sqrt{\frac{\kappa}{\gamma_p} \left(\varepsilon_p - \frac{\kappa}{2} \alpha_{s2}^2 \right)} dW_{\alpha s2}(t), \quad (3.17)$$

$$d\beta_{s2} = \left[-\gamma_s \beta_{s2} + \frac{\kappa}{\gamma_p} \left(\varepsilon_p - \frac{\kappa}{2} \beta_{s2}^2 \right) \alpha_{s2} - \zeta \beta_c e^{-i\theta} \right] dt + \sqrt{\frac{\kappa}{\gamma_p} \left(\varepsilon_p - \frac{\kappa}{2} \beta_{s2}^2 \right)} dW_{\beta s2}(t), \quad (3.18)$$

$$d\alpha_c = \left(-\gamma_c \alpha_c - \zeta \alpha_{s1} + \zeta \alpha_{s2} e^{i\theta} \right) dt, \quad (3.19)$$

$$d\beta_c = \left(-\gamma_c \beta_c - \zeta \beta_{s1} + \zeta \beta_{s2} e^{-i\theta} \right) dt. \quad (3.20)$$

Adding oscillators and injection paths is straightforward, thus this model allows a quantum mechanical treatment of oscillator networks with the positive P representation.

3.2.4 Adiabatic elimination of mid cavity mode

We further consider the limit where the mid-air mode is also adiabatically eliminated i.e. $\gamma_c \gg \gamma_s$, to investigate the model. For the purpose of emulating the Ising Hamiltonian with the procedure in Ref. 103, we are interested in the in-phase ($e^{i\theta} = e^{-i\theta} = 1$) and out-of-phase ($e^{i\theta} = e^{-i\theta} = -1$) mutual injections. This is indeed the case where the injection path behaves as a cavity. Here, the mid cavity field at the steady state is given by

$$\alpha_c^{ss} = \frac{1}{\gamma_c} (-\zeta \alpha_{s1} \pm \zeta \alpha_{s2}), \quad (3.21)$$

$$\beta_c^{ss} = \frac{1}{\gamma_c} (-\zeta \beta_{s1} \pm \zeta \beta_{s2}). \quad (3.22)$$

Regarding the plus-minus sign, the plus is for $e^{i\theta} = e^{-i\theta} = 1$ and the minus is for $e^{i\theta} = e^{-i\theta} = -1$. At the stable steady state under the in-phase and out-of-phase mutual injections, $(\langle \alpha_{s1} \rangle, \langle \beta_{s1} \rangle) = (\langle \alpha_{s2} \rangle, \langle \beta_{s2} \rangle)$ and $(\langle \alpha_{s1} \rangle, \langle \beta_{s1} \rangle) = (-\langle \alpha_{s2} \rangle, -\langle \beta_{s2} \rangle)$ are expected. Hence, the center cavity is thought to be empty there, i.e. $\langle \alpha_c^{ss} \rangle = \langle \beta_c^{ss} \rangle = 0$.

Substituting Eqs. (3.21) and (3.22) into (3.15) - (3.18), we have the SDEs for the intracavity signal fields with adiabatic elimination of the pump and mid cavity modes

$$d\alpha_{sj} = \left[-\left(\gamma_s + \frac{\zeta^2}{\gamma_c} \right) \alpha_{sj} + \frac{\kappa}{\gamma_p} \left(\varepsilon_p - \frac{\kappa}{2} \alpha_{sj}^2 \right) \beta_{sj} \pm \frac{\zeta^2}{\gamma_c} \alpha_{sk} \right] dt + \sqrt{\frac{\kappa}{\gamma_p} \left(\varepsilon_p - \frac{\kappa}{2} \alpha_{sj}^2 \right)} dW_{\alpha_{sj}}(t), \quad (3.23)$$

$$d\beta_{sj} = \left[-\left(\gamma_s + \frac{\zeta^2}{\gamma_c} \right) \beta_{sj} + \frac{\kappa}{\gamma_p} \left(\varepsilon_p - \frac{\kappa}{2} \beta_{sj}^2 \right) \alpha_{sj} \pm \frac{\zeta^2}{\gamma_c} \beta_{sk} \right] dt + \sqrt{\frac{\kappa}{\gamma_p} \left(\varepsilon_p - \frac{\kappa}{2} \beta_{sj}^2 \right)} dW_{\beta_{sj}}(t), \quad (3.24)$$

where $(j, k) = (1, 2), (2, 1)$. The plus and minus signs are for the in-phase and out-of-phase injections. Eqs. (3.23) and (3.24) indicate that the beamsplitter interaction results in the transmission loss ζ^2/γ_c for each field and the mutual injection terms with a coefficient $\pm \zeta^2/\gamma_c$.

We further define the effective signal loss γ'_s and the normalized beamsplitter coupling ξ as

$$\gamma'_s = \gamma_s + \frac{\zeta^2}{\gamma_c}, \quad \xi = \pm \frac{\zeta^2}{\gamma_s \gamma_c + \zeta^2}. \quad (3.25)$$

Finally, we reach the normalized SDEs for the signal modes as follows

$$d\eta_j = [-\eta_j + \mu_j (\lambda - \eta_j^2) + \xi\eta_k] d\tau + g\sqrt{\lambda - \eta_j^2} dW_{\eta_j}(\tau), \quad (3.26)$$

$$d\mu_j = [-\mu_j + \eta_j (\lambda - \mu_j^2) + \xi\mu_k] d\tau + g\sqrt{\lambda - \mu_j^2} dW_{\mu_j}(\tau). \quad (3.27)$$

Here, $\eta_j = g\alpha_{sj}$, $\mu_j = g\beta_{sj}$ and $g = \kappa/\sqrt{2\gamma'_s\gamma_p}$ is the normalized parametric gain coefficient serving as a noise parameter. $\lambda = \varepsilon_p/\varepsilon_{th}$ is the normalized pumping rate and $\varepsilon_{th} = \gamma'_s\gamma_p/\kappa$ is the classical oscillation threshold. The time is scaled with the signal cavity lifetime, i.e. $\tau = \gamma'_s t$. $dW_{\eta_j}(\tau)$ and $dW_{\mu_j}(\tau)$ are rescaled Wiener increments. The linear mutual injection terms $\xi\eta_k$ and $\xi\mu_k$ have the same forms as those phenomenologically introduced in the semi-classical model [103]. Therefore, the theoretical framework studied here guarantees the validity of the injection model called *coherent injection* or *coherent drive* also in the quantum mechanical phase space representations, if the dynamics in the injection path can be neglected.

3.3 Simulation Substances

3.3.1 Simulation setting

In this section, I discuss and review other elements important for the simulation. First, I describe the simulation setting. Here, I focus on the out-of-phase mutual injection, namely $e^{i\theta} = e^{-i\theta} = -1$. In this case, the out-of-phase correlation between the two intracavity DOPO fields and even-number macroscopic superposition components $|- \alpha\rangle + |\alpha\rangle$ in each DOPO is expected. For the simulation, we introduce the normalized equations also corresponding to Eqs. (3.15) - (3.20) as

$$d\eta_j = [-\gamma_{sn}\eta_j + \mu_j (\lambda - \eta_j^2) + \zeta_n\eta_c] d\tau + g\sqrt{\lambda - \eta_j^2} dW_{\eta_j}(\tau), \quad (3.28)$$

$$d\mu_j = [-\gamma_{sn}\mu_j + \eta_j (\lambda - \mu_j^2) + \zeta_n\mu_c] d\tau + g\sqrt{\lambda - \mu_j^2} dW_{\mu_j}(\tau). \quad (3.29)$$

$$d\eta_c = (-\gamma_{cn}\eta_c - \zeta_n\eta_1 - \zeta_n\eta_2) d\tau, \quad (3.30)$$

$$d\mu_c = (-\gamma_{cn}\mu_c - \zeta_n\mu_1 - \zeta_n\mu_2) d\tau, \quad (3.31)$$

where

$$\gamma_{sn} = \frac{\gamma_s}{\gamma'_s} = \frac{\gamma_s\gamma_c}{\gamma_s\gamma_c + \zeta^2}, \quad (3.32)$$

$$\gamma_{cn} = \frac{\gamma_c}{\gamma'_s} = \frac{\gamma_c^2}{\gamma_s\gamma_c + \zeta^2}, \quad (3.33)$$

$$\zeta_n = \frac{\zeta}{\gamma'_s} = \frac{\zeta\gamma_c}{\gamma_s\gamma_c + \zeta^2}. \quad (3.34)$$

I simulate the normalized equations (3.26) - (3.27) and (3.28) - (3.31) in all cases, hence the time unit in all the results here is the effective cavity lifetime $1/\gamma'_s$.

Here, I again refer to the fact that the beamsplitter coupling can take into account a large part of dissipation for the DOPO cavities explicitly in this model. The rest incoherent and non-resonant decay, which may phenomenologically include absorption and scattering in the nonlinear crystal, is considered by the conventional parameter γ_s . Therefore, we can expect the case $\zeta > \gamma_s$, and this is an important condition for the system to show non-trivial quantum effects. I set $\zeta = 1$, and γ_s and γ_c can be smaller in the simulations on Eqs. (3.28) - (3.31).

The noise parameter $g = \kappa/\sqrt{2\gamma'_s\gamma_p}$ determines the typical order of the photon number inside the DOPOs above the oscillation threshold. Basically, I focus on the case of potentially larger photon numbers from the practical point of view, thus fix this parameter as $g \sim 0.01$. This gives $1/g^2 \sim 10000$ photons in the DOPOs at oscillation. For different decay parameters γ'_s and γ_p , the nonlinearity κ is changed accordingly to keep the value of g .

3.3.2 Observable moments and distribution functions

Drummond and Gardiner [107] have shown that normally ordered moments of the single mode oscillator can be obtained by the expectation value of corresponding c -number products. The trivial extension to the two-mode case with the commutability of bosonic operators for different modes indicates

$$\langle \hat{a}_{s1}^{\dagger j} \hat{a}_{s2}^{\dagger k} \hat{a}_{s1}^l \hat{a}_{s1}^m \rangle = \int \beta_{s1}^j \beta_{s2}^k \alpha_{s1}^l \alpha_{s2}^m P(\{\alpha\}, \{\beta\}) d^2\alpha_{s1} d^2\alpha_{s2} d^2\beta_{s1} d^2\beta_{s2}. \quad (3.35)$$

Here, $\{\alpha\} = \{\alpha_{s1}, \alpha_{s2}\}$, $\{\beta\} = \{\beta_{s1}, \beta_{s2}\}$ and other irrelevant modes are traced out. I consider and simulate the moments up to second order including ones with different modes, by unrestricted sampling Monte Carlo integration.

In this study, I define the quadrature amplitudes in the DOPOs as $\hat{x}_j = (\hat{a}_j + \hat{a}_j^\dagger)/2$ and $\hat{p}_j = (\hat{a}_j - \hat{a}_j^\dagger)/(2i)$. The distribution functions [161] of them are given by the diagonal element of the density operator for the corresponding eigenstates

$$\begin{aligned} P(x_j) &= \langle x_j | \hat{\rho}_{sj} | x_j \rangle = \int P(\alpha_{sj}, \beta_{sj}) \frac{\langle x_j | \alpha_{sj} \rangle \langle \beta_{sj}^* | x_j \rangle}{\langle \beta_{sj}^* | \alpha_{sj} \rangle} d^2\alpha_{sj} d^2\beta_{sj} \\ &= \sqrt{\frac{2}{\pi}} \int P(\alpha_{sj}, \beta_{sj}) e^{-2x_j^2 + 2x_j(\alpha_{sj} + \beta_{sj}) - (\alpha_{sj} + \beta_{sj})^2/2} d^2\alpha_{sj} d^2\beta_{sj}, \end{aligned} \quad (3.36)$$

$$\begin{aligned} P(p_j) &= \langle p_j | \hat{\rho}_{sj} | p_j \rangle = \int P(\alpha_{sj}, \beta_{sj}) \frac{\langle p_j | \alpha_{sj} \rangle \langle \beta_{sj}^* | p_j \rangle}{\langle \beta_{sj}^* | \alpha_{sj} \rangle} d^2\alpha_{sj} d^2\beta_{sj} \\ &= \sqrt{\frac{2}{\pi}} \int P(\alpha_{sj}, \beta_{sj}) e^{-2p_j^2 - i2p_j(\alpha_{sj} - \beta_{sj}) + (\alpha_{sj} - \beta_{sj})^2/2} d^2\alpha_{sj} d^2\beta_{sj}. \end{aligned} \quad (3.37)$$

Here, $\hat{\rho}_{sj}$ is the partial density operator for the signal field in DOPO# j , with the other states traced out. Also, I used the expressions of the wavefunctions for the quadrature

amplitudes defined here

$$\langle x_j | \alpha_{sj} \rangle = (\pi/2)^{-1/4} \exp(-2x_j^2 + 2x_j\alpha_{sj} - \alpha_{sj}^2/2 - |\alpha_{sj}|^2/2), \quad (3.38)$$

$$\langle p_j | \alpha_{sj} \rangle = (\pi/2)^{-1/4} \exp(-2p_j^2 - i2p_j\alpha_{sj} + \alpha_{sj}^2/2 - |\alpha_{sj}|^2/2), \quad (3.39)$$

and the inner product of the coherent states

$$\langle \beta_{sj}^* | \alpha_{sj} \rangle = \exp(-|\alpha_{sj}|^2/2 - |\beta_{sj}|^2/2 + \alpha_{sj}\beta_{sj}). \quad (3.40)$$

It is known that a fringe in $P(p_j)$ is a clear evidence for the existence of coherent superposition components [156]. In Eq. (3.37), we see that in the classical subspace where α_{sj} and β_{sj} are real, the oscillation in $P(p_j)$ comes from the integration of the component $\exp[-i2p_j(\alpha_{sj} - \beta_{sj})]$. Here, the quantum noise causing stochastic discrepancy between α_{sj} and β_{sj} is found to be essential for the fringe. Also, in the other phase space representations where $\beta = \alpha^*$, $P(p_j)$ does not show any fringe in principle due to the real exponent in the integrand.

3.3.3 Criterion for entanglement

To examine the entanglement between two intracavity signal fields, we adopt the criterion proposed by Duan *et al* [158]. Here, we consider the pair of Einstein-Podolsky-Rosen (EPR)-type operators [131] $\hat{u}_+ = \hat{x}_1 + \hat{x}_2$, $\hat{v}_- = \hat{p}_1 - \hat{p}_2$ and their fluctuation operators $\Delta\hat{u}_+ = \hat{u}_+ - \langle \hat{u}_+ \rangle$ and $\Delta\hat{v}_- = \hat{v}_- - \langle \hat{v}_- \rangle$. The quadrature amplitudes defined here satisfy the commutation relation $[\hat{x}_j, \hat{p}_k] = i\delta_{jk}/2$. Thus, the condition for the entanglement (inseparability) between the two DOPO signal fields is given by

$$\langle \Delta\hat{u}_+^2 \rangle + \langle \Delta\hat{v}_-^2 \rangle < 1. \quad (3.41)$$

3.3.4 Quantum discord

Finally, I refer to quantum correlation and the quantum discord [163] which is computed in this study. Quantum correlation is referred to as the property of a composite system that a local measurement changes the state of the whole system. It is a weaker, but broader characteristic than entanglement, showing that even separable states can have some quantum features such as lack of complete distinguishability due to a nonorthogonal basis, and pure quantumness of each partial system.

Quantum discord [163] is a measure of quantum correlation, based on two different ways to describe the mutual information of a bipartite system. Suppose we have a system AB composed of partial systems A and B . The mutual information based on the total system entropy is

$$I(\hat{\rho}_{AB}) = S(\hat{\rho}_A) + S(\hat{\rho}_B) - S(\hat{\rho}_{AB}), \quad (3.42)$$

where $S(\hat{\rho}) = -\text{Tr}(\hat{\rho} \log \hat{\rho})$ is the von Neumann entropy. On the other hand, that based on the conditional entropy $S(A|B)$

$$J^\leftarrow(\hat{\rho}_{AB}) = S(\hat{\rho}_A) - S(A|B), \quad (3.43)$$

is not unique in quantum theory. It is because $S(A|B)$, the information left in the system after a local measurement on B , varies dependent on the measurement basis for B . It means that the local measurement can perturb the total system. Here, the measurement basis which disturbs the system least is chosen. As a result, the conditional mutual information in quantum theory is defined as its maximum in terms of the local measurement

$$J^\leftarrow(\hat{\rho}_{AB}) = S(\hat{\rho}_A) - \inf_{\Pi_i^B} \sum_i p_i S(\hat{\rho}_{A|i}), \quad (3.44)$$

where i is the index for the components of the POVM measurement basis $\{\Pi_i^B\}$ for B . $\hat{\rho}_{A|i}$ is the posterior state of A provided that the i th state is measured at B . Finally, the quantum discord is defined as the difference of them

$$\begin{aligned} D^\leftarrow(\hat{\rho}_{AB}) &= I(\hat{\rho}_{AB}) - J^\leftarrow(\hat{\rho}_{AB}) \\ &= S(\hat{\rho}_B) - S(\hat{\rho}_{AB}) + \inf_{\Pi_i^B} \sum_i p_i S(\hat{\rho}_{A|i}). \end{aligned} \quad (3.45)$$

In the case of classical states, these two quantities are equal due to Bayes rule thus the discord is always zero. If a bipartite system has a finite discord, the system surely has quantum correlation between its elements. A system without entanglement can have nonzero discord, and it has been reported that such a “dirty” state may be available for a nontrivial speedup in certain problems [164] with a quantum computing model called *DQC1* [165].

Gaussian quantum discord

In general, the optimization about the measurement basis in Eq. (3.45) and evaluation of the discord is hard. However, for Gaussian states, whose quasi-distribution functions are Gaussian, a good analytic formulae [166, 167] for the discord has been derived. In this study, I compute the approximate quantum discord between two DOPO signal fields as the Gaussian quantum discord. Here, I consider the unnormalized quadrature amplitudes for the two modes

$$[\hat{r}] = [2\hat{x}_1, 2\hat{p}_1, 2\hat{x}_2, 2\hat{p}_2]. \quad (3.46)$$

Then, a two-mode Gaussian state is characterized with the covariance matrix of them

$$\sigma_G = \left[\frac{1}{2} \langle \hat{r}_j \hat{r}_k + \hat{r}_k \hat{r}_j \rangle - \langle \hat{r}_j \rangle \langle \hat{r}_k \rangle \right] = \begin{pmatrix} \alpha_M & \gamma_M \\ \gamma_M^T & \beta_M \end{pmatrix}. \quad (3.47)$$

where α_M , β_M and γ_M are 2×2 matrices. The state can also be equivalently featured by the quantities called *symplectic invariants* defined as

$$A_{SI} = \det \alpha_M, \quad B_{SI} = \det \beta_M, \quad C_{SI} = \det \gamma_M, \quad D_{SI} = \det \sigma_G. \quad (3.48)$$

When we write the binary entropy function as

$$f_B(X) = \left(X + \frac{1}{2} \right) \log \left(X + \frac{1}{2} \right) - \left(X - \frac{1}{2} \right) \log \left(X - \frac{1}{2} \right), \quad (3.49)$$

and the quantities called *symplectic eigenvalues* as

$$\nu_{\pm}^2 = \frac{1}{2} \left(\Delta \pm \sqrt{\Delta^2 - 4D_{SI}} \right), \quad \Delta = A_{SI} + B_{SI} + 2C_{SI}, \quad (3.50)$$

the Gaussian quantum discord is given by

$$D^{\leftarrow}(\sigma_G) = f_B \left(\sqrt{B_{SI}} \right) - f_B(\nu_-) - f_B(\nu_+) + \inf_{\sigma_0} f_B \left(\sqrt{\det \epsilon} \right). \quad (3.51)$$

Here, σ_0 is the measurement basis for the partial system B . ϵ is the covariance matrix for the partial system A after B has been locally measured. The last term in Eq. (3.51) can be optimized analytically within the range of Gaussian POVMs (adding Gaussian ancilla bits, symplectic transformations and a homodyne detection), yielding [167]

$$\begin{aligned} \inf_{\sigma_0} \det \epsilon = & \frac{2C_{SI}^2 + (B_{SI} - 1)(D_{SI} - A_{SI}) + 2|C_{SI}|\sqrt{C_{SI}^2 + (B_{SI} - 1)(D_{SI} - A_{SI})}}{(-1 + B_{SI})^2} \\ \text{if } (D_{SI} - A_{SI}B_{SI})^2 \leq (1 + B_{SI})C_{SI}^2(A_{SI} + D_{SI}), & \\ & \frac{A_{SI}B_{SI} - C_{SI}^2 + D_{SI} - \sqrt{C_{SI}^4 + (D_{SI} - A_{SI})^2 - 2C_{SI}^2(A_{SI}B_{SI} + D_{SI})}}{2B_{SI}} \\ \text{otherwise.} & \end{aligned} \quad (3.52)$$

In addition, a simpler formula for two-mode squeezed thermal states (including squeezed vacuum) has been also derived as [166]

$$D^{\leftarrow}(\sigma_G) = f_B \left(\sqrt{B_{SI}} \right) - f_B(\nu_-) - f_B(\nu_+) + f_B \left(\frac{\sqrt{A_{SI}} + 2\sqrt{A_{SI}B_{SI}} + 2C_{SI}}{1 + \sqrt{B_{SI}}} \right). \quad (3.53)$$

A bipartite state with $D^{\leftarrow}(\sigma_G) \geq 1$ always has entanglement between its elements. On the other hand, an entangled state can have a value of the quantum discord smaller than 1.

In my simulation, the smaller value in those calculated with Eqs. (3.51), (3.52) and (3.53) is taken for each point to achieve a good approximation and avoid possible numerical instabilities, especially in the case of small pumping rates.

3.4 Simulation Result

In this section, I show the result of the numerical simulation on the system with out-of-phase mutual injection. Here, the initial state is fixed in the vacuum state, i.e. $\alpha = \beta = \mathbf{0}$. The system is gradually pumped [100], meaning that the pumping rate λ is slowly increased in time so that the DOPOs are continuously driven from the below to above

of the oscillation threshold. This helps the DOPOs hold the state with the minimum effective gain and avoid being dragged into an unstable solution created by the mutual injection terms. I set the linear schedule for the pumping as

$$\lambda(t) = \frac{\lambda_f t}{t_f}, \quad (3.54)$$

where λ_f and t_f are the pump and time parameters for the final state. Note that the state is always transient because the pumping rate is continuously increased. Transient effects get clear when the damping of the mid-cavity is small. However, the sweeping is sufficiently slow so that the DOPOs keeps themselves steady to the given instant environment. For the numerical integration on the SDEs, we adopt a second-order weak scheme [168] originally proposed by Kloeden and Platen [169], with a time step $\Delta t = 2 \times 10^{-3}$.

I consider three cases here. In the first case, the signal intracavity decay rate γ_s is varied under the condition that the loss in the injection path γ_c is larger than it. Here, I hold $\gamma_c = 2\gamma_s$, meaning that the loss of the total system is increased with those parameters. In the second case, we change only γ_c , keeping γ_s small ($\gamma_s = 0.01$). Eqs. (3.28) - (3.31) are numerically integrated with fixed parameters $t_f = 200$, $\lambda_f = 1.5$, $\gamma_p = 100$, $\zeta = 1$ and $g \sim 0.01$ for these two. The results for the first and second cases are symbolized as (a) and (b) in the following figures, respectively. In the last case, we simulate Eqs. (3.26) and (3.27), where the central mode is adiabatically eliminated. Here, the intracavity signal fields in the DOPOs are “directly” injected into each other. The parameters used here are $t_f = 100$, $\lambda_f = 1.1$ and $g = 0.01$. The figures for this case are marked by (c). I take 20000 stochastic trials to compute the observables for all the cases.

The classical stable solution of Eqs. (3.26) and (3.27) under the expected condition $\eta_j = \mu_j$, $\eta_2 = -\eta_1$ is given by

$$\eta_j = \mu_j = 0 \quad (\lambda < 1 - |\xi|), \quad (3.55)$$

$$\eta_1 = \mu_1 = -\eta_2 = -\mu_2 = \pm \sqrt{\lambda + |\xi| - 1} \quad (\lambda > 1 - |\xi|). \quad (3.56)$$

Here, their absolute values never get larger than $\sqrt{\lambda}$. The mutual injection path is empty, thus it has only noise fields inside below the threshold and its average amplitude is zero. Above the threshold, the two DOPOs are expected to give off the fields with the same amplitude and opposite phases in average, and they will cancel out in the mid cavity. Also, gradual pumping restricts highly transient behavior so that the magnitudes of the field variables converge at the steady values from the smaller side. Considering all of these, I implement the boundary condition in the numerical algorithm to assure that the trajectories do not go out of the manifold $\eta_j \leq \sqrt{\lambda}$, $\mu_j \leq \sqrt{\lambda}$.

3.4.1 Mean photon number

Fig. 3.2 shows the transits of the mean photon numbers in the first DOPO. Those in the second oscillator are omitted because they look the same. The photon number

rises, as the pumping rate increases linearly in time. The difference in the effective oscillation threshold and resulting intensity comes from the difference in the magnitude of the mutual injection. Eqs. (3.25), (3.26) and (3.27) are convenient to evaluate the threshold. When in the assumption that $\eta_1 = \mu_1 = -\eta_2 = -\mu_2$ and the mid-cavity field is eliminated, the effective classical threshold is given by $\lambda_{th} = 1 - |\xi|$. For the cases of $\gamma_s = (0.05, 0.1, 0.5, 1, 5)$ in Fig. 3.2 (a), the corresponding coupling coefficients and approximate thresholds are $\xi = (0.995, 0.980, 0.67, 0.33, 0.020)$ and $\lambda_{th} = (0.0050, 0.020, 0.33, 0.67, 0.98)$, respectively. Also, for $\gamma_c = (0.1, 0.5, 1, 5, 10)$ in Fig. 3.2 (b), $\xi = (0.999, 0.995, 0.990, 0.952, 0.909)$ and $\lambda_{th} = (0.0010, 0.0050, 0.0099, 0.048, 0.091)$. Note that $\lambda = (1.5/200)t$ for (a) and (b). The evaluation for (c) is straightforward and $\lambda = (1.1/100)t$ there. A sufficiently closed system with a mutual injection has a drastically lower threshold than a single DOPO. At the same time, however, quantum noise in the system interrupts oscillation of the DOPOs and leads to less photons around the threshold than those classically expected by the extrapolation of the linear region. Also, the curve for $\gamma_s = 0.05$ in (a) shows a relaxation oscillation due to the mid cavity. Such a dynamics suggests a possibility that the variables escape the classical subspace. Thus, the simulation with this condition might not be reliable. The line $\gamma_c = 0.1$ in (b) is also the case.

3.4.2 Correlation function of quadrature amplitudes

Fig. 3.3 displays the second order correlation functions for the quadrature amplitudes. Here, they are normalized with the products of the standard deviations of the relevant amplitudes. The negative correlation in x_1 and x_2 enhances as the pumping rate and hence the photon number in the DOPOs increases. It means that the system gives the macroscopic anti-phase order in x due to the mutual injection, corresponding to the anti-ferromagnetic order of the most fundamental Ising model $\hat{\mathcal{H}} = \hat{\sigma}_{z1}\hat{\sigma}_{z2}$ programmed in the system. When the loss of the system (γ_s, γ_c) is small, the relaxation oscillation in $\langle \hat{x}_1 \hat{x}_2 \rangle$ due to the center cavity occurs as seen in the curve for $\gamma_s = 0.05$ of Fig. 3.3 (a). The curves of $\langle \hat{p}_1 \hat{p}_2 \rangle$ show that the instantaneous amplitudes p_1 and p_2 correlate positively, despite that $\langle \hat{p}_1 \rangle = \langle \hat{p}_2 \rangle = 0$ due to the phase-sensitive nature of DOPOs. Also, in contrast to $\langle \hat{x}_1 \hat{x}_2 \rangle$, the correlation in p vanishes as the photon number rises. This indicates that it is a microscopic correlation induced by the quantum noise and mutual injection. In (a), $\langle \hat{p}_1 \hat{p}_2 \rangle$ decays fast with the increase in γ_s and γ_c because of both more dissipation and a less effective injection ξ .

In (b), the correlation in x with $\gamma_c = 1$ grows faster than those for $\gamma_c = 0.1$. Also, that in p with $\gamma_c = 0.1$ is worse than those with $\gamma_c = 0.5$ and $\gamma_c = 1$. It means that a highly closed injection path interrupts the formation of the correlation between the squeezed vacua in the DOPOs. It is clearly because of the cavity effect in the injection path. The mid cavity stores the squeezed vacuum outputs from the DOPOs because $\zeta > \gamma_c$. Thus, it works effectively as an additional noise source to the DOPOs. A larger γ_c also degrades $\langle \hat{p}_1 \hat{p}_2 \rangle$ due to dissipation, however, the effect is not so significant. We see that the system with $\gamma_c = 10$ gives a detectable correlation when before oscillation. Note that broader peaks with $\gamma_c = 5$ and 10 come from larger oscillation thresholds,

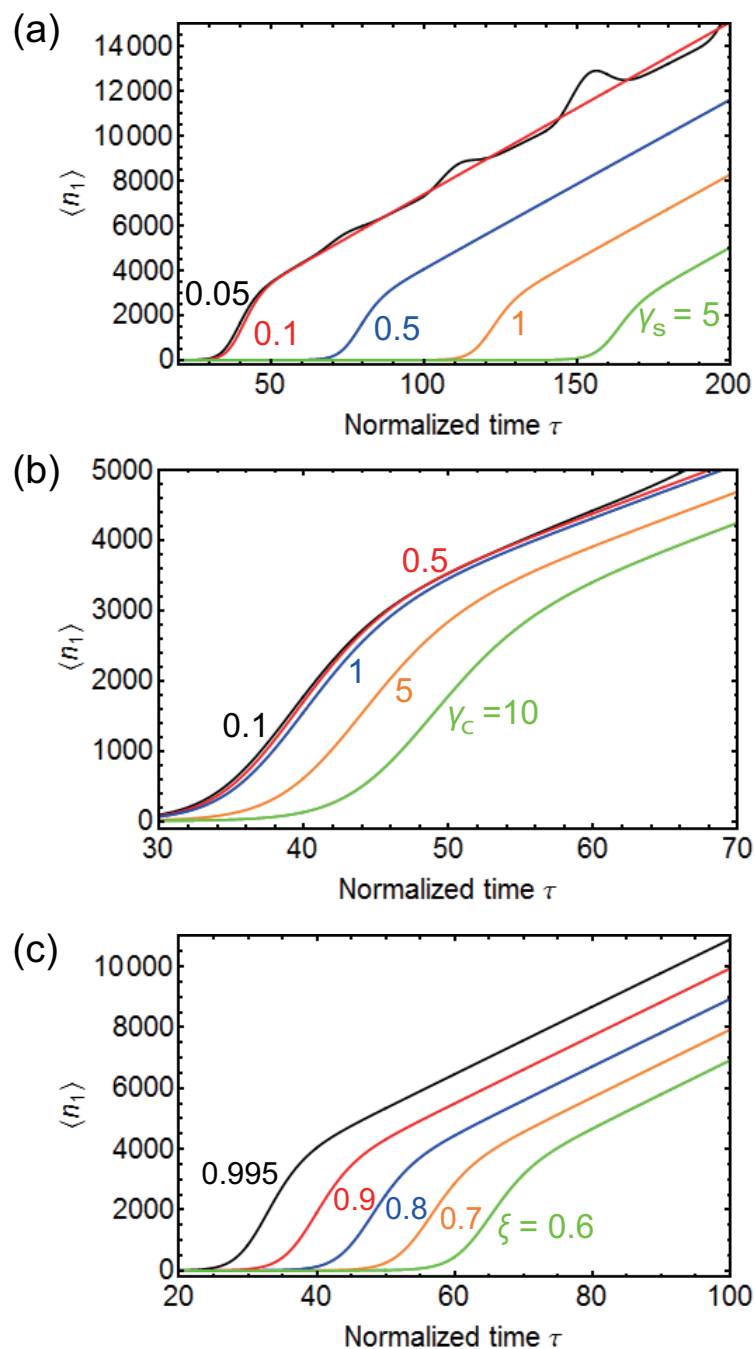


Figure 3.2: Transient of the intracavity photon number in a DOPO dependent on (a) the signal loss of the system under $\gamma_c = 2\gamma_s$, (b) the mid-cavity decay rate γ_c and (c) the mutual injection coefficient ξ . In (c), the center cavity is adiabatically eliminated. The normalized oscillation threshold depends on the effective mutual injection strength, varying with the parameters. 20000 stochastic runs for each curve.

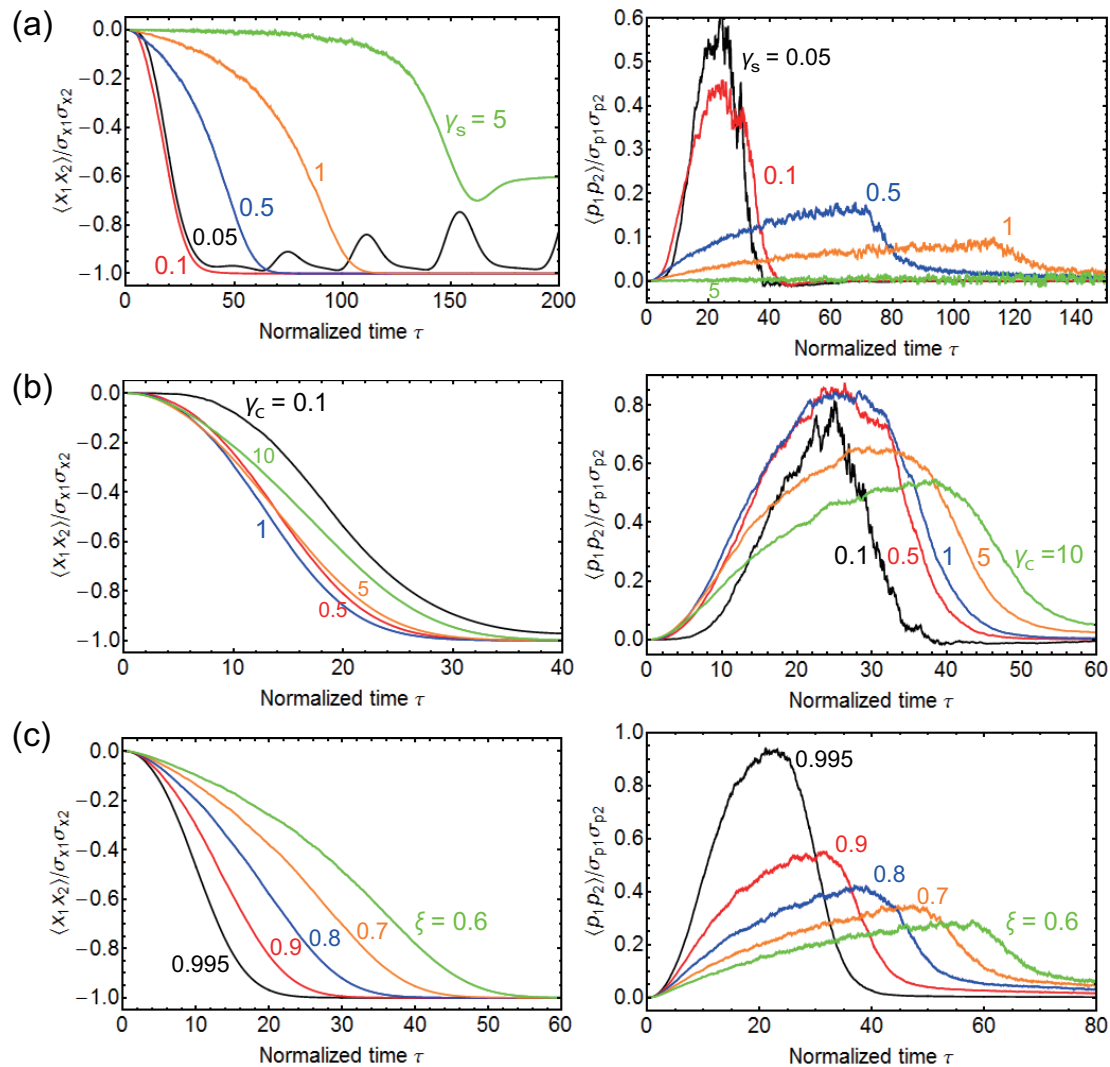


Figure 3.3: Time dependency of the correlation functions for the signal quadrature amplitudes. (a) The loss in the system with $\gamma_c = 2\gamma_s$, (b) the center cavity loss γ_c and (c) the mutual injection strength ξ are varied. x_j are negatively and macroscopically correlated along with the oscillation. p_j are positively and microscopically correlated before the oscillation. 20000 stochastic runs for each curve.

as seen in Fig. 3.2. The model for the system with an adiabatically eliminated mid cavity mode predicts a straightforward property that a larger injection gives a better correlation, as shown in Fig. 3.3 (c).

3.4.3 Total fluctuation of EPR-type operators

Fig. 3.4 presents the total variance of the EPR-type operators varying with time. $\langle \Delta u_+^2 \rangle + \langle \Delta v_-^2 \rangle < 1$ represents the entanglement between the DOPO signal fields. As shown in Fig. 3.4 (a), when the loss in the system is small the total fluctuation sharply rises from the vacuum level in spite of a respectable correlation in p , seen in the previous figure. This means that the fluctuation of $\hat{v}_- = \hat{p}_1 - \hat{p}_2$ falls under the vacuum level of 0.5 before oscillation while that of $\hat{u}_+ = \hat{x}_1 + \hat{x}_2$ gets much larger than that due to the squeezed noise field accumulated in the center cavity. Larger γ_s and γ_c denote more dissipation and a less mutual injection, thus the curves in (a) do not satisfy the criterion except for the small region around $\tau = 20$.

We see in Fig. 3.4 (b) that when only γ_c is increased, the total noise comes to drop clearly under the bound before oscillation. Thus, the system has the entanglement there. This is because the damping of the mid cavity field gets faster while the system keeps a fair amount of the mutual injection in this case. Here, a good part of the output fields from the DOPOs coherently inject to each other. It is known that an entangled state cannot be produced only with local operations and classical communication (LOCC) [159], thus the coherent mutual injection can be a quantum communication channel. As expected from the time range where the system shows the entanglement, it solely reflects the quantum correlation in p , i.e. $\langle \Delta v_-^2 \rangle < 0.5$. In fact, $\langle \Delta u_+^2 \rangle$ comes only down nearly to 0.5 hence the total noise level is always larger than 0.5. This indicates that the system is not in the EPR paradox, and in this sense the quantum correlation between the DOPOs is incomplete here.

In Fig. 3.4 (c), we can see the total noise level around the oscillation which is dependent on the magnitude of the injection ξ for the case of completely coherent coupling. When ξ becomes small, the curve has a region where the noise gets over the bound. To keep the entanglement until the oscillation we need $\xi \gtrsim 0.5$, i.e. 25 % in the feedback power from the injection path.

3.4.4 Quantum discord

Fig. 3.5 shows the approximate quantum discord when the state is considered as a Gaussian state. It basically reflects the quantum correlation in p_j . When p_j is squeezed and a some positive correlation with that in the other DOPO, the system holds a relatively large discord. In addition, many curves converge at a finite value $D^{\leftarrow} \sim 0.02$, except for the ones with $\gamma_s = 0.05, 1, 5$ in (a) and one with $\gamma_c = 0.1$ in (b). It is worth noting that this finite discord does not attribute to the squeezing in the DOPOs as previously discussed [166] for the case of squeezed thermal states, but the mixture of coherent states with perfect classical communication. I have found that the variance in x_j and p_j quickly verge on 1/4 after oscillation in the data here, thus the states there are well described as

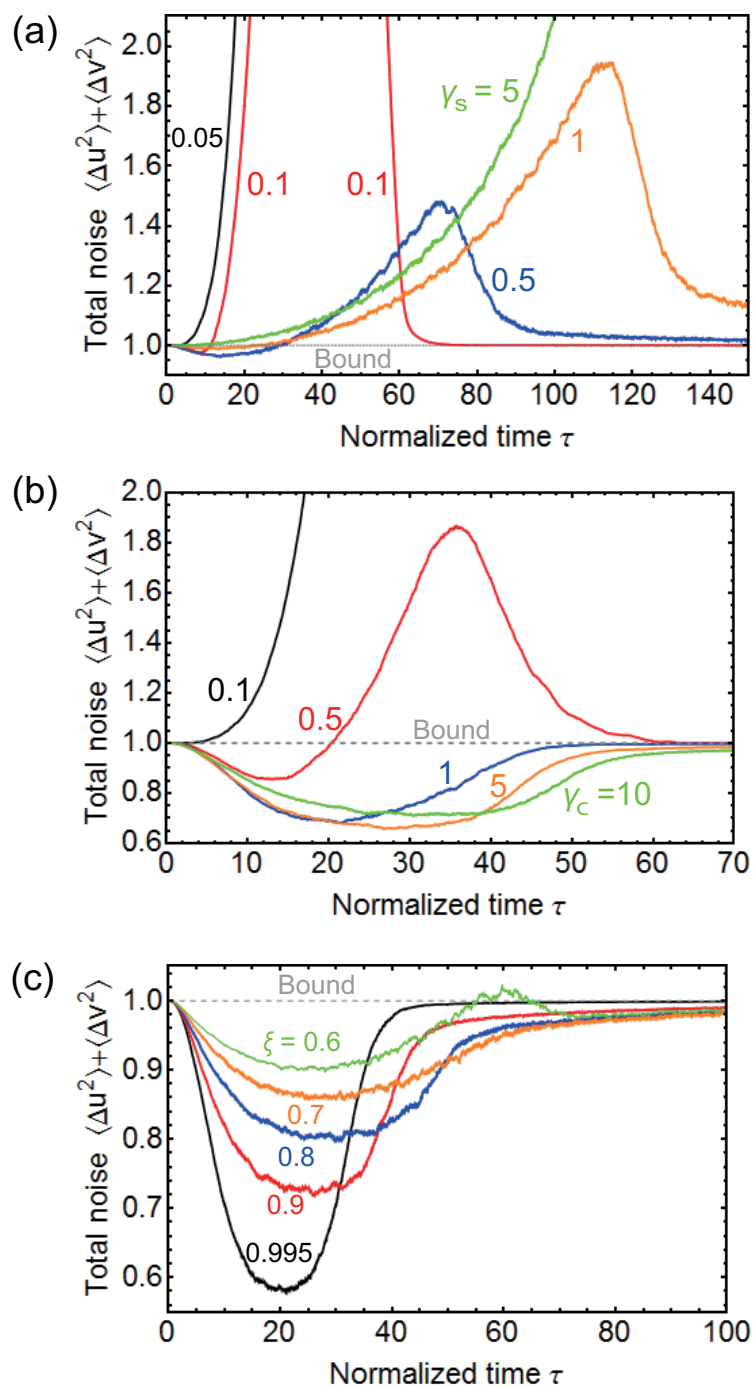


Figure 3.4: Time evolution of the total fluctuation in the EPR-type operators $\langle \Delta u_+^2 \rangle + \langle \Delta v_-^2 \rangle$ dependent on (a) the loss in the system with $\gamma_c = 2\gamma_s$, (b) the mid-cavity loss γ_c and (c) the coupling coefficient ξ . $\langle \Delta u_+^2 \rangle + \langle \Delta v_-^2 \rangle < 1$ means the entanglement between the DOPO signal fields. 20000 stochastic runs for each curve.

coherent states. Also, the lines with the finite discord give an almost perfect correlation of x (injection-locking) at the final state such as $\langle \hat{x}_1 \hat{x}_2 \rangle = -0.9999$ and -1.0000 . On the other hand, a closed central cavity or significant dissipation cancels out the discord. The lines without discord for $\gamma_s = 0.05, 1, 5$ in (a) and one with $\gamma_c = 0.1$ in (b) have $\langle \hat{x}_1 \hat{x}_2 \rangle = -0.957, -0.9975, -0.6036$ and -0.9615 , respectively.

The ideal field state of the two DOPOs well above the threshold with the classical out-of-phase correlation and its covariance matrix are given by

$$\hat{\rho}_{cl} = \frac{1}{2} |\alpha_{cl}\rangle_1 |-\alpha_{cl}\rangle_2 {}_2\langle -\alpha_{cl}| {}_1\langle \alpha_{cl}| + \frac{1}{2} |-\alpha_{cl}\rangle_1 |\alpha_{cl}\rangle_2 {}_2\langle \alpha_{cl}| {}_1\langle -\alpha_{cl}|, \quad (3.57)$$

$$\sigma(\hat{\rho}_{cl}) = \begin{pmatrix} 4\alpha_{cl}^2 + 1 & 0 & -4\alpha_{cl}^2 & 0 \\ 0 & 1 & 0 & 0 \\ -4\alpha_{cl}^2 & 0 & 4\alpha_{cl}^2 + 1 & 0 \\ 0 & 0 & 0 & 1 \end{pmatrix}, \quad (3.58)$$

where α_{cl} is the real and positive amplitude of the coherent states in the DOPOs. I have found that the Gaussian discord calculated with Eq. (3.58) verges on $D^{\leftarrow} \sim 0.02356$ for $\alpha_{cl} \gtrsim 50$, which is in a good agreement with the values in the simulation. Eq. (3.57) clearly represents a mixture of Gaussian states, thus the result indicates a genuine quantum correlation between coherent states with the coherent classical communication at the limit.

3.4.5 Distribution functions for quadrature amplitudes

Fig. 3.6 shows instantaneous distribution functions for the quadrature amplitudes at some time points for $\gamma_s = 0.1, \gamma_c = 0.2$. In (a), the distribution for x gets broadened as the pumping rate increases. The dashed lines are Gaussian fitting curves for each time point. We see that it has some deviation from the fitting curve at $\tau = 33$ and 35 . This indicates that the system is at the onset of the macroscopic bifurcation in x .

As shown in (b), after a while from the beginning of the pumping, both $P(p_1)$ and $P(p_2)$ come to have small humps at the sides of their central peaks. They are basically kept until the clear bifurcation in $P(x_1)$ and $P(x_2)$. The side peaks in $P(p_1)$ and $P(p_2)$ are as clear as those in an even cat state $|-\alpha\rangle + |\alpha\rangle$ with $\alpha \sim 0.9$. This is reasonable because a squeezed vacuum state with a Gaussian distribution function for x with its peaks at $x_j = 0$ does not correspond to any pure cat state with a finite amplitude. Therefore, $P(p_1)$ and $P(p_2)$ suggests the existence of the coherent superposition components in a sufficiently closed two-DOPO system. Here, the simultaneous humps completely vanish when $\gamma_s, \gamma_c \gtrsim 1 = \zeta$. This indicates that the quantum noise stored in the injection path is essential in the formation of superposition components. The central cavity here is associated with the realization of a squeezed heat bath [123, 162], which has been considered to prevent a macroscopic superposition state from decoherence. It is worth noting that the model considered here is totally different from that in the previous studies.

Here, I show the extra squeezing of the intracavity DOPO fields which supports the effect by the injection from the mid cavity mode. Fig. 3.7 displays the variances of

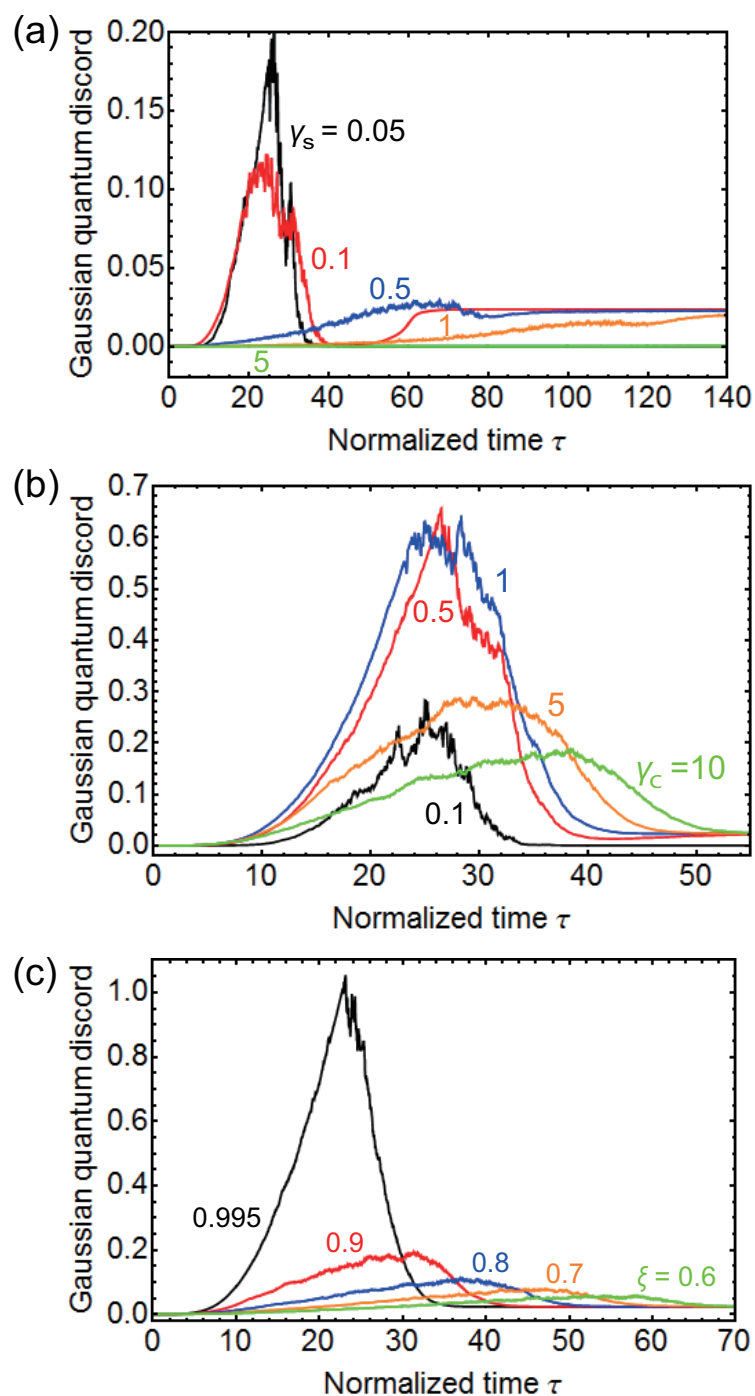


Figure 3.5: Quantum discord when the state is approximated as a bipartite Gaussian state. Squeezing in the DOPOs below the threshold and the mutual injection give a large discord. Coherent fields above the threshold in them and a coherent classical communication lead to a finite discord. 20000 stochastic runs for each curve.

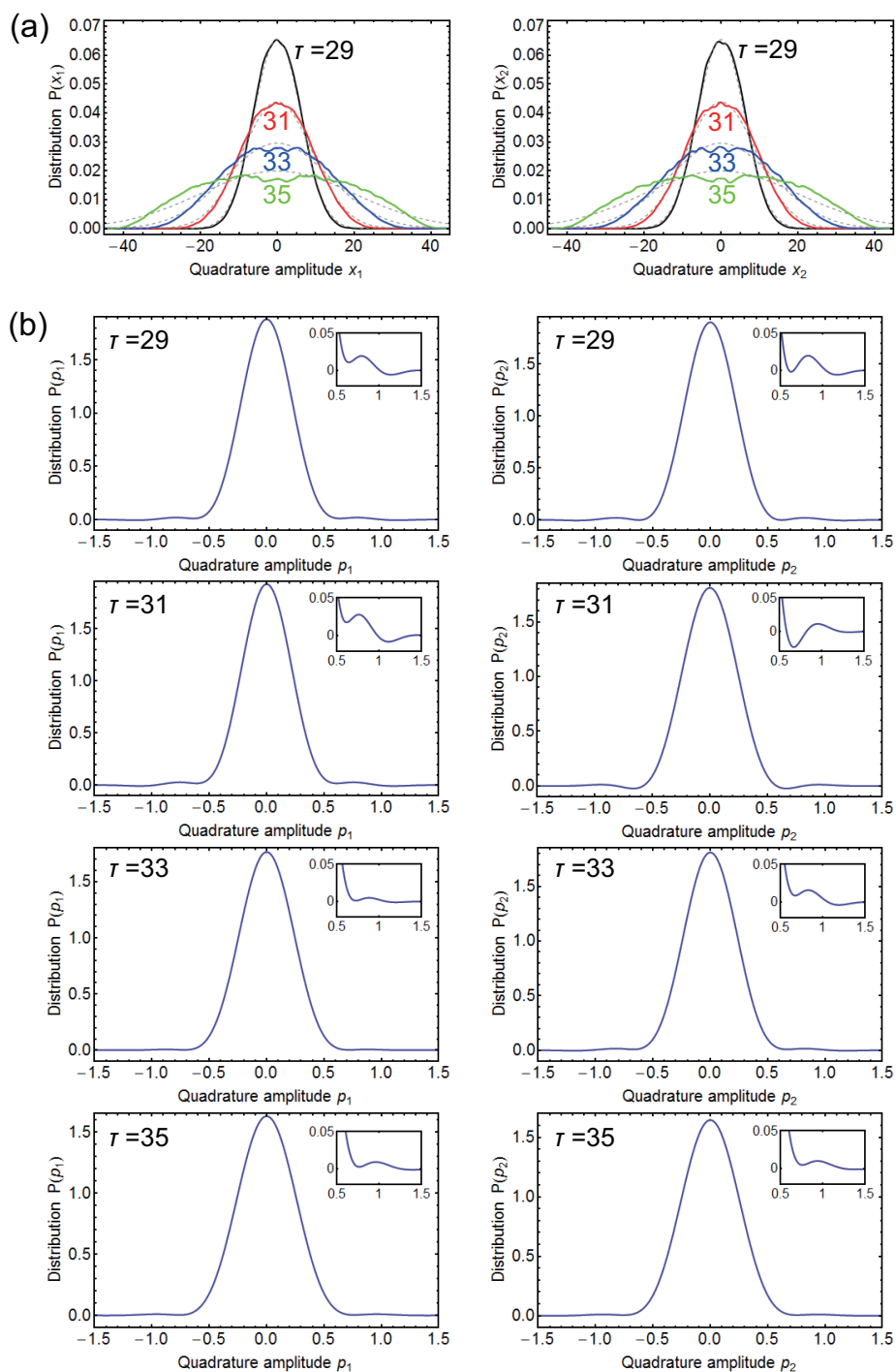


Figure 3.6: Distribution functions at different time points for (a) x_j and (b) p_j . The dashed lines in (a) are Gaussian fitting curves with $\sigma = (6.6, 9.1, 13.5, 20.0)$ for $\tau = (29, 31, 33, 35)$. The insets in (b) show the zoomed curves around the side peaks. 200000 trajectories are used. $\gamma_s = 0.1$, $\gamma_c = 0.2$ and $g = 0.01$.

p_1 and p_2 dependent on time (i.e. the pumping rate). When the system is below the threshold, they decrease with the rise in the pumping rate. Following the oscillation of the DOPOs, they get back to the value for a coherent state and the vacuum state (0.25). The minimum value ~ 0.043 is smaller than that for a single intracavity DOPO field [117] (0.125, meaning -3 dB squeezing). It clearly suggests that the squeezing in the both DOPOs is enhanced due to the mutual injection via the center cavity.

Compared to expectation values of observables (e.g. Fig. 3.7. See also Appendix A), the convergence of the distribution functions (Fig. 3.6) to the number of sampling is slower, because the sampled points have to cover the whole space where the distribution can have a non-negligible value. Thus, I have taken 200000 runs to draw the curves here. Simultaneous formation of the side peaks in both $P(p_1)$ and $P(p_2)$ is a good indicator that the accuracy is not bad, because the two DOPOs obey the SDEs of the same form. However, numerical errors still lead to obvious negative values in some curves. Also, one of the p distribution functions is fluctuated a lot at some time points, leading to a larger fringe and negative values.

3.5 Discussion

In this section, I discuss other potential theoretical schemes to simulate the system considered here and the validity of the simulation in this study.

3.5.1 Other theoretical schemes

First, I refer to the difficulty in the simulation in this study with other theoretical schemes. Regarding a numerical analysis for an open quantum system, direct integration on the master equation with the Fock state basis is the most standard method as investigated in the previous relevant studies [123, 162]. It treats a series of ordinary differential equations for the components of the density matrix for the system. Single-shot numerical integration for them gives all the information of the solution, thus we do not have to repeat stochastic simulations nor take ensemble averages over a number of samples. Also, it is relatively easy to get a good accuracy in numerical integration of an ordinary differential equation. However, the basis has an infinite number of eigenstates hence we have to truncate some of them. Here, the more photons possible in the system, the more eigenstates needed. In addition, the number of modes crucially affects the complexity of the simulation. When we consider two DOPOs and the mid cavity with m eigenstates for each, the number of components of the density matrix is m^6 . This amounts to unrealistic numbers such as 1000^6 and 10000^6 thus the simulation will be too costly.

Solving the Fokker-Planck equation will be useful if we can find a potential solution. However, it supposes a system at the steady state thus cannot treat the transient regime, which is thought to be important for a DOPO to have coherent superposition components [125, 156]. Also, when the mutual injection path is explicitly considered, we will not be able to find a potential solution.

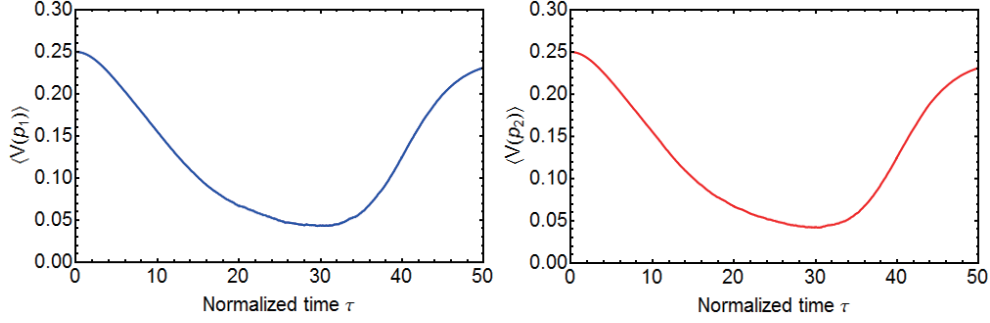


Figure 3.7: Variances of p_1 (blue curve) and p_2 (red curve). The two curves are almost identical due to the same form of the SDEs for each DOPO. 200000 trajectories are used. $\gamma_s = 0.1$, $\gamma_c = 0.2$ and $g = 0.01$.

The linearized analysis has been used to investigate the output squeezing spectra for the quadrature amplitudes of a DOPO [150] and the entanglement between the output fields of two DOPOs coupled with evanescent coupling [137, 139]. We can apply this method to get some information about the intracavity fields of the DOPOs. However, this is also limited in the steady state, and basically gives a result in the frequency domain. To consider the properties in the time domain, we have to integrate the noise spectra over the entire frequency space. Here, a well-known relation between the covariance of input and output bosonic operators [117] is not satisfied. It is because the input field originating from the mutual injection is not a coherent or vacuum state but a squeezed state. Straightforward application of this relation results in negative values in the spectrum of $\langle \Delta v_-^2 \rangle$.

3.5.2 Accuracy and limit of simulation

Next, I discuss the stability of the simulation in this study. I recognize that the positive P representation can give unreliable results in some cases [170]. However, the simulation here is considered to be relatively stable, because the dynamics of the variables are bounded in a finite manifold, as explained before. In the theoretical model, the pump modes are adiabatically eliminated. This significantly helps DOPO fields be bounded as Ref. 170 pointed. It is also supported by the fact that the Fokker-Planck equation for a DOPO with the adiabatic elimination has the solution [108] which comprises Gaussian components decaying exponentially in the phase space. In addition, a real and diagonal diffusion amplitude matrix assists them to be real. The classical solution (3.55), (3.56) and the gradual pumping scheme also help the variables be bounded. For all of the reasons, the simulation here are thought to be hardly affected by the instability of the dynamics in the complex phase space.

Nevertheless, the center cavity can enhance the numerical error of the simulation, especially when its loss γ_c is quite small. As mentioned, a relaxation oscillation might be a sign for the unreliability of the simulation. We have not seen large variance in the

amplified quantities such as the photon number, the correlation, and fluctuation for x . However, those for the damped amplitude p directly reflects the feature of the noise in the system. Thus, it can be difficult to acquire a good accuracy for them. We see that the curves for them with $\gamma_s = 0.05$ in the first case and $\gamma_c = 0.1$ in the second have large dispersions and visible spikes, around which the simulation is unreliable [170]. Thus, I have taken $\gamma_s = 0.1$, $\gamma_c = 0.2$ and 200000 samples for the distribution functions to avoid large numerical errors. The critical fluctuation around the oscillation can also be another difficulty because the range of the variables here is big due to a small g . However, it is worth noting that the noise in p is rather decreased there, and that in x does not diverge in principle because the nonlinear pump depletion is fully taken into account here. To reduce the number of samples by removing unexpected correlation in the noise terms and the instability, the introduction of the gauge terms [171] would be needed.

3.5.3 Application for coherent Ising machine

Finally, I comment on possible applications of the quantum states in the DOPOs for a coherent Ising machine [103], an oscillator network emulating the Ising model with mutual injections. Here, the system assigns the up and down spin states to the discrete phase states $|0\rangle$ and $|\pi\rangle$ with a finite amplitude and opposite phases (Eq. (3.56) for the two-site case). Coherent superposition components are presumed to be important for the machine to oscillate with the minimum total gain which corresponds to the lowest eigenvalue of the mapped Ising Hamiltonian. In a hard instance, the network has to avoid local minima whose number scales exponentially with the problem size. Therefore, it will need to hold the information of all the eigenstates simultaneously at the onset of the oscillation. To exploit the superposition components in the DOPOs, we have to keep the loss of the system as small as possible, and pursue large nonlinear interaction in the gain media.

Another possible direction is using the quantum correlation. Here, there might exist a scheme to drive the system using quantum correlation, such as one where we exploit a measurement to detect hidden relative instability of the quadrature amplitudes in the DOPOs and apply some feedback to push the state along with a good direction in the phase space and kick out of a local minimum. It looks like rather realization of a chaotic neural network [172, 173] which jumps between metastable states searching for the optimum, while hopefully has a better efficiency. It is challenging and beyond the scope of this study to investigate whether or not there is a systematic algorithm like this which explicitly utilizes the quantum correlation and shows a sensible quantum speedup.

3.6 Conclusion

I have founded and simulated a fully quantum mechanical model of the system of two DOPOs with the out-of-phase mutual injection. The field between the two DOPO facets is introduced as a cavity mode to treat the input-output relation and the memory effect in the mutual injection path correctly. The model can be extended easily to the case of

a larger network. I have shown that the linear mutual injection terms in the positive P representation are derived *ab initio* in the limit where the dynamics of the injection path is neglected. The simulation result has revealed that the gradually pumped system can have quantum correlation, entanglement and weak coherent superposition components. The quantum correlation and entanglement require a noise-free mutual injection with some loss in its path, and this is referred to as a quantum communication channel via the existence of the entanglement. On the other hand, additional quantum noise stored in the low-loss injection path is rather essential to generate coherent superposition components in the DOPOs. This suggests that the closed injection path with squeezed vacuum inputs is realization of the squeezed heat bath alleviating decoherence with a practical system. Quantum effects of the reservoir in such a simple setup may also play a role not only in a coherent Ising machine but also in broader contexts such as nano- and opto-mechanics, circuit QED and superconducting devices.

Chapter 4

Design and Operation of Pulsed Sub-Harmonic OPO

In this chapter, I design and show the experimental result of a pulsed optical parametric oscillator (OPO) with telecom wavelengths which is applied to the implementation of a coherent computing system.

4.1 Introduction and Basic Theory

4.1.1 Pulsed OPO

The early idea and study of the OPO by R. H. Kingston [146] date back to 1962. He had already been aware that the energy conservation and “coherence” in the amplification process were indispensable to the device. Soon after that, a semi-classical theory for the nonlinear polarization and the well-known wave equation model considering the phase matching condition were investigated by J. A. Armstrong *et al* [148]. The studies on the parametric process at that time [146–148, 174, 175] focused on the possibility of realization and application of optical parametric oscillators and amplifiers. The main topics then were such as the quantum noise in the amplified light and the condition for an enough parametric gain in terms of the optical wavelength, the material length and refractive index. The first experimental realization of an OPO was reported in 1965 [176]. It was not until 1980s that its quantum features were studied as referred to in the previous chapters.

When an ordinary bulk nonlinear crystal is used for parametric amplification based on the birefringent phase matching, the requirement on the optical wavelength, polarization and incident angle is severe due to the inflexibility of material properties such as the refractive index and nonlinear susceptibility tensor. Also, the nonlinear coefficient is relatively low. These had constricted the wide application of the OPO. The idea of *quasi phase matching* (QPM), which relaxes the difficulty using a gain medium with periodically modulated dipole moments, was in the work by J. A. Armstrong *et al* [148]. And, it is 1990s when the techniques were well established to realize QPM OPOs [177, 178] with

periodically poled crystals. This enabled a variety of available nonlinear crystals and dramatically extended the operation range of parametric amplification and oscillation. Currently, the OPO draws broad attentions as a tunable light source [113, 179].

The great potential of the pulsed OPO has been recognized especially since the realization of femtosecond mode-locked lasers with stable frequency and phase characteristics [180], and the advent of optical frequency combs with them [181, 182]. The frequency comb is referred to as a pulsed coherent light source with a stabilized and precise repetition frequency ω_R . Its spectrum looks like a comb of narrow peaks aligned at regular intervals (ω_R for each) around its optical frequency. The relative phase between the pulse envelope and carrier is called *carrier envelope offset* (CEO) $\Delta\phi$. And, the CEO frequency $\omega_{CEO} = \Delta\phi/T_R$ (T_R : the pulse repetition period) is the other important parameter of the comb. These two frequencies are in the radio frequency regime hence can be precisely determined with conventional techniques. Thus, taking the beat frequency between the comb and a target light results in an extremely precise measurement of the optical frequency. It has been applied mainly to metrology and standards of physical quantities as typified by optical clocks [183].

Femtosecond pulsed DOPOs [184–189] are good implementation of frequency combs complementary to mode-locked lasers [190]. It has been in the spotlight because of its desirable properties such as (i) a high effective conversion efficiency and hence low threshold pump power (< 100 mW), (ii) a broad optical gain spectrum and its robustness to environmental noise, (iii) intrinsic phase locking of the signal pulse carriers hence the comb modes to the pump modes and (iv) a broad range of available central wavelengths ranging the mid-infrared (IR) regime. The techniques to build and handle it have been rapidly developed recently. Here, I exploit the femtosecond pulsed DOPOs with telecom [189] and mid-IR [188] wavelengths as genuinely self-phase-locked light sources to construct time-multiplexed networks of oscillator pulses for two experimental demonstrations of the coherent Ising machine based on DOPOs.

4.1.2 Condition for large gain

In the following, I review the classical theory of parametric amplification [112, 179] which is convenient for designing a pulsed OPO. To obtain a large parametric gain, the energy and momentum of the relevant photons need to be conserved in the process. We can write the energy conservation with the common coefficient \hbar removed as

$$\omega_p = \omega_s + \omega_i, \quad (4.1)$$

where ω_p , ω_s and ω_i are the pump, signal and idler frequencies, respectively. Similarly, the momentum conservation is

$$k_p = k_s + k_i, \quad (4.2)$$

where k_p , k_s and k_i are the pump, signal and idler wave numbers in the propagation direction. Here, we consider the type-0 phase matching where the relevant modes are all co-propagating extraordinary waves. The wave-vector mismatch is defined as

$$\Delta k = k_p - k_s - k_i, \quad (4.3)$$

and characterizes the coherence of the process. Eq. (4.2) means $\Delta k = 0$ and is called phase matching condition. The wave number is expressed with the mode refractive index n as $k = n\omega/c$ (c : the speed of light in the vacuum). Thus, the condition is actually imposed on the mode refractive indices for the pump n_p , signal n_s and idler n_i dependent on their wavelengths and the material. This was a major obstacle to the wide range of operations as previously mentioned.

4.1.3 Quasi phase matching

QPM with a periodically poled crystal drastically eases the phase matching condition. It is known that the three wave equations derived from Maxwell equations [179] for the electric fields of the pump, signal and idler modes suffice to argue the properties of a pulsed OPO. These consider the superposition of the three continuous-wave (CW) complex fields for the pump E_p , signal E_s and idler E_i and are given by

$$\frac{dE_s}{dz} = i \frac{\omega_s d_Q}{n_s c} E_p E_i^* \exp(i\Delta k_Q z), \quad (4.4)$$

$$\frac{dE_i}{dz} = i \frac{\omega_i d_Q}{n_i c} E_p E_s^* \exp(i\Delta k_Q z), \quad (4.5)$$

$$\frac{dE_p}{dz} = i \frac{\omega_p d_Q}{n_p c} E_s E_i \exp(-i\Delta k_Q z). \quad (4.6)$$

Here, the waves propagate in the z axis. d_Q and Δk_Q are the effective nonlinear interaction coefficient and the wave-vector mismatch under QPM.

In QPM, we introduce the spatial periodicity of the material nonlinear interaction coefficient $d(z)$. It can be expanded as a Fourier series

$$d(z) = d_{\text{eff}} \sum_{m=-\infty}^{\infty} G_m \exp(-ik_m z). \quad (4.7)$$

d_{eff} is the nonlinear interaction coefficient of the bulk crystal. In this study, I use a LiNbO₃ crystal and extraordinary beams, and its value is $d_{\text{eff}} = d_{33} = 27$ pm/V. $k_m = 2\pi m/\Lambda$ is the grating vector of the m th Fourier component with m an integer. Λ is the poling period determined by the device fabrication. The expansion coefficient G_m depends on the actual form of $d(z)$. The most prevalent realization of $d(z)$ is the rectangular function with a magnitude of d_{eff} and sign inversions at each interval of $\Lambda/2$, and here G_m is

$$G_m = \frac{2}{m\pi} \sin\left(\frac{m\pi}{2}\right). \quad (4.8)$$

In QPM, we can consider the phase matching condition for a grating vector of a certain order m . In fact, d_Q in Eqs. (4.4) - (4.6) is the coefficient for the selected order and given by

$$d_Q = d_{\text{eff}} G_m. \quad (4.9)$$

Also, the wave vector mismatch is modified to

$$\begin{aligned}\Delta k_Q &= k_p - k_s - k_i - k_m \\ &= k_p - k_s - k_i - \frac{2\pi m}{\Lambda}.\end{aligned}\quad (4.10)$$

The effective interaction d_Q gets smaller with a larger m . Thus, we take $m = 1$ and design Λ to satisfy the “first order” QPM condition

$$0 = \frac{n_p \omega_p}{c} - \frac{n_s \omega_s}{c} - \frac{n_i \omega_i}{c} - \frac{2\pi}{\Lambda}.\quad (4.11)$$

Here, the effective interaction coefficient for (4.8) is

$$d_Q = \frac{2}{\pi} d_{\text{eff}}.\quad (4.12)$$

The mode refractive indices n_p , n_s and n_i depend also on temperature. Therefore, choosing a good pump laser, designing the poling period Λ and controlling the crystal temperature enable us to amplify and oscillate the signal beam with a desired wavelength and frequency.

4.1.4 Gain bandwidth

Eqs. (4.4) - (4.6) can be solved and the solution can be expressed with elliptic functions. It gives the approximate intensity gain $G(L)$ when the beams propagates by a small distance L [191]

$$\begin{aligned}G(L) &= \frac{|E_s(z=L)|^2}{|E_s(z=0)|^2} - 1 \\ &\approx \Gamma_g^2 L^2 \text{sinc}^2 \left[\left(\frac{\Delta k_Q^2}{4} - \Gamma_g^2 \right)^{\frac{1}{2}} L \right],\end{aligned}\quad (4.13)$$

where

$$\Gamma_g^2 = \left(\frac{\omega_s d_Q}{n_s c} \right)^2 |E_p|^2 = \frac{2\omega_s \omega_i d_Q^2 I_p}{n_s n_i n_p \epsilon_0 c^3}.\quad (4.14)$$

Here, I_p is the pump intensity. This provides the gain spectrum for the signal and idler modes with a given pump field. Δk_Q includes ω_s and ω_i , thus the sinc function dominantly affects the gain bandwidth. It shows that a smaller L gives a broader gain spectrum. Signal pulses with a short duration require a broad optical spectrum, hence a short crystal. However, a small L leads to a small absolute gain due to its quadratic dependence on L .

4.1.5 Phase sensitive gain and phase states at degeneracy

When in the degenerate operation, the signal and idler photons get indistinguishable. Here, their frequencies and electric fields are identical, i.e. $\omega_s = \omega_i$, $E_s = E_i$. Thus, the wave equations are simplified as

$$\frac{dE_s}{dz} = i \frac{\omega_s d_Q}{n_s c} E_p E_s^* \exp(i\Delta k_Q z), \quad (4.15)$$

$$\frac{dE_p}{dz} = i \frac{\omega_p d_Q}{n_p c} E_s^2 \exp(-i\Delta k_Q z). \quad (4.16)$$

We further decompose these fields into the real and positive amplitudes and phases

$$E_s = \tilde{E}_s \exp i\phi_s, \quad E_p = \tilde{E}_p \exp i\phi_p, \quad (4.17)$$

and substitute these into Eqs. (4.15) and (4.16) to obtain the equations for the amplitudes and phases, resulting

$$\frac{d\tilde{E}_s}{dz} = \frac{\omega_s d_Q}{n_s c} \tilde{E}_p \cos\left(2\phi_s - \phi_p - \frac{\pi}{2}\right) \tilde{E}_s, \quad (4.18)$$

$$\frac{d\phi_s}{dz} = -\frac{\omega_s d_Q}{n_s c} \tilde{E}_p \sin\left(2\phi_s - \phi_p - \frac{\pi}{2}\right), \quad (4.19)$$

$$\frac{d\tilde{E}_p}{dz} = -\frac{\omega_p d_Q}{n_p c} \tilde{E}_s^2 \cos\left(2\phi_s - \phi_p - \frac{\pi}{2}\right), \quad (4.20)$$

$$\frac{d\phi_p}{dz} = -\frac{\omega_p d_Q}{n_p c} \frac{\tilde{E}_s^2}{\tilde{E}_p} \sin\left(2\phi_s - \phi_p - \frac{\pi}{2}\right). \quad (4.21)$$

The right hand side of Eq. (4.18) represents the gain for the signal amplitude \tilde{E}_s . We see that it is maximum when

$$\phi_s - \frac{\phi_p}{2} - \frac{\pi}{4} = 0 \text{ or } \pi. \quad (4.22)$$

Also, when Eq. (4.22) is satisfied, the gain for the pump \tilde{E}_p gets minimum. In addition, from Eqs. (4.19) and (4.21) the phase equilibrium state fulfills Eq. (4.22). This means that the signal mode in a DOPO oscillates with one of the two possible phases (4.22) which are different by π . These distinct phase states were firstly reported with a CW DOPO in 1990 [192].

4.1.6 Frequency states

As well known, there are two resonant conditions for pulsed cavity modes. One is that the cavity length equals to an even multiple of the half of the effective central wavelength. Here, the signal carrier phase of the pulses at a certain spatial point is the same after round trips. On the other hand, when the cavity length is an odd multiple of the half wavelength, the pulses flip their phases with each round trip. These two kinds of

longitudinal modes for the signal pulses correspond to the two frequency states of the sub-harmonic frequency comb [187]. The coherent Ising machine explicitly utilizes the interference of the resonating signal pulses with discrete phases, thus their phases have to be static in round trips. We therefore need to prepare degenerate signal pulses in an “even” frequency state by tuning the cavity length.

4.2 Design of a Pulsed OPO

4.2.1 Pump laser

Fig. 4.1 displays a schematic illustration of the pulsed OPO designed for the sixteen-pulse experiment. The pump laser here (Laser Quantum Ltd., Taccor-s 10) is a mode-locked Ti:Sapphire laser with a central wavelength of 794 nm, a spectral width (FWHM) of 50 nm and a pulse duration of 15 fs. The pulse repetition frequency measured with a RF spectrum analyzer is 1.009 GHz. The maximum output power detected by a thermal sensor tuned for 794 nm is 1.688 W. The beam diameter at the output shutter is 2 mm, and the output beam divergence is 2.5 mrad. The half wave plate (HWP) and polarizing beamsplitter (PBS) placed in front of the pump output works as a power controller.

4.2.2 Cavity stability

The bow-tie ring cavity with a round trip length of about 4.8 m can contain separate sixteen pump pulses with a repetition rate of 1 GHz inside. It will result in as many independent degenerate OPO pulses running in a single ring resonator, and they can be used to emulate sixteen-spin systems.

M1 and M2 in Fig. 4.1 are concave mirrors and compose a short-arm concentric cavity. This focuses the beam spot and gives a large spatial power density at the inside of the nonlinear crystal placed in the middle. According to the previous study [188], it is desirable to get a signal spot size smaller than 10 μm at the center of the crystal. Then, I investigated the stability of the whole cavity in terms of the signal mode using an analysis software named *BeamSim* which is based on the ray transfer matrix method [109]. Here, I use curved mirrors with a radius of curvature (ROC) of 50 mm. The nonlinear medium is a 1-mm thick periodically poled LiNbO_3 (PPLN) crystal with an approximate refractive index of 2.1. I set a well-collimated eigenmode with a spot size ($1/e^2$ intensity radius) of 2 mm and the expected signal central wavelength 1.588 μm as the input. The free-space propagation length out of the short cavity is 4.750 m. The spot sizes in the vertical direction and horizontal direction (set as x and y axis) are assumed to be the same. Fig. 4.2 shows the minimum spot size w_{\min} in the crystal dependent on the short cavity length which satisfies the stability condition. It indicates that the system has a stability range of the short cavity length centered at 50.8 mm with a width of 520 μm . The central point (50.8 mm) is the stablest point for the cavity. The minimum spot size there is found to be 8.2 μm , which is small enough for the oscillation.

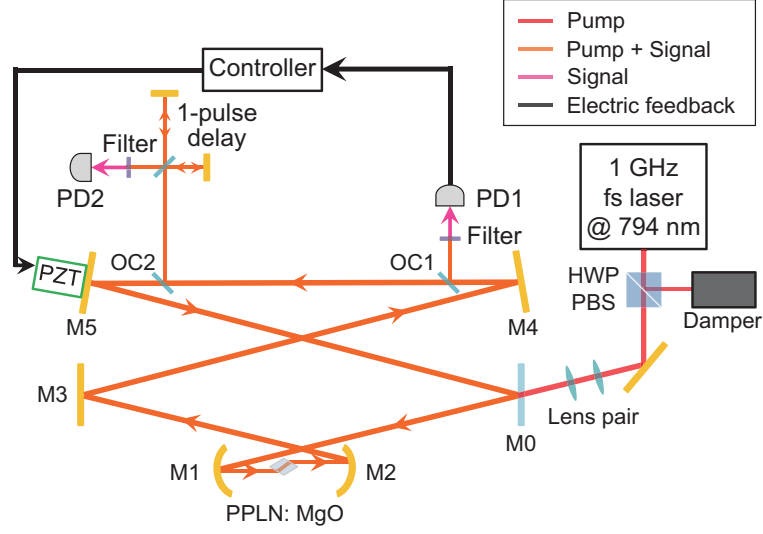


Figure 4.1: Schematic illustration of the pulsed OPO system. HWP: half wave plate. PBS: polarizing beam splitter. M: mirror. PD: photo detector. OC: output coupler. PZT: piezoelectric transducer.

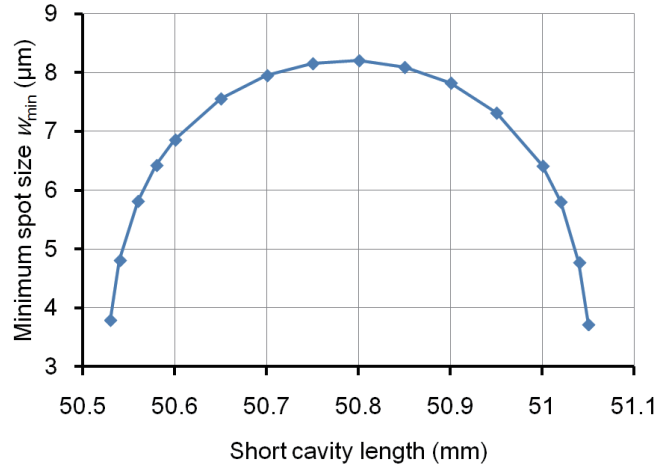


Figure 4.2: Cavity stability dependent on the short cavity length. The width of stability range is found to be 520 μm . The minimum spot size in the crystal is 8.2 μm for the stablest short cavity length.

4.2.3 Mode matching

To obtain an enough gain for the signal, we also have to tune the size of the pump beam incident on the crystal. According to the detailed theoretical study on the parametric process of focused beams [193], the condition to achieve the minimum oscillation threshold possible is

$$w_p = \frac{w_s}{\sqrt{2}}, \quad (4.23)$$

where w_p and w_s are the minimum spot sizes of the pump and signal beams in the middle of the nonlinear crystal. Thus, $w_p = 5.80 \mu\text{m}$ is needed to achieve the optimum oscillation of the signal with the designed spot size $w_s = 8.2 \mu\text{m}$.

To match the two spatial modes, I compute the spatial transition of the desired pump spot size first. Here, the spot size is given by the back calculation of the complex beam parameter $q(z)$ defined as [109]

$$\frac{1}{q(z)} = \frac{1}{R(z)} - i \frac{\lambda_0}{\pi n w(z)}, \quad (4.24)$$

where $R(z)$ is the ROC of the phase front and λ_0 is the wavelength of the beam in the vacuum. The spot size $w(z)$ is obtained from the imaginary part of $q(z)$. The beam parameter q_f after the propagation in an optical system with the ray transfer matrix (A_T, B_T, C_T, D_T) can be represented with the initial parameter q_i by

$$q_f = \frac{A_T q_i + B_T}{C_T q_i + D_T}. \quad (4.25)$$

I start with the center of the crystal with $z = z_0$ where the beam waist is located, i.e. $R(z_0) = \infty$ and $w(z_0) = 5.80 \mu\text{m}$. Applying Eq. (4.25) and the ray transfer matrices for propagation, refraction at a flat surface and reflection at a curved mirror lead to the desirable z dependence of the pump spot size [194].

Next, I design a lens pair to achieve the divergence of the pump beam which fits the desired curve as well as possible. The original beam waist and divergence of the pump laser are obtained with the fitting by the measured spot sizes at different points with a beam profiler. The lens pair works as a Keplerian telescope and collimator, meaning that it changes both the spot size and divergence of the incident beam. When the focal lengths of the input and output lenses are f_i and f_o , a good interval between the lenses is $\sim f_i + f_o$. Also, the ratio of the input and output spot size is $\sim f_o/f_i$. I search for a good position of the first lens and interval between the lenses, repeatedly calculating the transition of the spot size.

Fig. 4.3 presents the simulated and desirable pump spot size dependent on propagation distance of the beam. The calculated position of the waist inside the pump laser is the reference of the distance. The solid line shows the simulated spot size with the measured data of the pump laser and a lens pair. The dashed line gives the desired size from the waist at the middle of the crystal. The dots are the averages of the measured spot sizes in x and y directions. Here, $f_i = 50 \text{ mm}$ and $f_o = 40 \text{ mm}$ are used. The

positions 20 cm and 29.19 cm for the input and output lenses accomplish good sizes and divergence of the simulated beam compared to the desired characteristics. Note that fitting the divergence is more important than small differences in the spot size because it affects the focusing in the crystal more.

4.2.4 Astigmatism compensation with angled mirrors

The nonlinear crystal in the short arm cavity has angled surfaces at the Brewster angle to the incident beam. It allows almost perfect transmissions of the pump and signal beams, while it results in different effective propagation lengths of the x and y components of the beam in the crystal. This astigmatism degrades the coherence of the beam, however, it is known that the angled concave mirrors M1 and M2 can compensate it [195].

Fig. 4.4 shows the simplified illustration of the system. The reference in the propagation direction (z axis) is taken so that the propagation lengths before and after the short cavity are the same. The mirror angle to the symmetry axis is denoted by θ_M . t_C is the crystal thickness. v and h represent the vertical and horizontal axes. Here, the ray transfer matrix for one round trip of the signal beam is written as

$$\begin{pmatrix} A_1 & B_1 \\ C_1 & D_1 \end{pmatrix} = \begin{pmatrix} 1 & \frac{l_L}{2} \\ 0 & 1 \end{pmatrix} \begin{pmatrix} 1 & 0 \\ -\frac{2}{R_d} & 1 \end{pmatrix} \begin{pmatrix} 1 & \frac{l_S}{2} \\ 0 & 1 \end{pmatrix} \begin{pmatrix} 1 & t_d \\ 0 & 1 \end{pmatrix} \\ \times \begin{pmatrix} 1 & \frac{l_S}{2} \\ 0 & 1 \end{pmatrix} \begin{pmatrix} 1 & 0 \\ -\frac{2}{R_d} & 1 \end{pmatrix} \begin{pmatrix} 1 & \frac{l_L}{2} \\ 0 & 1 \end{pmatrix}, \quad (4.26)$$

where l_S and l_L are the free-space propagation lengths in and out of the short arm cavity, respectively. $d = v, h$ is the index for the spatial component of the beam. The effective ROC of the curved mirrors and the thickness of the crystal dependent on the spatial axes are given by [195]

$$R_v = \frac{R_C}{\cos \theta_M}, \quad (4.27)$$

$$R_h = R_C \cos \theta_M, \quad (4.28)$$

$$t_v = \frac{t_C}{n^2} \sqrt{n^2 + 1}, \quad (4.29)$$

$$t_h = \frac{t_C}{n^4} \sqrt{n^2 + 1}, \quad (4.30)$$

where R_C is the ROC of the concave mirrors. The system can be regarded as the periodic sequence of the one round trips (4.26). Therefore, the stability condition for the resonator is given by [196]

$$-1 < \frac{1}{2} (A_1 + D_1) < 1. \quad (4.31)$$

The used parameters are $n = 2.13$, $R_C = 50$ mm and $t_C = 1$ mm. I change l_S around $l_S = R_C = 50$ mm. The effective round trip length for the beam is $L = 4.8$ m, and the length out of the short cavity is obtained with $l_L = L - l_S - t_d$.

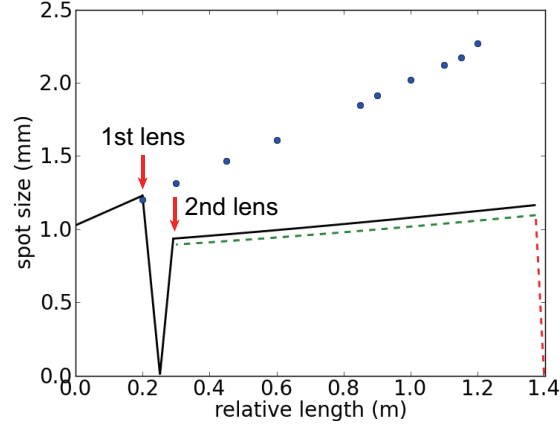


Figure 4.3: The pump spot size dependent on the propagation distance. Solid line: the simulated spot size with the measured data of the pump laser and a lens pair. Dashed line: the desired spot size calculated from the waist $w_p = 5.80 \mu\text{m}$ at the middle of the crystal. Dots: mean of the measured spot sizes in vertical (x) and horizontal (y) directions.

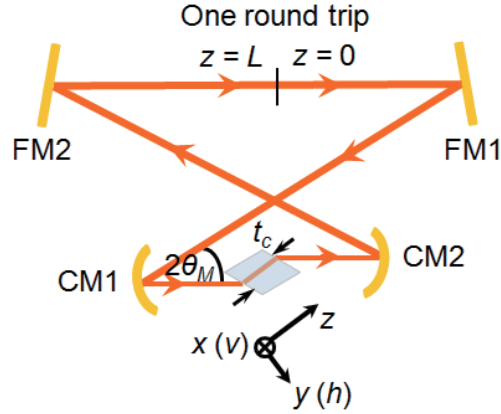


Figure 4.4: Simplified drawing of the system with angled concave mirrors. FM: flat mirror. CM: concave mirror. θ_M : mirror angle. t_C : thickness of the crystal. The reference in the propagation direction (z axis) is taken so that the free-space propagation lengths before and after short arm cavity are the same.

Fig. 4.5 (a) shows the stability ranges with colored points for both the vertical and horizontal components of the beam which depend on the short cavity length $l_s + t_C$ and mirror angle θ_M . The regions of stability for both components move in opposite directions as θ_M increases. The overlap of the two regions means the stability range of the signal beam. We see that $\theta_M = 5$ degrees hence the beam angle of 10 degrees gives the broadest stability range. 4.5 (b) represents the width of the stability range as a function of θ_M . The broadest width for $\theta_M = 5$ degrees is found to be $504 \mu\text{m}$. Thus, to achieve the stable oscillation of the sub-harmonic pulses, we have to tune the beam angle to be 10 degrees with a good accuracy, and set the spacing between the concave mirrors to be within the range with a width of $504 \mu\text{m}$ in the construction.

4.2.5 Poling period of nonlinear crystal

Next, we design the poling period of the nonlinear crystal which satisfies the type-0 ($e + e \rightarrow e$) QPM condition (4.11). Here, I rewrite the equation so that we can see the explicit dependence of the quantities on the wavelength and temperature in the degenerate case ($\lambda_p = \lambda_s/2$, $\lambda_s = \lambda_i$) as [197]

$$2\pi \left[2 \frac{n_e(\lambda_s/2, T)}{\lambda_s} - 2 \frac{n_e(\lambda_s, T)}{\lambda_s} - \frac{1}{\Lambda(T)} \right] = \Delta k_{\text{opt}}. \quad (4.32)$$

Δk_{opt} is the optimum wave vector mismatch dependent on beam focusing [193], although it is ignored here, i.e. $\Delta k_{\text{opt}} = 0$ (plane wave approximation). n_e is the refractive index of the extraordinary wave in 5% MgO-doped congruent LiNbO₃, which is determined with the Sellmeier equation [197]

$$n_e^2 = a_1 + b_1 f_T + \frac{a_2 + b_2 f_T}{\lambda^2 - (a_3 + b_3 f_T)^2} + \frac{a_4 + b_4 f_T}{\lambda^2 - a_5^2} - a_6 \lambda^2, \quad (4.33)$$

where $a_1 = 5.756$, $a_2 = 0.0983$, $a_3 = 0.2020$, $a_4 = 189.32$, $a_5 = 12.52$, $a_6 = 1.32 \times 10^{-2}$, $b_1 = 2.860 \times 10^{-6}$, $b_2 = 4.700 \times 10^{-8}$, $b_3 = 6.113 \times 10^{-8}$ and $b_4 = 1.516 \times 10^{-4}$. The temperature dependent parameter f_T is defined as

$$f_T = (T - 24.5)(T + 570.82), \quad (4.34)$$

where the temperature T here is in degree Celsius. Eq. (4.33) gives the results showing a good agreement with the experiments with telecom and mid-IR wavelengths.

The poling period meeting the QPM condition for the expected degenerate signal wavelength $\lambda_s = 1.588 \mu\text{m}$ is plotted as a function of the crystal temperature in Fig. 4.6 (a). Here I consider the room temperature operation because heating the crystal can be an additional noise source, though it may allow the self phase-locked operation without an electric controller for a longer crystal. Also, I expect that the MgO-doped PPLN crystal is well resistant to the photorefractive damage [198]. A period of $20.4 \mu\text{m}$ is seen to achieve phase matching at about 38 degrees. There is a commercialized ready-made crystal with that period and a thickness of 1 mm (Covesion MSHG1550-1.0), thus I use

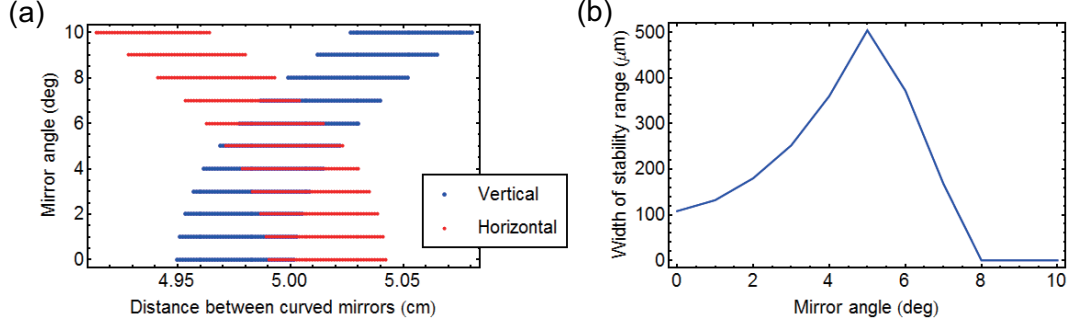


Figure 4.5: Simulated stability range depending on the short cavity length for a 4.8 m cavity with curved mirrors with a ROC of 50 mm and a 1-mm long PPLN crystal at Brewster angle. (a) Stability ranges for the two orthogonal components of the beam and different mirror angles θ_M drawn by colored points. (b) Width of the range of the whole signal beam for varying θ_M .

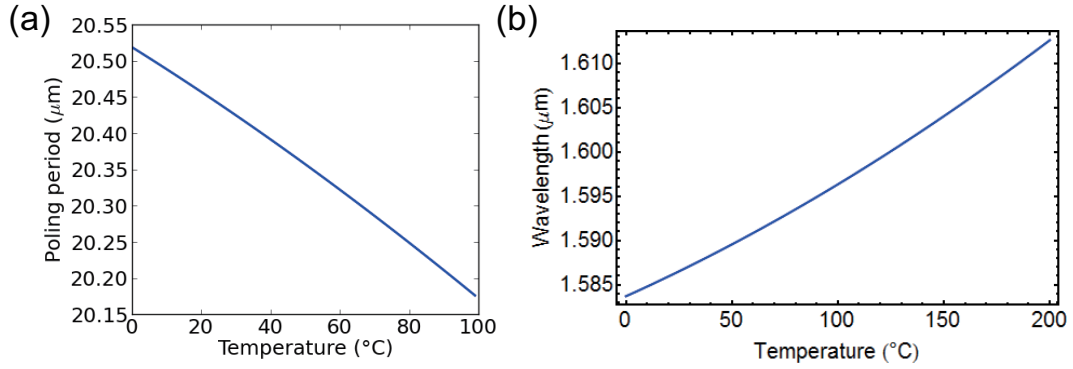


Figure 4.6: Quasi phase matching condition (a) for the poling period and crystal temperature under a fixed degenerate signal wavelength $\lambda_s = 1.588 \mu\text{m}$. (b) That for the degenerate signal wavelength and temperature in a crystal with a period of $20.4 \mu\text{m}$.

one after having it cut at Brewster angle. The spectral intensities from 790 nm to 798 nm of the pump laser are nearly equal, thus the DOPO will operate in a good range of temperatures. Fig. 4.6 (b) depicts the phase matching condition for the degenerate signal wavelength and temperature under a poling period of 20.4 μm . This indicates that the main spectral components of the pump will allow phase matching up to about 100 degrees.

4.2.6 Gain bandwidth

In the sub-harmonic generation process of pulses, the signal spectrum is expected to get about twice as broad as that of the pump. Thus, it has to be made sure that the crystal provides a good gain bandwidth to keep the whole modes down-converted from the pump. Fig. 4.7 presents the normalized gain spectrum simulated with Eq. (4.13) for different crystal lengths. Here, I numerically bound $\Delta k_Q^2/4 - \Gamma_g$ in the equation to be positive. The refractive indices for the relevant modes are obtained with Eq. (4.33). A shorter crystal gives a broader bandwidth, while the spectrum for a 1 mm-long crystal also keeps nearly its maximum in a large range from 1.54 μm to 1.64 μm . This almost covers the expected major spectral range of the signal pulses whose peak is at $\lambda_s = 1.588 \mu\text{m}$ and FWHM is $50 \times 2 = 100 \text{ nm}$.

4.2.7 Pulse walk off

The temporal walk off between the signal and pump pulses is a critical factor which limits the parametric gain with ultrashort pulses. Because the signal and pump wavelengths are separate, their group velocities can be significantly different. With small durations of the pulses, the time where they overlap and induce the parametric gain is short.

The walk off can be estimated with the group velocity mismatch defined as the difference of the inverse group velocities [199]

$$GVM = \left| \frac{1}{v_{g,s}} - \frac{1}{v_{g,p}} \right|. \quad (4.35)$$

$v_{g,s}$ and $v_{g,p}$ are the group velocities of the signal and pump in the nonlinear crystal. The temporal walk off after a propagation distance L is given by $L \times GVM$. Also, the efficient nonlinear interaction is present only from the onset of the overlap until the walk off reaches the pump duration τ_p . Thus, the propagation length for the interaction is estimated as τ_p/GVM . Here, the group velocity can be obtained with Sellmeier equation (4.33) as [199]

$$v_g = c \left(n - \lambda \frac{dn}{d\lambda} \right)^{-1}, \quad (4.36)$$

and hence GVM for the pump wavelength $\lambda_p = 794 \text{ nm}$ in LiNbO_3 at 38 degrees is calculated as $2.78 \times 10^{-10} \text{ s/m}$. Accordingly, τ_p/GVM for 100 fs pump pulses is 0.36 mm and that for 15 fs pulses is only 0.054 mm. Thus, the crystal length of 1 mm is long for the output pump-pulse duration 15 fs, although I expect some pulse broadening for

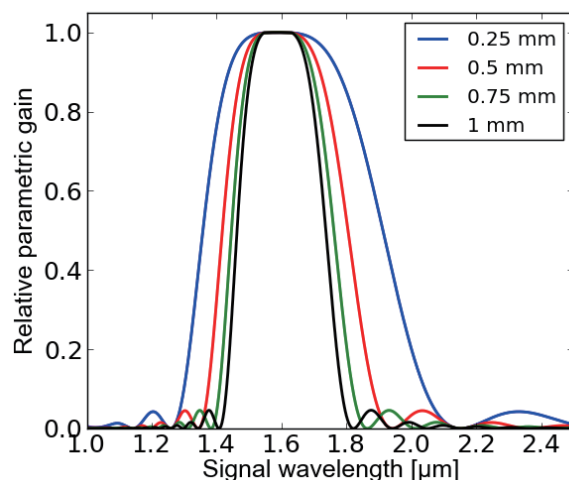


Figure 4.7: Normalized gain spectrum for the signal mode. Different curves are for different crystal lengths. A 1 mm-long crystal has a good bandwidth for the given pump laser properties.

the pump due to group velocity dispersion in the optical components such as the HWP, PBS, OCs, PPLN crystal and dielectric mirror M0 (shown in Fig. 4.1).

4.2.8 Electrical cavity locking system

The pulsed OPO oscillates only in some limited ranges of the round-trip cavity length whose centers are multiples of the half central wavelength and widths are about 100 nm. For the continuous operation, the cavity length needs to be locked to the one where the longitudinal signal mode is resonant and the output signal power is maximal. Here, an electronic servo controller system (TEM Messtechnik, LaseLock Digital) is used to stabilize the cavity. It produces the error signal based on the Pound-Drever-Hall method [200], and applies PID feedback to the cavity length using that error signal.

Fig. 4.8 displays a schematic drawing of the servo controller. It places an electric sinusoidal modulation of several kHz on the PZT with the internal local oscillator. The modulated detector output has the information of the differential power of the signal and undergoes the synchronous detection. Here, it is mixed with the modulation signal, then the error signal is detected as the DC output after passing through the low-pass filter. The integral term in the PID feedback signal gets indispensable when there is some drift noise in the system.

4.2.9 Other information of the system

Here I describe some missing information of the system drawn in Fig. 4.1. The mirror M0 is a dielectric mirror with a high transmission for the pump ($T > 90\%$ in 750 - 850

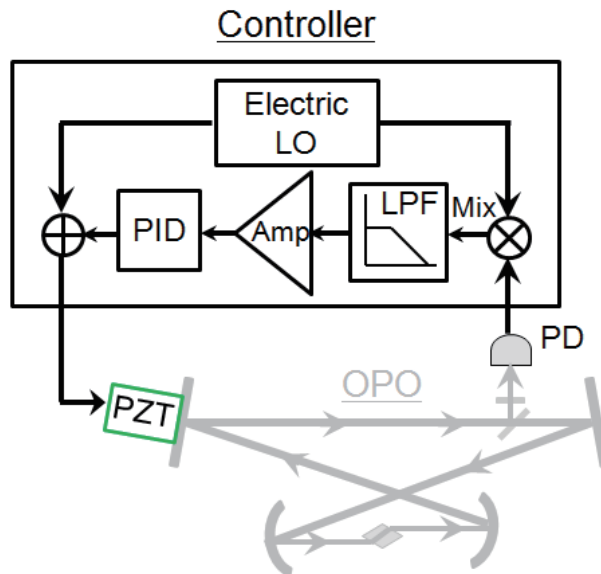


Figure 4.8: A schematic of the servo controller used to keep the signal output power maximum.

nm) and a high reflectivity for the signal ($R > 99.8\%$ in 1500 - 1700 nm). Each output coupler OC is a beamsplitter which has 10 % reflection of the signal and about 20 % for the pump. The optical filter is long-pass so that PDs pick only the signal pulses. To change the operating point, I sometimes replace the filter in front of PD1 with a band-pass filter with a narrow bandwidth of 12 nm. PD1 (Thorlabs PDA20C) is a InGaAs detector with a bandwidth of 5 MHz to see the average power of the signal pulses. I call it “slow detector” afterwards. PD2 (Newport 818-BB-51) is an extended InGaAs detector with a cut-off frequency of 12.5 GHz. This measures the intensity of each signal pulses coming from the unequal-arm Michelson interferometer in front. I call this “fast detector”. The interferometer superposes pairs of spatially adjacent signal pulses picked from the OPO.

4.3 Operation of a 16-Pulse OPO with Telecom Wavelengths

The construction and operation of a pulsed OPO are performed in the two modes. First, I run the system in the *scanning operation*, where the cavity length is scanned over hundreds of micrometers with a periodical triangular modulation signal (at about 1 Hz). This modulation is applied to another PZT stage (with Newport NPM140) on M3 in Fig. 4.1. This mode is used for (i) the alignment for the parametric oscillation and fine tuning and (ii) the characterization of the longitudinal modes and oscillation threshold.

Next, I move to the *continuous operation*, where the OPO keeps the maximum power in one longitudinal mode with the servo controller. I define the oscillation threshold of the OPO as the pump power where all the oscillation peaks get invisible, and it is 113 mW for the system with two OCs here.

4.3.1 Cavity modes in scanning operation

A well-aligned system gives some resonant longitudinal down-converted modes in the scanning operation as shown in Fig. 4.9. Here, the cavity has two 90:10 output couplers as shown in Fig. 4.1, and the average pump power is 300 mW. The normalized signal power at the slow detector has separate peak structures with their intervals about a half wavelength ($\sim 0.79 \mu\text{m}$). I call them *oscillation peaks* afterwards, and put numbers on the three highest peaks. The reference of the cavity length is set as the one at the top of the highest peak. The number of resonant peaks increases as the pumping power rises. Peak 1 is the degenerate peak and has the narrowest range of resonant cavity lengths in the three. It is probably because the degenerate peak has a narrower spectral range of the oscillating modes than a non-degenerate peak which has separate signal and idler spectral peaks. Peak 3 is a totally non-degenerate peak. We can see a small dip in peak 2, indicating that it has both degenerate and non-degenerate components [189].

4.3.2 Power stability in continuous operation

Next, the servo controller is turned on and the cavity is locked to the top of the highest peak (peak 1). Fig. 4.10 depicts the stability of the average output power in time. We see that the system achieves a stable continuous operation with the fluctuation up to about 20% of the average power. This fluctuation includes the fictitious electric noise in the detector and the oscilloscope and the small modulation from the controller with a frequency of 8.5 kHz. The fine structure of the peak also affects the magnitude of the fluctuation. In addition, the resonant cavity length drifts in time possibly because of the temperature drift of the coolant in the cooling system due to a large thermal burden of the pump laser. This seems to be a major noise source in the continuous operation. However, the integral feedback signal can well compensate for the drift, and the system can keep the oscillation as long as the peak stays in the travel range of the fast PZT ($\sim 15 \mu\text{m}$).

4.3.3 Pulse pattern

The fast detector and the filter is put before the interferometer, and the pulse envelope patterns of oscillation peak 1, 2 and 3 are measured as in Fig. 4.11 (a), (b) and (c), respectively. Unsplit signal pulses for all the longitudinal modes are considered to be good signs of a broad gain bandwidth of the crystal and the self-phase-locking among the comb lines. While peak 1 and 3 give stable pulses, those for peak 2 have some instability in their tail shapes and peak powers. It also indicates that peak 2 contains comparable

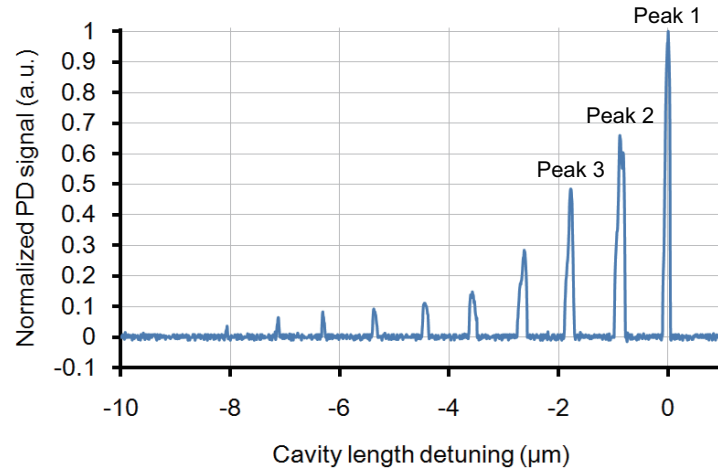


Figure 4.9: Average power of the OPO output dependent on the cavity length, showing longitudinal oscillation peaks. The average pump power is 300 mW.

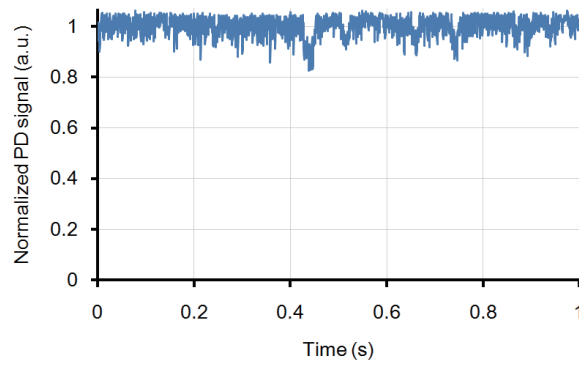


Figure 4.10: Temporal stability of the average output power of the OPO locked to the strongest oscillation peak. The average pump power is 300 mW.

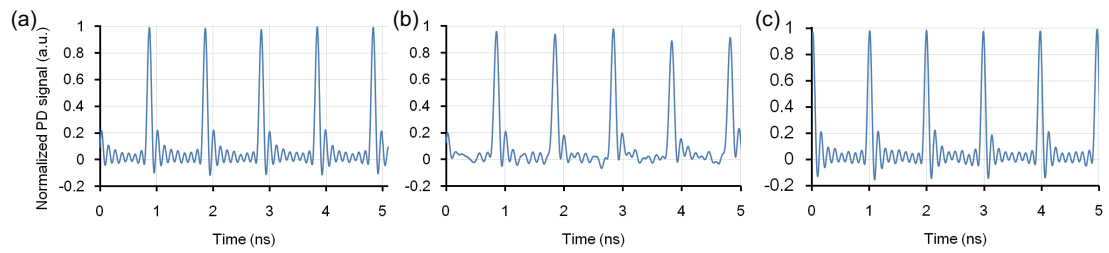


Figure 4.11: Temporal pulse envelopes for (a) peak 1, (b) peak 2 and (c) peak 3. The average pump power is 300 mW.

degenerate and non-degenerate components, because it appears that the fluctuation in (b) is of more than GHz and other physically inessential noises are not that fast.

4.3.4 Output power

The average powers of the three strongest peaks as functions of the pump power are presented in Fig. 4.12. The signal power is measured with the output port from OC2. OC1 and PD1 are also used to lock the cavity. The mode of Peak 2 oscillates with a smaller pump power than peak 1 probably because peak 2 has a broader wavelength range in the optical spectrum. However, the mode of peak 1 has a larger nonlinear gain hence a large external quantum efficiency than that of peak 2. On the other hand, those for peak 2 and 3 are close. Considering the phase matching, this indicates that peak 1 is degenerate while the major components of peak 2 and 3 are non-degenerate. The efficiencies are 1.8, 1.3 and 1.2 % for peak 1, 2 and 3, respectively. Such small values are because of a small reflection rate of 10 % of OC2 and the existence of two OCs in the system. In the case of only one output coupler, the threshold is 85 mW. Another factor in the restriction of an efficient conversion is the sum frequency generation, which consumes the pump and signal then generates a bright green beam in this experiment.

4.3.5 Spectrum

The output beam from OC2 is coupled to a multi-mode fiber and directed into an optical spectrum analyzer. The optical spectrum is measured as the average of 1000 sweep data and shown in Fig. 4.13 for the three oscillation peaks. We see that the spectrum for peak 1 is degenerate. Its peak wavelength and FWHM are 1574 nm and about 80 nm. Those for peak 2 and 3 have two separate spectral peaks, meaning that they are non-degenerate. Here, peak 2 has more spectral components including small spikes around the sub-harmonic wavelengths centered at 1588 nm. While the data is taken under the stable locking at the top of each oscillation peak, a large fluctuation sometimes makes the spectrum of peak 2 instantly switch to a single-peak structure like that for peak 1. This suggests that the second highest top in the right of peak 2 in Fig. 4.9 is a degenerate or intermediate mode as the previous study referred to [189].

4.3.6 Pulse duration

The temporal pulse duration for the degenerate signal mode (peak 1) is obtained by the autocorrelation measurement with a Michelson interferometer. Here, an interference fringe via the two-photon absorption in a Si detector (Thorlabs PDA36A) is depicted in Fig. 4.14. The measured FWHM of the trace is 127 fs. When assumed as a sech^2 pulse, the sub-harmonic pulses have a duration of 80 fs [199], corresponding to about 15 optical cycles. The spectral width of degenerate pulses in frequency is 9.6 THz, thus a pulse length of 32.7 fs is expected for a transform-limited sech^2 pulse [199]. I presume that the deviation of the measured duration from that in the transform limit mainly comes from the GVD and chirping on the pump pulses at the power controlling part (HWP:

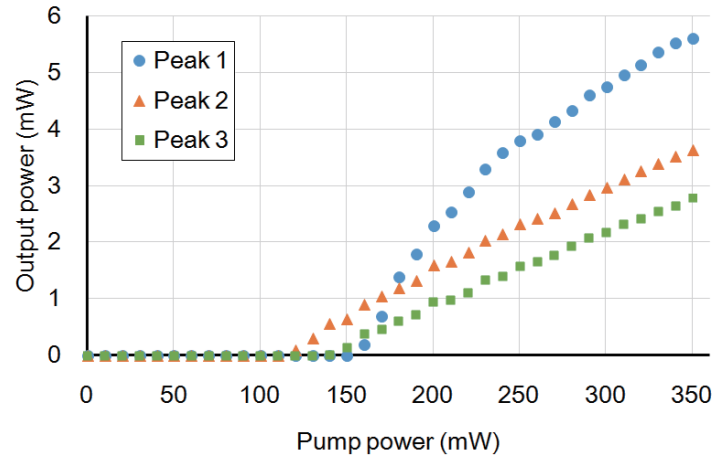


Figure 4.12: Average output powers of the tops of the three oscillation peaks dependent on the pump power. One of the two output couplers with 10% reflection is used to take the signal.

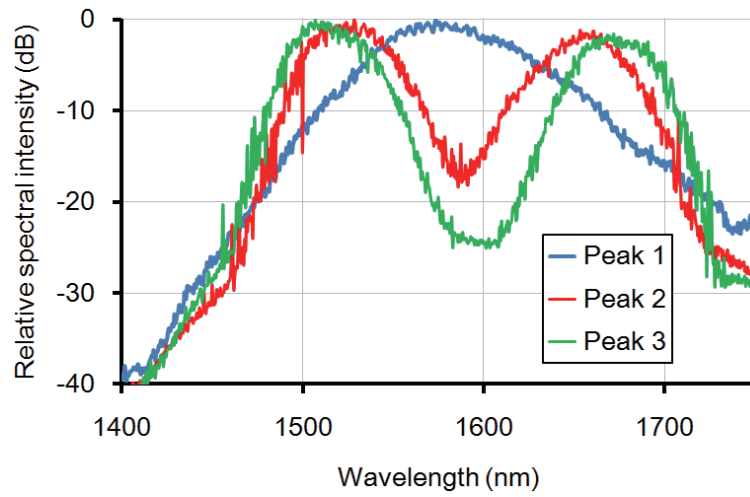


Figure 4.13: Optical power spectra for the three oscillation peaks.

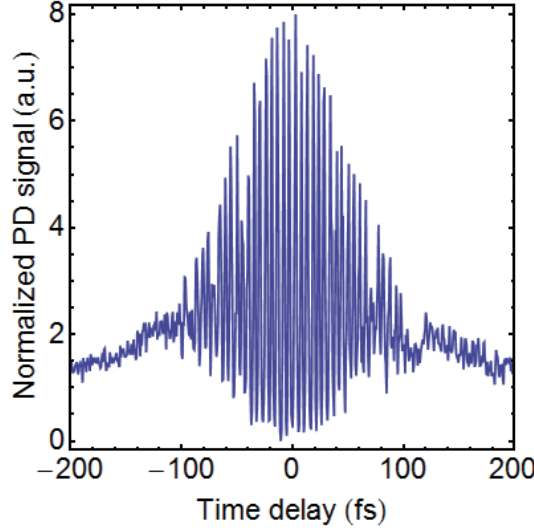


Figure 4.14: Autocorrelation trace of the two-photon absorption for the degenerate OPO pulses.

Thorlabs AHWP10M-980, PBS: Newport UPBS-1). The duration of the pump pulses coming from OC2 has been measured with a GaAsP photodiode (Hamamatsu G6262) and found to be 44 fs, which is much larger than the value in the specification (15 fs).

4.3.7 Coherence property

The ring cavity contains 16 spatially separate signal pulses with the repetition rate 1 GHz. It is expected that the mode-locked pump pulses have a good phase correlation thus there is a good coherence between degenerate OPO pulses, which oscillate with one of the two relative carrier phases 0 and π . It is measured with the unequal-arm interferometer which couples adjacent pulses. The difference of the arm lengths is locked so that the output power of interfered pump pulses is nearly at the maximum, using another channel of the servo controller. Fig. 4.15 shows two examples of patterns of the interferometer output pulses in the degenerate signal mode measured with the fast detector. When two adjacent DOPO pulses have the same phase state, the interferometer output pulse has a high intensity. If they are of different phase states, the output pulse is low-intensity. The period of pulse patterns is about 16 ns, meaning sixteen oscillating DOPO pulses in the cavity. In (a), the arm length is kept so that the interference output has a high visibility. The pulses are detected with an interval of 1 ns, and the low-intensity interfered pulses are of the power level comparable with pulse tails and noise. The power fluctuation high-intensity pulses is up to about 10% to the maximum. The data indicates that the DOPO pulses in the whole ring cavity are well described by the two phase states and keep the phase coherence [187]. Fig. (b) is another example with a detuned arm length hence a lower visibility so that the low-intensity pulses are visible. The pulse intensity

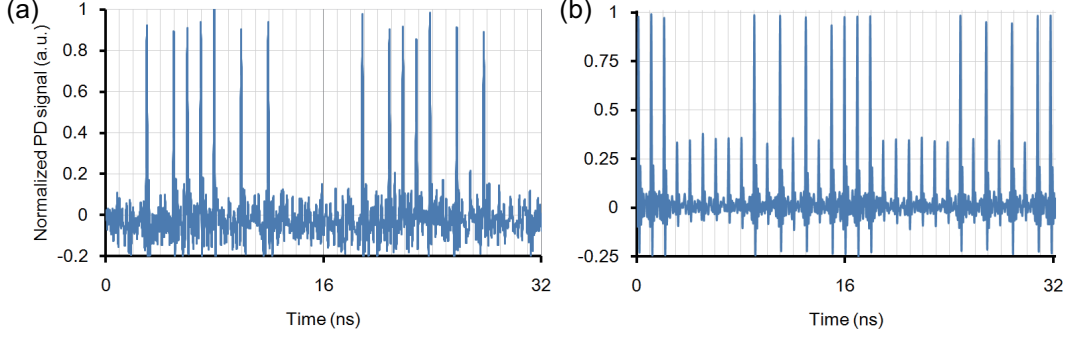


Figure 4.15: The interference output of pairs of adjacent DOPO pulses. (a) A high-visibility example. (b) A low-visibility example. High-intensity pulses come from pairs of in-phase pulses. Low-intensity pulses are because of pairs of out-of-phase pulses. Each pulse randomly takes a relative phase of 0 or π , leading to a random pulse-intensity configuration at every operation.

hence the phase state configuration holds up without a large fluctuation in the average power. The pattern changes with every oscillation, meaning the random choice of binary phases [201] by each pulse.

4.4 Summary

I designed and operated a 16-pulse degenerate femtosecond OPO for a coherent Ising machine. The system has a 4.8 m ring cavity and a pulse repetition rate of 1 GHz. The servo controller with PID feedback can stably lock the cavity length to the tops of the longitudinal oscillation peaks. The telecom-band frequency comb has a 9 THz spectral bandwidth and a peak wavelength of $1.58 \mu\text{m}$. The oscillation threshold for the system with two 90:10 output couplers is 113 mW. The mode-locked Ti:sapphire pump laser has an average output power as large as 1.6 W, thus I can increase the number of output couplers and implement the mutual injection among the DOPO pulses. The degenerate pulses randomly take one of the binary phase states and keep the phase coherence over the whole cavity by self-phase-locking among the comb modes. This enables the time-division multiplexing implementation of the coherent Ising machine, which assigns each spin in the simulated Ising model to binary phase states of each DOPO pulses.

Chapter 5

Demonstration of Coherent Ising Machine with Time-Multiplexed DOPO Networks

In this chapter, I present the results of the two projects for the first-time and second-time experimental demonstrations of the coherent Ising machine based on DOPOs. The first experiment [202] has been conducted in Byer laboratory at Stanford University and in collaboration with Dr. Alireza Marandi. Here, the network of four $2\text{ }\mu\text{m}$ DOPO pulses are implemented with a single ring cavity, and three optical delay lines are used to couple all the pulses. The smallest instance of an NP-hard problem is programmed, and the result has shown no computational error. The second demonstration in RIKEN has been performed with a 16-pulse DOPO of telecom wavelengths. Here, the couplings along with the 1-D ring structure and a cubic graph are implemented with two and three delay lines. The ground states for the Ising models on the ferromagnetic ring, anti-ferromagnetic ring and the anti-ferromagnetic cubic graph have been obtained with probabilities of as high as 99.8 %, 99.7 % and 99.8 %, respectively.

5.1 Background

5.1.1 Short introduction

There are many non-trivial tasks in our daily life and business, such as planning an efficient travel route, doing efficient packing, arranging a good rotating roster and designing a compact electric circuit [5, 27]. They can be modeled as combinatorial optimization problems [11], however, many of them are believed to be computationally difficult. Such problems belong to the complexity classes called non-deterministic polynomial (NP)-complete and NP-hard problems, and it is believed that they require a computational time scaling exponentially with the number of input variables (called problem size). Efficient schemes to compute these problems have been extensively searched for.

One of the most familiar combinatorial optimization problems relevant with physics

is finding a ground state of the Ising Hamiltonian

$$\mathcal{H} = - \sum_{i,j=1}^N J_{ij} \sigma_i \sigma_j - \sum_{i=1}^N h_i \sigma_i. \quad (5.1)$$

Here, $\sigma_i = +1, -1$ is a normalized eigenvalue of a $1/2$ -spin and called an Ising spin, and J_{ij} determines the order and magnitude of magnetic interaction. h_i denotes a magnetic field affecting the energy of each spin. This problem is called Ising problem here, and is important to understand mysterious properties of spin glasses and magnetic disorders. However, the task for planer systems with external fields and for three-dimensional systems has been proven to be NP-hard [3]. Also, their decision problem versions are NP-complete. Many NP-complete and hard problems such as the MAX-CUT problem, graph partitioning problem and some families of SAT problems can be reduced to the Ising problem [23, 203]. Thus, the physical realization of an efficient simulator and computer for the Ising model will be of a wide range of applications.

Meta-heuristic algorithms originating from physics have also been vastly studied to attack these intractable problems. Simulated annealing (SA) [82] is one of the most prevalent and successful schemes in practice. Quantum annealing (QA) [80, 81] has been proposed as a method which can potentially give better solutions than SA. The commercial hardware to physically perform QA has also been quickly developed [93–96], although there is still controversy over its true performance [97]. Adiabatic quantum computation [83, 85] is closely related to QA and based on the Hamiltonians of adiabatic systems. Here, some attempts [87, 88] are made to avoid the transition [86, 89] from a ground state to an excited state mainly due to the closing energy gap between them.

We have recently proposed a computational system [98, 99], called a coherent Ising machine, based on a laser network with mutual injections for the Ising problem. In the system, the circular polarization of each injection-locked laser is regarded as an artificial spin. In addition, the mutual injections between the lasers induce the optical coupling emulating Ising interaction. The Ising Hamiltonian is mapped to the effective total gain per photon in the coupled oscillator system, and the system is expected to self-organize for the minimum gain, meaning the maximum number of intracavity photons. However, it has been found that the complex instances lead to almost the same photon numbers of the two circular modes in some lasers, and this is the major source of computational errors [102]. It is because lasers do not have intrinsic phase-ordering forces in themselves.

5.1.2 Phase transition in DOPOs

The bistable nature of the DOPO field is the key to improve the performance of a coherent Ising machine [103]. Fig. 5.1 shows the schematic of the non-equilibrium phase transition in the distribution function for the complex field amplitude written as α . In a single DOPO pumped below the oscillation threshold, the fluctuation in the component of the real axis (corresponding to $(\hat{a} + \hat{a}^\dagger)/2$) is magnified, while that for the orthogonal component ($(\hat{a} - \hat{a}^\dagger)/2i$) is damped (squeezed vacuum). When the pumping power gets above the threshold, the distribution is divided into the two parts whose phases are

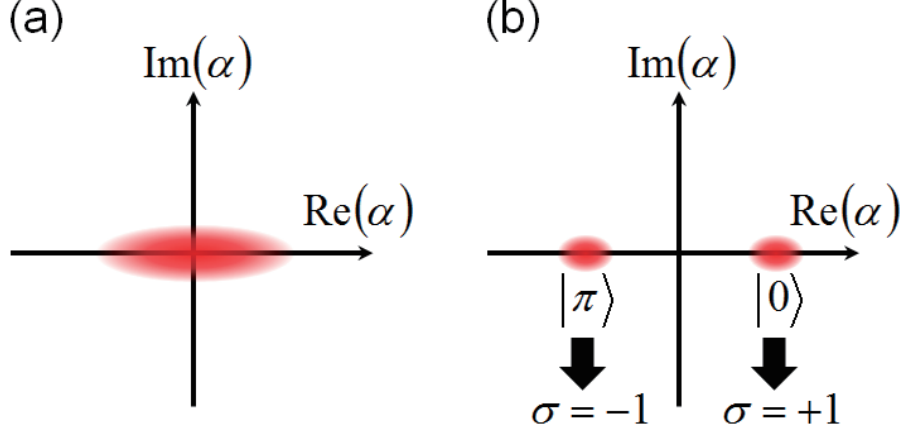


Figure 5.1: Schematic illustration of the optical field for an OPO pumped (a) below the threshold and (b) above the threshold

differed by π . Here, the state synchronizing the pump is written as $\{|0\rangle\} \equiv \{0\}$, and that with the opposite phase denoted by $\{|\pi\rangle\} \equiv \{\pi\}$. The Ising machine assigns $\sigma_i = +1$ to $\{0\}_i$ and $\sigma_i = -1$ to $\{\pi\}_i$ in the DOPO pulse $\#i$.

5.1.3 Gradual pumping scheme of the Ising machine

We have proposed the operational scheme named gradual pumping [100, 202], which helps the system oscillate at the state with the minimum total gain corresponding to the exact or approximate ground states of the mapped Ising Hamiltonian [Fig. 5.2]. Here, the pumping power into the system is slowly increased. In the system, the effective loss landscape is considered to be realized when the mutual injection paths are implemented. When pumped below the oscillation threshold [Fig. 5.2 (a)], the DOPO network has the squeezed vacua only weakly correlating with each other in the real components. When the pumping power is increased and approaches the net oscillation threshold, the state with the minimum gain will oscillate after the phase transition [Fig. 5.2 (b)]. Further rising the pump will lead to deamplification of other states with the gain saturation.

5.2 Experiment on the 4-pulse system

5.2.1 Setup and implementation

Here, I describe the first experimental demonstration of a coherent Ising machine for 4-spin systems with a 4-pulse DOPO [202], which has been conducted in Stanford University. Fig. 5.3 displays the schematic of the system. The system is based on time-division multiplexing with the DOPO pulses running in a single ring cavity. The pump laser (Menlo Systems Orange) is a mode-locked Yb-doped fiber laser emitting pulses with a

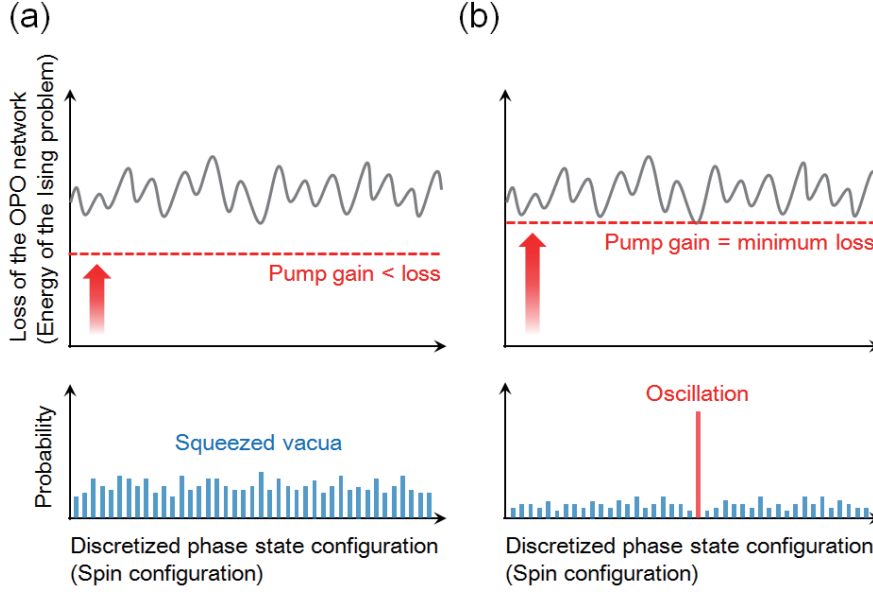


Figure 5.2: Mapped energy and probability landscapes in the DOPO network (a) below the threshold and (b) above the threshold, illustrating the gradual pumping scheme.

duration of about 80 fs, a central wavelength of 1045 nm and a repetition frequency of 250 MHz. A mechanical chopper (CP) is placed in front of the pump laser and periodically blocks the pump beam with a frequency of ~ 1 kHz. This high-speed switching enables many independent trials. Also, the pump beam has a finite spot size of about 1 mm, thus the chopper gives a rise time for the average pump power (10 % - 90 % of the maximum) of 180 μ s. It achieves the gradual pumping. The round-trip length of the ring cavity composed of M1 - M4 are 4.8 m. Thus, it contains four independent degenerate signal pulses at regular spatial and temporal intervals (1.2 m and $T_R = 4$ ns for each). The dielectric mirror M1 transmits 99.8 % of the pump power while reflects 99 % of the signal. The mirrors M3 and M4 are gold-coated concave mirrors with a radius of curvature of 50 mm. These focus the pump and signal beam at the nonlinear crystal and achieve a large parametric gain. The nonlinear crystal is a MgO-doped 1-mm periodically poled lithium niobate (PPLN) with a poling period of 31.254 μ m and put at the Brewster angle. Tuning the cavity length enables the degenerate operation with the type 0 ($e + e \rightarrow e$) quasi phase matching. The degenerate signal pulses [188] have a central wavelength of 2090 nm, a spectral width of 91 nm and a pulse duration of 85 fs.

The couplings between the DOPO pulses are implemented with the three pairs of output and input couplers in the cavity. Each of them has a reflection of $\sim 4\%$ in power of DOPO pulses. It means that the pairs of output and input couplers result in $\sim 4\%$ of field couplings between them. Fig. 5.4 illustrates the couplings given by different delay

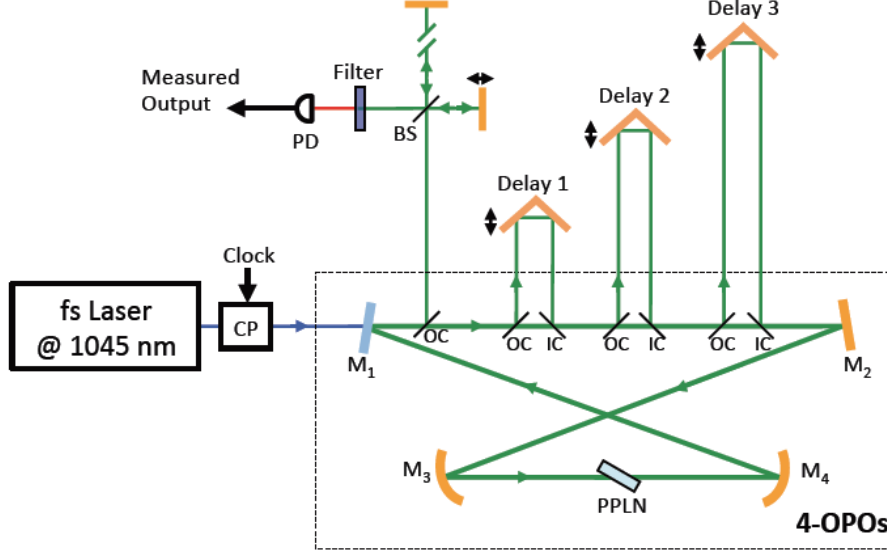


Figure 5.3: A schematic of a coherent Ising machine based on a 4-pulse DOPO. The pump laser is a femtosecond fiber laser with a center wavelength of 1045 nm. The three delay lines implement the optical coupling between the pulses. An unequal-arm Michelson interferometer measures the relative phases of adjacent DOPO pulses.

lines in Fig. 5.3. Delay 1 feeds back the pulses with the shortest temporal delay $T_R = 4$ ns and couples OPO_n to OPO_{n+1} , giving $(J_{12}, J_{23}, J_{34}, J_{41})$. Delay 2 is twice as long as Delay 1 and gives the mutual injections between OPO_n to OPO_{n+2} $(J_{13}, J_{24}, J_{31}, J_{42})$. Delay 3 is for the couplings from OPO_n to OPO_{n+3} $(J_{14}, J_{21}, J_{32}, J_{43})$.

The measurement is achieved with the unequal-arm Michelson interferometer. The path length difference is the spatial interval of the pulses (1.2 m), thus the interferometer output after the long-pass filter gives the relative phases between adjacent DOPO pulses. When an output pulse has high and low intensities, the adjacent pulses interfered are in-phase and out-of-phase, respectively. I write the high- and low-intensity output pulses as [1] and [0] here. We measure both the intensity of each output pulse with a fast detector and their average power with a slow detector. The output coupler for the interferometer has a reflection of $\sim 15\%$.

Fig. 5.5 presents all the possible output pulse patterns measured with a fast detector. The measured intensity configuration of each pattern (e.g. [0000]) is written above the corresponding graph. There are four DOPO pulses oscillating in the cavity, thus the period of the patterns is four times of the repetition period ($4T_R = 16$ ns). Here, we do not have a time reference in the measurement hence we do not distinguish a pulse pattern and its cyclic permutations. Table 5.1 gives all the possible phase states of the four DOPO pulses and corresponding interferometer pulse patterns and average powers. Here, I_m denotes the maximum power in terms of phase states. Considering

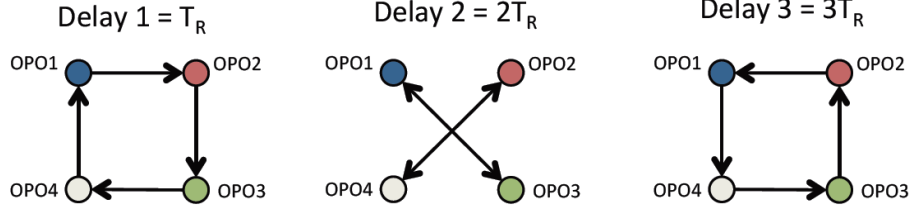


Figure 5.4: Illustration of the couplings between DOPO pulses with the optical delay lines. Delay 1, 2 and 3 give $(J_{12}, J_{23}, J_{34}, J_{41})$, $(J_{13}, J_{24}, J_{31}, J_{42})$ and $(J_{14}, J_{21}, J_{32}, J_{43})$, respectively.

cyclic permutations, we see that the output pulse patterns [0000], [1100], [1010], [1111] originate from 2, 8, 4 and 2 phase states, respectively. On the other hand, the average power can have the three distinct levels $(0, I_m/2 \text{ and } I_m)$ according to the numbers of high-intensity output pulses ([1]s).

We use servo controllers which produce the error signals from the detector readouts with the Pound-Drever-Hall technique [200] and place their proportional feedback to lock the optical paths. The average power of DOPO pulses is harnessed to lock the main ring cavity. The interference output powers of the pump pulses coming out from ICs and the Michelson interferometer are utilized for the delay lines and the interferometer, respectively.

5.2.2 Result

First, we drive the system with the delay lines blocked for a test of the randomness [201] of the binary phase states $\{0\}$ and $\{\pi\}$ in the DOPO pulses. Here, the 4-pulse phase states are expected to be distributed uniformly. The resulting ratio of frequencies of the interferometer output pulse patterns [0000], [1100], [1010] and [1111] reflects the numbers of corresponding phase states hence is $2 : 8 : 4 : 2 = 1 : 4 : 2 : 1$ as seen in Table 5.1. Same applies to that of the output average intensity levels 0, $I_m/2$ and I_m , and it will be $2 : 12 : 2 = 1 : 6 : 1$. Fig. 5.6 (a) presents the slow detector readout in this case. The system is turned on every 1 ms and held for $500 \mu\text{s}$ by the chopper. The low, middle and high levels of the PD output correspond to these expected, i.e. 0, $I_m/2$ and I_m , respectively. The numbers of them in the graph are 5, 34 and 5, which well reproduce the expected ratio. Fig. 5.6 (b) displays the frequencies of the interferometer output pulse trains out of 1000 independent trials. The error of the measured counts for every pattern from the expected is within 20 counts. It also represents the randomness and independence of the binary phase states in the DOPO pulses.

Next, we implement an instance of an NP-hard problem in the system. Here, we introduce all the delay lines and set all the coupling phases to π , i.e. $J_{ij} \in \mathbf{R}$ and $J_{ij} < 0$ with the servo controllers. The OCs and ICs for the delay lines all give the same reflection rate, thus the well-aligned system implements almost the same magnitude of

Table 5.1: Measurement of phase states

Phase state	Interferometer pulse pattern	Average intensity
$\{0000\}$	[1111]	I_m
$\{\pi 000\}$	[1001]	$I_m/2$
$\{0\pi 00\}$	[0011]	$I_m/2$
$\{\pi\pi 00\}$	[1010]	$I_m/2$
$\{00\pi 0\}$	[1001]	$I_m/2$
$\{\pi 0\pi 0\}$	[0000]	0
$\{0\pi\pi 0\}$	[0101]	$I_m/2$
$\{\pi\pi\pi 0\}$	[1100]	$I_m/2$
$\{000\pi\}$	[1100]	$I_m/2$
$\{\pi 00\pi\}$	[0101]	$I_m/2$
$\{0\pi 0\pi\}$	[0000]	0
$\{\pi\pi 0\pi\}$	[1001]	$I_m/2$
$\{00\pi\pi\}$	[1010]	$I_m/2$
$\{\pi 0\pi\pi\}$	[0011]	$I_m/2$
$\{0\pi\pi\pi\}$	[0110]	$I_m/2$
$\{\pi\pi\pi\pi\}$	[1111]	I_m

the couplings. It emulates the uniformly anti-ferromagnetic Ising model of four spins in the tetrahedral lattice, and corresponds to the smallest instance of the NP-hard MAX-CUT problem in cubic graphs. The solutions of the instance are two $\{0\}$ s and two $\{\pi\}$ s, which are shown as the blue entries in Table 5.1. Also, it exactly corresponds to the output pulse patterns [0000] and [1010]. Fig. 5.7 (a) depicts the slow detector output for the NP-hard instance. Only low and middle intensity levels are seen. Their frequencies 13 and 29 out of 42 trials nearly correspond to the expected ratio 1:2 for 0 and $I_m/2$ seen in Table 5.1. However, $I_m/2$ corresponds to both answer and non-answer states, thus we need to see the fast detector signal to evaluate the success rate in this case. Fig. 5.6 (b) shows the necessary histogram of the interferometer pulse patterns out of 1000 runs. The measured patterns are distributed to only the answer states [0000] and [1010], and no computational error is obtained. It indicates the potential of the precisely tuned system for more complex problems.

5.3 Experiment on the 16-pulse system

5.3.1 Implementation

The computational possibility of the coherent Ising machine based on pulsed DOPOs is further investigated using another medium-scale system. Here, we continue to adopt a free-space femtosecond pulsed DOPO. The system is not subject to significant group

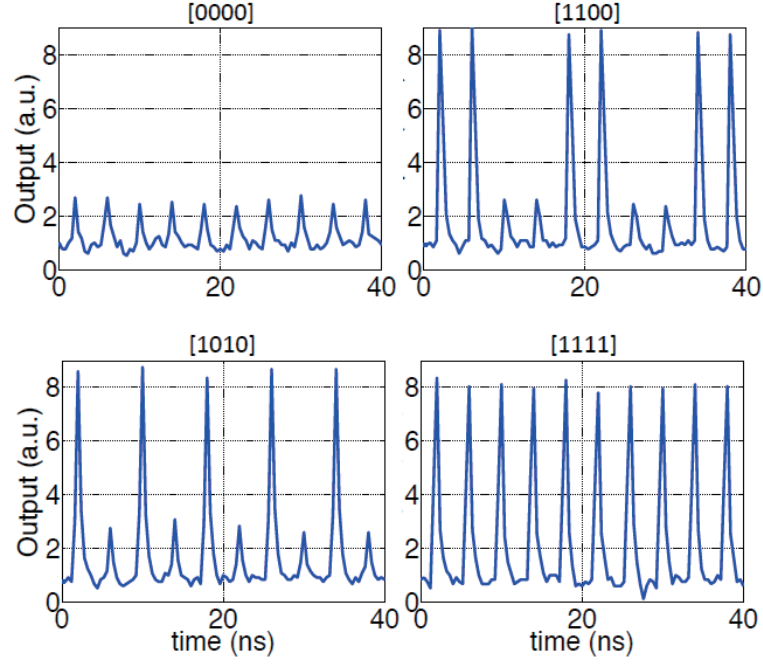


Figure 5.5: All the possible pulse patterns of the output of the unequal-arm Michelson interferometer in the 4-DOPO system. We do not have a time reference in the measurement hence we do not distinguish a pulse pattern and its cyclic permutations.

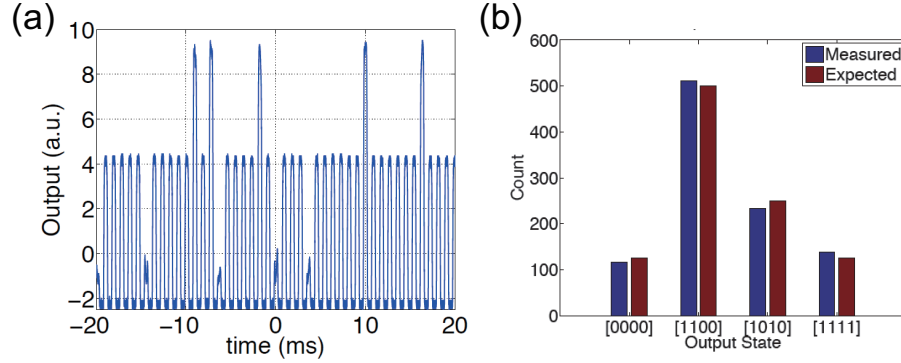


Figure 5.6: (a) Slow detector readout and (b) histogram of the measured interferometer output pulse patterns for the system with no mutual injection. The expected frequencies of the low, middle and high intensities of the detector signal in (a) is 1:6:1. That for the output pulse trains [0000], [1100], [1010] and [1111] in (b) is 1:4:2:1.

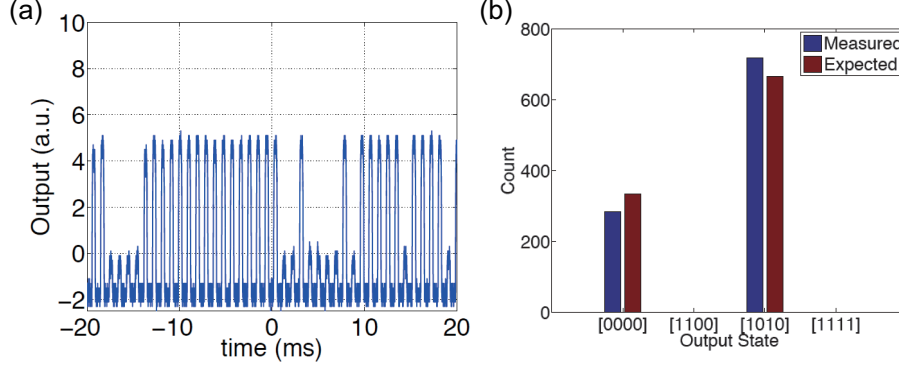


Figure 5.7: (a) Slow detector readout and (b) histogram of the measured interferometer output pulse patterns for the system with out-of-phase couplings between all the DOPO pulses via the three delay lines. Here, the MAX-CUT problem for the four-node complete graph is programmed in the system. The expected frequencies of the low, middle and high intensities of the detector signal in (a) is 1:2:0. That for the output pulse trains [0000], [1100], [1010] and [1111] in (b) is 1:0:2:0. No erroneous pattern is obtained in 1000 independent trials as seen in (b).

velocity dispersion and third-order nonlinear effects [199] which might be strong in other technical candidates such as optical fibers and planer wave circuits, and hence allows a simple setup. Fig. 5.8 depicts a schematic of the 16-pulse DOPO Ising machine studied here. Here, we use a mode-locked Ti:sapphire femtosecond pulse laser with a repetition rate of 1 GHz (Laser Quantum, Taccor 10s) for the pump so that the system contains 16 resonating DOPO pulses in the ring cavity with the same length as that utilized in the previous section (4.8 m). The spatial and temporal interval between the pulses are 30 cm and 1 ns. The central wavelength of the pump is 794 nm, whose subharmonic is in the telecom band [189]. The pump pulse duration is specified as 14 fs at the output shutter, while the evaluated pulse length with an autocorrelation measurement is 44 fs. It is possibly because of the group velocity dispersion and chirping at the power controlling part composed of a half wave plate (HWP) and polarizing beam splitter (PBS). The mirror M0 is a dielectric mirror which has a high transmission rate for the pump of $T > 90\%$ in 750 - 850 nm and a high reflection rate for the signal of $R > 99.8\%$ in 1500 - 1700 nm. The spot size and divergence of the pump beam is matched to the short cavity comprised of the two concave mirrors M1 and M2, to minimize the oscillation threshold of the DOPO. The radius of curvature of M1 and M2 is 50 mm. The nonlinear crystal placed at Brewster angle is a 1 mm thick MgO-doped PPLN with a poling period of $20.4 \mu\text{m}$, which meets the type-0 ($e + e \rightarrow e$) quasi phase matching condition for 1588 nm at 38 degree Celsius. All the input and output couplers (ICs and OCs) are 1 mm thick plate beamsplitter with a reflection of $R \sim 10\%$ for the sub-harmonic wavelengths. PD1 is a slow detector for the average signal power and is used for monitoring and cavity stabilization. The main servo controlling system (Controller 1, TEM Messtechnik,

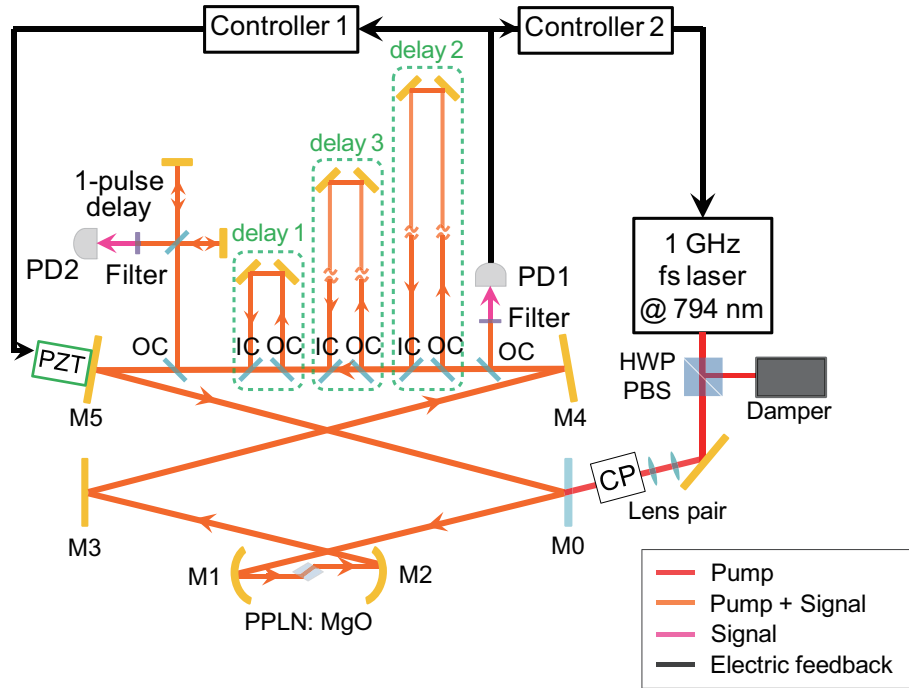


Figure 5.8: A coherent Ising machine based on a 16-pulse DOPO. The pump laser is a Ti:sapphire femtosecond pulse laser with a center wavelength of 794 nm. The two servo controllers are used to operate the system stably under the operation of the chopper.

LaseLock Digital) places a PID feedback based on the Pound-Drever-Hall error signal to the cavity length via the piezoelectric transducer (PZT). The mechanical chopper (CP) enables automated and independent trials, while the resulting abrupt changes in the PD output induce some instability in the cavity locking by Controller 1. We thus use another servo controlling circuit with a very low cut-off frequency (Controller 2). Here, we put another small and relatively fast modulation of 20 kHz on the fast PZT channel of the pump laser, then the circuit gives the proportional feedback with the fast error signal to the slow PZT channel. The measured central wavelength and -3 dB spectral width of the strongest degenerate signal mode is 1574 nm and 80 ns. Its pulse duration is 80 fs. Each pair of an IC and OC establishes an optical delay line and provides $\sim 10\%$ field couplings between the DOPO pulses. Delay 1 is 30 cm-long and gives the couplings from OPO_n to OPO_{n+1} and J_{nn+1} . Delay 2 is 4.5 m-long and gives the couplings from OPO_{n+1} to OPO_n and J_{n+1n} . Delay 3 is 2.4 m and provides the couplings between OPO_n and OPO_{n+8} , corresponding to $J_{nn+8(\text{mod } 16)}$. The oscillation threshold of the system with only PD1 and the interferometer is 113 mW, and that including the three delay lines is 334 mW. The unequal-arm interferometer is again for the measurement of the relative phases between adjacent signal pulses via both a slow and fast detector. The servo controllers of the same model as Controller 1 also lock the interferometer and delay lines with the interference of the pump pulses, although they are omitted from the figure for simplicity.

5.3.2 Result

Random phase states of each pulse

I show the result of the experiment on the 16-pulse OPO Ising machine. Here, I drive the system with the DOPO pulses in an even frequency state, which keeps the fixed carrier phase with every round trip. In this case, the number of high-intensity pulses of the interferometer output never fails to be an even number. First, I introduce delay 1 and 2 and drive the system with them blocked. The pump power is 2.5 times the oscillation threshold. Fig. 5.9 (a) displays an example of the interferometer output pulse patterns measured with the fast detector. The period of 16 pulses (~ 16 ns) in the pattern means the system contains as many pulses. The binary intensity levels indicate that the signal pulses are degenerate. An even number of high-intensity pulses (eight here) suggests that the DOPO pulses have an even frequency state. The power fluctuation of about 5 % mainly reflects that of the pump laser and the fine structure of the cavity length dependence of the DOPO pulse intensity. I observed various pulse patterns in an even frequency state via 100 automated measurements.

When we consider to test the randomness of the binary phase states, the possible output pulse patterns is too many to list. Here, I use the average power of the interferometer output under the chopping with a frequency of 60 Hz. Fig. 5.9 (b) is the average power normalized by the twice of the mean of the DOPO signals (with the chopper open). Here, the number of high-intensity pulses are even thus the normalized average power is discretized to $n/8$ ($n = 0, 1, \dots, 8$). The change in the average power at restarts

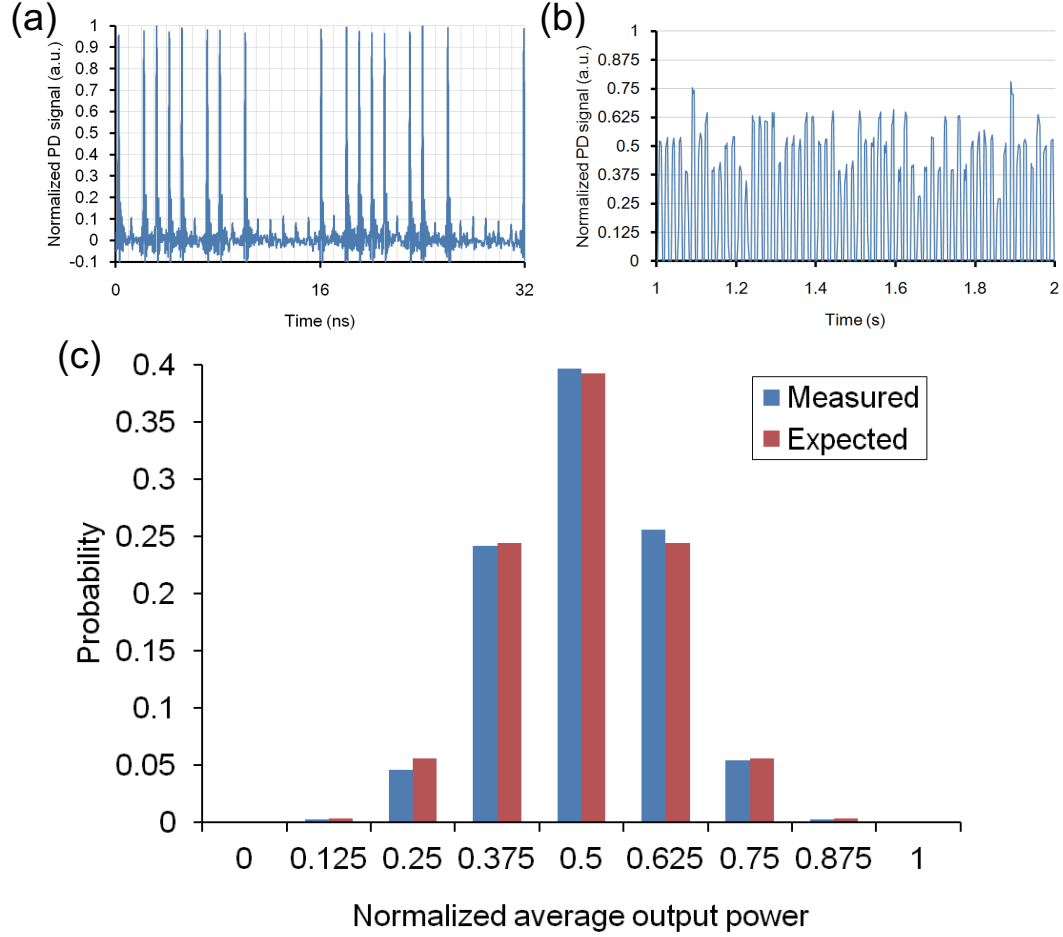


Figure 5.9: Detector readouts for the system without the mutual injection. (a) An example of the interferometer pulse patterns measured with the fast detector. (b) The average output power under the chopping with a frequency of 60 Hz. (c) Distribution of the average output power out of 1500 trials.

is seen, indicating that the DOPO pulses are damped at each blocking of the pump by the chopper.

5.9 (c) presents the probabilities of detecting the normalized output power levels out of 1500 independent trials. The measured data is close to that in the case of random phase states calculated by the brute-force counting. The observation here supports the randomness and independence of the binary phase states of each DOPO pulse.

Phase locking by injection with a single delay line

Next, I introduce the shortest delay line and run the system without the chopping. 5.10 (a) and (b) depict the fast detector outputs of the signal interference in this case. Tuning and locking the length of the delay line with the pump interference enable us to obtain the DOPO pulse with the in-phase and out-of-phase order at steady states as represented in 5.10 (a) and (b), respectively. The locking points for the in-phase and out-of-phase order appear alternately because the center wavelength of the pump is about twice longer than that of the sub-harmonic mode. 5.10 (c) is a slow detector readout of the signal interferometer output when the delay path length is scanned with a PZT. The high- and low-level signal correspond to the states in the in-phase and out-of-phase order (5.10 (a) and (b)). The maximum path detuning of $12\ \mu\text{m}$ is computed by the specification of the PZT. It corresponds to about 7.6 cycles for the carrier wave at the sub-harmonic wavelength $1.574\ \mu\text{m}$, giving a good agreement with the number of interference cycles in the figure. The slopes in the graph are possibly because of different extents of overlaps between the pulses for different locking points, in terms of the peak amplitudes and chirping. The graph has been obtained by decreasing the detuning, while that acquired by increasing it gives the levels corresponding to the erroneous states referred to later.

Phase states in the case of two delay lines

Then, I unblock delay 1 and 2 and implement the mutual injections which bidirectionally couple the DOPOs along with the one-dimensional ring. The 60Hz-chopping of the pump is turned on, and the probability to obtain a ground state of the 1-D ring Ising Hamiltonian (success probability) is evaluated for both the ferromagnetic and anti-ferromagnetic cases. Here, the locking points of the delay lines significantly affect the performance probably due to the residual coupling phases arising in each frequency component when the resonator pulses and the feedback pulses do not completely overlap. Fig. 5.11 shows the examples of the fast detector outputs from the interferometer in the case of in-phase mutual injections emulating the ferromagnetic Ising model ($J_{ii+1} \approx J_{i+1i} > 0$). I add an schematic mapped spin configuration expected from each pulse pattern. The phase states with the global in-phase order identified by Fig. 5.11 (a) are the most probable, and the power fluctuation here is smaller than that seen in the unidirectional injection case (Fig. 5.10 (a)). On the other hand, some excited phase states are detected with a finite probability. Major erroneous states have two domains of in-phase DOPO pulses corresponding to two ferromagnetic domains as shown in Fig. 5.11 (b) and (c). The real-time observation of the fast detector output indicates that patterns similar to Fig.

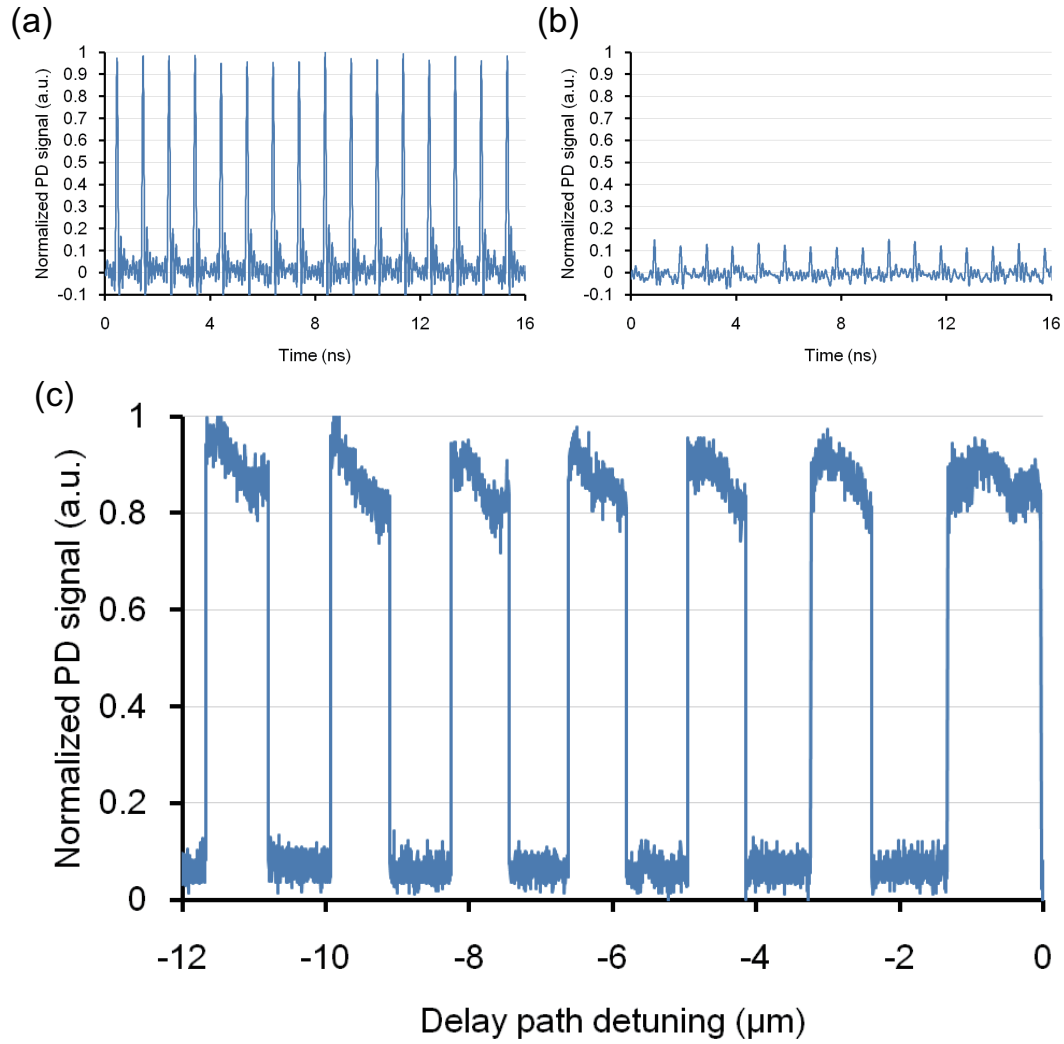


Figure 5.10: The temporal interferometer output power for the system with a single delay line. (a) Fast detector readout in the case of in-phase unidirectional couplings. (b) That for out-of-phase unidirectional couplings. (c) Slow detector readout under the scanning of the delay path length.

5.11 (b) are dominant when the success probability is high. It suggests that the deviation of the coupling phase from zero is very small in each delay line hence the phases of the boundary pulses are stable. Meanwhile, the error rate depends on the locking points and can be relatively high. In this case, we see pairs of sequential output pulses whose powers are not binary, as shown in Fig. 5.11 (c). Their powers also vary in time, indicating that the phase of the pulse at the domain boundary gets unstable due to the residual coupling phases in the delay lines. Same applies also to the case of the out-of-phase mutual injections (emulating the anti-ferromagnetic Hamiltonian $J_i i+1 \sim J_{i+1} i < 0$) as shown in Fig. 5.12. Fig. 5.12 (a) comes from the stablest phase-state configuration with the global out-of-phase order, while major excited phase states like in Fig. 5.12 (b) indicate two anti-ferromagnetic domains. When the locking points are not good ones, the phases of the boundary pulses rotate and output peak powers around them get non-discrete.

Success probability in emulation of one-dimensional Ising model

The ground states of the emulated one-dimensional Ising model can be identified by the average power measured with the slow detector, as seen in the previous figures. In the ferromagnetic case, the only interference pulse pattern giving the maximum average power (I_{\max}) corresponds to the two ground states, and the other states all denote excited states. When the couplings are anti-ferromagnetic, all the interference peak powers hence the average power gets minimum ($I_{\min} \sim 0$) in the case of the two ground states. The average power difference between the answer and non-answer states is at least $(I_{\max} - I_{\min})/8$, thus we can tell apart a success and failure as done in Fig. 5.9 (b) and (c). I take the data for 1200 trials in 10 times (2 s for each record) for both the ferromagnetic and anti-ferromagnetic cases and estimate the success probabilities. The path length of the interferometer is locked to the one where the average pump power is maximum during all the measurements.

Fig. 5.13 (a) presents the normalized average interferometer output power of the signal when the ferromagnetic 1-D Hamiltonian is programmed in the system. The maximal level obtained by each restart corresponds to I_{\max} and fluctuates by less than $\pm 5\%$ to the mean level, except for the last peak. Its level is less than 0.875 thus denotes an error. However, it originates from the instant degradation of the visibility of the interferometer due to environmental noise. Fig. 5.13 (b) shows the average power of the pump interference. Here, we see that the last two peaks give lower visibilities than the other ones. Such errors are detectable and do not reflect the essential performance of the machine, thus we discard them. Also, a peak where its power relaxes onto the optimum by tuning off is counted as a success. Under the good locking condition, we have obtained 1193 successes and 7 failures out of 1200 trials. 5 failures have been found to be due to low visibilities of the interferometer, thus the estimated success probability is $1193/1195 \sim 99.8\%$.

Fig. 5.14 (a) depicts the average signal output power for the anti-ferromagnetic case. The PD signal here is normalized by the maximum level in the ferromagnetic case. The level of the arrowed peak is higher than the others by ~ 0.1 thus this peak is detected as an error. The corresponding average pump interference output is shown

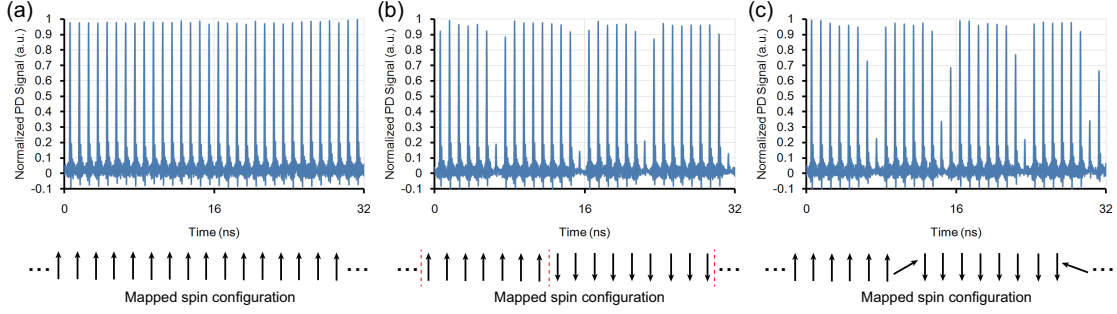


Figure 5.11: Fast detector readouts of the interferometer output for the 16-DOPO pulse system with the bidirectional in-phase couplings in the form of the one-dimensional ring. The performance depends on the temporal interference between the cavity pulses and injected pulses. (a) The stablest state corresponding to the ground state of the ferromagnetic Hamiltonian. (b) An excited state with two domains of in-phase pulses. (c) An excited state seen when the locking points of the delay lines are not good. Finite residual coupling phases rotate the phases of the boundary pulses and make the output peak powers non-discrete around them. The mapped spin configuration for each output is added.

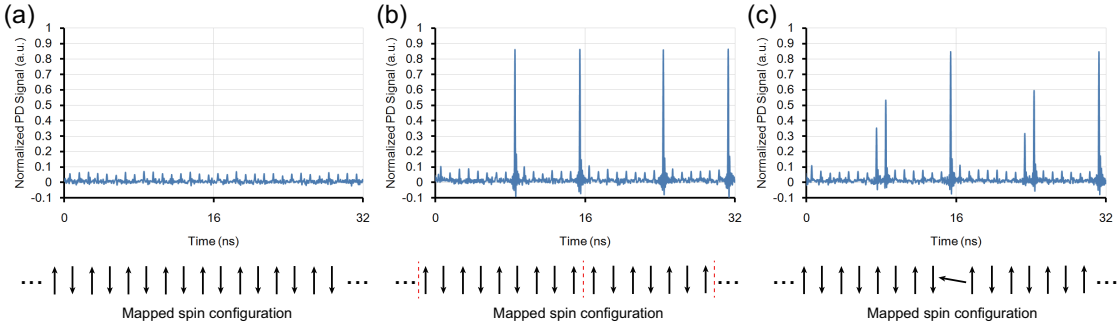


Figure 5.12: Fast detector signal of the output for the 16-DOPO system with the bidirectional out-of-phase couplings in one dimension. (a) The state with the minimum gain, corresponding to the ground state of the anti-ferromagnetic Hamiltonian. (b) An excited state with two clusters of out-of-phase pulses. (c) An excited state for the case of bad locking points of delay lines. The output peak powers are not binary around the boundary pulses. The mapped spin configuration for each output is added.

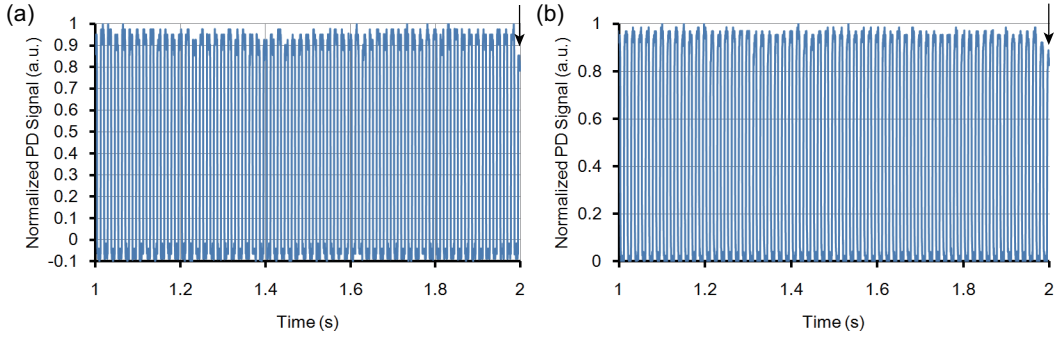


Figure 5.13: An example of the normalized slow detector readout for the (a) signal and (b) pump interference in the case of the emulation of the 1-D ring ferromagnetic Ising model of 16 spins. The peaks around the maximum level in (a) correspond to the phase state configuration with the global in-phase order hence one of the ground states of the ferromagnetic Ising model. The power fluctuation of them is about 5% to the mean thus the ground states can be detected with the average power. The arrowed peak in (a) is a possible error, however, it can be seen in (b) that it is just due to a sudden degradation of the visibility of the interferometer by environmental noise. Such inessential and few errors are omitted in the evaluation of the success probability.

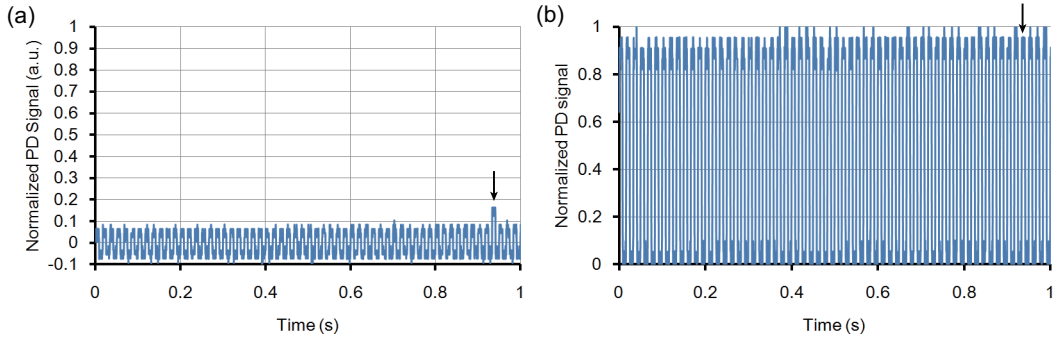


Figure 5.14: An example of the slow detector readout for the (a) signal and (b) pump interference in the case of the emulation of the 1-D ring anti-ferromagnetic Ising model of 16 spins. The PD signal is normalized by the maximum power in the ferromagnetic case. The arrowed peak with a relatively high level in (a) is counted as an intrinsic error because the corresponding power level of the pump interferometer output is as high as the other ones.

in 5.14 (b). Here, the visibility of the pump interference for the erroneous peak is not bad, meaning that this peak is counted as an intrinsic error occurring in the system. In the anti-ferromagnetic case, we have achieved 1196 successes and 4 failures. Here, no error due to the interferometer is detected, thus the success probability is estimated $1196/1200 \sim 99.7\%$. It suggests that the machine can accomplish almost the same and high rate of success regardless whether the mutual couplings are in-phase or out-of-phase.

Computation on a cubic graph case

Finally, delay 3 is introduced and all the delay lines are opened with their coupling phases π . Fig. 5.15 (a) displays the graph implemented in the system. Here, the couplings along with the diameter chords are added to the previous 1-D ring graph. This is one of the cubic graphs (or 3-regular graphs) where each node is connected to three other nodes with as many edges. The anti-ferromagnetic Ising problem programmed here is an NP-hard instance, because that on cubic graphs is NP-hard due to its equivalence to the MAX-CUT problem. The pump power is set to 900 mW, being 2.7 times the oscillation threshold. The blade of the chopper is changed so that it can switch the machine with 20 Hz.

5.15 (b) presents the fast detector signal for the interferometer output corresponding to the ground states of the problem. The ground states forms two anti-ferromagnetic domains including eight spins and have two frustrated couplings at the boundaries between them. When the numbering of the spins (i.e. high-level pulses in Fig. 5.15 (b)) is considered, the sixteen spin configurations are counted as the ground states. These cannot be identified from the average power obtained by a slow detector, thus the fast detector signal is automatically and repeatedly measured with a programmed oscilloscope. Here, each measurement is locked to the trigger signal from the chopper with a constant time delay. In addition, time intervals more than $1/20 = 0.05$ s are artificially introduced between measurements so that the scope can record the results of different trials for different measurements.

The computation is performed with the system in the enclosure of black hardboards. With the optimized locking points for the main cavity and delay line lengths, the system has given ground states for 998 times out of 1000 measurements, meaning a success rate of 99.8 %. Fig. 5.16 depicts the interferometer outputs obtained as the two failed cases. Both are ones of the 34 local minima. Fig. 5.16 (a) reflects $J_{n \ n+8(mod\ 16)}$ and the corresponding state has six frustrated couplings. Fig. 5.16 (b) indicates the anti-ferromagnetic order along with the 1-D ring and gives eight frustrated edges along with the diameter chords. These results of local minima mean that the interaction between artificial spins works well also in the cases of failure.

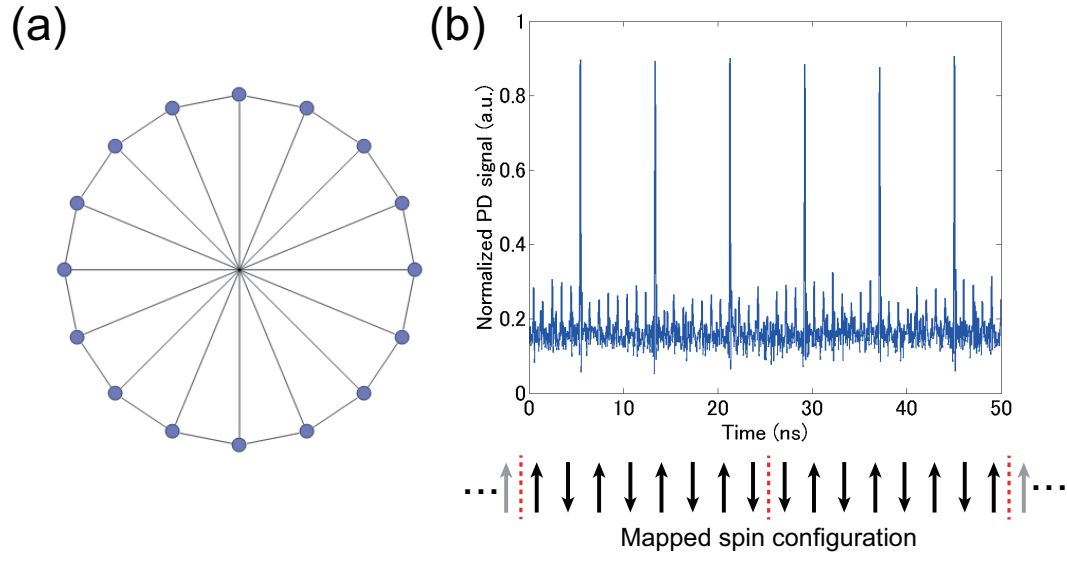


Figure 5.15: (a) The cubic graph implemented in the system with the three delay lines of 0.3, 2.4 and 4.5 m. (b) Fast detector signal of the interferometer output corresponding to the ground states of the anti-ferromagnetic Ising problem on (a). A mapped spin configuration along with the spatial pulse sequence in the ring cavity is added. Red dashed lines denote the frustration between adjacent artificial spins.

5.4 Discussion

Erroneous states

Here, I discuss possible reasons for the erroneous states of the system. First, the residual coupling phases depending on the lengths of the delay lines seem to be probable factors, as discussed with the experimental data for the 1-D case. Here, the frequency components with phase deviations can also resonate in the cavity and repeatedly pass through the delay lines. The effective phase deviations in the total pulse system can get larger than that in the single delay line, and the erroneous components can be amplified. Thus, increasing the number of delay lines might enhance the error. To achieve a fine tuning of the locking point, we have to adjust the set point of the error signal in the servo controlling system.

Second, the power fluctuation in the pump pulses can vary the timing of the oscillation of each DOPO pulse. This can break down the mapping protocol of the Ising machine around the oscillation and result in getting a local minimum dominated by the pulses which oscillate early. A well-stabilized pump laser is indispensable for a good performance of the system.

Working principle

I have shown the good experimental capabilities of the two time-multiplexed Ising machines with essentially the same, simple implementation. Here, considering the prospect for high-performance computing of large-scale and complex problems, it is interested in whether the systems have any quantum computing ability. Unfortunately, it is currently difficult to state that the present systems utilize quantum effects other than quantum noise for the efficient search for the mapped ground states, because implementing a delay line with a pair of beamsplitters never fails to introduce some loss for the signal photons. I have shown in Chapter 3 that the amplitude feedback ratio needs to be large ($\gtrsim 0.5$) to keep the quantum correlation between the DOPO fields, and that the losses in the DOPOs and mutual injection paths have to be small for the system to hold coherent superposition components. On the other hand, the amplitude feedback ratios to the out-coupling flux for each delay line are $\sqrt{0.04} \sim 0.2$ (4 DOPOs) and $\sqrt{0.1} \sim 0.31$ (16 DOPOs). In addition, the actual effect of the feedback is smaller due to the additional losses of the readout part, detector in the main cavity and the input couplers (ICs). These losses induce the dephasing of the coherent superposition components [157] and also degrade the magnitude of squeezing [122]. Nevertheless, the story above is limited in the continuous-wave and single mode case. Broadband DOPO pulses have numerous frequency modes which are phase-locked to each other [184, 185], and such correlated modes [204] may cooperate to attack the problem in a non-trivial way. Nonetheless, the experiment so far is considered to be in the optical computing regime [205], and pursuing the quantumness of the machine by closing the system is an important direction. Fig. 5.17 presents a proposition of replacing a cavity mirror with a partially transmitting one and introducing an empty ring cavity as a closed delay line.

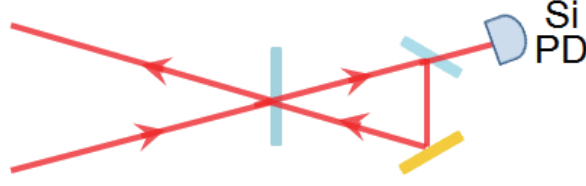


Figure 5.17: A possible implementation for a closed delay line. It replaces a cavity mirror (M3, 4 or 5 in Fig. 5.8) with a partially transmitting mirror. The transmitted pulses are fed back with a short ring cavity. The cavity length is locked with the resonance of the pump beam detected by the Si PD.

5.5 Conclusion

We have build time-multiplexed DOPO networks working as coherent Ising machines for the first time. The machines are based on femtosecond pulsed DOPOs, and they contain independent but identical signal pulses corresponding to as many artificial spins in a single ring cavity. Pairs of input and output couplers introduce the delayed mutual couplings between the DOPO pulses. The first system composed of 4 signal pulses at $2\ \mu\text{m}$ is applied to the NP-hard instance on the smallest cubic graph, and has shown no computational error in 1000 trials. The second system has 16 pulses at $1.57\ \mu\text{m}$ and its performance has been investigated for the one-dimensional ring and an NP-hard cubic-graph instance. The result has given the success probabilities more than 99.7% for both the ferromagnetic and anti-ferromagnetic ring. It indicates no intrinsically erroneous factors dependent on the order of coupling (in-phase or out-of-phase). The machine has kept a success probability of 99.8 % also for the case of a cubic graph and the anti-ferromagnetic couplings. This suggests that we can realize an optimized condition where adding delay lines does not significantly accumulate the error due to their instability. The proof-of-principle result has shown a good possibility of the application of the system to more complex problems, and there has already been propositions for next steps, such as improving the programmability with a measurement-feedback technique [206] and increasing the number of oscillators with the fiber technology [202].

Chapter 6

Conclusion

6.1 Summary

A coherent computing system or coherent Ising machine [98, 99, 103] is referred to as a coupled oscillator network coupled with mutual injections emulating the Ising model. In this dissertation, I have theoretically and experimentally studied the machine based on degenerate optical parametric oscillators (DOPOs), whose binary phase states can be utilized as artificial spins. On the theoretical side, it is important if the machine can have any quantum state and effect which possibly contribute to quantum speedup compared to digital computing algorithms. Here, I have developed the quantum mechanical model for the DOPO network coupled with mutual injections based on the positive P representation [107, 108], and numerically investigated the system of two DOPOs with out-of-phase mutual injections. In this model, I explicitly consider the signal field in the mutual injection path between the two DOPO facets as a cavity mode. When the system is in the limit where the damping in the mutual injection path is sufficiently fast, the injection terms in the stochastic differential equations are linear with respect to the field variables, as in the previous phenomenological model [103]. The stochastic simulation has been conducted under a small noise parameter and the gradually increasing pumping rate from below to above the threshold. The result has shown that small incoherent intracavity loss rates are indispensable in quantum effects in the system. When the incoherent loss in the injection path is of the same order as the coherent transmission rates at the DOPO facets, the signal fields in the two DOPOs have the quantum correlation in terms of the squeezed quadrature amplitude $\hat{p} = (\hat{a} - \hat{a}^\dagger)/2i$. This indicates the entanglement between the two DOPO fields. When the loss of the injection is smaller than the transmission, the two intracavity fields can show weak coherent superposition components via the fringes in the distribution functions for \hat{p} . The superposition components with a small noise parameter and under a relatively non-transient has not been expected by the previous relevant studies on a single DOPO [125, 162]. It suggests that the mutual injection path storing the squeezed vacuum is simple realization of the squeezed heat bath or squeezed reservoir [123], which suppresses the decoherence on the superposition components. Such an effect can play a role in other systems such as

nano- and opto-mechanical devices and superconducting circuits as well as in the Ising machine.

On the experimental side, I have achieved the first-time and second-time experimental demonstrations of the coherent Ising machines based on degenerate optical parametric oscillators in collaboration with Dr. Alireza Marandi at Stanford University. The system is based on the time-multiplexed DOPO network which is composed of femtosecond DOPO pulses [188, 189] running in a single ring cavity. Each DOPO pulse randomly takes one of the binary phase states with their phase difference being π [201], and these states are utilized as artificial spins. Also, the signal pulses keep the phase coherence [187] allowing the interference between different pulses. Mutual injections between the DOPO pulses are implemented by the optical delay lines with pairs of input and output couplers placed in the resonator. We have built the first system containing four DOPO pulses at $2\ \mu\text{m}$ and three delay lines which introduce all the possible couplings between them. It has been applied to the instance of the NP-hard MAX-CUT problem on the smallest cubic graph, and the result has shown no computational error out of 1000 trials. Next, I have constructed another system with 16 signal pulses at telecom wavelengths. Here, I have realized the couplings effectively aligned in the periodically bounded one-dimensional ring and a cubic graph with two and three delay lines, respectively. The system has been applied to the ferromagnetic and anti-ferromagnetic 1-D ring and the NP-hard anti-ferromagnetic cubic graph instances. Despite some instability of the Ti:sapphire pump laser, the system has found ground states of all the corresponding Ising spin systems with probabilities more than 99.7 %. The result suggests that the system does not give significant intrinsic errors originating from the change in the order (i.e. sign) of the couplings and adding delay lines, showing a big potential of this machine for intractable problems.

6.2 Future prospects

The studies on coherent computing systems are getting more and more extensive. There has already been a proposition to improve the programmability of the machine using the effective couplings between the signal pulses via a measurement-feedback technique [206]. Also, the prospect for applying the fiber technology to this machine expects the realization of the systems with 1000 and 10000 artificial spins [202]. Numerical benchmarking on such large systems with a semi-classical model expects that the Ising machine shows a better performance than a well-known approximation algorithm based on semidefinite programming which assures the worst approximation ratio of 87.8 % [103]. On the other hand, both theoretical and experimental evidences in terms of its working principle are still desired. Considering the simulation result in this thesis, it is possible that the current experimental systems do not have quantum correlation between DOPOs or coherent superposition components in its states due to large losses of the system, in spite of their promising performances. Also, there is a comment that it will not be in the quantum computing but optical computing regime [205]. Possible objections to this story are quantum correlation (discord) in phase-locked coherent states

shown in this thesis and that among the massive comb modes in DOPO pulses. Quantum mechanical properties of the pulsed photonic states in the machine may be explored both theoretically and experimentally. At the same time, a more closed system may be considered for both free-space and fiber-based cases to pursue its quantumness. I have proposed an example of the implementations of closed feedback lines. In addition, a well-designed measurement-feedback algorithm might make use of quantum correlation in the coherent states and possibly exert a good efficiency. In the meantime, when the system is considered as an optical or semi-classical computing device, how good is the performance limit of the Ising machine? For example, the theory on coherent feedback control [207–209] can treat oscillator networks with linear quantum feedback. Does such a framework give any properties of the Ising machine in terms of its performance? Or, does the theory on quantum and chaotic systems [210] provide some knowledge about the machine? Can we apply a quantum mechanical simulation scheme like Monte-Carlo wavefunction method [211] to this machine and compare the result with that of the semiclassical benchmarking? There are various directions to develop and study the coherent computing systems, and I hope that this thesis might inspire and help the arising projects.

Appendix A

Simulation Result of the Two-DOPO System with Statistical Convergence

Here, I show the various data from the simulation on the two DOPOs with the mutual injection. They are the statistical averages of 200000 trajectories and well statistically convergent. Fig. A.1 presents the result for the parameters $\gamma_s = 0.1$, $\gamma_c = 0.2$ and $g \sim 0.01$. Fig. A.2 depicts those for $\gamma_s = 0.03$, $\gamma_c = 0.25$ and $g \sim 0.03$. The parameters for Fig. A.2 leads to an intracavity photon number being about ten times smaller than that for Fig. A.1. Both reproduce the properties introduced in Chapter 3 in this thesis. A point worth noting is that the total fluctuation of the EPR-type operators (Fig. A.1 (e)) has oscillatory behavior due to the cavity effect of the mutual injection path and the gradually increasing pumping rate.

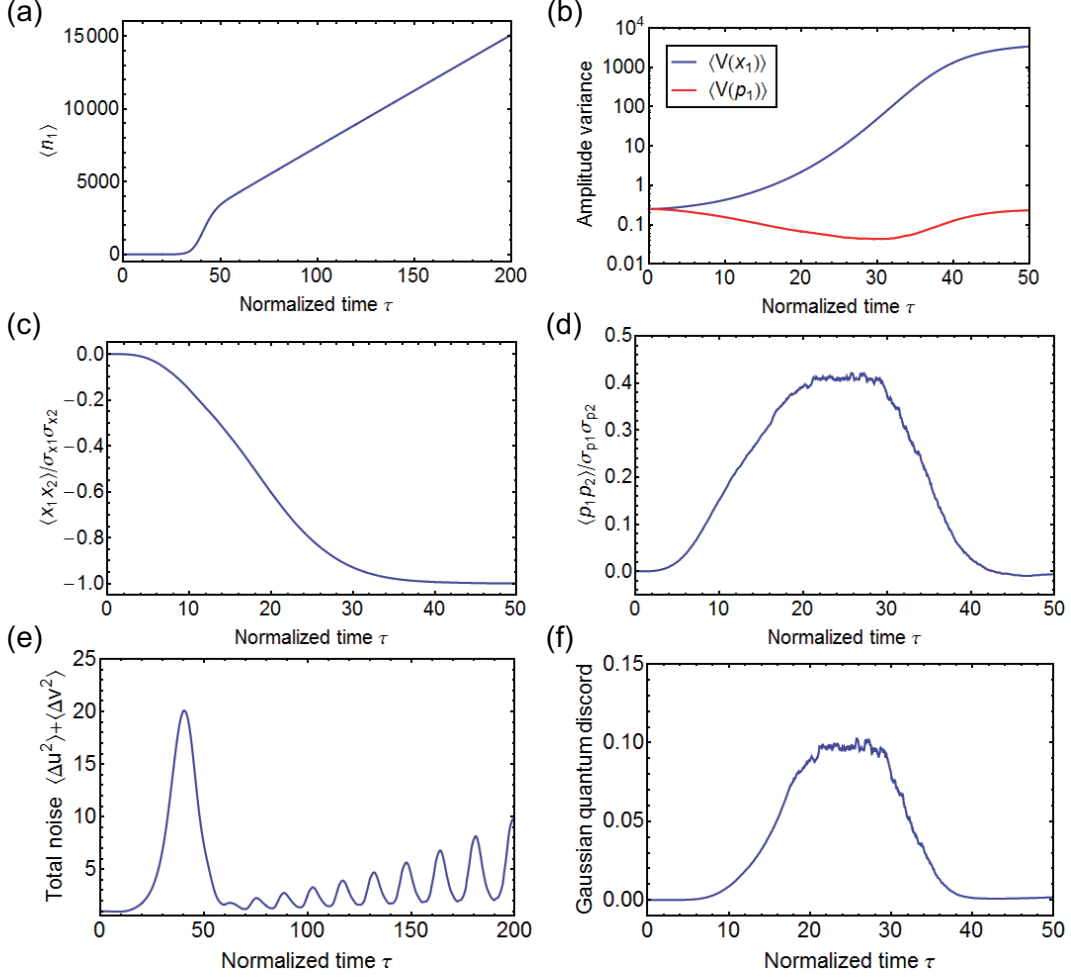


Figure A.1: Simulation result of the 2-DOPO system with 200000 samples. $\gamma_s = 0.1$, $\gamma_c = 0.2$ and $g \sim 0.01$. (a) Signal photon number in DOPO1. (b) Variances of the quadrature amplitudes $V(x_1)$ and $V(p_1)$ indicating the intracavity squeezing. (c) Correlation function $\langle x_1 x_2 \rangle$. (d) Correlation function $\langle p_1 p_2 \rangle$. (e) Total fluctuation of the EPR-type operators $\langle \Delta u^2 \rangle + \langle \Delta v^2 \rangle$. (f) Gaussian quantum discord in the system.

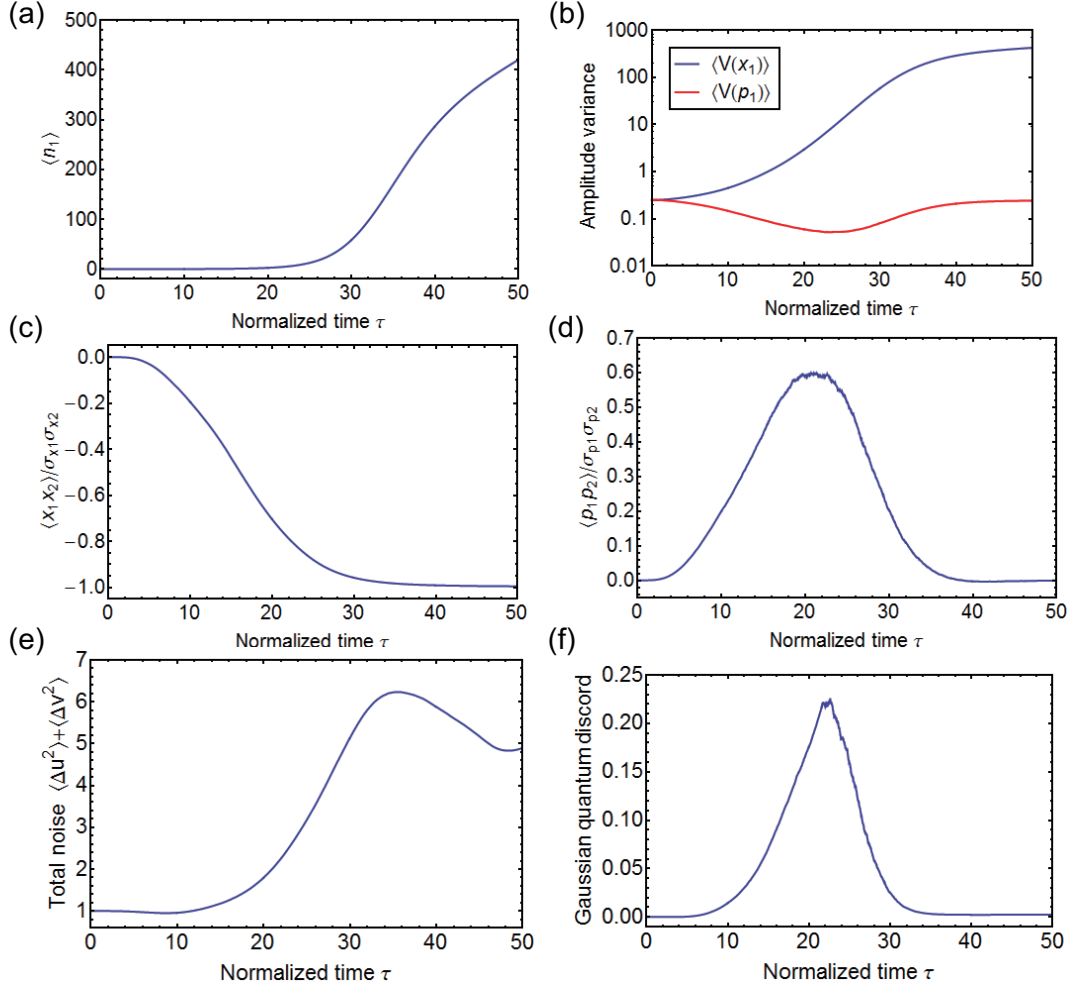


Figure A.2: Simulation result of the 2-DOPO system with 200000 samples up to $\tau = 50$. $\gamma_s = 0.03$, $\gamma_c = 0.25$ and $g \sim 0.03$. (a) Signal photon number in DOPO1. (b) Variances of the quadrature amplitudes $V(x_1)$ and $V(p_1)$ indicating the intracavity squeezing. (c) Correlation function $\langle x_1 x_2 \rangle$. (d) Correlation function $\langle p_1 p_2 \rangle$. (e) Total fluctuation of the EPR-type operators $\langle \Delta u^2 \rangle + \langle \Delta v^2 \rangle$. (f) Gaussian quantum discord in the system.

Appendix B

Additional Data of the Experiment

Here, I show the extra data of the pulsed DOPO.

B.1 RF spectrum

Fig. B.1 (a) and (b) show the RF spectra of the degenerate and non-degenerate oscillation peaks (peak 1 and 2 in Chapter 4) of the pulsed DOPO without delay lines. The spectral peak frequency reflecting the pulse repetition rate is 1.00957 GHz and is fluctuated by the order of 1 kHz. Peak 1 (Fig. B.1 (a)) has larger background spectral components than peak 2 (Fig. B.1 (b)). It is probably because the locking of peak 1 is more unstable due to a narrower oscillation peak in terms of the cavity detuning. Fig. B.1 (b) (peak 2) has clear side peaks about ± 200 kHz away from the main peak. This indicates the unstable operation of the oscillator because of the co-existence of a degenerate and non-degenerate modes, as was reported previously [212].

B.2 Beam spot

Fig. B.2 displays the beam spots of the degenerate signal modes in the system with eight beamsplitters. A slit beam profiler is used for the measurement. The pump power is 900 mW, and the delay lines are blocked except for an output port for the measurement. Fig. B.2 (a) is the spot for an even frequency state, and (b) is one for an odd frequency state. The spot size (radius) in the horizontal (w_x) and vertical (w_y) directions are $(w_x, w_y) = (1.7 \text{ mm}, 1.9 \text{ mm})$ and $(1.7 \text{ mm}, 1.5 \text{ mm})$ for Fig. B.2 (a) and (b), respectively. The shape of the spot for the odd frequency state is closer to that of the pump beam indicating that the odd frequency state is closer to the stablest condition for the main OPO ring cavity.

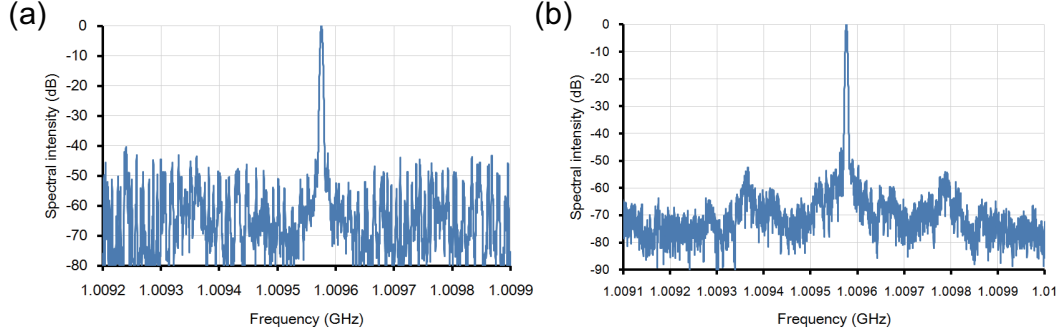


Figure B.1: RF spectra for the signal modes of the DOPO without delay lines. The peak frequency is 1.00956 GHz and corresponds to the pulse repetition frequency. The pump power is 300 mW. (a) The strongest degenerate mode (peak 1 in Chapter 4). (b) The second strongest non-degenerate mode (peak 2). (b) has side peaks indicating the unstable operation.

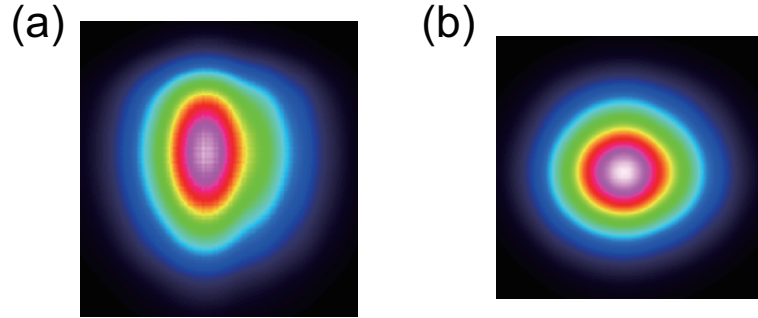


Figure B.2: Beam spots measured with a slit beam profiler for the DOPO with three delay lines. The system is strongly pumped and has degenerate modes in an odd and even frequency state. (a) Spot of an even frequency state (suitable for coherent computing). (b) One in an odd frequency state.

Bibliography

- [1] E. Ising. Beitrag zur theorie des ferromagnetismus. *Zeitschrift für Physik*, 31:253–258, 1925.
- [2] L. Onsager. Crystal statistics. I. a two-dimensional model with an order-disorder transition. *Physical Review*, 65(3,4):117–149, 1944.
- [3] F. Barahona. On the computational complexity of Ising spin glass models. *Journal of Physics A: Mathematical and General*, 15(10):3241–3253, 1982.
- [4] K. Mehlhorn and P. Sanders. *Algorithms and Data Structures: The Basic Toolbox*. Springer-Verlag, Berlin Heidelberg, 2008.
- [5] M. R. Garey and D. S. Johnson. *Computers and Intractability: A Guide to the Theory of NP-Completeness*. W. H. Freeman, New York, 1979.
- [6] S. A. Cook. The complexity of theorem-proving procedures. In *Proceedings of the 3rd ACM Symposium on Theory of Computing*, pages 151–158, New York, 1971. ACM.
- [7] R. Karp. Reducibility among combinatorial problems. In R. Miller and J. Thatcher, editors, *Complexity of Computer Computations*, pages 85–103. Plenum Press, New York, 1972.
- [8] P vs np problem. <http://www.claymath.org/millennium-problems/p-vs-np-problem>.
- [9] L. Fortnow. *The Golden Ticket: P, NP, and the Search for the Impossible*. Princeton University Press, Princeton, 2013.
- [10] L. Fortnow. The status of the P versus NP problem. *Communication of the ACM*, 52(9):78–86, 2009.
- [11] B. Korte and J. Vygen. *Combinatorial Optimization*. Springer-Verlag, Berlin Heidelberg, 2012.
- [12] W. Lenz. Beiträge zum verständnis der magnetischen eigenschaften in festen körpern. *Physikalische Zeitschrift*, 21:613–615, 1920.

- [13] R. P. Feynman. *Statistical Mechanics: A Set of Lectures*. Westview Press, Boulder, Colorado, 2nd edition, 1998.
- [14] H. A. Kramers and G. H. Wannier. Statistics of the two-dimensional ferromagnet. part I. *Physical Review*, 60:252–262, 1941.
- [15] S. M. Bhattacharjee and A. Khare. Fifty years of the exact solution of the two-dimensional Ising model by Onsager. *Current Science*, 69(10):816–820, 1995.
- [16] B. Kaufman. Crystal statistics. II. partition function evaluated by spinor analysis. *Physical Review*, 76(8):1232–1243, 1949.
- [17] M. Kac and J. C. Ward. A combinatorial solution of the two-dimensional Ising model. *Physical Review*, 88(6):1332–1336, 1952.
- [18] T. D. Schultz, D. C. Mattis, and E. H. Lieb. Two-dimensional Ising model as a soluble problem of many fermions. *Reviews of Modern Physics*, 36:856–870, 1964.
- [19] C. N. Yang. The spontaneous magnetization of a two-dimensional Ising model. *Physical Review*, 85(5):808–816, 1952.
- [20] B. Kaufman and L. Onsager. Crystal statistics. III. short-range order in a binary Ising lattice. *Physical Review*, 76(8):1244–1252, 1949.
- [21] L. Bieche, R. Maynard, R. Rammal, and J. P. Uhry. On the ground states of the frustration model of a spin glass by a matching method of graph theory. *Journal of Physics A: Mathematical and General*, 13(8):2553–2576, 1980.
- [22] Sorin Istrail. Statistical mechanics, three-dimensionality and NP-completeness: I. universality of intractability for the partition function of the Ising model across non-planar surfaces (extended abstract). In *Proceedings of the 32nd Annual ACM Symposium on Theory of Computing*, STOC '00, pages 87–96, New York, 2000. ACM.
- [23] M. Jerrum and A. Sinclair. Polynomial-time approximation algorithms for the Ising model. *SIAM Journal on Computing*, 22(5):1087–1116, 1993.
- [24] A. Sly and N. Sun. The computational hardness of counting in two-spin models on d-regular graphs. In *Proceedings of the 2012 IEEE 53rd Annual Symposium on Foundations of Computer Science*, FOCS '12, pages 361–369, Washington, DC, USA, 2012. IEEE Computer Society.
- [25] A. Sinclair, P. Srivastava, and M. Thurley. Approximation algorithms for two-state anti-ferromagnetic spin systems on bounded degree graphs. *Journal of Statistical Physics*, 155(4):666–686, 2014.
- [26] M. R. Garey, D. S. Johnson, and L. Stockmeyer. Some simplified np-complete graph problems. *Theoretical Computer Science*, 1(3):237–267, 1976.

- [27] F. Barahona, M. Grötschel, M. Jünger, and G. Reinelt. An application of combinatorial optimization to statistical physics and circuit layout design. *Operations Research*, 36(3):493–513, 1988.
- [28] M. Yannakakis. Node- and edge-deletion np-complete problems. In *Proceedings of the 10th Annual ACM Symposium on Theory of Computing*, pages 253–264, New York, 1978. ACM.
- [29] M. X. Goemans and D. P. Williamson. Improved approximation algorithms for maximum cut and satisfiability problems using semidefinite programming. *Journal of the ACM*, 42(6):1115–1145, 1995.
- [30] J. Håstad. Some optimal inapproximability results. *Journal of the ACM*, 48(4):798–859, 2001.
- [31] J. Hass, J. C. Lagarias, and N. Pippenger. The computational complexity of knot and link problems. *Journal of the ACM*, 46(2):185–211, 1999.
- [32] E. Bernstein and U. Vazirani. Quantum complexity theory. In *Proceedings of the 25th Annual ACM Symposium on Theory of Computing*, STOC '93, pages 11–20, New York, 1993. ACM.
- [33] P.W. Shor. Algorithms for quantum computation: Discrete logarithms and factoring. In *Proceedings of 35th Annual Symposium on Foundations of Computer Science*, FOCS '94, pages 124–134. IEEE, 1994.
- [34] M. A. Nielsen and I. L. Chuang. *Quantum Computation and Quantum Information*. Cambridge University Press, Cambridge, 2000.
- [35] T. D. Ladd, F. Jelezko, R. Laflamme, Y. Nakamura, et al. Quantum computers. *Nature*, 464:45–53, 2010.
- [36] P. Benioff. The computer as a physical system: A microscopic quantum mechanical hamiltonian model of computers as represented by turing machines. *Journal of Statistical Physics*, 22(5):563–591, 1980.
- [37] R. P. Feynman. Simulating physics with computers. *International Journal Theoretical Physics*, 21(6):467–488, 1982.
- [38] D. Deutsch. Quantum theory, the church-turing principle and the universal quantum computer. *Proceedings of the Royal Society of London A*, 400(1818):97–117, 1985.
- [39] D. Deutsch. Quantum computational networks. *Proceedings of the Royal Society of London A*, 425(1868):73–90, 1989.
- [40] D. Deutsch and R. Jozsa. Rapid solution of problems by quantum computation. *Proceedings of the Royal Society of London A*, 439(1907):553–558, 1992.

- [41] L. K. Grover. A fast quantum mechanical algorithm for database search. In *Proceedings of the 28th Annual ACM Symposium on the Theory of Computing*, STOC '96, pages 212–219. ACM, 1996.
- [42] L. K. Grover. Quantum mechanics helps in searching for a needle in a haystack. *Physical Review Letters*, 79:325–328, 1997.
- [43] M. Brune, E. Hagley, J. Dreyer, X. Maître, et al. Observing the progressive decoherence of the “meter” in a quantum measurement. *Physical Review Letters*, 77:4887, 1996.
- [44] P. W. Shor. Scheme for reducing decoherence in quantum computer memory. *Physical Review A*, 52:R2493(R), 1995.
- [45] D. Gottesman and I. L. Chuang. Demonstrating the viability of universal quantum computation using teleportation and single-qubit operations. *Nature*, 402:390–393, 1999.
- [46] E. Knill, R. Laflamme, and G. J. Milburn. A scheme for efficient quantum computation with linear optics. *Nature*, 409:46–52, 2001.
- [47] R. Raussendorf and H. J. Briegel. A one-way quantum computer. *Physical Review Letters*, 86(22):5188–5191, 2001.
- [48] R. Raussendorf, D. E. Browne, and H. J. Briegel. Measurement-based quantum computation on cluster states. *Physical Review A*, 68(2):022312, 2003.
- [49] S. B. Bravyi and A. Yu. Kitaev. Quantum codes on a lattice with boundary. arXiv:quant-ph/9811052v1, 1998.
- [50] R. Raussendorf and J. Harrington. Fault-tolerant quantum computation with high threshold in two dimensions. *Physical Review Letters*, 98(19):190504, 2007.
- [51] A. G. Fowler, A. M. Stephens, and P. Groszkowski. High-threshold universal quantum computation on the surface code. *Physical Review A*, 80(5):052312, 2009.
- [52] Y. Nakamura, Yu. A. Pashkin, and J. S. Tsai. Coherent control of macroscopic quantum states in a single-cooper-pair box. *Nature*, 398:786, 1999.
- [53] I. Chiorescu, Y. Nakamura, C. J. P. M. Harmans, and J. E. Mooij. Coherent quantum dynamics of a superconducting flux qubit. *Science*, 299:1869, 2003.
- [54] H. Paik, D. I. Schuster, L. S. Bishop, G. Kirchmair, et al. Observation of high coherence in josephson junction qubits measured in a three-dimensional circuit QED architecture. *Physical Review Letters*, 107(24):240501, 2011.
- [55] R. Barends, J. Kelly, A. Megrant, A. Veitia, et al. Superconducting quantum circuits at the surface code threshold for fault tolerance. *Nature*, 508:500–503, 2014.

- [56] N. C. Jones, R. Van Meter, A. G. Fowler, P. L. McMahon, et al. Layered architecture for quantum computing. *Physical Review X*, 2(3):031007, 2012.
- [57] M. Van den Nest, W. Dür, and H. J. Briegel. Classical spin models and the quantum-stabilizer formalism. *Physical Review Letters*, 98(11):117207, 2007.
- [58] M. Van den Nest, W. Dür, R. Raussendorf, and H. J. Briegel. Quantum algorithms for spin models and simulable gate sets for quantum computation. *Physical Review A*, 80(5):052334, 2009.
- [59] G. De las Cuevas, W. Dür, M. Van den Nest, and M. A. Martin-Delgado. Quantum algorithms for classical lattice models. *New Journal of Physics*, 13:093021, 2011.
- [60] K. Fujii and T. Morimae. Quantum commuting circuits and complexity of Ising partition functions. arXiv:1311.2128v1, 2013.
- [61] A. Matsuo, K. Fujii, and N. Imoto. Quantum algorithm for an additive approximation of Ising partition functions. *Physical Review A*, 90(2):022304, 2014.
- [62] I. Buluta and F. Nori. Quantum simulators. *Science*, 326(5949):108–111, 2009.
- [63] S. Lloyd. Universal quantum simulators. *Science*, 273(5278):1073–1078, 1996.
- [64] M. Greiner, O. Mandel, T. Esslinger, T. W. Hänsch, et al. Quantum phase transition from a superfluid to a Mott insulator in a gas of ultracold atoms. *Nature*, 415:39–44, 2002.
- [65] J. Billy, V. Josse, Z. Zuo, A. Bernard, et al. Direct observation of Anderson localization of matter waves in a controlled disorder. *Nature*, 453:891–894, 2008.
- [66] G. Roati, C. D’Errico, L. Fallani, M. Fattori, et al. Anderson localization of a non-interacting Bose-Einstein condensate. *Nature*, 453:895–898, 2008.
- [67] R. Jördens, N. Strohmaier, K. Günter, H. Moritz, et al. A Mott insulator of Fermionic atoms in an optical lattice. *Nature*, 455:204–207, 2008.
- [68] J. Simon, W. S. Bakr, R. Ma, M. E. Tai, et al. Quantum simulation of antiferromagnetic spin chains in an optical lattice. *Nature*, 472:307–312, 2011.
- [69] S. Taie, R. Yamazaki, S. Sugawa, and Y. Takahashi. An SU(6) Mott insulator of an atomic Fermi gas realized by large-spin Pomeranchuk cooling. *Nature Physics*, 8:825–830, 2012.
- [70] A. Friedenauer, H. Schmitz, J. Glueckert, D. Porras, et al. Simulating a quantum magnet with trapped ions. *Nature Physics*, 4(10):757–761, 2008.
- [71] K. Kim, M. S. Chang, S. Korenblit, R. Islam, et al. Quantum simulation of frustrated Ising spins with trapped ions. *Nature*, 465(7298):590–593, 2010.

- [72] R. Gerritsma, G. Kirchmair, F. Zähringer, E. Solano, et al. Quantum simulation of the dirac equation. *Nature*, 463:68–71, 2010.
- [73] J. T. Barreiro, M. Müller, P. Schindler, D. Nigg, et al. An open-system quantum simulator with trapped ions. *Nature*, 470:486–491, 2011.
- [74] K. R. Brown, C. Ospelkaus, Y. Colombe, A. C. Wilson, et al. Coupled quantized mechanical oscillators. *Nature*, 471:196–199, 2011.
- [75] C. W. Lai, N. Y. Kim, S. Utsunomiya, G. Roumpos, et al. Coherent zero-state and π -state in an exciton-polariton condensate array. *Nature*, 450:529–532, 2007.
- [76] G. Roumpos, M. D. Fraser, A. Löffler, S. Höfling, et al. Single vortex-antivortex pair in an exciton-polariton condensate. *Nature Physics*, 7:129–133, 2011.
- [77] N. Y. Kim, K. Kusudo, C. Wu, N. Masumoto, et al. Dynamical d-wave condensation of exciton-polaritons in a two-dimensional square-lattice potential. *Nature Physics*, 7:681–686, 2011.
- [78] D. Tanese, H. Flayac, D. Solnyshkov, A. Amo, et al. Polariton condensation in solitonic gap states in a one-dimensional periodic potential. *Nature Communications*, 4:1749, 2013.
- [79] F. Manni, Y. Léger, Y.G. Rubo, R. André, et al. Hyperbolic spin vortices and textures in exciton-polariton condensates. *Nature Communications*, 4:2590, 2013.
- [80] A. Das and B. K. Chakrabarti. Colloquium: Quantum annealing and analog quantum computation. *Reviews of Modern Physics*, 80(3):1061–1081, 2008.
- [81] T. Kadowaki and H. Nishimori. Quantum annealing in the transverse Ising model. *Physical Review E*, 58(5):5355–5363, 1998.
- [82] S. Kirkpatrick, C. D. Gelatt Jr., and M. P. Vecchi. Optimization by simulated annealing. *Science*, 220(4598):671–680, 1983.
- [83] E. Farhi, J. Goldstone, S. Gutmann, and M. Sipser. Quantum computation by adiabatic evolution. arXiv:quant-ph/0001106v1, 2000.
- [84] D. Aharonov, W. van Dam, J. Kempe, Z. Landau, et al. Adiabatic quantum computation is equivalent to standard quantum computation. In *Proceedings of the 45th Annual IEEE Symposium on Foundations of Computer Science*, FOCS '04, pages 42–51. IEEE, 2004.
- [85] E. Farhi, J. Goldstone, S. Gutmann, J. Lapan, et al. A quantum adiabatic evolution algorithm applied to random instances of an NP-complete problem. *Science*, 292(5516):472–475, 2001.
- [86] A. P. Young, S. Knysh, and V. N. Smelyanskiy. First-order phase transition in the quantum adiabatic algorithm. *Physical Review Letters*, 104(2):020502, 2010.

- [87] R. Schützhold and G. Schaller. Adiabatic quantum algorithms as quantum phase transitions: First versus second order. *Physical Review A*, 74(6):060304(R), 2006.
- [88] M. H. S. Amin and V. Choi. First-order quantum phase transition in adiabatic quantum computation. *Physical Review A*, 80(6):062326, 2009.
- [89] V. Choi. Avoid first order quantum phase transition by changing problem hamiltonians. arXiv:quant-ph/1004.2226, 2011.
- [90] M. H. S. Amin, P. J. Love, and C. J. S. Truncik. Thermally assisted adiabatic quantum computation. *Physical Review Letters*, 100(6):060503, 2008.
- [91] D-Wave Systems, Inc. <http://www.dwavesys.com/our-company/meet-d-wave>.
- [92] W. van Dam. In the ‘death zone’? *Nature Physics*, 3:220–221, 2007.
- [93] M. W. Johnson, M. H. S. Amin, S. Gildert, T. Lanting, et al. Quantum annealing with manufactured spins. *Nature*, 473:194–198, 2011.
- [94] S. Boixo, T. Albash, F. M. Spedalieri, N. Chancellor, et al. Experimental signature of programmable quantum annealing. *Nature Communications*, 4:2067, 2013.
- [95] N. G. Dickson, M. W. Johnson, M. H. Amin, R. Harris, et al. Thermally assisted adiabatic quantum computation. *Nature Communications*, 4:1903, 2013.
- [96] S. Boixo, T. F. Rønnow, S. V. Isakov, Z. Wang, et al. Evidence for quantum annealing with more than one hundred qubits. *Nature Physics*, 10:218–224, 2014.
- [97] T. F. Rønnow, Z. Wang, J. Job, S. Boixo, et al. Defining and detecting quantum speedup. *Science*, 345(6195):420–424, 2014.
- [98] S. Utsunomiya, K. Takata, and Y. Yamamoto. Mapping of Ising models onto injection-locked laser systems. *Optics Express*, 19(19):18091–18108, 2011.
- [99] K. Takata, S. Utsunomiya, and Y. Yamamoto. Transient time of an Ising machine based on injection-locked laser network. *New Journal of Physics*, 14(1):013052, 2012.
- [100] K. Takata and Y. Yamamoto. Data search by a coherent Ising machine based on an injection-locked laser network with gradual pumping or coupling. *Physical Review A*, 89(3):032319, 2014.
- [101] K. Takata. Master Thesis (in Japanese), 2012.
- [102] K. Wen. Injection-locked laser network for solving np-complete problems. Ph. D. Thesis, Stanford University, 2012.
- [103] Z. Wang, A. Marandi, K. Wen, R. L. Byer, et al. Coherent Ising machine based on degenerate optical parametric oscillators. *Physical Review A*, 88(6):063853, 2013.

- [104] R. J. Glauber. Photon correlations. *Physical Review Letters*, 10(3):84–86, 1962.
- [105] E. C. G. Sudarshan. Equivalence of semiclassical and quantum mechanical descriptions of statistical light beams. *Physical Review Letters*, 10(7):277, 1963.
- [106] R. J. Glauber. Coherent and incoherent states of the radiation field. *Physical Review*, 131(6):2766–2788, 1963.
- [107] P. D. Drummond and C. W. Gardiner. Generalised p-representations in quantum optics. *Journal of Physics A: Mathematical and General*, 13(7):2353–2368, 1980.
- [108] P.D. Drummond, K.J. McNeil, and D.F. Walls. Non-equilibrium transitions in sub/second harmonic generation. *Optica Acta*, 81(28):211–225, 1981.
- [109] A. Yariv and P. Yeh. *Photonics: Optical Electronics in Modern Communications*. Oxford University Press, Oxford, 2006.
- [110] D. Gottesman. The heisenberg representation of quantum computers. arXiv:quant-ph/9807006v1, 1998.
- [111] S. D. Bartlett, B. C. Sanders, S. L. Braunstein, and K. Nemoto. Efficient classical simulation of continuous variable quantum information processes. *Physical Review Letters*, 88:097904, 2002.
- [112] R. L. Byer. Optical parametric oscillators. *Quantum Electronics: A Treatise*, 1(B):587–701, 1975.
- [113] C. Tang, W. R. Bosenberg, T. Ukachi, R. J. Lane, and L. K. Cheng. Optical parametric oscillators. *Proceedings of the IEEE*, 80(3):365–374, 1992.
- [114] A. B. Dodson and Reeta Vyas. Homodyne photon statistics of the subthreshold degenerate parametric oscillator. *Physical Review A*, 47(4):3396–3412, 1993.
- [115] M. Scholz, L. Koch, and O. Benson. Statistics of narrow-band single photons for quantum memories generated by ultrabright cavity-enhanced parametric down-conversion. *Physical Review Letters*, 102(6):063603, 2009.
- [116] D. F. Walls. Squeezed states of light. *Nature*, 306(5939):141–146, 1983.
- [117] M. J. Collett and C. W. Gardiner. Squeezing of intracavity and traveling-wave light fields produced in parametric amplification. *Physical Review A*, 30(3):1386–1391, 1984.
- [118] M. J. Collett and D. F. Walls. Squeezing spectra for nonlinear optical systems. *Physical Review A*, 32(5):2887–2892, 1985.
- [119] L.-A. Wu, H. J. Kimble, J. L. Hall, and H. Wu. Generation of squeezed states by parametric down conversion. *Physical Review Letters*, 57(20):2520–2523, 1986.

- [120] K. Dechoum, P. D. Drummond, S. Chaturvedi, and M. D. Reid. Critical fluctuations and entanglement in the nondegenerate parametric oscillator. *Physical Review A*, 70(5):053807, 2004.
- [121] Y. Takeno, M. Yukawa, H. Yonezawa, and A. Furusawa. Observation of -9 db quadrature squeezing with improvement of phase stability in homodyne measurement. *Optics Express*, 15(7):4321–4327, 2007.
- [122] H. Vahlbruch, M. Mehmet, S. Chelkowski, B. Hage, et al. Observation of squeezed light with 10-db quantum-noise reduction. *Physical Review Letters*, 100(3):033602, 2008.
- [123] T. A. B. Kennedy and D. F. Walls. Squeezed quantum fluctuations and macroscopic quantum coherence. *Physical Review A*, 37(1):152–157, 1988.
- [124] M. Wolinsky and H. J. Carmichael. Quantum noise in the parametric oscillator: From squeezed states to coherent-state superpositions. *Physical Review Letters*, 60(18):1836–1839, 1988.
- [125] L. Krippner, W. J. Munro, and M. D. Reid. Transient macroscopic quantum superposition states in degenerate parametric oscillation: Calculations in the large-quantum-noise limit using the positive P representation. *Physical Review A*, 50(5):4330–4338, 1994.
- [126] M. Dakna, T. Anhut, T. Opatrný, L. Knöll, et al. Generating Schrödinger-cat-like states by means of conditional measurements on a beam splitter. *Physical Review A*, 55(4):3184–3194, 1997.
- [127] A. Ourjoumtsev, R. Tualle-Brouri, J. Laurat, and P. Grangier. Generating optical Schrödinger kittens for quantum information processing. *Science*, 312(5770):83–86, 2006.
- [128] J. S. Neergaard-Nielsen, B. Melholt Nielsen, C. Hettich, K. Mølmer, et al. Generation of a superposition of odd photon number states for quantum information networks. *Physical Review Letters*, 97(8):083604, 2006.
- [129] K. Wakui, H. Takahashi, A. Furusawa, and M. Sasaki. Photon subtracted squeezed states generated with periodically poled KTiOPO₄. *Optics Express*, 15(6):3568–3574, 2007.
- [130] T. Gerrits, Scott Glancy, T. S. Clement, B. Calkins, et al. Generation of optical coherent-state superpositions by number-resolved photon subtraction from the squeezed vacuum. *Physical Review A*, 82(3):031802(R), 2010.
- [131] A. Einstein, B. Podolsky, and N. Rosen. Can quantum-mechanical description of physical reality be considered complete? *Physical Review*, 47(10):777–780, 1935.

- [132] M. D. Reid and P. D. Drummond. Quantum correlations of phase in nondegenerate parametric oscillation. *Physical Review Letters*, 60(26):2731–2733, 1988.
- [133] M. D. Reid. Demonstration of the Einstein-Podolsky-Rosen paradox using nondegenerate parametric amplification. *Physical Review A*, 40(2):913–923, 1989.
- [134] M. D. Reid and P. D. Drummond. Correlations in nondegenerate parametric oscillation: Squeezing in the presence of phase diffusion. *Physical Review A*, 40(8):4493–4506, 1989.
- [135] P. D. Drummond and M. D. Reid. Correlations in nondegenerate parametric oscillation. II. below threshold results. *Physical Review A*, 41(7):3930–3949, 1990.
- [136] Z. Y. Ou, S. F. Pereira, H. J. Kimble, , and K. C. Peng. Realization of the Einstein-Podolsky-Rosen paradox for continuous variables. *Physical Review Letters*, 68(25):3663–3666, 1992.
- [137] M. K. Olsen and P. D. Drummond. Entanglement and the Einstein-Podolsky-Rosen paradox with coupled intracavity optical down-converters. *Physical Review A*, 71(5):053803, 2005.
- [138] A. S. Villar, L. S. Cruz, K. N. Cassemiro, M. Martinelli, et al. Generation of bright two-color continuous variable entanglement. *Physical Review Letters*, 95(24):243603, 2005.
- [139] N. Olivier and M.K. Olsen. Bright entanglement and the Einstein-Podolsky-Rosen paradox with coupled parametric oscillators. *Optics Communications*, 259(2):781–788, 2006.
- [140] J. Jing, S. Feng, R. Bloomer, and O. Pfister. Experimental continuous-variable entanglement from a phase-difference-locked optical parametric oscillator. *Physical Review A*, 74(4):041804, 2006.
- [141] X. Su, A. Tan, X. Jia, Q. Pan, et al. Experimental demonstration of quantum entanglement between frequency-nondegenerate optical twin beams. *Optics Letters*, 31(8):1133–1135, 2006.
- [142] J. Janousek, K. Wagner, J-F. Morizur, N. Treps, et al. Optical entanglement of co-propagating modes. *Nature Photonics*, 3(7):399–402, 2009.
- [143] D. Bouwmeester, J.-W. Pan, K. Mattle M. Eibl, et al. Experimental quantum teleportation. *Nature*, 390(6660):575–579, 1997.
- [144] S. L. Braunstein and H. J. Kimble. Teleportation of continuous quantum variables. *Physical Review Letters*, 80(4):869–872, 1998.
- [145] A. Furusawa, J. L. Sorensen, S. L. Braunstein, C. A. Fuchs, et al. Unconditional quantum teleportation. *Science*, 282(5389):706–709, 1998.

- [146] R. H. Kingston. Parametric amplification and oscillation at optical frequencies. *Proceedings of the Institute of Radio Engineers*, 50(4):472, 1962.
- [147] N. M. Kroll. Parametric amplification in spatially extended media and application to the design of tuneable oscillators at optical frequencies. *Physical Review*, 127(4):1207–1211, 1962.
- [148] J. A. Armstrong, N. Bloembergen, J. Ducuing, and P. S. Pershan. Interactions between light waves in a nonlinear dielectric. *Physical Review*, 127(6):1918–1939, 1962.
- [149] H. J. Carmichael. *Statistical Methods in Quantum Optics 1: Master Equations and Fokker-Planck Equations*. Springer-Verlag, Berlin Heidelberg, 2002.
- [150] D. F. Walls and G. J. Milburn. *Quantum Optics*. Springer-Verlag, Berlin Heidelberg, 2008.
- [151] P. D. Drummond, P. Deuer, T. G. Vaughan, and J. F. Corney. Quantum dynamics in phase space: from coherent states to the gaussian representation. *Journal of Modern Optics*, 54(16-17):2499–2512, 2007.
- [152] E. Wigner. On the quantum correction for thermodynamic equilibrium. *Physical Review*, 40(5):749–759, 1932.
- [153] Kôdi Husimi. Some formal properties of the density matrix. *Proceedings of the Physico-Mathematical Society of Japan. 3rd Series*, 22(4):264–314, 1940.
- [154] C. Gardiner. *Stochastic Methods: A Handbook for the Natural and Social Sciences*. Springer-Verlag, Berlin Heidelberg, 2009.
- [155] P. D. Drummond, K. J. McNeil, and D. F. Walls. Non-equilibrium transitions in sub/second harmonic generation: I. semiclassical theory. *Optica Acta*, 27(3):321–335, 1980.
- [156] M. D. Reid and B. Yurke. Effect of bistability and superpositions on quantum statistics in degenerate parametric oscillations. *Physical Review A*, 46(7):4131–4137, 1992.
- [157] S. Glancy and H. M. de Vasconcelos. Methods for producing optical coherent state superpositions. *Journal of Optical Society of America B*, 25(5):712–733, 2008.
- [158] L.-M. Duan, G. Giedke, J. I. Cirac, and P. Zoller. Inseparability criterion for continuous variable systems. *Physical Review Letters*, 84(12):2722–2725, 2000.
- [159] V. Vedral, M. B. Plenio, M. A. Rippin, and P. L. Knight. Quantifying entanglement. *Physical Review Letters*, 78(12):2275–2279, 1997.
- [160] M. O. Scully and M. S. Zubairy. *Quantum Optics*. Cambridge University Press, Cambridge, 1997.

- [161] B. Yurke and D. Stoler. Generating quantum mechanical superpositions of macroscopically distinguishable states via amplitude dispersion. *Physical Review Letters*, 57(1):13–16, 1986.
- [162] W. J. Munro and M. D. Reid. Transient macroscopic quantum superposition states in degenerate parametric oscillation using squeezed reservoir fields. *Physical Review A*, 52(3):2388–2391, 1995.
- [163] H. Ollivier and W. H. Zurek. Quantum discord: A measure of the quantumness of correlations. *Physical Review Letters*, 88(1):017901, 2001.
- [164] B. P. Lanyon, M. Barbieri, M. P. Almeida, and A. G. White. Experimental quantum computing without entanglement. *Physical Review Letters*, 101(20):200501, 2008.
- [165] E. Knill and R. Laflamme. Power of one bit of quantum information. *Physical Review Letters*, 81(25):5672–5675, 1998.
- [166] P. Giorda and M. G. A. Paris. Gaussian quantum discord. *Physical Review Letters*, 105(2):020503, 2010.
- [167] G. Adesso and A. Datta. Quantum versus classical correlations in gaussian states. *Physical Review Letters*, 105(3):030501, 2010.
- [168] H.-P. Breuer and F. Petruccione. *The Theory of Open Quantum Systems*. Oxford University Press, Oxford, 2007.
- [169] P. E. Kloeden and E. Platen. *Numerical Solution of Stochastic Differential Equations*. Springer-Verlag, Berlin Heidelberg, 1992.
- [170] A. Gilchrist, C. W. Gardiner, and P. D. Drummond. Positive P representation: Application and validity. *Physical Review A*, 55(4):3014–3031, 1998.
- [171] P. Deuar and P. D. Drummond. Gauge P representations for quantum-dynamical problems: Removal of boundary terms. *Physical Review A*, 66(3):033812, 2002.
- [172] K. Aihara, T. Takabe, and M. Toyoda. Chaotic neural networks. *Physics Letters A*, 144(6,7):333–340, 1990.
- [173] M. Adachi and K. Aihara. Associative dynamics in a chaotic neural network. *Neural Networks*, 10(1):83–98, 1997.
- [174] W. H. Louisell, A. Yariv, and A. E. Siegman. Quantum fluctuations and noise in parametric processes. I. *Physical Review*, 124(6):1646–1654, 1961.
- [175] J. P. Gordon, W. H. Louisell, and L. R. Walker. Quantum fluctuations and noise in parametric processes. II. *Physical Review*, 129(1):481–485, 1963.

- [176] J. A. Giordmaine and R. C. Miller. Tunable coherent parametric oscillation in linbo_3 at optical frequencies. *Physical Review Letters*, 14(24):481–485, 1965.
- [177] M. L. Bortz, M. A. Arbore, and M. M. Fejer. Quasi-phase-matched optical parametric amplification and oscillation in periodically poled linbo_3 waveguides. *Optics Letters*, 20(1):49–51, 1995.
- [178] L. E. Myers, G. D. Miller, R. C. Eckardt, M. M. Fejer, et al. Quasi-phase-matched $1.064\text{-}\mu\text{m}$ -pumped optical parametric oscillator in bulk periodically poled linbo_3 . *Optics Letters*, 20(1):52–54, 1995.
- [179] L. E. Myers, R. C. Eckardt, M. M. Fejer, R. L. Byer, et al. Quasi-phase-matched optical parametric oscillators in bulk periodically poled linbo_3 . *Journal of Optical Society of America B*, 12(11):2102–2116, 1995.
- [180] D. E. Spence, P. N. Kean, and W. Sibbett. 60-fsec pulse generation from a self-mode-locked ti:sapphire laser. *Optics Letters*, 16(1):42–44, 1991.
- [181] D. J. Jones, S. A. Diddams, J. K. Ranka, A. Stentz, et al. Carrier-envelope phase control of femtosecond mode-locked lasers and direct optical frequency synthesis. *Science*, 288(5466):635–639, 2000.
- [182] R. Holzwarth, Th. Udem, and T.W. Hänsch. Optical frequency synthesizer for precision spectroscopy. *Physical Review Letters*, 85(11):2264–2267, 2000.
- [183] Th. Udem, R. Holzwarth, and T.W. Hänsch. Optical frequency metrology. *Nature*, 416(6877):233–237, 2002.
- [184] S. T. Wong, T. Plettner, K. L. Vodopyanov, K. Urbanek, et al. Self-phase-locked degenerate femtosecond optical parametric oscillator. *Optics Letters*, 33(16):1896–1898, 2008.
- [185] S. T. Wong, K. L. Vodopyanov, and R. L. Byer. Self-phase-locked divide-by-2 optical parametric oscillator as a broadband frequency comb source. *Journal of Optical Society of America B*, 27(5):876–882, 2010.
- [186] N. Leindecker, A. Marandi, R. L. Byer, and K. L. Vodopyanov. Broadband degenerate opo for mid-infrared frequency comb generation. *Optics Express*, 19(7):6296–6302, 2011.
- [187] A. Marandi, N. C. Leindecker, V. Pervak, R. L. Byer, et al. Coherence properties of a broadband femtosecond mid-ir optical parametric oscillator operating at degeneracy. *Optics Express*, 20(7):7255–7262, 2012.
- [188] C. W. Rudy, A. Marandi, K. A. Ingold, S. J. Wolf, et al. Sub-50 fs pulses around 2070 nm from a synchronously-pumped, degenerate opo. *Optics Express*, 20(25):27589–27595, 2012.

- [189] M. Vainio, M. Merimaa, L. Halonen, and K. Vodopyanov. Degenerate 1 ghz repetition rate femtosecond optical parametric oscillator. *Optics Letters*, 37(21):4561–4563, 2012.
- [190] A. Schliesser, N. Picqué, and Th. W. Hänsch. Mid-infrared frequency combs. *Nature Photonics*, 6(7):440–449, 2012.
- [191] R. L. Byer. Parametric oscillators and nonlinear materials. *Nonlinear Optics*, 4:47–160, 1977.
- [192] C. D. Nabors, S. T. Yang, T. Day, and R. L. Byer. Coherence properties of a doubly resonant monolithic optical parametric oscillator. *Journal of Optical Society of America B*, 7(5):815–820, 1990.
- [193] G. D. Boyd and D. A. Kleinman. Parametric interaction of focused gaussian light beams. *Journal of Applied Physics*, 39(8):3597, 1968.
- [194] B. E. A. Saleh and M. C. Teich. *Fundamentals of Photonics*. John Wiley & Sons, New York, 2007.
- [195] H. Kogelnik, E. P. Ippen, A. Dienes, and C. V. Shank. Astigmatically compensated cavities for CW dye lasers. *IEEE Journal of Quantum Electronics*, QE-8(3):373–379, 1972.
- [196] H. Kogelnik and T. Li. Laser beams and resonators. *Applied Optics*, 5(10):1550–1566, 1966.
- [197] O. Gayer, Z. Sacks, E. Galun, and A. Arie. Temperature and wavelength dependent refractive index equations for MgO-doped congruent and stoichiometric LiNbO_3 . *Applied Physics B*, 91(2):343–348, 2008.
- [198] D. A. Bryan, R. Gerson, and H. E. Tomaschke. Increased optical damage resistance in lithium niobate. *Applied Physics Letters*, 44(9):847–849, 1984.
- [199] A. M. Weiner. *Ultrafast Optics*. John Wiley & Sons, New York, 2009.
- [200] E. D. Black. An introduction to Pound-Drever-Hall laser frequency stabilization. *American Journal of Physics*, 69(1):79–87, 2001.
- [201] A. Marandi, N. C. Leindecker, K. L. Vodopyanov, and R. L. Byer. All-optical quantum random bit generation from intrinsically binary phase of parametric oscillators. *Optics Express*, 20(17):19322–19330, 2012.
- [202] A. Marandi, Z. Wang, K. Takata, R. L. Byer, et al. Network of time-multiplexed optical parametric oscillators as a coherent Ising machine. *Nature Photonics*, 8(12):937–942, 2014.
- [203] M. Mézard, G. Parisi, and M. A. Virasoro. *Spin Glass Theory and Beyond*. World Scientific, Singapore, 1987.

-
- [204] J. Roslund, R. M. de Araújo, S. Jiang, C. Fabre, et al. Wavelength-multiplexed quantum networks with ultrafast frequency combs. *Nature Photonics*, 8(2):109–112, 2014.
- [205] Claude Fabre. Optical computing: The optical Ising machine. *Nature Photonics*, 8(12):883–884, 2014.
- [206] Y. Haribara, Y. Yamamoto, Ken ichi Kawarabayashi, and S. Utsunomiya. A coherent ising machine with quantum measurement and feedback control. arXiv:quant-ph/1501.07030.
- [207] J. E. Gough, R. Gohm, and M. Yanagisawa. Linear quantum feedback networks. *Physical Review A*, 78(6):062104, 2008.
- [208] J. Gough and M. R. James. The series product and its application to quantum feedforward and feedback networks. *IEEE Transactions on Automatic Control*, 54(11):2530–2544, 2009.
- [209] J. E. Gough, M. R. James, and H. I. Nurdin. Squeezing components in linear quantum feedback networks. *Physical Review A*, 81(2):023804, 2010.
- [210] L. Reichl. *The Transition to Chaos: Conservative Classical Systems and Quantum Manifestations*. Springer-Verlag, Berlin Heidelberg, 2004.
- [211] K. Mølmer, Y. Castin, and J. Dalibard. Monte Carlo wave-function method in quantum optics. *Journal of Optical Society of America B*, 10(3):524–538, 1993.
- [212] A. Marandi. Sub-harmonic generation of frequency combs for spectroscopy and quantum optics. Ph. D. Thesis, Stanford University, 2012.

List of Related Publication

1. S. Utsunomiya, K. Takata, and Y. Yamamoto. Mapping of Ising models onto injection-locked laser systems. *Optics Express*, 19(19): 18091-18108, 2011.
2. K. Takata, S. Utsunomiya, and Y. Yamamoto. Transient time of an Ising machine based on injection-locked laser network. *New Journal of Physics*, 14(1): 013052, 2012.
3. Y. Yamamoto, K. Takata, and S. Utsunomiya. Quantum computing vs. coherent computing. *New Generation Computing*, 30(4): 327-356, 2012.
4. K. Takata, and Y. Yamamoto. Data search by a coherent Ising machine based on an injection-locked laser network with gradual pumping or coupling. *Physical Review A*, 89(3): 032319, 2014.

This thesis partially includes the following paper.

5. A. Marandi, Z. Wang, K. Takata, R. L. Byer, and Y. Yamamoto. Network of time-multiplexed optical parametric oscillators as a coherent Ising machine. *Nature Photonics*, 8(12): 937-942, doi:10.1038/nphoton.2014.249, 2014.

The publication of other parts of this thesis is in preparation.

6. K. Takata and Y. Yamamoto. Quantum states in degenerate parametric oscillators coupled with mutual injection. In preparation.
7. K. Takata, A. Marandi, D. Maruo, S. Tamate, H. Sakaguchi, S. Utsunomiya and Y. Yamamoto. In preparation.